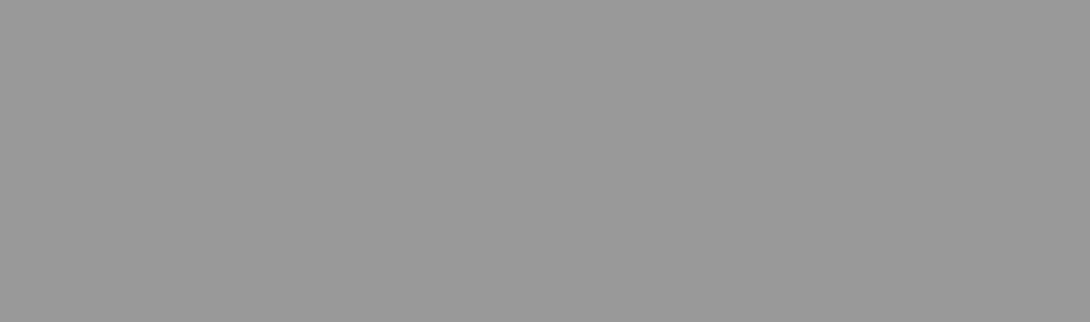

Design of new biocompatible osseointegrated and antimicrobial dental implant

Luísa Isabel Serra da Glória Fialho

UMinho | 2021

Universidade do Minho
Escola de Engenharia

Luísa Isabel Serra da Glória Fialho

Design of new biocompatible osseointegrated and antimicrobial dental implant

July 2021

Universidade do Minho
Escola de Engenharia

Luísa Isabel Serra da Glória Fialho

Design of new biocompatible osseointegrated and antimicrobial dental implant

Tese de Doutoramento
Programa Doutoral em Engenharia de Materiais

Trabalho efetuado sob a orientação da
Professora Doutora Sandra Carvalho
Professora Doutora Maria Helena Fernandes

julho de 2021

DIREITOS DE AUTOR E CONDIÇÕES DE UTILIZAÇÃO DO TRABALHO POR TERCEIROS

ACKNOWLEDGEMENTS

Em primeiro lugar, quero agradecer à minha orientadora, Professora Sandra Carvalho, por ter acreditado em mim e me ter proporcionado a oportunidade de realizar este trabalho, pelos conselhos e conhecimentos científicos transmitidos. Um "muito obrigada" não faz jus ao quão grata estou e me sinto! Quero agradecer à minha co-orientadora, Professora Maria Helena Fernandes, pela oportunidade de me orientar na realização dos ensaios biológicos. Agradeço ao grupo Bone Lab, particularmente à Doutora Liliana Grenho. Um especial agradecimento ao Professor Luís Silvino Marques do Departamento de Física da Universidade do Minho e à Professora Mariana Henriques do Departamento de Engenharia Biológica da Universidade do Minho. Cabe ainda um especial agradecimento ao colega Doutor Sebastian Calderon Velasco, do INL. A todos os meus colegas do grupo SMF obrigada por me ajudarem direta ou indiretamente no desenvolvimento deste trabalho, em particular à minha "mentora" – Cristiana Alves. Também quero agradecer aos colegas do grupo SEG-CEMMPRE.

A minha mais profunda gratidão ao meu André, por todo o amor e amizade. Obrigada ao "grupo do povo" por me fazerem sentir que a vossa tão amada cidade é agora a minha segunda casa. Às minhas amigas de uma vida (Raquel, Cátia, Tânia e Soraia) e à Ana Isabel e Sandra por estarem sempre à distância de uma chamada/mensagem e nunca me deixarem sentir que estou (fisicamente) longe. Aos amigos *FCTenses* por me lembrarem que Lisboa será sempre (também) minha casa. Por fim, mas não menos importantes, à minha família. Um especial agradecimento aos meus pilares, os meus pais e a minha irmã, sem eles não teria sido impossível chegar até aqui. Quero também demonstrar a minha gratidão à vida, que me permite evoluir diariamente, às oportunidades, aos sucessos, aos desafios e conquistas. Às minhas estrelas, obrigada por iluminarem o meu caminho, sobretudo nos momentos mais escuros.

Agradeço os apoios financeiros recebidos no âmbito do projeto HEALTHYDENT, POCI-01-0145-FEDER-030708, que tornou possíveis as minhas participações em conferências internacionais e deslocações científicas.

Este trabalho foi financiado pelo Programa Operacional Norte 2020, cofinanciado pelo Fundo Social Europeu, no âmbito do projeto NORTE-08-5369-FSE-000047, Programa de Doutoramento Nacional em Engenharia e Proteção de Superfícies, com referência UMINHO/BD/31/2016.

STATEMENT OF INTEGRITY

I hereby declare having conducted this academic work with integrity. I confirm that I have not used plagiarism or any form of undue use of information or falsification of results along the process leading to its elaboration.

I further declare that I have fully acknowledged the Code of Ethical Conduct of the University of Minho.

RESUMO

Como alternativa aos implantes dentários convencionais de Ti, foi realizada uma biofuncionalização de superfícies de Ta por diferentes tratamentos de superfície de modo a aumentar a bioatividade da superfície bem como dotá-la de capacidade bactericida. Para alcançar este design inovador, a estratégia adotada prendeu-se com duas etapas principais: i) desenvolvimento de uma superfície bioativa baseada no efeito sinergético da camada anódica de Ta_2O_5 com (nano a micro) porosidades e enriquecida por elementos osteocondutores; ii) desenvolvimento do sistema antimicrobiano pela deposição, por pulverização catódica, de NPs de Zn/ZnO na superfície de Ta_2O_5, com ou sem uma fina camada de carbono.

O primeiro tratamento funcional consistiu em duas etapas de anodização. A anodização inicial revelou-se sensível à concentração do eletrólito levando a uma curva j-t instável, ao aumento de temperatura do eletrólito e a uma morfologia final porosa ordenada e homogénea. A segunda anodização teve como finalidade incorporar elementos osteocondutores (Ca; P e/ou Mg) com uma razão de Ca/P biomimética. Duas abordagens foram propostas: anodização e/ ou polarização inversa. Os elementos osteocondutores foram incorporados na camada porosa de Ta_2O_5 sem comprometer a morfologia, porém a secção transversal das superfícies revelou uma estrutura lamelar inviável para aplicações biomédicas. Numa segunda abordagem, foi adotado o processo de oxidação por micro-arco onde foi possível otimizar uma estrutura (micro+nano) -porosa de Ta_2O_5 com Ca e P. Posteriormente, NPs de Zn (Zn/ZnO – *core/shell*) foram depositadas por pulverização catódica nas superfícies bioativas com (ou sem) uma camada adicional de carbono para controlar a libertação dos iões Zn^{2+}.

A adesão celular inicial foi garantida em todas as superfícies, destacando-se a superfície de Ta_2O_5 com NPs e a camada de carbono, que traduziu a maior taxa de proliferação celular. As duas superfícies com NPs apresentaram atividade antibacteriana contra *S. aureus* e a maior inibição das bactérias sésseis foi observada na superfície com as NPs Zn/ZnO sem a camada de carbono. Graças ao excelente desempenho *in vitro* das superfícies de Ta nanoestruturadas com elementos osteocondutores, este trabalho é um progresso na estratégia para desenvolver uma nova geração de implantes dentários simultaneamente capazes de promover a osteointegração e prevenir infeções implantares.

Palavras-chave: Anodização; Biofuncionalização; MAO/PEO; Pulverização catódica; Tântalo.

ABSTRACT

As alternative to the conventional Ti dental implants surfaces, Ta surface biofunctionalization was investigated using different surface treatments in order to enhance the surface bioactivity as well as endow it with bactericidal ability. To achieve this innovative design, the adopted strategy was accomplished in two main steps: i) development of a bioactive surface based on the synergetic effect of anodic Ta_2O_5 with multilevel porosity (nano to micro) with osteoconductive elements incorporated; ii) development of an antimicrobial delivery system by deposition, by magnetron sputtering, of Zn/ZnO nanoparticles deposited onto the anodic Ta_2O_5 structured surface with or without an additional thin carbon layer.

The first functional treatment consisted of two anodization steps. The initial anodization-step was sensible to the electrolyte concentration leading to an unstable j-t curve and to a strong electrolyte temperature increase and a quite ordered and homogeneous porous nanopattern. A second anodization was carried out to obtain a porous structure enriched with osteoconductive elements (Ca, P and/or Mg), attaining a biomimetic Ca/P ratio. Two approaches were proposed: anodization and/or reverse polarization. The osteoconductive elements were successfully incorporated onto the porous Ta_2O_5 layer without compromising the nanostructure, however the cross-sectional analysis revealed an unsuitable lamellar structure for biomedical applications. As second approach, micro-arc oxidation process was adopted where it was possible to optimize a (micro+nano)porous CaP-containing Ta_2O_5 surface. Afterwards, Zn NPs (Zn/ZnO core-shell structure) were deposited by magnetron sputtering onto the bioactive surfaces with (or without) an additional carbon layer, for Zn^{2+} ions release control.

The initial osteoblasts adhesion was ensured on all surfaces, but the porous Ta_2O_5 surface with the Zn/ZnO NPs and the carbon layer stood out, which also translated to a higher proliferation rate. Both Zn-containing surfaces presented antibacterial activity against *S. aureus* and the greatest sessile bacteria inhibition was observed on the surface with the Zn/ZnO NPs without the carbon layer. Due to the excellent *in vitro* performance of the nanostructured Ta surface with osteoconductive elements, this work is clearly a progress on the strategy to develop a new generation of dental implants that can simultaneously promote osseointegration and prevent implant's infection.

Keywords: Anodization; Biofunctionalization; MAO/PEO; Sputtering; Tantalum.

TABLE OF CONTENTS

LIST OF FIGURES

LIST OF TABLES

LIST OF ABBREVIATIONS

AFM – Atomic force microscopy

at.% - atomic % concentration

bcc - body-centered cubic

BE – Binding energy

BSE – Backscattered electrons

C – Carbon

Ca – Calcium

Ca^{2+} - Calcium ions

CaA – Calcium Acetate

CaP – Calcium phosphate(s)

CFU – Colony forming units

CP-TI – Commercially pure Titanium grade 2

DC- Direct current

EDS - Energy dispersive spectroscopy

EG - Ethylene glycol

ES – Electrolyte solution

F^- – Fluoride ion

FDA – Food drugs administration

FIB – Focused ion beam

H_2SO_4 – Sulfuric acid

HF – Hydrofluoric acid

ICS-OES - Inductively coupled plasma optical emission spectroscopy

j-t curve – current density – time curve

KE – Kinetic energy

MAO – Micro-arc oxidation

Mg – Magnesium

Na- Sodium

NH_4F – Ammonium fluoride

NPs - nanoparticles

OD – Optical density

P – Phosphorous

PEO- Plasma electrolytic oxidation

PO_4^{3-} - Phosphate ion

RFU - Relative fluorescent units

ROS – Reactive oxygen species

RP- Reverse polarization

SBF- Simulated body fluid

SD – Standard deviation

SE – Secondary electrons

SEM – Scanning electron microscopy

STEM – Scanning transmission electron microscopy

Ta – Tantalum

Ta_2O_5 – Tantalum oxide (tantalum pentoxide)

Ti - Titanium

TiO_2 – Titanium oxide (titanium dioxide)

TEM – Transmission electron microscopy

XPS - X-ray Photoelectron Spectroscopy

XRD - X-ray diffraction

Z – Atomic number

Zn – Zinc

Zn^{2+} - Zinc ion

ZnO – Zinc oxide

β-GP - β-glycerolphosphate disodium salt pentahydrate

θ – Contact angle

θ_w – Water contact angle

CHAPTER I - INTRODUCTION

1 Introduction

The past years have seen an intensification of technological development in instruments and equipment that enhance the quality of life of the human being. In medicine, the development and/or the improvement of diagnostic methods and surgery procedures have been crucial to the cure of some diseases, such as in the odontology area. As a reliable and popular treatment for replace the missing teeth with an improvement of aesthetic issues [1], the current trend in dental implant use has been substantially increasing worldwide and a boost is estimated at around 23% until 2026 in U.S. [2]. However, there are concerns about the rate of dental implants failures that ranges from 3% to 8% [3]. These non-survival implants are related to biological complications regarding the poor surface bioactivity, delaying the osseointegration, and peri-implantitis, an inflammatory disease occurring after the soft-hard tissue margin recedes [4] triggering subsequently aesthetic issues. Nevertheless, some post-surgery complications can occur and can cause the implant removal [5], such as an improper healing process (early osseointegration), that affects around 47% of patients, and an improper implant loading, affecting 53% of the cases [6]. In fact, only after the osseointegration is complete the artificial crown will support the daily loads of the patient during the occlusion [7], which means that a delayed osseointegration requires a long non-operational time, while can lead to a probability increase of microorganism entry near the surgical site. It thus emerges the need to overcome these problems by looking for bioactive materials and functionalization's techniques to improve osseointegration and, at the same time, endowing the implant with an antimicrobial behaviour.

Nowadays, titanium (Ti) segment dominates the product market to the wide use of dental implants made up of titanium due to its biocompatible nature [8]. However, as Ti dental implants have a poor bioactivity, they show a slow osseointegration, enhancing the probability of microorganisms' entrance in the oral environment, which can induce the appearance of infections and consequent complications [9].

Bioactivity can be enhanced by controlling the implant chemical composition [10] as well as by modifying the oxide film properties, such as roughness [11-14], porous structures [11, 12, 15] and wettability [16]. The oxide surface shows bioactivity since it promotes the interaction between bone progenitor cells and the oxide layer [5, 15]. Furthermore, the incorporation of bioactive elements, such as calcium [10, 17, 18], phosphorus [10, 18] and magnesium [19], demonstrates a better bone-bonding ability [20] and thus higher bioactivity [21], and consequently influences the osseointegration of the implant, the osteoconductivity surface and the early bone formation [22].

Tantalum (Ta) and its oxides are pointed as promising materials because they are bioactive *in vivo* and have a high surface energy which furthers the osseous growth and bone matrix mineralization [21, 23]. Ta porous structures have the ability to enhance/anticipate bioactivity [23] as well as calcium phosphates on metal implants [10]. There are several methods developed to create different nanotopography features, aiming to enhance osseointegration of dental implants. Among them, anodization [21, 24] and plasma electrolyte oxidation (PEO), also known as micro-arc oxidation (MAO), can be highlighted [25]. Zinc is also a bioactive element that raise the biological activity [26] but it is mostly related to its better antibacterial activity, especially as zinc oxide (ZnO) nanoparticles (NPs) [27]. Therefore, zinc incorporation has been investigated under different techniques such as magnetron sputtering [28, 29]. Thus, the surface modification of Ta substrates must be studied to achieve a bioactive and antimicrobial surface.

Concerning these issues, the challenge was to develop a new bioactive, biocompatible and antibacterial Ta-based surface of dental implants by surface modifications.

1.1 Work objectives, methodology and thesis organization

The aim of this work consisted of designing an innovative biocompatible, bioactive and antimicrobial Ta dental implant, produced by surface modification of Ta-based surfaces. This goal was achieved through two main steps: (i) production by anodization and characterization of tantalum-porous layers incorporated with Ca, P and/or Mg ions; (ii) deposition of antimicrobial agents, such as zinc nanoparticles, by DC magnetron sputtering into bioactive porous Ta surface. The surfaces' morphology and chemical composition were characterized during the optimization process, and the structural, wettability and roughness characterizations of best samples were also performed. These selected surfaces were characterized by *in vitro* osteoblastic cytocompability response and antimicrobial activity.

i. Mimic bone tissue micro/nano-structure and chemical composition

By anodization process, the surface of Ta substrate was modified in order to form an oxide layer with a micro/nano-porous structure with bioactive ions incorporated. To successfully complete this, the following objectives had to be achieved:

1. Anodization of the Ta surface: understanding the relationship between anodization conditions (electrolyte, potential, current and time) on the size, geometry and distribution of nanopores in the anodic layer.
2. Optimization of the Ta_2O_5 micro/nano-porous structure to mimic the bone tissue morphology.

3. Optimization of the protocol for the incorporation of the mentioned ions in the anodic oxide layer responsible for the improvement of the osseointegration process in order to achieve a Ca/P ratio similar to the stoichiometric hydroxyapatite (1.67) [30, 31].

ii. Antimicrobial Ta surfaces

An optimized bioactive and antimicrobial Ta dental implant was developed, followed by *in vitro* testing. This included:

1. Deposition of Zn/ZnO nanoparticles on Ta surfaces, sample surface that better mimic bone tissue morphology and chemical composition, by DC magnetron sputtering.
2. Deposition of an additional thin carbon layer above the Zn/ZnO nanoparticles to create a diffusion barrier to the zinc ions release.
3. Evaluation of the osteoblastic cytocompability (cell adhesion and proliferation): understanding the importance of the ZnO nanoparticles deposited in the osteogenic cell response.
4. *In vitro* evaluation of the antimicrobial behavior of the Ta developed surfaces.

The following chronogram summarizes the work methodology followed in this thesis, Figure I.1, which is described along the chapters.

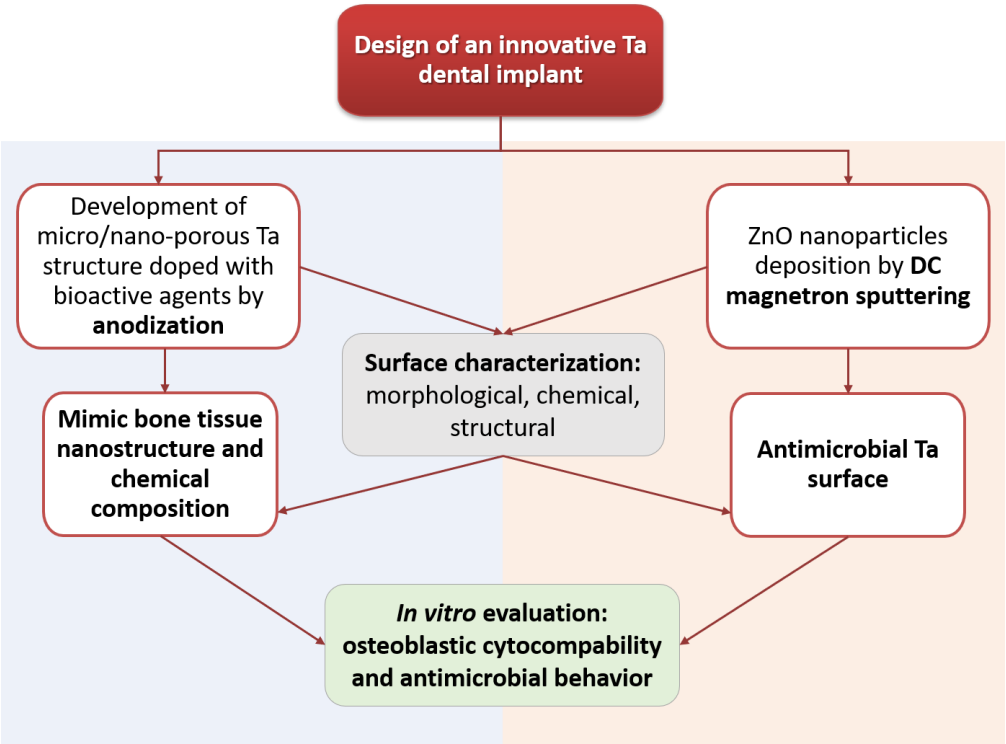

Figure I.1. Represented chronogram of work methodology followed in this thesis.

This thesis document is organized in 9 chapters in order to provide a logical sequence to understand the development of porous nanostructure of tantalum oxide by anodization or micro-arc oxidation processes and the deposition of Zn/ZnO nanoparticles by DC magnetron sputtering, and their consequent characterization. Some chapters are based on papers published in international journals, or in submission process.

CHAPTER I introduces the topic of the thesis, identifying the main objectives to be achieved based on the main challenges in the odontology area, fundamentally focused on the dental implants

CHAPTER II is dedicated on a detailed review of the literature related to biological dental implant failures and studies developed to overcome these problems.

CHAPTER III includes a brief description of the surface modification methodologies used in this thesis, as well as a brief description of the characterization techniques. Moreover, the experimental parameters and/or procedures details are provided.

CHAPTER IV presents a review of the literature related to anodization and micro-arc oxidation of Ta surface and its final properties, with special focus on biomedical applications.

CHAPTER V describes the first developed study of the anodization process in order to achieve a porous structure to mimic the bone morphology.

CHAPTER VI is related to the optimization of the biofunctionalization (i.e., bioactive agents' incorporation by anodization). The optimized surfaces were fully characterized regarding cross-section morphology, structural, wettability, roughness, and chemical composition.

CHAPTER VII is focused on mimicking the morphological and chemical composition bone by micro-arc oxidation followed by the deposition of Zn nanoparticles by DC magnetron sputtering on the micro-porous Ta_2O_5. Their complete validation concerning the osteoblastic cytocompability and the antimicrobial behavior is described in the CHAPTER VIII.

Lastly, CHAPTER IX gives an overall conclusion of this thesis and discusses the future research perspectives.

1.2 References

[1] Y. Oshida, E. B. Tuna, O. Aktören, and K. Gençay, "Dental implant systems," *International Journal of Molecular Sciences,* vol. 11, pp. 1580-1678, 2010.

[2] H. W. Elani, J. R. Starr, J. D. Da Silva, and G. O. Gallucci, "Trends in Dental Implant Use in the U.S., 1999–2016, and Projections to 2026," *Journal of Dental Research,* vol. 97, pp. 1424-1430, 2018.

[3] R. Nguyen, N. Soldatos, D. Tran, P. Stylianou, N. Angelov, and R. Weltman, "Survival of Dental Implants Replacing Previously Failed Implants: A Retrospective Study in a University Setting," *The International Journal of Oral & Maxillofacial Implants,* vol. 33, pp. 1312-1319, 2018.

[4] T. Albrektsson, B. Chrcanovic, P. O. Östman, and L. Sennerby, "Initial and long-term crestal bone responses to modern dental implants," *Periodontology 2000,* vol. 73, pp. 41-50, 2017.

[5] C. F. A. Alves, "Desenvolvimento de revestimentos nanoestruturados para implantes osteointegrados," Master, Physics Department, University of Minho, 2013.

[6] M. Esposito, J. M. Hirsch, U. Lekholm, and P. Thomsen, "Biological factors contributing to failures of osseointegrated oral implants. (I). Success criteria and epidemiology," *European Journal of Oral Sciences,* vol. 106, pp. 527-551, 1998.

[7] M. A. L. Hernandez-Rodriguez, G. R. Contreras-Hernandez, A. Juarez-Hernandez, B. Beltran-Ramirez, and E. Garcia-Sanchez, "Failure analysis in a dental implant," *Engineering Failure Analysis,* vol. 57, pp. 236-242, 2015.

[8] R. Osman and M. Swain, "A Critical Review of Dental Implant Materials with an Emphasis on Titanium versus Zirconia," *Materials,* vol. 8, pp. 932-958, 2015.

[9] C. F. Almeida Alves, A. Cavaleiro, and S. Carvalho, "Bioactivity response of Ta1-xOx coatings deposited by reactive DC magnetron sputtering," *Materials Science and Engineering C,* vol. 58, pp. 110-118, 2016.

[10] Y. T. Sul, "The significance of the surface properties of oxidized titanium to the bone response: Special emphasis on potential biochemical bonding of oxidized titanium implant," *Biomaterials,* vol. 24, pp. 3893-3907, 2003.

[11] G. Mendonça, D. B. S. Mendonça, F. J. L. Aragão, and L. F. Cooper, "Advancing dental implant surface technology - From micron- to nanotopography," *Biomaterials,* vol. 29, pp. 3822-3835, 2008.

[12] A. T. Nguyen, S. R. Sathe, and E. K. F. Yim, "From nano to micro: topographical scale and its impact on cell adhesion, morphology and contact guidance," *Journal of physics. Condensed matter : an Institute of Physics journal,* vol. 28, pp. 183001-183001, 2016.

[13] K. Anselme and M. Bigerelle, "Topography effects of pure titanium substrates on human osteoblast long-term adhesion," *Acta Biomaterialia,* vol. 1, pp. 211-222, 2005.

[14] G. Wang and X. Zhao, "The synergistic effect of hierarchical micro / nano-topography and bioactive ions for enhanced osseointegration," *Biomaterials,* vol. 34, pp. 3184-3195, 2014.

[15] L. Le Guéhennec, A. Soueidan, P. Layrolle, and Y. Amouriq, "Surface treatments of titanium dental implants for rapid osseointegration," *Dental Materials,* vol. 23, pp. 844-854, 2007.

[16] F. Rupp, R. A. Gittens, L. Scheideler, A. Marmur, B. D. Boyan, Z. Schwartz*, et al.*, "A review on the wettability of dental implant surfaces I: Theoretical and experimental aspects," *Acta Biomaterialia,* vol. 10, pp. 2894-2906, 2014.

[17] Y.-T. Sul, E.-s. Byon, and Y. Jeong, "Biomechanical measurements of calcium-incorporated oxidized implants in rabbit bone: effect of calcium surface chemistry of a novel implant," *Clinical Implant Dentistry and Related Research,* vol. 6, pp. 101-110, 2004.

[18] S. A. Alves, S. B. Patel, C. Sukotjo, M. T. Mathew, P. N. Filho, J. P. Celis*, et al.*, "Synthesis of calcium-phosphorous doped TiO2 nanotubes by anodization and reverse polarization: A promising strategy for an efficient biofunctional implant surface," *Applied Surface Science,* vol. 399, pp. 682-701, 2017.

[19] F. G. Oliveira, A. R. Ribeiro, G. Perez, B. S. Archanjo, C. P. Gouvea, J. R. Araújo*, et al.*, "Understanding growth mechanisms and tribocorrosion behaviour of porous TiO2 anodic films containing calcium, phosphorous and magnesium," *Applied Surface Science,* vol. 341, pp. 1-12, 2015.

[20] T. Miyazaki, H. M. Kim, T. Kokubo, C. Ohtsuki, H. Kato, and T. Nakamura, "Mechanism of bonelike apatite formation on bioactive tantalum metal in a simulated body fluid," *Biomaterials,* vol. 23, pp. 827-832, 2002.

[21] X. Liu, P. K. Chu, and C. Ding, "Surface modification of titanium, titanium alloys, and related materials for biomedical applications," *Materials Science and Engineering R: Reports,* vol. 47, pp. 49-121, 2004.

[22] S. Galli, Y. Naito, J. Karlsson, W. He, M. Andersson, A. Wennerberg*, et al.*, "Osteoconductive Potential of Mesoporous Titania Implant Surfaces Loaded with Magnesium: An Experimental Study in the Rabbit," *Clinical Implant Dentistry and Related Research,* vol. 17, pp. 1048-1059, 2015.

[23] V. K. Balla, S. Bodhak, S. Bose, and A. Bandyopadhyay, "Porous tantalum structures for bone implants: Fabrication, mechanical and in vitro biological properties," *Acta Biomaterialia,* vol. 6, pp. 3349-3359, 2010.

[24] F. Rupp, L. Liang, J. Geis-Gerstorfer, L. Scheideler, and F. Hüttig, "Surface characteristics of dental implants: A review," *Dental Materials,* vol. 34, pp. 40-57, 2018.

[25] T. W. Clyne and S. C. Troughton, "A review of recent work on discharge characteristics during plasma electrolytic oxidation of various metals," *International Materials Reviews,* vol. 64, pp. 127-162, 2019.

[26] Y. Li, W. Xiong, C. Zhang, B. Gao, H. Guan, H. Cheng*, et al.*, "Enhanced osseointegration and antibacterial action of zinc-loaded titania-nanotube-coated titanium substrates: In vitro and in vivo studies," *Journal of Biomedical Materials Research - Part A,* vol. 102, pp. 3939-3950, 2014.

[27] A. Sirelkhatim, S. Mahmud, A. Seeni, N. H. M. Kaus, L. C. Ann, S. K. M. Bakhori*, et al.*, "Review on zinc oxide nanoparticles: Antibacterial activity and toxicity mechanism," *Nano-Micro Letters,* vol. 7, pp. 219-242, 2015.

[28] S. Calderon V, B. Gomes, P. J. Ferreira, and S. Carvalho, "Zinc nanostructures for oxygen scavenging," *Nanoscale,* vol. 9, pp. 5254-5262, 2017.

[29] R. Wang, X. He, Y. Gao, X. Zhang, X. Yao, and B. Tang, "Antimicrobial property, cytocompatibility and corrosion resistance of Zn-doped ZrO2/TiO2 coatings on Ti6Al4V implants," *Materials Science and Engineering C,* vol. 75, pp. 7-15, 2017.

[30] C. Wang, F. Wang, and Y. Han, "The structure, bond strength and apatite-inducing ability of micro-arc oxidized tantalum and their response to annealing," *Applied Surface Science,* vol. 361, pp. 190-198, 2016.

[31] B. Wopenka and J. D. Pasteris, "A mineralogical perspective on the apatite in bone," *Materials Science and Engineering C,* vol. 25, pp. 131-143, 2005.

CHAPTER II- Work Context

2 Introduction

In this chapter, a summary of the literature related to the concepts of the main motivation of this work are presented, such as, tooth problems that can lead to its lost, dental implants materials and the main failures. Also, the most relevant works about the use of zinc (oxide) nanoparticles as antimicrobial agent are summarized.

2.1 The tooth

The tooth is an indispensable and strong structure and it has important functions, such as mastication (helps in grinding, chewing and tearing), in phonation (helps to speech) and also aesthetics (gives a good appearance to the face) [1]. There are four types of teeth with their own functions: incisors helps to cut up the food; canines, helps to tear and grasp food; premolars, helps to crush and tear food; and molars, helps to chew and grind food [2].

Each tooth has three sections: the crown, the neck and the root (Figure II.1). The crown is the visible part of the tooth which is constituted by three parts: anatomical crown (top portion of the visible tooth), enamel (cover the whole crown, is the hardest tissue in the human body which protects the tooth from bacteria and provides strength to withstand pressure for chewing), and dentine (mineralized tissue below the enamel that extends from the crown to the down root and protects the tooth from heat and cold). The neck, also called dental cervix, is located between the crown and the root where the enamel intersects the cementum. The neck is composed by the gum (also called gingiva, which is the connective tissue that is attached to the neck and the cementum), the pulp (innermost and neurovascular tissue of the tooth) and pulp cavity (also known as pulp chamber, which is the space that contains the pulp). Finally, the root is the tooth portion that extends into the bone and holds it in the place. It is formed by several parts: root canal (passageway with pulp), cementum (also named cement, which is the bone-like tissue that covers the root and it is connected to the periodontal ligament), periodontal ligament (connective tissue and collagen fiber which contains the nerves and blood vessels, that controls the force apply to chew and supply the ligament with nutrients, respectively) and jaw bone (also called alveolar bone, that surrounds the tooth's root holding it [2, 3]).

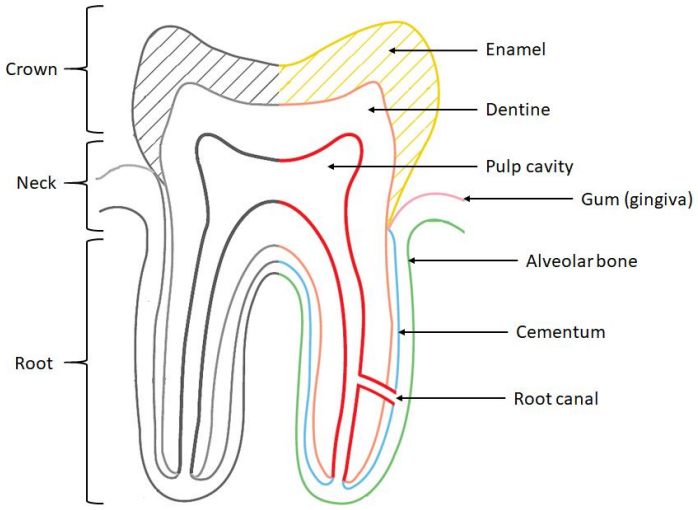

Figure II.1. Tooth anatomy. Adapted from [3].

As the teeth performed several functions on a daily basis, they are susceptible to different conditions. Mastication is the most important function of teeth, however the chewing cycles can cause wear of dental material [1, 4]. In addition, thegosis (action of sliding teeth into lateral positions) can induce friction and wear of dental material, bruxism (action of grinding or clenching the teeth without food, is related to stress and some pathologies) cause attrition and consequently the wear down enamel, leading to damage or even tooth loss [2, 3]. Thereby, friction and wear can result from direct contact between teeth and from any abrasive particles which affects around 97% of population [4]. Also tooth corrosion occurs caused by acid (from acidic foods, drinks and acid reflux) or friction (long-term dry mouth) leading to the breakdown and loss of the enamel. Additionally, the presence of bacteria provokes small holes called cavities that, when untreated, can extend reaching the pulp, leading to pulp inflammation (known as pulpitis), infection (such as abscess) or tooth loss. When this infection reaches the gum can result in the periodontal disease, which probability increases with bad oral habits, such as smoking and poor oral hygiene. In cases of severe periodontal diseases, the tooth is lost. More commonly, the presence of oral bacterial induces dental caries, causing the enamel demineralization and an early carious lesion [2, 3].

Thus, due to internal and external factors, like fatigue, poor oral hygiene, caries and accidents, around 69% of adults aged 35 to 40 have lost at least one tooth and 26% of adults aged 74 have lost all of their teeth [5]. To overcome this problem, new dental prostheses have been developed.

2.2 Dental implants

A dental prosthesis is an artificial tooth root surgically positioned in the jawbone below the gum to support an artificial crown, where the natural tooth is missing [5, 6]. Morphologically, the total implant is usually metallic and constituted by an artificial crown, an abutment to link the crown to the dental implant fixture, and whole system replace the missing tooth (Figure II.2) [7].

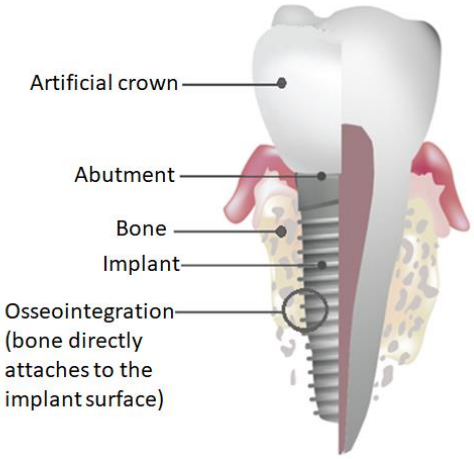

Figure II.2. Schematic representation of an endosseous dental prothesis attached to bone. Adapted from [8].

An ideal surface implant should be:

- Biocompatible: good interaction between the implant material and surrounding tissues, fluid and blood elements [6, 9];
- Bioactive: a favorable biological response is induced in organism. A bioactive material can create a mechanical and biological connection with the bone, enhancing osseointegration, its quality and resistance. The nature of the connection depends on the biomaterial surface properties [7];
- Mechanical resistant: the implant should be able to withstand forces resulting from chewing, wear and fatigue, so it must have an adequate toughness, strength and rigidity (values close to those of host bone) and also to be resistant to fracture [6, 9];
- Corrosion resistant: the organism, and specially the mouth, is a chemically aggressive environment. Also, the implant components must be resistant to corrosion, since it cannot release harmful particles to the organism [4, 6, 9, 10];
- Sterilization resistant: the implant should be sterilized before it is placed into the organism. Thus, it is important that the biomaterial does not degrade with the sterilization process [7].

The success of the dental implant is evaluated by the direct interactions between the implant and the surrounding tissues, which is a measurement of the degree of osseointegration [5].

2.2.1 Osseointegration

Dental implants have become a reliable treatment option for the replacement of missing teeth since their market entry by Brånemark in the 1960s [9]. Based on the clinical success of the first titanium (Ti) dental implant, Brånemark proposed the concept of osseointegration of the metallic biomaterial implant in bone tissue as "a direct structural and functional connection between ordered, living bone and the surface of a load carrying implant" [11, 12], on other words, osseointegration translates the stable anchorage of an implant by direct bone-to-implant contact [13-15]. During the bone healing, traumatized by surgery, the osseointegration occurs by growing the new bone (osteogenesis [16]) around the implant creating the strong structural anchorage [6]. From a clinical point of view, immediately after the implant implantation, a successful osseointegration, is a measure of implant stability: primary stability which is related to the mechanical anchorage of the implant with the surrounding bone (Figure II.3 – grey line); and the second stability is associated to the bone regeneration and remodeling phenomena (Figure II.3– orange line) [17-19].

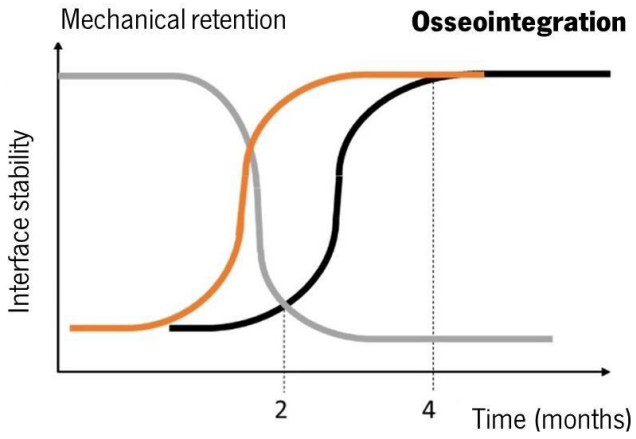

Figure II.3. Relation between the first (grey line) and the second anchorages (orange line) in the osseointegration process (black line) [20].

More recently, osseointegration was redefined as "a time-dependent healing process whereby clinical asymptomatic rigid fixation of alloplastic materials is achieved and maintained in bone during functional loading", which includes the early immune-inflammatory response, angiogenesis and osteogenesis stages [21].

During the first 24 h, the primary stability (i.e. the mechanical stability) starts with a rigidity of fixation and absence of micromotions [17, 19] and the first cell population that occupies the implant surface is composed by inflammatory cells as well as neutrophils (type of white blood cells) that dominate the implant site [21]. Also, as the injured bone matrix is exposed to extracellular fluid, non-collagenous

proteins and growth factors are released triggering the bone repair [19] (Figure II.4-a). In addition, on the first day after implantation, a blood clot is developed adjacent to the implant surface and neovascularization is initiated. After 2 to 4 days, the cells responsible for removing debris (like macrophages and monocytes) and secreting growth factors responsible for cell proliferation, angiogenesis (blood vessels formation) and collagen matrix deposition (Figure II.4-b). At the fourth day, osteoconduction (recruitment and migration of osteogenic cells) occurs [22] and the blood clot is gradually replaced by differentiating stem cells around the newly blood vessels. These stem cells differentiate into osteoblasts that it will attach to the implant surface and form collagen matrix, initiating the osteogenesis [21]. Later, the primary interlock and the implant stability decrease with time at the benefit of the secondary stability [18, 23] (Figure II.3). During this stage the bone remodeling occurs which consists on the removal of the old bone by osteoclasts and formation of new bone by osteoblasts [24]. The new bone formation, known as *de novo* bone formation [22], is observed on the implant surface (contact osteogenesis) bonding with the bone formed on the host bone (distant osteogenesis) [21] (Figure II.4-c). Then the gap (of about 60 μm) between the implant surface and host bone is completely filled with new bone, reaching the secondary stability (Figure II.4-d). At this point, the implant is able to support masticatory loads.

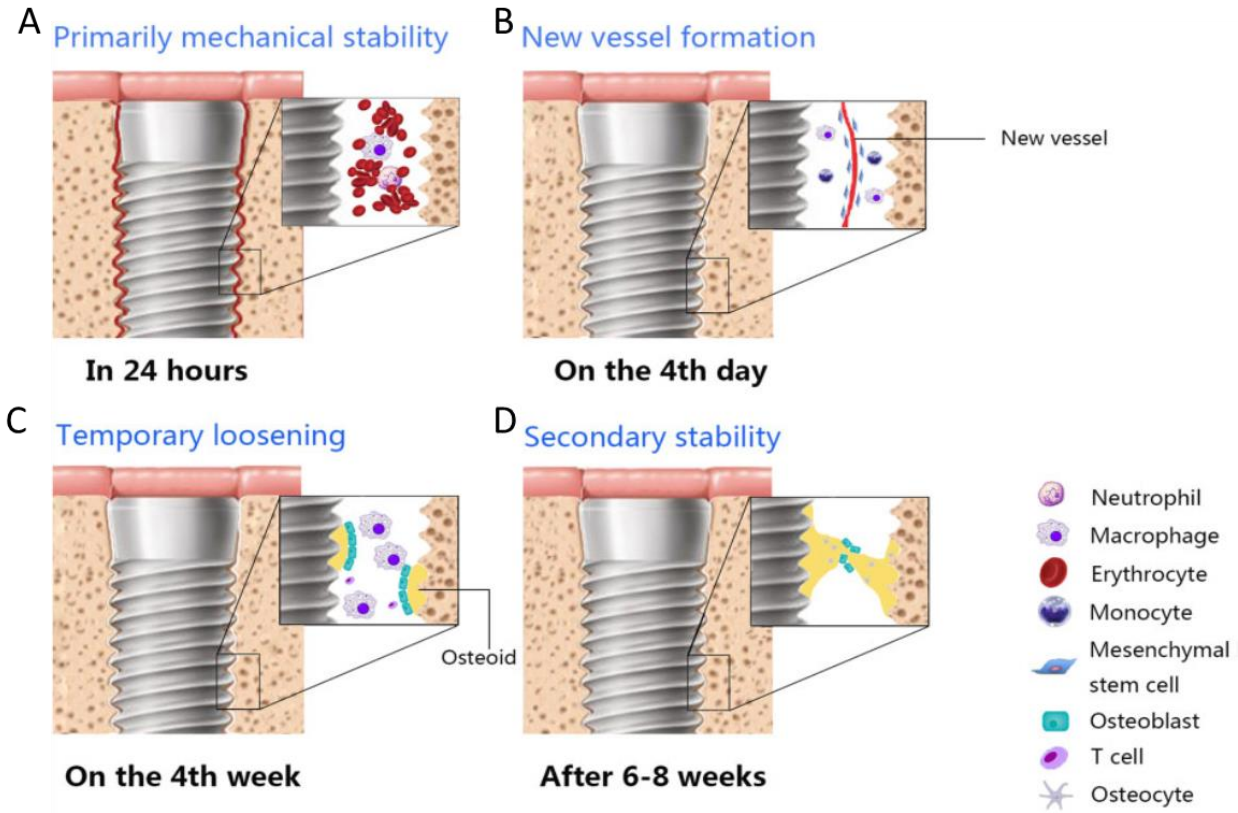

Figure II.4. Timeline for osseointegration of dental implants with respect to changes over time [21].

2.2.1.1 Key factors for the success of osseointegrated dental implants

Dental implants are designed to reach the primary mechanical stability and later osseointegration. The most popular root is the screw thread type [5, 11, 25], since it allows a great initial retention strengths [5]. In fact, the contribution of the design parameters to the implant stability is strongly related with the biomechanical behaviour and the load transfer.

The sustainability of the dental implant is firstly based on the overall analysis of the patient's clinical situation, such as periodontal conditions, occlusion, state of available host bone and general health conditions [11], osteoporosis, diabetes, endocrine and cardiovascular diseases, chemotherapy, microbial and immunoinflammatory factors and smoking habits [5, 19]. Higher bone density (higher bone quantity in the implant site) is associated to higher success rate [5, 17]. Bone quality is related to bone characteristics, as skeleton size, matrix properties, mineralization, trabecula orientation, architecture and structure. The bone quality influences the bone stimulation and consequently rules the osseointegration [5]. Surgical techniques can also influence the primary stability [17, 25, 26]. The surgical technique should have a minimal trauma and all the mechanical procedures should be performed with minimal tissue violence [19]. There are some dental implant protocols for the immediate loading (installation and prosthetic activation within 48 hours) that minimize the patient' masticator function disability during the healing time [27]. Furthermore, the induction of micromotions during functional loading will cause a lack of integration during the initial phases of bone healing [19], and later can lead to fibrous tissue formation around the implant inducing bone resorption (bone loss [26]) at the interface, negatively influencing bone remodeling and, consequently, compromising the osseointegration [17, 28]. A suitable primary stability positively affect the secondary stability [17].

The biomaterial used for dental implants include metals, ceramics and polymers. The polymers are soft with a low strength and more flexible than the other classes of biomaterials. In case of bioceramics, they also have a low strength but show an excellent biocompatibility and capacity to integrate with hard tissues and living bone. In contrast, metals show both high mechanical strength and biocompatibility [5]. Moreover, the mismatch of mechanical properties, such as stiffness and elastic modulus between the implant and the host bone, affects the long-term fixation and the implant-bone interface, respectively [29].

The dental implant surface is the only part in contact with the bio-environment and the only that directs the response and affects the mechanical strength of the implant-bone interface [6, 12]. As the biological responses will be mediated by the interactions through the implant surface, the contact between cells and the biomaterial occurs at micro/nano-level points to exchange information to lead the activation of

specific genes, remodeling, and consequently strongly determine the osseointegration process [5]. For example, a rough surface will provide a mechanical interlocking immediately after implantation and it will allow bone ingrowth [19].

Thus, regarding the implant material, there are crucial requirements for the successful early clinical outcomes of an implant system, including: the microstructure morphology (such as micro/nano-porous and nanotubular structures) and topography (moderate degree of surface roughness in a range between 0.5 to 2 μm); surface chemical composition (calcium phosphates/ apatite, grow-factors, oxide layer) and characteristics such as modulus of elasticity (close to the bone tissue), surface energy (high surface free energy) and wettability (hydrophilic surface) [5, 6, 9, 19, 28, 30, 31]. These surface properties have a strong impact on tissues responses to the implant either increasing or decreasing healing times and osseointegration [5]. Thereby, controlling all these parameters related to the implant (Figure II.5) it is possible to promote the integration of the implant with the surrounding bone tissue enhancing osseointegration [6, 9, 31].

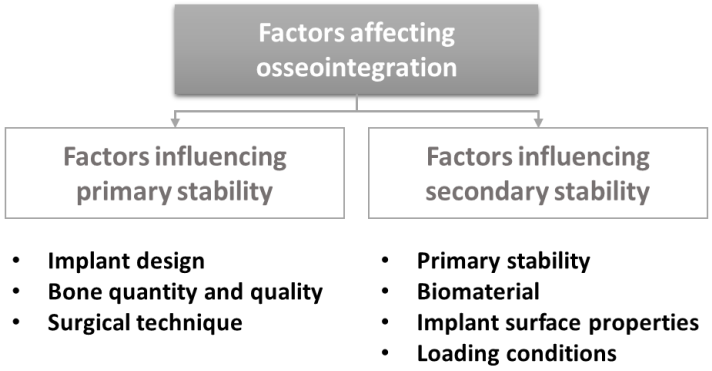

Figure II.5. Overview of the key factors that can control the stability and the long-term success of bone-implant integration [5, 6, 17, 19, 32, 33].

The dental implant success can be defined as a functional (ability to chew), osseointegrated without any pain or other pathological process and fulfill the user satisfaction (aesthetics and absence of discomfort) [34].

2.2.2 Titanium-based dental implant

Among the years, several kinds of materials have been used for fabrication of dental implants. From a chemical point of view, dental implant can be made from metals (cobalt-chromium-molybdenum, aluminium, Ti, Ti alloys, stainless steel, gold alloys, tantalum) and ceramics (alumina, hydroxyapatite, vitreous carbon) [9, 12, 35].

Bioactive ceramics, such as calcium phosphates (hydroxyapatite), present mechanical complications, including degradation and debonding. The inert ceramic zirconia oxide (ZrO_2), has been investigated due to its excellent mechanical properties [36]; however, ZrO_2 shows a low fracture strength, being significantly sensible to surface defects (manufacturing imperfections). Its mechanical failure arises mainly during surgical placement or subsequent functional loading. Although it is osteoconductive as the hydroxyapatite/calcium phosphates, from a histological and osseointegration perspectives, ZrO_2 can be recommended for biomedical applications by its good *in vitro* biological outcomes (great healing response and osseointegration) [9]. Besides the ceramic brittleness, the ceramics coated on top of metallic surfaces do not show ability to stablish covalent bonding with the metallic substrate, compromising the final performance [37].

These mechanical issues are not a concern in metallic biomaterials. Moreover, some metallic materials disclosed as biocompatible. However, in the dental implant market some of these metals, such as gold, stainless steel and cobalt-chromium, became obsoletes due to their adverse tissue reactions and low success rate. On the other hand, the "gold standard" material in dental implants is the commercially pure (CP) Ti and its alloys (e.g. Ti-6Al-4V), since it shows favorable long-term clinical survival rates due its excellent mechanical properties, low specific weight, corrosion resistant and highly biocompatible due to the stability of the passive film in biological system [6, 9, 35, 38, 39].

Even though Ti has excellent biomechanical properties, the long-term failure of Ti dental implants occurs, as around 5% of dental implant are lost during the first five years [11]. The present complications are mainly infectious, such as periimplantitis, which leads to a peri-implant osteolysis associated with an infection of soft tissues. Bone loss occurs around the implant due to risk factors (e.g., tobacco, poor oral hygiene, genetics). Moreover, Ti has a poor bioactivity which does not favor the osseointegration process, and could provoke infection and a consequent implant failure due to peri-implantitis disease [9].

2.2.2.1 Complications and failure mechanisms of titanium-based implants

The dental implant complications might indicate an increased risk of failure [34]. Failures can be divided on biological failures, mechanical failures of the implant components, iatrogenic failures and inadequate or insufficient patient adaptation (such as physiological, aesthetical and phonetical issues). These failures are depicted in Table II.1. Biological failures can be divided in primary failure, caused by traumatic surgery, infection or patient behaviour, affecting 1-2% of the modern implants, and secondary failure as consequence of a continuous marginal bone resorption [26, 40, 41]. Mechanical failures are related to the implant fracture, loss of screw access hole, abutment or occlusal screw loosing [26, 42], which with

the biological failures represent 33.6% of the implant failure [42]. Iatrogenic failures occur when there is a risk of implant malpositioning causing anatomical damages [34].

Table II.1. Dental implant failures according to osseointegration definition [34].

Classification	Characteristics
Biological • Early/ primary (before loading) • Late/ secondary (after loading)	Failure to stablish osseointegration Failure to sustain the achieved osseointegration
Mechanical	Fracture of implants, connecting screws
Iatrogenic	Nerve damages, wrong alignment of the implants
Inadequate patient adaptation	Phonetical, aesthetical, psychological problems

Ti dental implants fail due to surgical trauma, premature overloading, micro-motions caused by an inadequate prostheses geometry, inappropriate surgical placement, leakage of corrosion wear particles and insufficient quality and quantity of host bone [38].

The reported Ti implant fractures can be associated to a deficient implant design, manufacturing defects or physiological and biomechanical overload. It has been proposed that the Ti fatigue from high cyclic occlusal loading causes the Ti implant failure, as well as peri-implant marginal bone loss (resulted from the increasing bending moments and torque forces) leads to an increase of implant mobility and an eventual structural implant failure [9].

As already mentioned, osseointegration is a process dependent on the formation of a mechanical solid interface with complete union between the dental implant surface and the surrounding bone tissue [14]. After implantation, two events can happen (Figure II.6): the formation of a fibrous soft tissue capsule around the implant which does not ensure a suitable mechanical fixation causing the implant failure; or the direct bone-implant contact without a connective tissue layer (osseointegration). The fibrous encapsulation scenario is induced by micro-motions of the implant [17] and by smoother implant surfaces [28], compromising completely the early osseointegration.

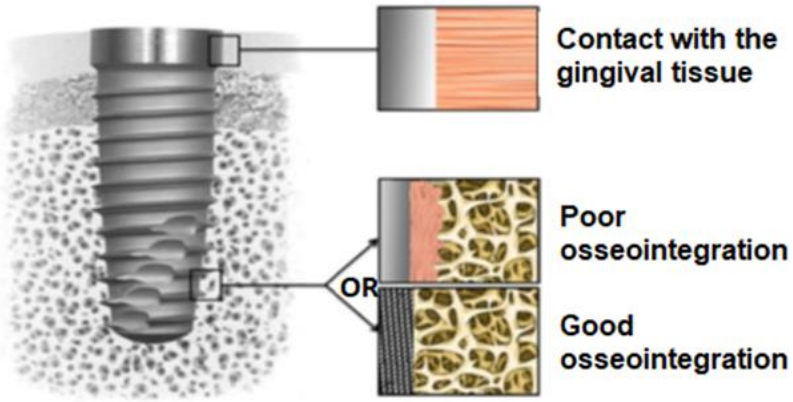

Figure II.6. Tissue integration of dental implant: intimate contact with gingival tissue, the desired contact osteogenesis (good osseointegration) rather than distance osteogenesis (poor osseointegration). Based on [18].

Another problem that could cause implant failure is the stress shielding resulting from the mismatch of mechanical properties between bone and Ti-based implants [43]. The majority of nowadays implants have a higher Young's modulus than bones (e.g. commercial Ti implants 110 GPa and cortical bones around 15 GPa) [44], and the bone is insufficiently loaded leading to bone resorption [43] and, finally end up in failure [32]. Bone resorption, also called periprosthetic osteolysis, can be induced by chronic inflammation of peri-implant tissues compromising the osseointegration process [32].

After dental implant integration, infection is a response to microbial (e.g., bacterial or fungal) contamination and it is normally followed by an inflammatory response. As there are bacterial species into oral cavity, bacterial colonization can occur during the surgery or later, from implant vicinity where bacteria are seeded [32, 45, 46]. This reaction is also one of the main causes of dental implant failure [7, 47]. Bacterial adhesion is the first and most critical step leading infection. After that, bacterial colonization and biofilm formation on the Ti implant surface can cause peri-implant diseases [32]. Peri-implant disease is a collective term for inflammatory reactions in the soft tissue surrounding functional implants. Peri-implant mucositis is a reversible inflammatory reaction in the soft tissues, whereas peri-implantitis is an inflammatory reaction in the peri-implant tissues [34], resulting in loss of supporting bone as consequence of a marginal bone resorption [34, 38], exposing the metallic implant [45]. Due to bacteria colonization and inflammation, bacterial cells and leucocytes may release lactic acid that can lead to the Ti surface corrosion, enhancing the inflammatory response and consequently leading to implant failure [32]. Therefore, poor osseointegration can be related to the presence of bacterial species at bone/implant interface.

Recently, there have been some concerns that Ti can provoke unwelcome cytotoxic and genotoxic reactions, like corrosion and hypersensitivity which can be related to debris and metallic ions release,

stimulating inflammatory reactions and consequently enhancing the peri-implant bone resorption and increasing bending forces [9, 32, 48, 49]. High concentration of Ti based material was detected in peri-implant tissues, reginal nodes and pulmonary tissues in animal models with failed implants [9]. In fact, Ti can release corrosion products (like TiO_2 and Ti hydro-oxide) into the surrounding tissues and fluids [6]. These wear particles induce the activation of the immunological system (monocytes, macrophages, neutrophils) with release of cytokines as well as induce osteoblastic cell necrosis. They also are toxic for fibroblasts through cellular DNA damage in peri-implant soft tissues, allowing bacterial colonization and increasing the inflammatory and infectious reactions and consequently peri-implantitis (Figure II.7) [50]. In addition, oxide stoichiometry's changes have been correlated to the Ti corrosion products *in vitro* [6]. The Ti hypersensitivity can impair healing which can lead to the implant failure [9].

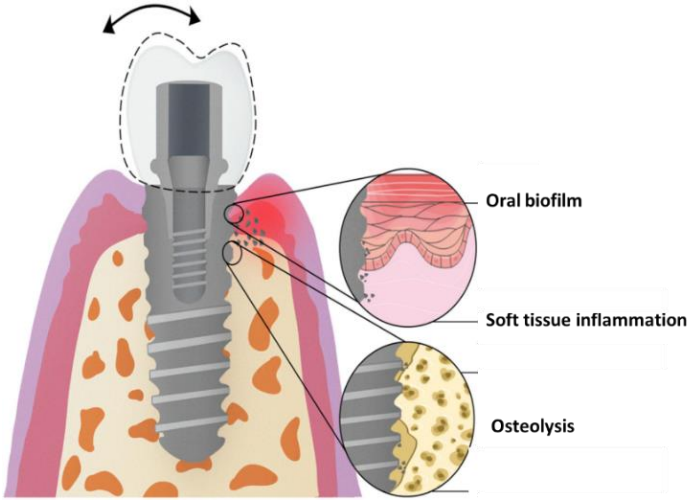

Figure II.7. Diagram of the inflammatory process induced by Ti wear particles. Based on [50].

Hence, over the year many investigations have been conducted to improve osseointegration of dental implants by several surface modifications [18]. Thus, surface biofunctionalization (i. e. material modification to have a biological function and/ or stimulus, either temporary or permanent being simultaneously biologically compatible) has emerged [51].

2.2.3 Surface modification and biofunctionalization

In a biofunctionalization strategy, the goal of surface modification is to provide surfaces with biological properties for proteins adsorption, the adhesion and differentiation of cells and tissue integration [18].

The proteins, produced by blood cells are adsorbed by implant surface having a direct effect on the subsequent biding of cells [28, 52]. Thereby protein adsorption is a critical step immediately after implantation [39]. Protein adsorption, cell migration, adhesion, proliferation and differentiation on an implant surface are extremely important pre-requisites to initiate the process of bone tissue regeneration.

These biological responses are strongly related with the implant surface chemical composition, roughness (at micro/nanoscale) and wettability (hydrophilicity) [18, 39]. Furthermore surface modification by incorporation of biological mediators of growth and differentiation may be potentially beneficial in enhancing bone healing and consequently accelerating the osseointegration process [19].

In fact, some works report that roughness at micro scale, with comparable size to cells dimensions, improve the biological responses [53]. More recent studies have reported that nanotopography may also determine the cellular responses [39], since nanoscale roughness corresponds to the dimensions of proteins and cell membrane receptors (Figure II.8) [53].

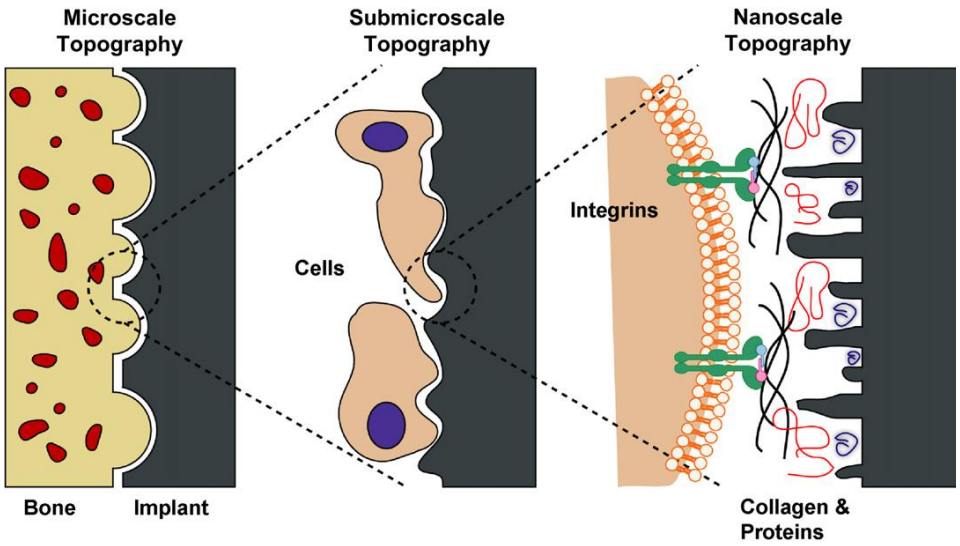

Figure II.8. Schematic of the interactions between bone and the implant surface at different topographical scales [51].

Therefore, the modification of dental implant surface at micro/nano-scale opens new investigation opportunities to decrease the healing time, consequently accelerating osseointegration, and simultaneously avoid the early bacteria adhesion and biofilm formation.

Surface modification can be broadly qualified either as the addition or removal of materials or as changing its chemical composition and/ or topography [54]. Those treatments can be achieved by methods that can be classified into three categories: mechanical, physical and chemical surface modifications (Table II.2). The most common mechanical modification procedures intend to achieve a specific topography or roughness, minimize surface contamination. This category includes machining, grinding, polishing or blasting. In physical treatments (such as, thermal spraying, physical vapour deposition and ion implantation and deposition) as well as in chemical modifications (which include chemical, electrochemical treatments, sol-gel process, chemical vapour deposition and biochemical modification)

the main goals are the enhancement of the surface protection and addition new functionalities [5, 54, 55].

Regarding to chemical modifications, these can be performed by adding inorganic phases, such as hydroxyapatite or calcium phosphates, and by incorporation of organic phases (growth factors) to stimulate direct bone-implant contact. The addition of inorganic phases induces osteoconductive properties to the implant surface, promoting the bone formation [56, 57].

Table II.2. Surface modification techniques. Based on [38, 55, 58, 59].

	Surface modification methods	Characteristics
Mechanical Methods	Machining	Remove oxide and contaminations; Produce a smooth or rough surface; Modulate in vitro bacteria adhesion
	Grinding	
	Polishing	
	Blasting	
Chemical Methods	Chemical treatment (acid etching and alkaline treatments)	Remove oxide and contaminations; Improve biocompatibility and bioactivity
	Sol-gel	Improve biocompatibility and bioactivity
	Electrochemical treatment (anodization/ micro-arc oxidation)	Produce specific surface topographies; Improve corrosion resistance; Improve biocompatibility, bioactivity or bone conductivity; Enhance BIC and osteoconductive capacity in animal studies

	CVD	Improve wear resistance, corrosion resistance and compatibility
Physical Methods	Thermal spray (plasma spray)	Improve wear resistance, corrosion resistance and biological properties
	PVD (sputtering, evaporation)	Improve wear resistance, corrosion resistance and blood compatibility
	Ion implantation and deposition	Improve wear resistance, corrosion resistance and biocompatibility

The most recent trend in titanium surface engineering is focused on mimicking natural bone architecture and chemical composition to stimulate osteoblast adhesion, proliferation and differentiation, and therefore enhancing bone formation and osseointegration [38]. Several studies demonstrate that rough surfaces (Sa around 1 μm) obtained by these modification treatments have a positive influence on bioactivity (apatite formation), protein absorption and cell behaviour [23, 36, 60]. Moreover, surface chemistry and topography separately or together play an important role in bone responses when in contact with the implant surface [61]. To mimic bone chemical composition, the main advantage of calcium phosphate coating is that it exhibits ability to bond to bone (i.e. bioactivity) [56, 57] as well as its osteoconductivity and osteoinductivity (i.e. intrinsic material properties that trigger the new bone formation) [6, 62]. Typically, Ti coated with hydroxyapatite is achieved by plasma-spraying, increasing osteoinduction, although the coating delaminates releasing particles [5]. Alternatively, calcium phosphates incorporation onto Ti surface has been investigated by anodization process (and micro-arc oxidation), modifying simultaneously the surface morphology/topography [57, 61], which accelerates the early healing [22]. Moreover, implants with an anodized surface have a better primary stability than acid etched and machined implants [25].

2.2.3.1 Biofunctionalization of titanium surfaces by anodization

The replace of missing tooth structure and restoration of oral functions with surface-modified titanium implants are the main goals in dentistry [38]. Fu *et al.* [63] presented a research trend in "titania ordered nanostructures by anodization method" shown in more than 200 publications per year in the past 7 years. Regarding biomedical applications, researchers have been paying more attention to Ti and its alloys

[54] due to the fact that about 40% of currently implant materials are based on Ti [64], and therefore, in this context, the majority of literature on anodization involves this metal and its alloys [65].

Ti anodization has been deeply investigated to develop nanostructured surfaces closely mimicking the human bone architecture [38]. TiO_2 nanotubes surface strongly improve the ability to induce the apatite formation when immersed in stimulated body fluid (SBF), when compared with flat TiO_2 surfaces [66], revealing its bioactivity. Osteoblastic cells have a rounded shape without extensions when they are on a flat Ti surface, but when they are on a nanotubular/nanoporous surface morphology they become elongated with a large number of extensions and filipodia [67], which can be related to the increased hydrophilicity of the surface. Moreover, this morphology stimulates higher levels of alkaline phosphatase (ALP) activity [68], which is a by-product of bone formation being an indicative of the activeness of osseointegration [39]. Thus, nanostructured Ti surfaces modulate cell responses, *in vitro* and *in vivo*, highlighting their potential to improve the initial healing around dental implant [30, 69]. An *in vivo* experiment with adult domestic pigs evidenced that the nanotubular morphology can in fact induce collagen type I and BMP-2 expression and higher bone-implant contact (BIC) is stabilized if the implant surface has a nanotubular layer [70]. Furthermore, TiO_2 nanotubes/nanopores layers on Ti-based implants or stents can be also efficiently used as drug delivery systems [64].

Better interlocking between the implant and ingrowth bone can be achieved by increasing the surface roughness at micrometer scale. Studies revealed that the adhesion strength of osteoblast was improved on rough surfaces as compared to smooth Ti surfaces, meaning that osteoblasts are sensible to the surface roughness [30, 32, 60, 69, 71]. The micro/nano-topography can promote mesenchymal stem cells adhesion, as their proliferation increased on the nanoscale materials [64, 68, 69]. It has been reported that nanotopography is associated with high levels of gene expression indicating rapid osteoblastic differentiation, such as the increased bone formation and torque removal value [69].

As the implant stability also depends on the fixation established with the surrounding tissues, this anchorage can be achieved by bone tissue growing into and through a porous matrix of metal. Young's modulus can be tailored to match the modulus of nanotubular Ti surface closer to the bone after anodization, and thus the stress shielding issue can be overcome [72].

Another attempt to improve implant-bone bonding involves the surface bioactivity property which is increased by the modification of the chemical implant surface [32]. Nanostructured hydroxyapatite (HAp) is reported as a reliable bone substitute and regeneration material due to its good osteoconductivity and osteoinductivity. HAp with appropriate geometry, composition (calcium to phosphorous ratio) and

crystalline structure can be similar to the natural bone mineral component and directly bind to bone tissue [73, 74]. Furthermore, HAp shows capacity to promote angiogenesis which enhances osseointegration [75, 76]. Therefore, calcium (Ca) and phosphorous (P) [32, 61, 75-81], the major components of HAp, and magnesium (Mg) [82, 83] ions within a TiO_2 layer enhances the biochemical interlocking between the bone matrix proteins and the surface, stimulating bone regeneration [13, 30, 83]. Coating Ti-based implants with hydroxyapatite (HAp) or other calcium phosphates enhance bone tissue ingrowth and vascularization by mimicking the mineral composition of natural bone [30, 57, 71]. Mg also integrates the bone mineral phase since it is known to promote bone healing which of promote the cell adhesion via ligand binding to the various integrins and also it can support better adhesion of osteoblastic cells [84, 85], contributing to a higher removal torque value [86]. Thus, nanostructured materials are able to promote cells adhesion, control their behaviour and enhance tissue formation *in vivo*.

In addition, it is important to highlight the presence of anodized surface Ti implants in the dental implants market, which can be found available in *TiUnite* (Nobel Biocare) implants since 2000 which have good survival rates and better osteoconductive behaviour *in vivo* than machined Ti [87-89], being the major surface treatment applied on titanium dental implant nowadays [90]. More recently, *TiUltra* (Nobel Biocare) surface is also tailored by anodization, from implant collar to apex (Figure II.9) [91].

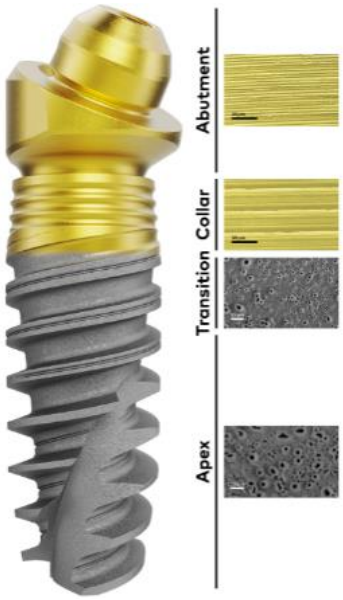

Figure II.9. TiUltra implant design [91].

2.2.4 Enhancement of antimicrobial activity

Notwithstanding, Ti implant surface allows an easy and quick bacteria colonization. [48]. Solid surfaces can be prone for bacteria attachment, proliferation and biofilm (or plaque) formation. At this stage (biofilm formation) the adherent bacteria produce a protective, polymeric, extracellular substance, turning up its eradication more complicated than planktonic bacteria (Figure II.10) [48, 92].

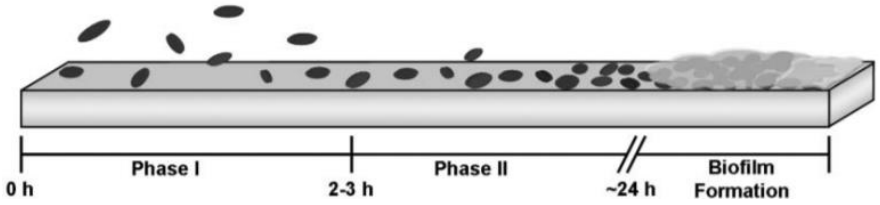

Figure II.10. Timeline of bacteria adhesion and consequent biofilm formation [89].

A wide variety of bacteria are present in the peri-implant site, but a subset of species is related to peri-implant infection, such as anaerobic Gram-negative bacilli (*Porphyromonas gingivalis*, *Campylobacter rectus*, *Aggregatibacter actinomycetemcomitans*, *Prevotella nigrescens* and *Prevotella intermedia*), anaerobic Gram-negative cocci (*Veillonella spp.*) and spirochaetes (*Treponema denticola*) [93-95]. *Staphylococcus aureus* (*S. aureus*) are responsible for infections in metallic biomaterials, such as Ti [93]. Conversely, a healthy oral environment is enriched mostly with aerobic Gram-positive bacteria, likewise *Streptococcus mitis*, *Streptococcus sanguis* and *Streptococcus oralis* [95].

In case of plaque-associated peri-implantitis (Figure II.11), factors like surgical and prosthetic as well as soft and hard tissues characteristics are suitable to biofilm adherence [96]. Moreover, rougher surfaces, (Ra around 1 to 2 μm [96]) can enhance the peri-implantitis, followed by higher bone loss [96, 97]. Therefore, it is critical to inhibit the adhesion/colonization of pathogenic bacteria on the implant surface as early as possible to minimize the risk of biofilm formation [48].

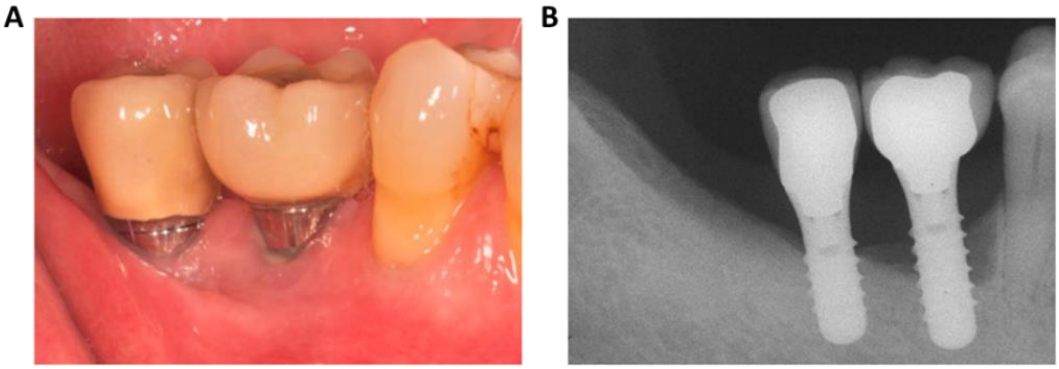

Figure II.11. A) Clinical and B) radiographic images of peri-implantitis [38].

The topographic, morphologic and physiochemical modification of Ti surfaces influence bacterial function minimizing implant-related infection [32]. Micro/nano-scale roughness substrates have been shown potential to decrease bacterial adhesion and proliferation [69]. Nanotubular structures of TiO_2 have a robust antimicrobial effect and their diameter plays a crucial role for their antibacterial ability [98].

In addition, the presence of antibacterial agents or antibacterial drug delivery from Ti nanotubes surfaces has been investigated to decrease primary bacterial adhesion and prevention of biofilm formation in order to reduce the risk of peri-implantitis-induced implant failure [38, 99]. The incorporation of inorganic bioactive elements, such as silver (Ag), copper (Cu) and zinc (Zn) have demonstrated excellent antibacterial activity against several pathogens involved in dental implants, Table II.3. [38, 99-103]. Ag is the most attractive bactericide because it shows efficacy to kill both Gram-positive and Gram-negative bacteria. Silver ions are released from Ag nanoparticles due to their high surface to volume ratios [48]. However, Ag nanoparticles revealed some cytotoxicity [104]. Copper shows attractive dual-property (both capacity of inhibiting bacterial adhesion and enhancing osteogenesis) [105], however Cu^{2+} ions does not exhibit antibacterial activity as significant as Ag^{+} and Zn^{2+} ions [106]. Zn also behaves as bone formation regulator, since Zn ion (Zn^{2+}) has the ability to regulate intracellular signaling cascades involved in osteoblastic differentiation [107] with a bactericidal effect [108]. Thus, Zn-loaded TiO_2 nanotubes had showed simultaneously ability to prevent infection and to promote the expression of osteogenesis-related genes, stimulating osteoblast proliferation and mineralization [100, 108]. Zinc has been employed to TiO_2 nanotubes by ion-implantation [109] and hydrothermal treatment [108], incorporated into TiO_2 coatings by cathodic arc deposition [110], and by micro-arc oxidation [100, 111-114].

Table II.3. Overview of antibacterial mechanisms and biological benefits of Ag^{+}, Cu^{2+} and Zn^{2+} ions. Based on [105].

Ion	Antibacterial mechanisms	Biological benefits
Ag^{+}	Disrupting functions of bacterial membranes, proteins and enzymes; Causing bacteria to form a nonculturable state; Interacting with bacteria via micro-galvanic effect.	

Cu^{2+}	High concentration of free ions that overwhelm cells; Generation of ROS causing cell membrane damage; Formation of cavities in the bacteria cell wall.	Potential to prevention of osteoporosis; Modulating differentiation of human MSCs towards an osteogenic lineage; Stimulating the proliferation of human endothelial cells and inducing vascularization.
Zn^{2+}	Generation of ROS; Excessive uptake of ions by cells; Inhibition of multiple bacterial activities.	Required for the synthesis and stabilization of many proteins; Constituent of antioxidant system; Anti-inflammatory; Stimulating bone formation and blood vessel growth.

At nanoscale size, nanoparticles show new and considerably enhanced physicochemical and biological properties as well as distinct phenomena and functionalities [115]. Moreover, this nanoscale size confers large surface areas to the nanoparticles, high surface reactivity and size-related properties (such as size, composition, crystallinity, morphology) significantly different than bulk materials. Hence, zinc oxide (ZnO) nanoparticles have been emerged as a potential candidate for several applications, likewise biomedical and antiviral areas.

2.2.5 Zinc/ zinc oxide nanoparticles to improve both biological and antibacterial properties

Several studies revealed that ZnO nanoparticles are non-toxic to human cells but are efficient against cancer cells [115]. ZnO exhibits a significant antibacterial activity when its size is in the nanometer range, since nano-sized ZnO can interact with bacteria surface and/or bacteria core opening distinct bactericidal mechanisms. The precise antibacterial mechanisms (Figure II.12) are under debate, although the proposed reactive oxygen species (ROS) formation and zinc ions release are the most suggested and accepted ones. The ROS (superoxide anion O^{2-}, hydrogen peroxide H_2O_2 and hydroxide OH^-) toxicity for bacteria is ascribed to their high reactivity and oxidizing properties. The toxicity involves the destruction of cellular components, like proteins, DNA and lipids due to their internalization through bacterial cell wall, leading to its destruction and triggering cell death. The Zn^{2+} ions released from the ZnO nanoparticles in medium also containing bacteria have a strong effect in the transport inhibition and in the amino acids metabolism and enzyme system disruption as well as trigger mechanical damage to the cell wall. Also,

the Zn^{2+} release has been reported dependent on ZnO nanoparticles size and concentration, such that larger surface area of the nanoparticles and higher concentration are responsible for antibacterial activity. Beyond these two main proposed antibacterial mechanisms, also ZnO nanoparticles internalization is pointed as bactericidal because it causes the membrane disruption and consequently its dysfunction. In addition, the creation of electrostatic forces between bacteria and ZnO nanoparticles is responsible for the bacteria growth inhibition and cell membrane damage [115]. In fact, the presence of zinc ions is associated to a bacteriostatic effect rather than bactericidal. In contrast ROS production and membrane disruption may be bactericidal. Additionally, the literature suggests that smaller nanoparticles are the most effective at reducing bacteria activity [116-118].

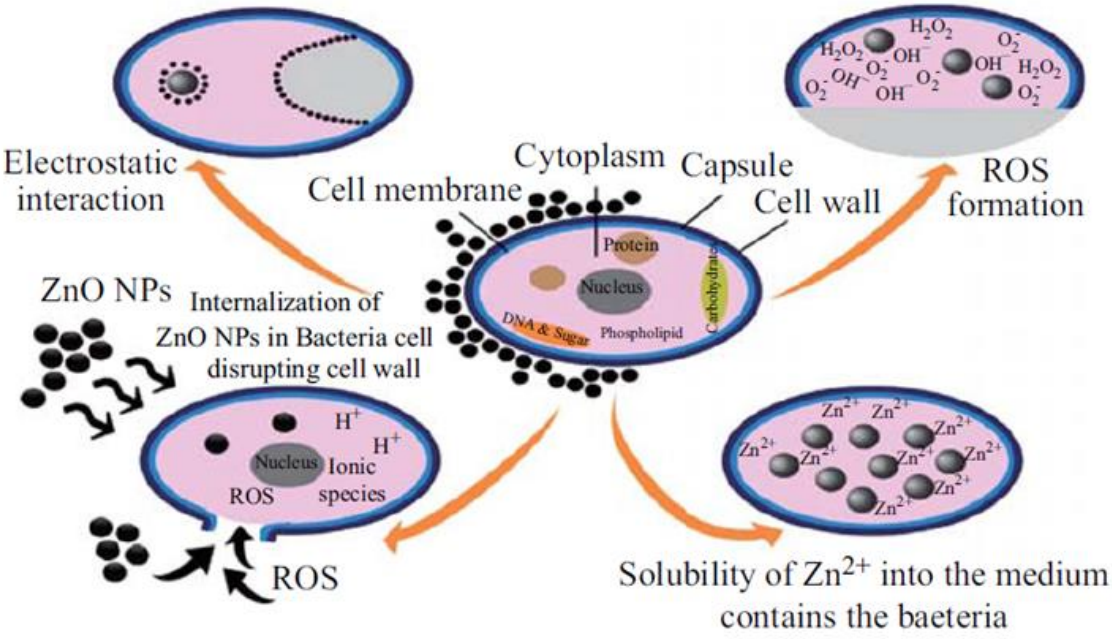

Figure II.12. Proposed mechanisms of ZnO nanoparticles antibacterial activity [112].

The nanoparticles properties can be tailored by their size and shape for the desired applications. Thus, some methods are used to synthetize ZnO nanoparticles including hydrothermal synthesis, sol-gel techniques, solution synthesis, arc discharge, laser ablation [115, 119], and more recently by magnetron sputtering [120]. Calderon *et al.* [120] used pulse DC magnetron sputtering to deposit zinc-zinc oxide (Zn-ZnO) nanoparticles with a core-shell structure, caused by Zn surface passivation, randomly distributed on the carbon surface. In this way, magnetron sputtering technique can be used to deposit ZnO particles over a metallic oxide porous substrate to develop a multifunctional antibacterial and bioactive surface.

2.3 Tantalum nanostructures for biomedical applications

As Ti based implants as already stated shows some drawbacks [9, 121], implantology is now focused on the improvement of bioactive surfaces [31]. In fact, Ta is more bioactive than CP-Ti (ANNEX I and ANNEX II) [122], having the ability to bond biologically with the bone through the formation of a bone-like apatite layer.

In this context, tantalum (Ta) is pointed as a promising material for biomedical applications. In fact, tantalum-based materials are already used in orthopedics and cardiovascular protheses, for example shoulder arthroplasty and coronary and peripheral stents, respectively [123]. Ta is a transition metal with a crystalline structure (with a predominant bcc α-Ta phase), and it has high mechanical resistance and ductility [7, 124]. It is biocompatible, highly inert and presents good corrosion resistance. However, it is limited by its high cost [123, 125] and mechanical stiffness (high elastic modulus). The development of porous surfaces can overcome this mechanical limitation [123, 125, 126]. In solid form, Ta has a Young's modulus of 186 GPa [126, 127], higher than Ti alloys (106-115 GPa) [124], which can be tailored by changing the pore volume ratio [125] from 1.4 [128] to 20 GPa [125], which is more approximate to those of cancellous (0.1-0.5 GPa) and cortical (12-18 GPa) bone [126], as observed for porous Ti (4-43 GPa) [32].

Tantalum oxide is the most common state of Ta due to its high chemical affinity to oxygen. It can have different stoichiometry being the tantalum pentoxide (Ta_2O_5) the oxide produced spontaneously. When exposed in air, a passivation layer of Ta_2O_5 is formed on the surface of Ta enhancing the corrosion resistance [126]. Furthermore, bone progenitor cells interact with the oxide layer, forming a zone which promotes a stronger bond, facilitating osseointegration. These biochemical interactions can be controlled by the oxide properties [7, 31]. Nevertheless, with high volumetric porosity and interfacial shear strength, porous Ta can achieve stronger fixation with bone tissues [126].

Metallic Ta can provide a suitable environment to the adhesion, proliferation and differentiation and mineralization of osteoblasts and hMSCs [126], which can be improved by nanostructured Ta films with hierarchical micro/nanostructured surfaces [46, 129]. Comparing with porous Ti, porous Ta structures reveal excellent cellular adherence, growth and differentiation of osteoblasts with abundant extracellular matrix formation [125]. Additionally, porous Ta can increase the differentiation of primary human osteoblasts [126]. Ta_2O_5 surface chemistry can enhance alkaline phosphate activity and promote a 30% higher rate of matrix mineralization and bone-nodule formation comparing with TiO_2 [130]. Also, the

presence of the bioactive agent (sodium) on Ta surface accelerates the apatite nucleation compared with the untreated Ta surface [122].

Pure Ta presents a significant lower bacteria adhesion compared with Ti alloy and tantalum-coated stainless steel [131]. Nanostructured Ta also presents a good antibacterial activity against *Streptococcus mutans* and *Porphyromonas gingivalis* [46]. Porous Ta does not show evidence on cytotoxicity and inflammatory responses *in vivo* [126]. However, the study developed by Chang *et al.* [132] demonstrated that amorphous Ta_2O_5, produced by reactive magnetron sputtering, has better antibacterial effect and worse cell viability when compared with crystalline β-T_2O_5, obtained by thermal annealing of Ta_2O_5 film.

Additionally, there is already a commercialized tantalum-based dental implant named *Trabecular Metal Implant* (Zimmer), displayed in Figure II.13, which accelerates healing and bone formation reveling a two-weeks final loading protocol with a 97-100% survival rate after five years [133].

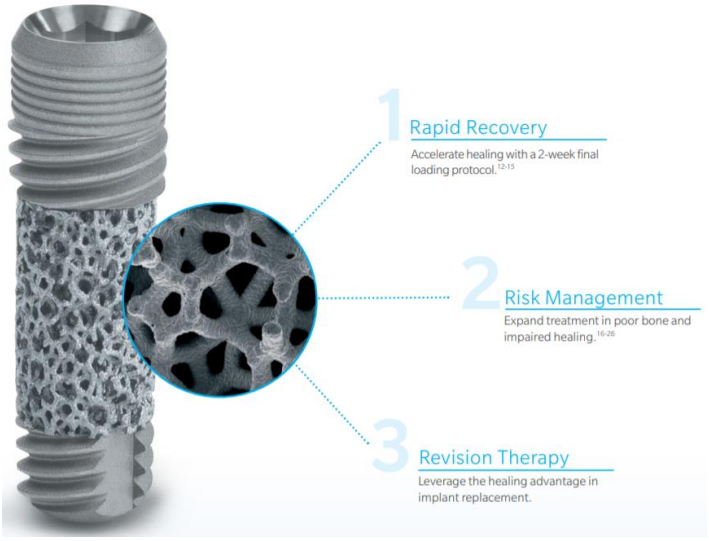

Figure II.13. Trabecular Metal Implant (Zimmer) [133].

The porous Ta metal provides a good support to the mechanical attachment [125] and offers excellent osseointegration properties [43, 124, 125]. The increased cell-material interactions on porous Ta are attributed to its chemical activity, wettability and greater surface energy compared to porous Ti [7, 125].

2.4 References

[1] P. S. Kumar, *Dental anatomy and tooth morphology*: Jaypee Brothers Publisher, 2004.

[2] A. S.-L. K. Luo. (2018, 2020-06-12). *Tooth Anatomy*. Available: https://www.healthline.com/health/tooth-anatomy

[3] C. Hollins, "Tooth anatomy," First ed: John Wiley & Sons, Inc, 2012, pp. 142-157.

[4] Z. R. Zhou and J. Zheng, "Tribology of dental materials: a review," *Journal of Physics D: Applied Physics,* vol. 41, pp. 113001-113001, 2008.

[5] L. Gaviria, J. P. Salcido, T. Guda, and J. L. Ong, "Current trends in dental implants," *Journal of the Korean Association of Oral and Maxillofacial Surgeons,* vol. 40, pp. 50-60, 2014.

[6] Y. Oshida, E. B. Tuna, O. Aktören, and K. Gençay, "Dental implant systems," *International Journal of Molecular Sciences,* vol. 11, pp. 1580-1678, 2010.

[7] C. F. A. Alves, "Desenvolvimento de revestimentos nanoestruturados para implantes osteointegrados," Master, Physics Department, University of Minho, 2013.

[8] S. Froum and G. M. Kurtzman. (2017, 2020-09-23). *Top 5 anatomical differences between dental implants and teeth that influence treatment outcomes*. Available: https://www.perioimplantadvisory.com/clinical-tips/periodontal-complications/article/16412223/top-5-anatomical-differences-between-dental-implants-and-teeth-that-influence-treatment-outcomes

[9] R. Osman and M. Swain, "A Critical Review of Dental Implant Materials with an Emphasis on Titanium versus Zirconia," *Materials,* vol. 8, pp. 932-958, 2015.

[10] T. P. Chaturvedi, "An overview of the corrosion aspect of dental implants (titanium and its alloys)," *Indian journal of dental research : official publication of Indian Society for Dental Research,* vol. 20, pp. 91-8, 2009.

[11] B. Guillaume, "Les implants dentaires: revue," *Morphologie,* vol. 100, pp. 189-198, 2016.

[12] C. M. Abraham, "A brief historical perspective on dental implants, their surface coatings and treatments," *The open dentistry journal,* vol. 8, pp. 50-55, 2014.

[13] D. M. Dohan Ehrenfest, P. G. Coelho, B. S. Kang, Y. T. Sul, and T. Albrektsson, "Classification of osseointegrated implant surfaces: Materials, chemistry and topography," *Trends in Biotechnology,* vol. 28, pp. 198-206, 2010.

[14] T. Albrektsson and C. Johansson, "Osteoinduction, osteoconduction and osseointegration," *European Spine Journal,* vol. 10, pp. 96-101, 2001.

[15] T. Albrektsson, P. I. Brånemark, H. A. Hansson, and J. Lindström, "Osseointegrated titanium implants: Requirements for ensuring a long-lasting, direct bone-to-implant anchorage in man," *Acta Orthopaedica Scandinavica ISSN:,* vol. 52, pp. 155-170, 1981.

[16] H. Pan, X. Zhao, B. W. Darvell, and W. W. Lu, "Apatite-formation ability - Predictor of "bioactivity"?," *Acta Biomaterialia,* vol. 6, pp. 4181-4188, 2010.

[17] F. Javed, H. B. Ahmed, R. Crespi, and G. E. Romanos, "Role of primary stability for successful osseointegration of dental implants: Factors of influence and evaluation," *Interventional medicine & applied science,* vol. 5, pp. 162-7, 2013.

[18] S. Lavenus, J. Rozé, G. Louarn, and P. Layrolle, "Impact of nanotechnology on dental implants," ed, 2018, pp. 83-97.

[19] S. Parithimarkalaignan and T. V. Padmanabhan, "Osseointegration: An update," *Journal of Indian Prosthodontist Society,* vol. 13, pp. 2-6, 2013.

[20] A. Cristiana Filipa Almeida, "Development of bioactive surfaces for bone ingrowth on dental implants," PhD, Department of Physics, University of Minho, 2018.

[21] Y. Wang, Y. Zhang, and R. J. Miron, "Health, Maintenance, and Recovery of Soft Tissues around Implants," *Clinical Implant Dentistry and Related Research,* vol. 18, pp. 618-634, 2016.

[22] J. E. Davies, "Understanding Peri-Implant Endosseous Healing," *Journal of Dental Education,* vol. 67, pp. 932-949, 2003.

[23] R. Smeets, B. Stadlinger, F. Schwarz, B. Beck-Broichsitter, O. Jung, C. Precht*, et al.*, "Impact of Dental Implant Surface Modifications on Osseointegration," *BioMed Research International,* vol. 2016, 2016.

[24] P. R. T. Kuzyk and E. H. Schemitsch, "The basic science of peri-implant bone healing," *Indian Journal of Orthopaedics,* vol. 45, pp. 108-115, 2011.

[25] C. N. Elias, F. A. Rocha, A. L. Nascimento, and P. G. Coelho, "Influence of implant shape, surface morphology, surgical technique and bone quality on the primary stability of dental implants," *Journal of the Mechanical Behavior of Biomedical Materials,* vol. 16, pp. 169-180, 2012.

[26] T. Albrektsson, B. Chrcanovic, P. O. Östman, and L. Sennerby, "Initial and long-term crestal bone responses to modern dental implants," *Periodontology 2000,* vol. 73, pp. 41-50, 2017.

[27] C. N. Elias, Y. Oshida, J. H. C. Lima, and C. A. Muller, "Relationship between surface properties (roughness, wettability and morphology) of titanium and dental implant removal torque," *Journal of the Mechanical Behavior of Biomedical Materials,* vol. 1, pp. 234-242, 2008.

[28] K. Kieswetter, Z. Schwartz, D. D. Dean, and B. D. Boyan, "The role of implant surface characteristics in the healing of bone," *Critical Reviews in Oral Biology and Medicine,* vol. 7, pp. 329-345, 1996.

[29] Y. J. Chen, B. Feng, Y. P. Zhu, J. Weng, J. X. Wang, and X. Lu, "Fabrication of porous titanium implants with biomechanical compatibility," *Materials Letters,* vol. 63, pp. 2659-2661, 2009.

[30] L. Le Guéhennec, A. Soueidan, P. Layrolle, and Y. Amouriq, "Surface treatments of titanium dental implants for rapid osseointegration," *Dental Materials,* vol. 23, pp. 844-854, 2007.

[31] C. F. Almeida Alves, A. Cavaleiro, and S. Carvalho, "Bioactivity response of Ta1-xOx coatings deposited by reactive DC magnetron sputtering," *Materials Science and Engineering C,* vol. 58, pp. 110-118, 2016.

[32] S. Alves, "A new concept of bio-multifunctional nanotubular surfaces for dental implants : tribocorrosion resistant , antibacterial and osteogenic," 2017.

[33] F. Rupp, L. Liang, J. Geis-Gerstorfer, L. Scheideler, and F. Hüttig, "Surface characteristics of dental implants: A review," *Dental Materials,* vol. 34, pp. 40-57, 2018.

[34] M. Esposito, J. M. Hirsch, U. Lekholm, and P. Thomsen, "Biological factors contributing to failures of osseointegrated oral implants. (I). Success criteria and epidemiology," *European Journal of Oral Sciences,* vol. 106, pp. 527-551, 1998.

[35] R. Van Noort, "Titanium: The implant material of today," *Journal of Materials Science,* vol. 22, pp. 3801-3811, 1987.

[36] X. Chen, A. Nouri, Y. Li, J. Lin, P. D. Hodgson, and C. Wen, "Effect of Surface Roughness of Ti , Zr , and TiZr on Apatite Precipitation From Simulated Body Fluid," *Biotechnology and Bioengineering,* vol. 101, pp. 378-387, 2008.

[37] M. Sowa, M. Woszczak, A. Kazek-Kęsik, G. Dercz, D. M. Korotin, I. S. Zhidkov*, et al.*, "Influence of process parameters on plasma electrolytic surface treatment of tantalum for biomedical applications," *Applied Surface Science,* vol. 407, pp. 52-63, 2017.

[38] K. Subramani and R. T. Mathew, "Titanium Surface Modification Techniques for Dental Implants—From Microscale to Nanoscale," *Emerging Nanotechnologies in Dentistry,* pp. 85-102, 2012.

[39] K. Subramanian, D. Tran, and K. T. Nguyen, "Cellular Responses to Nanoscale Surface Modifications of Titanium Implants for Dentistry and Bone Tissue Engineering Applications," *Emerging Nanotechnologies in Dentistry,* pp. 113-136, 2012.

[40] M. C. L. G. Santos;, M. I. G. Campos;, and S. R. P. Line, "Early dental implant failure : A review of the literature," *Brazilian journal of oral sciences,* vol. 1, pp. 103-111, 2002.

[41] B. R. Chrcanovic, T. Albrektsson, and A. Wennerberg, "Reasons for failures of oral implants," *Journal of Oral Rehabilitation,* vol. 41, pp. 443-476, 2014.

[42] B. E. Pjetursson, D. Thoma, R. Jung, M. Zwahlen, and A. Zembic, "A systematic review of the survival and complication rates of implant-supported fixed dental prostheses (FDPs) after a mean observation period of at least 5 years," *Clinical Oral Implants Research,* vol. 23, pp. 22-38, 2012.

[43] G. Ryan, A. Pandit, and D. P. Apatsidis, "Fabrication methods of porous metals for use in orthopaedic applications," *Biomaterials,* vol. 27, pp. 2651-2670, 2006.

[44] X. Jiang, Y. Yao, W. Tang, D. Han, L. Zhang, K. Zhao*, et al.*, "Design of dental implants at materials level: An overview," *Journal of Biomedical Materials Research Part A,* 2020.

[45] A. Mombelli and N. P. Lang, "The diagnosis," *Periodontology 2000,* vol. 17, pp. 1-51, 1998.

[46] Y. Zhu, Y. Gu, S. Qiao, L. Zhou, J. Shi, and H. Lai, "Bacterial and mammalian cells adhesion to tantalum-decorated micro-/nano-structured titanium," *Journal of Biomedical Materials Research - Part A,* vol. 105, pp. 871-878, 2017.

[47] S.-S. Gao, Y.-R. Zhang, Z.-L. Zhu, and H.-Y. Yu, "Micromotions and combined damages at the dental implant/bone interface," *International journal of oral science,* vol. 4, pp. 182-8, 2012.

[48] J. Raphel, M. Holodniy, S. B. Goodman, and S. C. Heilshorn, "Multifunctional coatings to simultaneously promote osseointegration and prevent infection of orthopaedic implants," *Biomaterials,* vol. 84, pp. 301-314, 2016.

[49] M. Noronha Oliveira, W. V. H. Schunemann, M. T. Mathew, B. Henriques, R. S. Magini, W. Teughels*, et al.*, "Can degradation products released from dental implants affect peri-implant tissues?," *Journal of Periodontal Research,* vol. 53, pp. 1-11, 2018.

[50] C. Dini, R. C. Costa, C. Sukotjo, C. G. Takoudis, M. T. Mathew, and V. A. R. Barão, "Progression of Bio-Tribocorrosion in Implant Dentistry," *Frontiers in Mechanical Engineering,* vol. 6, pp. 1-14, 2020.

[51] M. R. Casanova, R. Reis, A. Martins, and N. M. Neves, "Surface biofunctionalization to improve the efficacy of biomaterial substrates to be used in regenerative medicine," *Materials Horizons,* 2020.

[52] K. Anselme, "Osteoblast adhesion on biomaterials," *Biomaterials,* vol. 21, pp. 667-681, 2000.

[53] R. A. Gittens, T. McLachlan, R. Olivares-Navarrete, Y. Cai, S. Berner, R. Tannenbaum*, et al.*, "The effects of combined micron-/submicron-scale surface roughness and nanoscale features on cell proliferation and differentiation," *Biomaterials,* vol. 32, pp. 3395-3403, 2011.

[54] S. Minagar, C. C. Berndt, J. Wang, E. Ivanova, and C. Wen, "A review of the application of anodization for the fabrication of nanotubes on metal implant surfaces," *Acta Biomaterialia,* vol. 8, pp. 2875-2888, 2012.

[55] X. Liu, P. K. Chu, and C. Ding, "Surface modification of titanium, titanium alloys, and related materials for biomedical applications," *Materials Science and Engineering R: Reports,* vol. 47, pp. 49-121, 2004.

[56] S. Samavedi, A. R. Whittington, and A. S. Goldstein, "Calcium phosphate ceramics in bone tissue engineering: A review of properties and their influence on cell behavior," *Acta Biomaterialia,* vol. 9, pp. 8037-8045, 2013.

[57] R. A. Surmenev, M. A. Surmeneva, and A. A. Ivanova, "Significance of calcium phosphate coatings for the enhancement of new bone osteogenesis - A review," *Acta Biomaterialia,* vol. 10, pp. 557-579, 2014.

[58] M. Rathee and M. Bhoria, "Nanoscale Surface Modifications of Dental Implants: A Mini Review," *International Journal of Biosciences and Nanosciences,* vol. 1, pp. 126-129, 2014.

[59] A. Civantos, E. Martinez-Campos, V. Ramos, C. Elvira, A. Gallardo, and A. Abarrategi, "Titanium coatings and surface modifications: toward clinically useful bioactive implants," *ACS Biomaterials Science & Engineering,* vol. 3, pp. 1245-1261, 2017.

[60] K. Anselme and M. Bigerelle, "Topography effects of pure titanium substrates on human osteoblast long-term adhesion," *Acta Biomaterialia,* vol. 1, pp. 211-222, 2005.

[61] Y. T. Sul, "The significance of the surface properties of oxidized titanium to the bone response: Special emphasis on potential biochemical bonding of oxidized titanium implant," *Biomaterials,* vol. 24, pp. 3893-3907, 2003.

[62] Y. C. Chai, A. Carlier, J. Bolander, S. J. Roberts, L. Geris, J. Schrooten*, et al.*, "Current views on calcium phosphate osteogenicity and the translation into effective bone regeneration strategies," *Acta Biomaterialia,* vol. 8, pp. 3876-3887, 2012.

[63] Y. Fu and A. Mo, "A Review on the Electrochemically Self- organized Titania Nanotube Arrays: Synthesis, Modifications, and Biomedical Applications," *Nanoscale Research Letters,* vol. 13, pp. 2-21, 2018.

[64] P. Roy, S. Berger, and P. Schmuki, "TiO2 Nanotubes: Synthesis and Applications," *Angew. Chem. Int,* vol. 50, pp. 2904-2939, 2011.

[65] K. Prasad, O. Bazaka, M. Chua, M. Rochford, L. Fedrick, J. Spoor*, et al.*, "Metallic Biomaterials: Current Challenges and Opportunities," *Materials,* vol. 10, pp. 884-884, 2017.

[66] J. M. M. L. M. J. K. F. M. P. G. S. V. Hiroaki Tsuchiya and P. Schmuki, "Hydroxyapatite growth on anodic TiO2 nanotubes," *Journal of Biomedical Materials Research Part A,* vol. 77A, pp. 534-541, 2006.

[67] K. S. Brammer, S. Oh, C. J. Cobb, L. M. Bjursten, H. v. d. Heyde, and S. Jin, "Improved bone-forming functionality on diameter-controlled TiO2 nanotube surface," *Acta Biomaterialia,* vol. 5, pp. 3215-3223, 2009.

[68] A. T. Nguyen, S. R. Sathe, and E. K. F. Yim, "From nano to micro: topographical scale and its impact on cell adhesion, morphology and contact guidance," *Journal of physics. Condensed matter : an Institute of Physics journal,* vol. 28, pp. 183001-183001, 2016.

[69] G. Mendonça, D. B. S. Mendonça, F. J. L. Aragão, and L. F. Cooper, "Advancing dental implant surface technology - From micron- to nanotopography," *Biomaterials,* vol. 29, pp. 3822-3835, 2008.

[70] C. Von Wilmowsky, S. Bauer, R. Lutz, M. Meisel, F. W. Neukam, T. Toyoshima*, et al.*, "In Vivo Evaluation of Anodic TiO2 Nanotubes; An Experimental Study in the Pig," *Journal of Biomedical Materials Research - Part B Applied Biomaterials,* vol. 89, pp. 165-171, 2009.

[71] T. J. Webster and C. Yao, "Anodization: A Promising Nano-Modification Technique of Titanium-based Implants for Orthopedic Applications," in *Surgical Tools and Medical Devices*, ed Boston, MA: Springer US, 2016, pp. 55-79.

[72] D. R. Barjaktarević, I. Lj, C. Alagić, I. D. Dimić, V. R. Đokić, M. P. Rakin*, et al.*, "Anodization of Ti-based materials for biomedical applications: a review," *Metallurgical and Materials Engineering,* vol. 22, pp. 129-143, 2016.

[73] V. S. Kattimani, S. Kondaka, and K. P. Lingamaneni, "Hydroxyapatite–-Past, Present, and Future in Bone Regeneration," *Bone and Tissue Regeneration Insights,* vol. 7, pp. BTRI.S36138-BTRI.S36138, 2016.

[74] R. Z. LeGeros, "Properties of osteoconductive biomaterials: Calcium phosphates," *Clinical Orthopaedics and Related Research,* pp. 81-98, 2002.

[75] L. Bai, Z. Du, J. Du, W. Yao, J. Zhang, Z. Weng*, et al.*, "A multifaceted coating on titanium dictates osteoimmunomodulation and osteo / angio-genesis towards ameliorative osseointegration," *Biomaterials,* vol. 162, pp. 154-169, 2018.

[76] X. Yao, R. Hang, Z. Weng, W. Yao, Y. Liu, Y. Xiao*, et al.*, "Differential effect of hydroxyapatite nano-particle versus nano-rod decorated titanium micro-surface on osseointegration," *Acta Biomaterialia,* vol. 76, pp. 344-358, 2018.

[77] S.-D. Wu, H. Zhang, X.-D. Dong, C.-Y. Ning, A. S. L. Fok, and Y. Wang, "Physicochemical properties and in vitro cytocompatibility of modified titanium surfaces prepared via micro-arc oxidation with different calcium concentrations," *Applied Surface Science,* vol. 329, pp. 347-355, 2015.

[78] X. Zhu, K. H. Kim, and Y. Jeong, "Anodic oxide films containing Ca and P of titanium biomaterial," *Biomaterials,* vol. 22, pp. 2199-2206, 2001.

[79] S. A. Alves, S. B. Patel, C. Sukotjo, M. T. Mathew, P. N. Filho, J. P. Celis*, et al.*, "Synthesis of calcium-phosphorous doped TiO2 nanotubes by anodization and reverse polarization: A promising strategy for an efficient biofunctional implant surface," *Applied Surface Science,* vol. 399, pp. 682-701, 2017.

[80] J. Chen, Z. Zhang, J. Ouyang, X. Chen, and Z. Xu, "Bioactivity and osteogenic cell response of TiO2 nanotubes coupled with nanoscale calcium phosphate via ultrasonification-assisted electrochemical deposition," *Applied Surface Science,* vol. 305, pp. 24-32, 2014.

[81] Q. Du and D. Wei, "TEM analysis and in vitro and in vivo biological performance of the hydroxyapatite crystals rapidly formed on the modi fi ed microarc oxidation coating using microwave hydrothermal technique," *Chemical Engineering Journal,* vol. 373, pp. 1091-1110, 2019.

[82] S. E. Kim, J. H. Lim, S. C. Lee, S. C. Nam, H. G. Kang, and J. Choi, "Anodically nanostructured titanium oxides for implant applications," *Electrochimica Acta,* vol. 53, pp. 4846-4851, 2008.

[83] F. G. Oliveira, A. R. Ribeiro, G. Perez, B. S. Archanjo, C. P. Gouvea, J. R. Araújo*, et al.*, "Understanding growth mechanisms and tribocorrosion behaviour of porous TiO 2 anodic films containing calcium , phosphorous and magnesium," *Applied Surface Science,* vol. 341, pp. 1-12, 2018.

[84] Y. T. Sul, J. Jonsson, G. S. Yoon, and C. Johansson, "Resonance frequency measurements in vivo and related surface properties of magnesium-incorporated, micropatterned and magnesium-

incorporated TiUnite, Osseotite, SLA and TiOblast implants," *Clinical Oral Implants Research,* vol. 20, pp. 1146-1155, 2009.

[85] S. Galli, Y. Naito, J. Karlsson, W. He, M. Andersson, A. Wennerberg*, et al.*, "Osteoconductive Potential of Mesoporous Titania Implant Surfaces Loaded with Magnesium: An Experimental Study in the Rabbit," *Clinical Implant Dentistry and Related Research,* vol. 17, pp. 1048-1059, 2015.

[86] Y.-T. Sul, C. Johansson, A. Wennerberg, L.-R. Cho, B.-S. Chang, and T. Albrektsson, "Optimum surface properties of oxidized implants for reinforcement of osseointegration: surface chemistry, oxide thickness, porosity, roughness, and crystal structure," *The International journal of oral & maxillofacial implants,* vol. 20, pp. 349-359, 2005.

[87] J. M. Cordeiro and V. A. R. Barão, "Is there scientific evidence favoring the substitution of commercially pure titanium with titanium alloys for the manufacture of dental implants?," *Materials Science and Engineering C,* vol. 71, pp. 1201-1215, 2017.

[88] B. R. Chrcanovic, T. Albrektsson, and A. Wennerberg, "Turned versus anodised dental implants : a meta-analysis," *Journal of Oral Rehabilitation 2016,* vol. 43, pp. 716-728, 2016.

[89] N. Biocare. (2016, 2020-11-13). *TiUnite – implant surface matters*. Available: https://www.nobelbiocare.com/blog/products-and-solutions/tiunite-implant-surface-matters/

[90] M. A. P. C. Goularte, G. F. Barbosa, N. C. da Cruz, and L. M. Hirakata, "Achieving surface chemical and morphologic alterations on tantalum by plasma electrolytic oxidation," *International Journal of Implant Dentistry,* vol. 2, 2016.

[91] K. Chris, "Dental Implant Surface Treatments: What You Need to Know," ed, 2020.

[92] E. M. Hetrick and M. H. Schoenfisch, "Reducing implant-related infections: Active release strategies," *Chemical Society Reviews,* vol. 35, pp. 780-789, 2006.

[93] A. D. Pye, D. E. A. Lockhart, M. P. Dawson, C. A. Murray, and A. J. Smith, "A review of dental implants and infection," *Journal of Hospital Infection,* vol. 72, pp. 104-110, 2009.

[94] F. Carinci, D. Lauritano, C. A. Bignozzi, D. Pazzi, V. Candotto, P. S. de Oliveira*, et al.*, "A new strategy against peri-implantitis: Antibacterial internal coating," *International Journal of Molecular Sciences,* vol. 20, pp. 1-9, 2019.

[95] A. Han, J. K. H. Tsoi, F. P. Rodrigues, J. G. Leprince, and W. M. Palin, "Bacterial adhesion mechanisms on dental implant surfaces and the influencing factors," *International Journal of Adhesion and Adhesives,* vol. 69, pp. 58-71, 2016.

[96] A. Monje, A. Insua, and H.-L. Wang, "Understanding Peri-Implantitis as a Plaque-Associated and Site-Specific Entity: On the Local Predisposing Factors," *Journal of Clinical Medicine,* vol. 8, pp. 279-279, 2019.

[97] M. Sánchez-Siles, D. Muñoz-Cámara, N. Salazar-Sánchez, J. F. Ballester-Ferrandis, and F. Camacho-Alonso, "Incidence of peri-implantitis and oral quality of life in patients rehabilitated with implants with different neck designs: A 10-year retrospective study," *Journal of Cranio-Maxillofacial Surgery,* vol. 43, pp. 2168-2174, 2015.

[98] B. Ercan, E. Taylor, E. Alpaslan, and T. J. Webster, "Diameter of titanium nanotubes influences anti-bacterial efficacy," *Nanotechnology,* vol. 22, pp. 295102-295102, 2011.

[99] C. Moseke, F. Hage, E. Vorndran, and U. Gbureck, "TiO2 nanotube arrays deposited on Ti substrate by anodic oxidation and their potential as a long-term drug delivery system for antimicrobial agents," *Applied Surface Science,* vol. 258, pp. 5399-5404, 2012.

[100] H. Hu, W. Zhang, Y. Qiao, X. Jiang, X. Liu, and C. Ding, "Antibacterial activity and increased bone marrow stem cell functions of Zn-incorporated TiO2 coatings on titanium," *Acta Biomaterialia,* vol. 8, pp. 904-915, 2012.

[101] K. Huo, X. Zhang, H. Wang, L. Zhao, X. Liu, and P. K. Chu, "Osteogenic activity and antibacterial effects on titanium surfaces modified with Zn-incorporated nanotube arrays," *Biomaterials,* vol. 34, pp. 3467-3478, 2013.

[102] G. Jin, H. Qin, H. Cao, S. Qian, Y. Zhao, X. Peng*, et al.*, "Synergistic effects of dual Zn/Ag ion implantation in osteogenic activity and antibacterial ability of titanium," *Biomaterials,* vol. 35, pp. 7699-7713, 2014.

[103] S. A. Alves, A. L. Rossi, A. R. Ribeiro, J. Werckmann, J. P. Celis, L. A. Rocha*, et al.*, "A first insight on the bio-functionalization mechanisms of TiO2 nanotubes with calcium, phosphorous and zinc by reverse polarization anodization," *Surface and Coatings Technology,* vol. 324, pp. 153-166, 2017.

[104] L. Zhao, H. Wang, K. Huo, L. Cui, W. Zhang, H. Ni*, et al.*, "Antibacterial nano-structured titania coating incorporated with silver nanoparticles," *Biomaterials,* vol. 32, pp. 5706-5716, 2011.

[105] X. Lin, S. Yang, K. Lai, H. Yang, T. J. Webster, and L. Yang, "Orthopedic implant biomaterials with both osteogenic and anti-infection capacities and associated in vivo evaluation methods," *Nanomedicine: Nanotechnology, Biology, and Medicine,* vol. 13, pp. 123-142, 2017.

[106] A. Top and S. Ülkü, "Silver, zinc, and copper exchange in a Na-clinoptilolite and resulting effect on antibacterial activity," *Applied Clay Science,* vol. 27, pp. 13-19, 2004.

[107] T. Fukada, S. Hojyo, and T. Furuichi, "Zinc signal: A new player in osteobiology," *Journal of Bone and Mineral Metabolism,* vol. 31, pp. 129-135, 2013.

[108] Y. Li, W. Xiong, C. Zhang, B. Gao, H. Guan, H. Cheng*, et al.*, "Enhanced osseointegration and antibacterial action of zinc-loaded titania-nanotube-coated titanium substrates: In vitro and in vivo studies," *Journal of Biomedical Materials Research - Part A,* vol. 102, pp. 3939-3950, 2014.

[109] G. Jin, H. Cao, Y. Qiao, F. Meng, H. Zhu, and X. Liu, "Osteogenic activity and antibacterial effect of zinc ion implanted titanium," *Colloids and Surfaces B: Biointerfaces,* vol. 117, pp. 158-165, 2014.

[110] M. T. Tsai, Y. Y. Chang, H. L. Huang, J. T. Hsu, Y. C. Chen, and A. Y. J. Wu, "Characterization and antibacterial performance of bioactive Ti-Zn-O coatings deposited on titanium implants," *Thin Solid Films,* vol. 528, pp. 143-150, 2013.

[111] R. Wang, X. He, Y. Gao, X. Zhang, X. Yao, and B. Tang, "Antimicrobial property, cytocompatibility and corrosion resistance of Zn-doped ZrO2/TiO2 coatings on Ti6Al4V implants," *Materials Science and Engineering C,* vol. 75, pp. 7-15, 2017.

[112] L. Zhang, Q. Gao, and Y. Han, "Zn and Ag Co-doped Anti-microbial TiO2 Coatings on Ti by Micro-arc Oxidation," *Journal of Materials Science and Technology,* vol. 32, pp. 919-924, 2016.

[113] L. Sopchenski, K. Popat, and P. Soares, "Bactericidal activity and cytotoxicity of a zinc doped PEO titanium coating," *Thin Solid Films,* vol. 660, pp. 477-483, 2018.

[114] Y. Qiao, W. Zhang, P. Tian, F. Meng, H. Zhu, X. Jiang*, et al.*, "Stimulation of bone growth following zinc incorporation into biomaterials," *Biomaterials,* vol. 35, pp. 6882-6897, 2014.

[115] A. Sirelkhatim, S. Mahmud, A. Seeni, N. H. M. Kaus, L. C. Ann, S. K. M. Bakhori*, et al.*, "Review on zinc oxide nanoparticles: Antibacterial activity and toxicity mechanism," *Nano-Micro Letters,* vol. 7, pp. 219-242, 2015.

[116] N. Jones, B. Ray, K. T. Ranjit, and A. C. Manna, "Antibacterial activity of ZnO nanoparticle suspensions on a broad spectrum of microorganisms," *FEMS Microbiology Letters,* vol. 279, pp. 71-76, 2008.

[117] N. Padmavathy and R. Vijayaraghavan, "Enhanced bioactivity of ZnO nanoparticles—an antimicrobial study," *Science and technology of advanced materials,* vol. 9, p. 035004, 2008.

[118] J. T. Seil and T. J. Webster, "Reduced Staphylococcus aureus proliferation and biofilm formation on zinc oxide nanoparticle PVC composite surfaces," *Acta Biomaterialia,* vol. 7, pp. 2579-2584, 2011.

[119] T. C. Bharat, Shubham, S. Mondal, H. S. Gupta, P. K. Singh, and A. K. Das, "Synthesis of doped zinc oxide nanoparticles: A review," *Materials Today: Proceedings,* vol. 11, pp. 767-775, 2019.

[120] S. Calderon V, B. Gomes, P. J. Ferreira, and S. Carvalho, "Zinc nanostructures for oxygen scavenging," *Nanoscale,* vol. 9, pp. 5254-5262, 2017.

[121] S. M. F. Carvalho and C. F. A. Alves, "Dental implant," Portugal Patent WO2016042515A1, 24 March 2016, 2016.

[122] T. Miyazaki, H. M. Kim, T. Kokubo, C. Ohtsuki, H. Kato, and T. Nakamura, "Mechanism of bonelike apatite formation on bioactive tantalum metal in a simulated body fluid," *Biomaterials,* vol. 23, pp. 827-832, 2002.

[123] D. Cristea, I. Ghiuţă, and D. Munteanu, "Tantalum based materials for implants and prosthesis applications," *Bulletin of the Transilvania University of Braşov,* vol. 857, 2015.

[124] B. R. Levine, S. Sporer, R. A. Poggie, C. J. Della Valle, and J. J. Jacobs, "Experimental and clinical performance of porous tantalum in orthopedic surgery," *Biomaterials,* vol. 27, pp. 4671-4681, 2006.

[125] V. K. Balla, S. Bodhak, S. Bose, and A. Bandyopadhyay, "Porous tantalum structures for bone implants: Fabrication, mechanical and in vitro biological properties," *Acta Biomaterialia,* vol. 6, pp. 3349-3359, 2010.

[126] Y. Liu, C. Bao, D. Wismeijer, and G. Wu, "The physicochemical/biological properties of porous tantalum and the potential surface modification techniques to improve its clinical application in dental implantology," *Materials Science and Engineering C,* vol. 49, pp. 323-329, 2015.

[127] T. Lu, J. Wen, S. Qian, H. Cao, C. Ning, X. Pan*, et al.*, "Enhanced osteointegration on tantalum-implanted polyetheretherketone surface with bone-like elastic modulus," *Biomaterials,* vol. 51, pp. 173-183, 2015.

[128] L. D. Zardiackas, D. E. Parsell, L. D. Dillon, D. W. Mitchell, L. A. Nunnery, and R. Poggie, "Structure, metallurgy, and mechanical properties of a porous tantalum foam," *Journal of Biomedical Materials Research,* vol. 58, pp. 180-187, 2001.

[129] D. M. Findlay, K. Welldon, G. J. Atkins, D. W. Howie, A. C. W. Zannettino, and D. Bobyn, "The proliferation and phenotypic expression of human osteoblasts on tantalum metal," *Biomaterials,* vol. 25, pp. 2215-2227, 2004.

[130] K. S. B. K. N. G. J. S. J. Christine J. Frandsen, "Tantalum coating on TiO2 nanotubes induces superior rate of matrix mineralization and osteofunctionality in human osteoblasts," *Materials science & engineering C, Materials for biological applications,* vol. 37, pp. 332-341, 2014.

[131] T. a. Schildhauer, B. Robie, G. Muhr, and M. Köller, "Bacterial adherence to tantalum versus commonly used orthopedic metallic implant materials," *Journal of orthopaedic trauma,* vol. 20, pp. 476-84, 2006.

[132] Y.-Y. Chang, H.-L. Huang, H.-J. Chen, C.-H. Lai, and C.-Y. Wen, "Antibacterial properties and cytocompatibility of tantalum oxide coatings," *Surface and Coatings Technology,* vol. 259, pp. 193-198, 2014.

[133] T. Discovery. (2018, 13/11/2020). *Trabecular Metal ™ Implant*. Available: https://www.zimmerbiometdental.com/fr-FR/wps/wcm/connect/dental/4f76ced2-31a8-47e4-99d5-a00436542061/ZB0049_REV_A_TM_Implant_Brochure_final_SECURED.pdf?MOD=AJPERES&CACHEID=ROOTWORKSPACE.Z18_1O041O02L8PAF0A9JPRUH520H74f76ced2-31a8-47e4-99d5-a00436542061

CHAPTER III- Ta-based micro/nano-structures production and characterization techniques

3 Introduction

Chapter III is dedicated to the description of the experimental methodologies adopted through the present work. The porous Ta_2O_5 nanostructures were developed by two processes: anodization and micro-arc oxidation (or plasma electrolytic oxidation). In addition, DC magnetron sputtering process was used for the zinc nanoparticles deposition. A theoretical overview and fundamental concepts of each process are provided. Also, this chapter outlines a variety of surface characterization techniques for analyzing all the modified surfaces. Additionally, specific materials and methods related to standard cell culture technique is described as well as cytocompatibility and antimicrobial assays.

3.1 Surface modification methodologies

3.1.1 Anodization assisted by electric field

Anodic oxidation, also known as anodization, is an electrochemical, low-cost and easily scale-up method [1, 2], which operates as an electrochemical cell. A potential is applied between the anode (metallic surface) and the cathode (counter electrode such as graphite, platinum, lead), transferring charges and ions and subsequently an oxide layer is formed [3]. When the process works in low voltages is called dissolution of the anodic layer assisted by electric field process. On the other hand, if it works in voltages higher than breakdown potential of the anodic layer (i.e., high voltages that create an electric field higher than the electric field that the anodic layer can support) is called the micro-arc oxidation (MAO) process.

Other advantage of this technique is the incorporation of chemical elements from the electrolyte in the oxide layer during anodization [1], such as sulfur (S) [4] and F^- [5-7]. Particularly, Ca and P-enriched surfaces (Figure III.1-A) demonstrated to improve cell attachment, and proliferation [8] and even to accelerate the primary osteogenic response in *in vivo tests* [9]. The incorporation of the ionic species from the electrolyte composition onto the anodic layer can be improved combining reverse polarization (RP) and anodization. Reverse polarization (RP), also known as cathodic polarization, consists of switching the cathode and anode (relatively to the previous described anodization), samples and graphite rod, respectively (Figure III.1-B). The RP combined with anodization was studied to enhance the incorporation of osteoconductive elements from their precursors present in the electrolyte. The main focus was to improve the surface bio-functionalization without compromising the morphology of the nanopores neither their high order [5, 10, 11].

A review of literature about the dissolution/oxidation mechanisms of anodization in order to achieve Ta_2O_5 nanostructures for biomedical applications and their anodic layer properties is described and discussed in CHAPTER IV. The investigation carried out to develop a uniform porous morphology of Ta_2O_5 surface and its biofunctionalization by incorporation of osteoconductive elements are presented and discussed in CHAPTER V and CHAPTER VI, respectively.

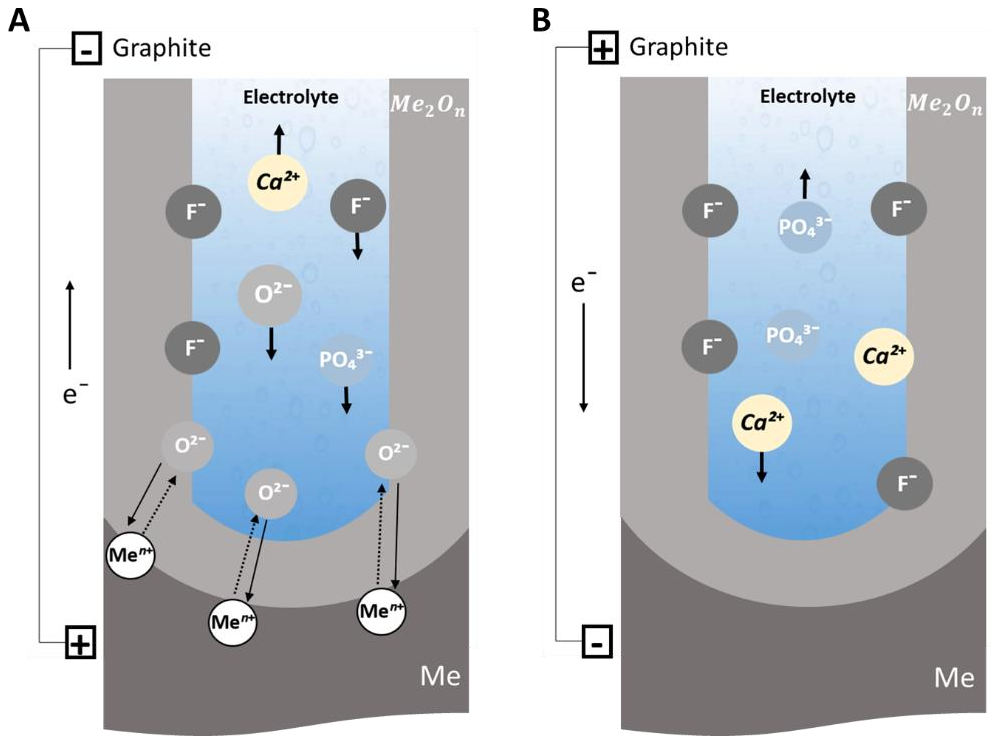

Figure III.1. Bio-functionalization mechanism of a metal oxide (Me_2O_n) nanopores by A) anodization and B) reverse polarization. Adapted from [12].

3.1.2 Micro-arc oxidation (MAO)

MAO technique, also known as plasma electrolytic oxidation (PEO), is originated from anodization but distinguished by higher voltage employed. The MAO step-up and procedure are relatively similar to anodization, with the difference that the oxidation occurs by the combination of metal and oxygen atoms or ions within a discharge plasma (as it cools and collapses) instead of a continuous transport of ions through the electrolyte and within a thin oxide layer [12].

The growth and porous formation of the Ta_2O_5 layer mechanism by MAO is discussed in detail in CHAPTER IV, where is also discussed the surface properties achieved under different anodizing parameters. Moreover, the development of porous morphology and simultaneous incorporation of osteoconductive elements on Ta surface by MAO is provided in CHAPTER VII.

3.1.3 Magnetron sputtering

The PVD techniques allows the production of thin films with good adhesion being the magnetron sputtering the most versatile one [13-15]. Sputter deposition is the deposition of particles from a surface (target) which is being sputtered by ionized species, due to generation of a plasma containing argon ions (Ar^+) and electrons (by applying a potential between anode and cathode). By momentum and energy transfer from bombarding energetic particles neutral target particles are ejected, travelling through the plasma towards the substrate [16-18]. Using magnets, a magnetic field is applied perpendicularly to the electric field and directly in front of the target surface. Thus, free electrons are trapped near target confining the plasma, increasing the gas ionization efficiency, consequently increasing the current density at lower voltages and pressures [13, 17, 19]. As main advantages, this method can work at low temperatures, the sample does not need any treatment after deposition, does not have environmental impact and allows the control of the coating thickness [13, 17]. This technique is mostly used to form films to coat the substrate in presence of an inert gas (Ar is the most employed noble gas) [14, 15]. In addition, nano-sized particles for drug transport has been studied as new healthcare treatment [18].

In this work, Zn/ZnO core-shell nanoparticles were deposited onto porous tantalum oxide with Ca and P ions incorporated samples obtain by MAO (TaCaP samples), using a DC magnetron sputtering at non-reactive mode, provided with a high purity 200x100 mm^2 Zn target (99.99%, Testbourne) located at 70 mm from the rotational substrate holder (Figure III.2). The rotation speed of substrate holder was maintained at 7 rpm to guarantee a homogenous particle distribution. The temperature was kept constant during the deposition at approximately 30 °C. The chamber was evacuated to around $2x10^{-4}$ Pa and filled with argon as an inert gas. The discharge was performed with a current density of 0.5 mA cm^{-2}, a pressure of 6.3 Pa and a deposition time of 250 s. Finally, the samples were removed from the chamber and stored in a desiccator until analysed. These samples were called TaCaP-Zn. An additional thin carbon layer was deposited onto TaCaP-Zn samples in order to control the Zn^{2+} ions release. For this purpose, the sample holder was connected to the DC-pulsed power supply to dissociate the acetylene (C_2H_2) used as carbon precursor, generating a plasma with electrons and ions. The deposition of the carbon layer was carried out in C_2H_2 (partial pressure 1.3 Pa) with Ar atmosphere (partial pressure 1.7 Pa). The discharge was performed with a current of 0.4 A and pressure of 3 Pa, frequency of 200 kHz and deposition time of 60 s. Samples were stored in a desiccator until analyzed. These samples were assigned as TaCaP-ZnC. This investigation is explored in CHAPTER VII.

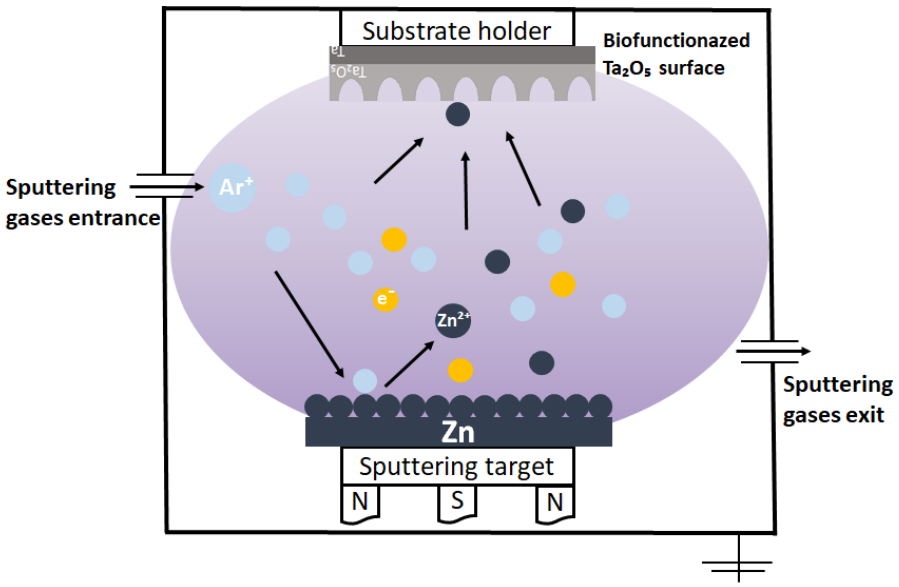

Figure III.2. Schematic illustration of sputtering process in an Ar atmosphere with a Zn metallic target and porous Ta_2O_5 samples as substrates.

3.2 Surface characterization techniques

3.2.1 Morphological and topographic characterization

3.2.1.1 Scanning Electron Microscopy (SEM)

Scanning electron microscopy (SEM) is one of the most widely employed characterization technique in surface engineering. This technique gives high-resolution and high depth of field images of the sample surface [20]. This technique is based on the incidence of a high-energy electron beam over the specimen surface (Figure III.3). The electrons penetrate the surface occurring several interactions which can result in the emission of electrons or photons from the surface. These interactions result in different mechanisms: inelastic and elastic collisions. Inelastic scattering occurs when the primary electrons of the focus beam interact with an atomic electron and some amount of energy is transferred to another electron which can be emitted. The low energy of the emitted secondary electron (SE) means that they are originated from the top surface (until around 10 nm), providing information about both morphology and topography of the surface. High-energy electrons elastically scattered without loss of kinetic energy by the atomic nucleus are designated by backscattered electrons (BSE) which probability of emission increases with the atomic number (Z) of the sample, meaning much less topological contrast in the image but more information about the atomic contrast [21, 22].

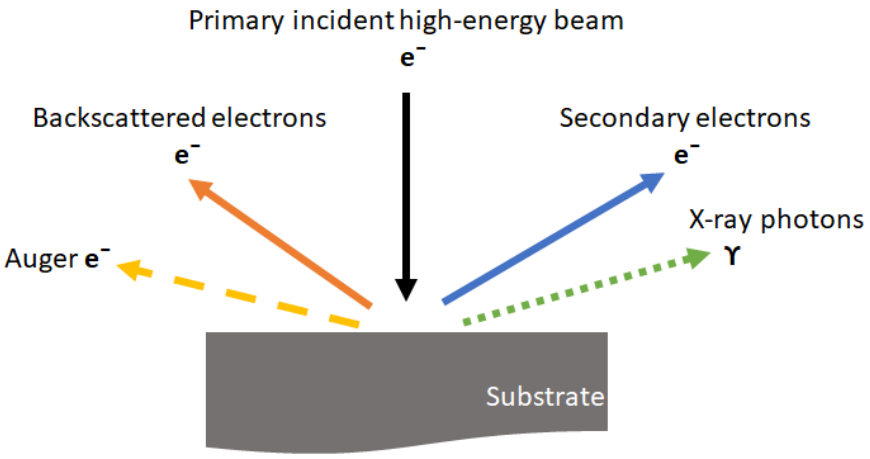

Figure III.3. Materials signals resulting from the interaction between electrons from a focused electron beam and a surface substrate. Adapted from [20].

As sample requirement, it is important to ensure that the sample surface is sufficiently electrically conductive. Thus, the anodic surfaces were firstly coated with an Au/Pd film with 1.5 nm of thickness by sputtering using the SPI Module Sputter Coater equipment. The surfaces' morphologies were studied by SEM (Nova NanoSEM 200 microscope, FEI) operating at 5 kV in secondary mode.

In a specific case, cells adhesion and morphology and bacteria cultures adhesion and proliferation were assessed by SEM (Quanta 400 FEG ESEM / EDAX Genesis X4M) operating at 10 kV in secondary mode.

3.2.1.2 Focused Ion Beam (FIB)

The focus ion beam (FIB) represents a recent tool for samples preparation [22] for STEM or TEM analysis. Briefly, the basic principle of the FIB instrument is the use of a narrow ion beam, typically gallium liquid-metal ion source, that is scanned across the sample occurring ion-solid interactions and many species are generated including sputtered atoms and molecules, SE, BSE and secondary ions [23]. Sputtering occurs as the results of a series of elastic collisions where momentum is transferred from the incident ions to the target atoms within a collision cascade region. When operates at high currents for sample milling, FIB is used to create a very precise cross-sections of a sample, imaging via SEM (Figure III.4). Additionally, operating at low currents, FIB imaging can be used directly detecting the emitted electrons, but only the morphological information can be obtained [24], although the gallium ions contaminate the specimens, introduce artifacts and removes material. [22]. FIB instrument may be stand-alone single beam instrument or, alternatively, FIB columns can be incorporated into other analytic instruments such as a SEM or TEM, being the most common a FIB/SEM dual platform instrument [23].

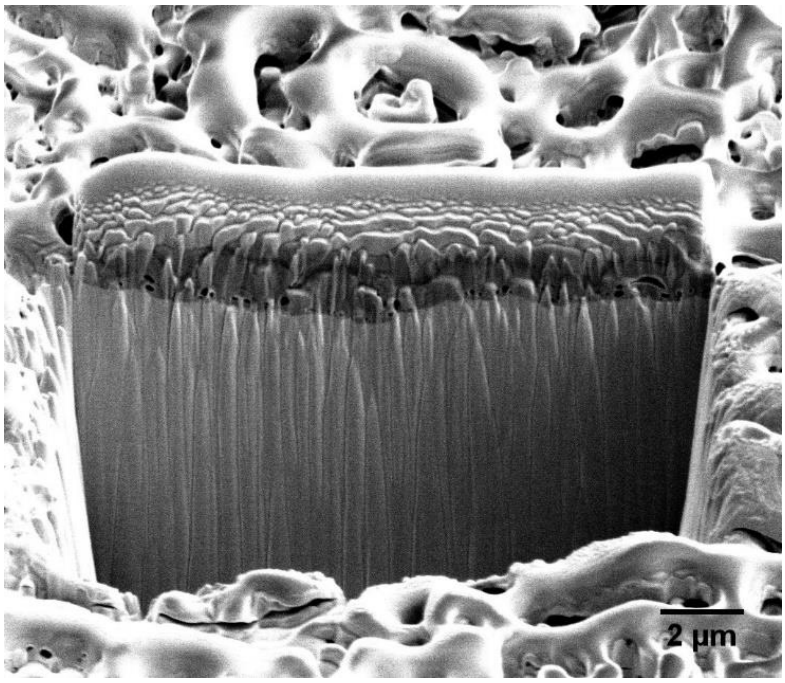

Figure III.4. Example of a cross-section sample preparation by FIB.

A Zeiss Crossbeam (Auriga Compact) equipped with Focus Ion Beam (FIB) and SEM was used to analyse the cross-section and thickness of the anodic layer. FIB cross-sections were performed on an anodic sample using a range of ion currents from 10 µA down to 200 pA and beam energy of 30 kV. At the end of the sample preparation, a low-kV cleaning was performed, and the anodic layer thickness was estimated by *ImageJ*.

3.2.1.3 Atomic Force Microscopy (AFM)

By atomic force microscopy (AFM) is possible determine the surface roughness as well as achieve very high-resolution 3D images of sample surfaces. AFM technique is based on the detection of interatomic forces between the tip and the closer atoms of the surface, during the surface scan. The sample is mounted on a piezoelectric scanner being scanned against a short sharp tip at the end of the cantilever, and the cantilever deflection is usually measured using a laser deflection sensor [21, 25]. There are two basic modes of operation: static or dynamic mode. In static mode (also called repulsive or contact mode) the tip is brought into contact with the sample surface. The force acting on the tip causes the cantilever deflection which is continuously monitored and measured. Instead, in dynamic mode (also referred as attractive force imaging or non-contact mode) the tip is brought into close proximity of the sample surface, but not in contact with it [22, 25]. Additionally, to minimize the effects of friction on topography measurements in the static mode, AFM can operate in the called tapping or intermittent contact mode. In tapping mode, during the surface scanning, the cantilever/tip assembly is vibrated by a piezo. The oscillating tip slightly taps the surface at a resonant frequency of the cantilever (Figure III.5) [25].

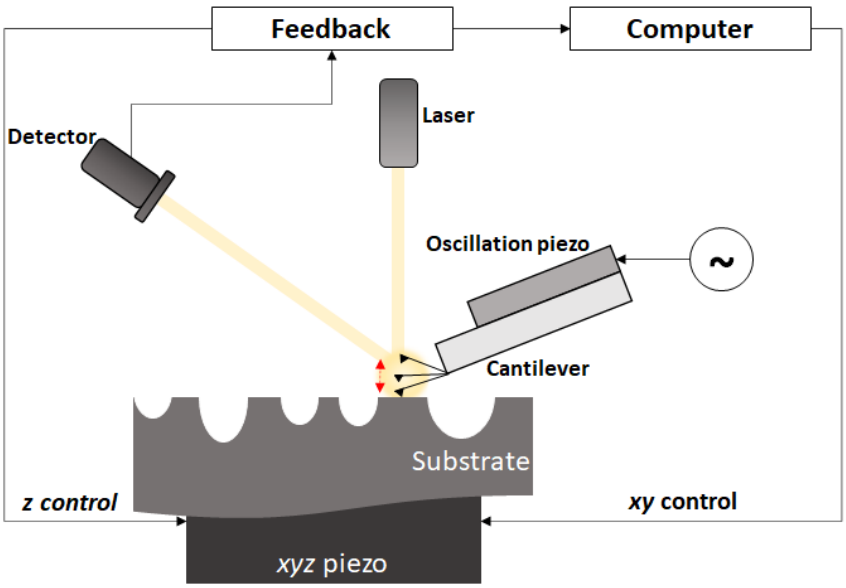

Figure III.5. Surface roughness measurement by AFM tapping mode. Adapted from [25].

Samples' surface topographies were evaluated by atomic AFM (Icon Dimension, Bruker) in tapping mode. AFM micrographs were taken over scanning areas of 5x5 μm^2 and a 2D and 3D profile of each surface was generated (ScanAsyst, Bruker). The average roughness (Sa) and the root mean square (Sq) were obtained through the roughness subroutine of the AFM apparatus from three independent measurements.

3.2.1.4 Transmission Electron Microscopy (TEM)

Transmission electron microscopy (TEM) is used to obtain morphological and structural information. The basic principle of this technique is based on the incidence of a highly-focused monoenergetic electron beam able to penetrate the thin sample (Figure III.6). TEM offers two methods of specimen observation: diffraction mode and image mode. In diffraction mode, an electron diffraction pattern is got on a fluorescent screen. This diffraction pattern is equivalent to an XRD pattern since a single pattern produces a spot pattern on the screen, a polycrystal produces a ring pattern and an amorphous material generates a series of diffuse halos. The image mode generates an image of the illuminated area and, like described in STEM, has BF and DF images. Besides the capability to provide both structural information (crystallography) and atomic-resolution images that are in focus, TEM coupled with EDS allows the elemental identification of the illuminated spot through the measurement of characteristic X-rays [21, 22, 27].

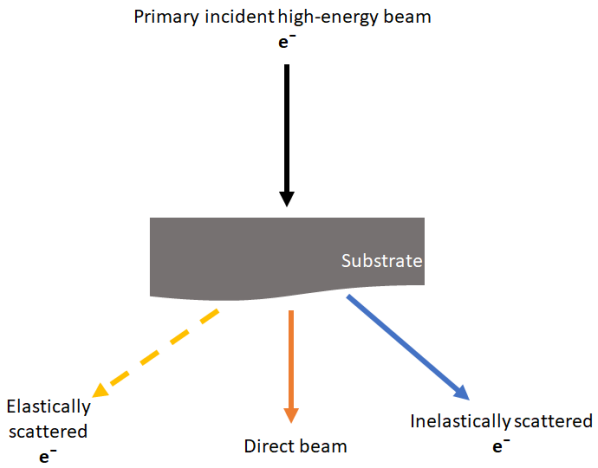

Figure III.6. Generated signals when a focused high-energetic electron beam interacts with a thin sample, detected by TEM. Based on [27].

The Zn nanoparticles and the carbon layer deposited onto the carbon lacey TEM grids were analysed by phase contrast transmission electron microscopy (TEM) images using a JEOL 2100F, operated at 200 kV (in International Laboratory of Nanotechnology – INL).

3.2.1.5 Scanning Transmission Electron Microscopy (STEM)

Scanning transmission electron microscopy (STEM) is a powerful high-resolution technique which is ideally used for nanoparticles characterization, such as size, core/shell investigation and agglomeration [26]. As basic principle, a thin solid specimen is bombarded in vacuum by a demagnified and highly-focused electron beam [21] and the signal is generated at a point on the specimen being detected, amplified and modulated [27]. Then the acquired signal is displayed on the computer monitor as a series of bright spots in synchronism with the scanning electron-probe position. The obtained image resolution is determined by the probe diameter [28]. In STEM mode, an electron detector can be a bright-field (BF) detector or annular dark-field (ADF) detector (Figure III.7-a). The BF detector collects the direct beam which changes in intensity depending on the specific point on the specimen forming bright-field images. Annular dark-field images can be obtained in two ways: selecting the scattered electrons, using a BF detector; or by collecting all of the diffracted or scattered electrons beyond a certain minimum angle (around 3° or less) on ADF detector, where bright areas are related to regions of the specimen that are thick, strongly diffracting or higher Z [21, 27, 28]. Moreover, inelastic scattered electrons are detected by the high-angle annular dark-field (HAADF) detector (Figure III.7-b), acquiring images highlighting elemental contrast, since HAADF image intensity is proportional to Z, such as heavy atoms are observed brighter. Z-contrast (HAADF) images can show atomic-level resolution [27]. STEM can also provide a crystallographic characterization (phase, orientation) and elemental maps (using EDS) [26].

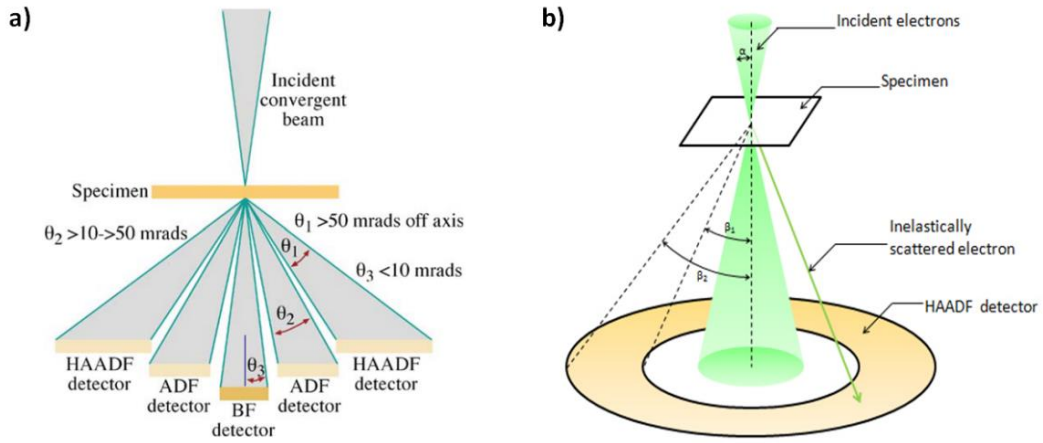

Figure III.7. a) Schematic of conventional BF and ADF and HAADF detectors with a range of electrons scattering angles [27]; b) representation of HAADF STEM mode [29].

The Zn nanoparticles deposited onto the carbon lacey TEM grids were evaluated by the detector scanning transmission electron microscopy coupled with SEM (SEM/STEM, Nova NanoSEM 200 microscope, FEI) operating at 15 kV in A+B (dark and bright fields) mode, in order to evaluate their morphology.

3.2.2 Chemical characterization

3.2.2.1 Energy Dispersive Spectroscopy (EDS)

Energy dispersive spectroscopy (EDS) is used as chemical analysis tool. EDS is based on the collection and energy dispersion of characteristic X-rays (Figure III.4). These X-rays are generated when the atoms in the sample are ionized by a high-energy radiation (electron beam) [21]. The characteristic X-ray generation process is initiated with the ejection of an inner shell electron to form a vacancy, then an X-ray is emitted (Figure III.8) [30]. EDS spectrometers are most frequently coupled to electron column instruments (e.g., SEM, TEM or STEM), providing spatially resolved elemental analysis from small areas, individual points, line scans or maps distribution of elements from the imaged area [21, 22]. X-rays that go into the Si (Li) detector are converted into signals which are processed into an X-ray energy histogram. This X-ray spectrum consists of a series of peaks representative of the type and relative amount of each element into the sample. The number of counts in each peak may be converted into elemental concentration [21], providing a quick "first look" of the qualitative and semi-quantitative chemical composition of the sample [26], however some elemental peaks can overlap.

Qualitative chemical composition of the samples' surfaces was assessed by EDS using the EDAX-Pegasus X4M spectrometer (EDAX, USA) at 10 kV. For each sample, fifteen measurements were randomly performed to validate the results. EDS mapping was also acquired at 25 kV to analyse the elemental Zn distribution over the surfaces with Zn/ZnO nanoparticles.

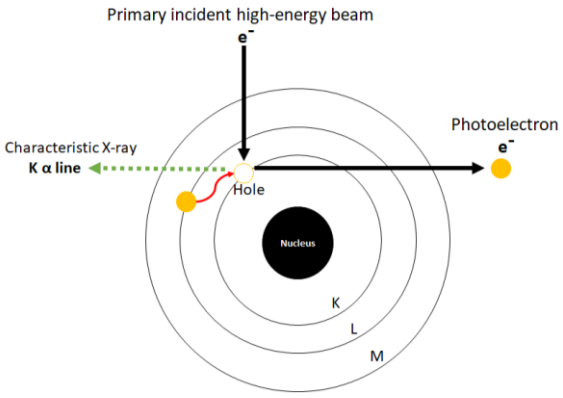

Figure III.8. X-ray generation by filling of the inner shell vacancy from a higher shell. Adapted from [30].

3.2.2.2 X-ray Photoelectron Spectroscopy (XPS)

X-ray Photoelectron Spectroscopy (XPS) is a surface sensitive analysis technique for analyzing the surface chemistry. XPS provides the elemental composition, empirical formula, chemical state and electronic state information of the elements within a sample. This technique is based on the ionization of an atom of the sample when the surface is irradiated by an X-ray beam (monochromatic Al Kα or Mg Kα) producing an ejected electron (photoelectron) from the top 1-10 nm of the surface (Figure III.9). The measured kinetic energy (KE) of the emitted electrons is characteristic of the element which the photoelectron is originated and depends upon the photon (X-ray) energy (hv) and the binding energy (BE) of the electron, by the Einstein photoelectric law (Eq. III.1) [21, 31, 32].

$$KE = hv - BE \qquad \text{Eq. III.1}$$

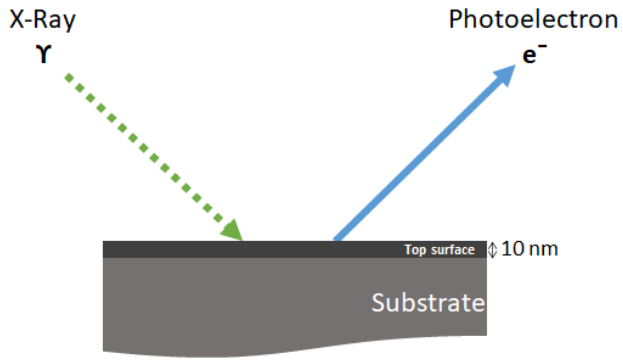

Figure III.9. Material signal resultant from the interaction between the X-rays beam and the top-surface substrate. Adapted from [21, 33].

The chemical state of an atom changes the BE of a photoelectron and consequently alters the measured KE. Hence, the bonding information results from these chemical shifts. A photoelectron spectrum is recorded by counting the ejected electrons over a range of electrons kinetic energies. The peaks appear in the spectrum from atoms emitting electrons with a particular characteristic energy. The position and intensity of the peaks in an energy spectrum provides the identification and quantification of all surface

elements (except hydrogen). Moreover, XPS can be also used for sputter depth profiling to characterize the top surface by quantifying matrix-level elements as a function of depth, using an ion beam to etch the top surface and, thus, revealing subsurface information [21, 32, 33].

The binding states of the elements detected on the samples' surfaces were analyzed by XPS, performed at CEMUP, Portugal, using Kratos Axis Ultra HAS, VISION software for data acquisition. The analysis was carried out with a monochromatic Al Kα X-ray source (1486.7 eV), operating at 15kV (150 W), in FAT mode (Fixed Analyzer Transmission), with a pass energy of 80 eV for survey and 40 eV for elemental spectrum. In addition, to obtain the depth-profile of anodized samples, the surfaces of the specimens were sputtered with Ar^+ with acceleration voltage of 4 keV and a current density of 25 $\mu A/cm^2$ in an etching area of 9 mm^2. The deconvolution of the spectra and the calculation of peak areas were carried out using the CASAXPS standard software. The energy scale of the XPS spectra was corrected using the binding energy of adventitious carbon (C1s at 285 eV). A Gaussian-Lorentzian (GL) product with 30% Gaussian contribution was used to better fit the peaks, considering the respective atomic relative sensitive factors (RSF), the full width at half maximum (FWHM) as well as the specific area ratio for the two spin orbit peaks, using a common Shirley background.

3.2.2.3 Inductively Coupled Plasma Optical Emission Spectroscopy (ICP-OES)

Inductively coupled plasma optical emission spectroscopy (ICS-OES) is an analytical technique that provides quantitative of trace to minor elemental composition of sample solutions. On this analysis, the sample is introduced into the nebulizer, where the solution is vaporized, atomized and ionized. The atoms and ions are thermally excited emitting characteristic light in the ultraviolet-visible region. The species are detected and quantified with an optical emission spectrometer. The intensity of light emitted at characteristic wavelength is proportional to the concentration of the element in the sample. Intensity measurements are converted to elemental concentration via calibration curves [34].

ICP-OES was used to estimate the amount of zinc ions (Zn^{2+}) released from the TaCaP-Zn and TaCaP-ZnC sample's surfaces with time. The samples were immersed in 25 mL of phosphate buffered saline (PBS) solution for 4 h, 1, 3 and 7 days at RT. For that, 3 replicas of each sample were used for each time-point. The amount of Zn leached to the PBS solutions were diluted in HNO_3 (2%) in 1:3 and then measured by ICP-OES (ICP PerkinElmer spectrometer model Optima 8000) three times. TaCaP samples were used as control. A calibration curve, displayed in Figure III.10, was firstly performed using a zinc standard solution (Sigma-Aldrich, 1000 mg/L) for ICP-OES prepared in different concentrations of HNO_3.

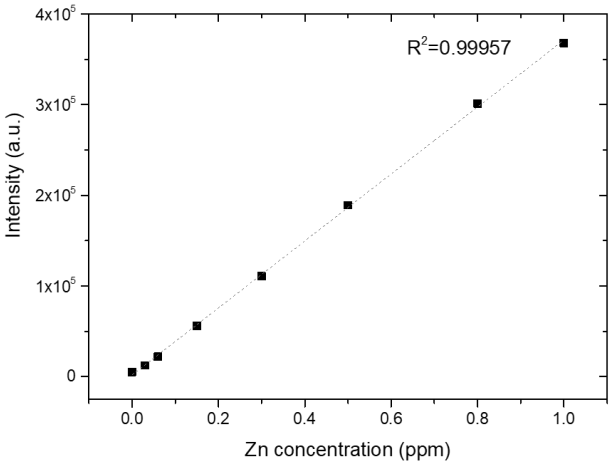

Figure III.10. ICP-OES calibration curve with nitric acid.

3.2.2.4 Fourier Transform Infrared Spectroscopy (FTIR)

Fourier transform infrared spectroscopy (FTIR) is an inexpensive and non-destructive technique that provides information about the chemical bonding in a material. The FTIR spectrum is considered a chemical fingerprint. The fundamental goal of the infrared experiment is to determine alterations in the intensity of the infrared radiation beam as function of wavelength or frequency, after it interacts with the material surface. During this interaction, infrared radiation can activate molecular vibrations (absorption), while the remaining light is transmitted and collected. Thus, the data can be acquired in three different formats: absorbance, which enables to quantify the concentrations; transmittance or reflectance, which provide qualitative information about chemical bonds [21].

FTIR measurements (4500–600 cm^{-1}) were performed on a JASCO FT/IR-4100 spectrometer (JASCO Analytical Instruments, USA) equipped with a Golden Gate Single Reflection Diamond ATR (attenuated total reflectance) accessory (Specac Ltd, UK) with a ZnSe crystal plate. The acquisition was performed using 64 scans and the acquisition resolution was set to 8 cm^{-1}.

3.2.3 Structural analysis techniques

3.2.3.1 X-Ray Diffraction (XRD)

X-ray diffraction (XRD) is a powerful non-contact and non-destructive technique used to characterize the crystalline structure of the materials, providing information on crystal structure, phase, preferred crystal orientation, grain size and crystal defects, among others. The principle is based on a collimated beam of X-rays incidence on a specimen, at a specific angle (θ) in relation to the sample surface. The X-ray is diffracted by constructive interference at the parallel crystallographic planes in the sample with an angle (2θ) between the incident and diffracted X-rays (Figure III.11) according to Bragg's law, Eq. III.2 (where

n is the order of diffraction, λ the wavelength of the incident beam in nm and d_{hkl} the lattice spacing in nm). The peaks intensity is determined as function of the diffracted angle 2θ. The diffraction pattern is used to identify the sample's crystalline phases and to determine its structural properties. The identification is performed based on the ICDD (International Center of Diffraction Data) database of XRD pattern [21, 35].

$$n\lambda = 2d_{hkl} \sin\theta \qquad \text{Eq. III.2}$$

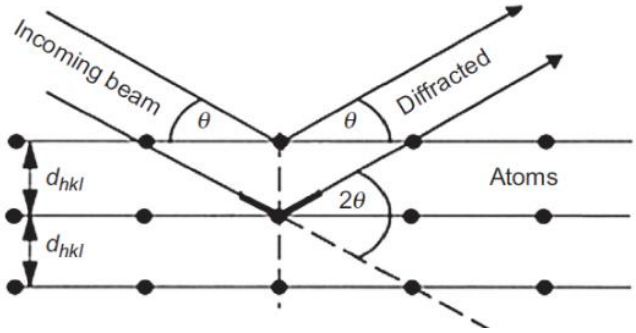

Figure III.11. Geometrical condition for diffraction from lattice planes [35].

Crystalline structure and phase distribution of anodized samples were analyzed by XRD (Bruker D8 Discover) using a Cu radiation Kα radiation (λK_{α_1}=1.5406 Å and λK_{α_2}=1.54439 Å) at 40 kV and 40 mA. The experiments were performed in grazing angle geometry of 3° with a step size of 0.04°, a time per step of 1s and 2θ range of 10-130° (or grazing angle geometry of 1° and a range of 10-80° for samples modified by MAO).

3.2.4 Surface wettability characterization

The technique most used to evaluate the wetting behavior of a solid material is the sessile drop technique. This method is based on measurement of the contact angle of a liquid drop on the surface. This angle (CA or θ) is measured between the tangent of the drop at the liquid/vapor interface (Figure III.12) and the horizontal baseline of the solid surface. The contact angle quantifies the wetting of the surface by the liquid and therefore characterizes the surface hydrophilicity for water [36, 37]. In principle, the sessile drop technique allows to measure two types of contact angles: dynamic or static modes. Dynamic contact angles are measured when a relative movement between the solid material and the wetting liquid occurs, instead static contact angle is measured without such movement [36, 38].

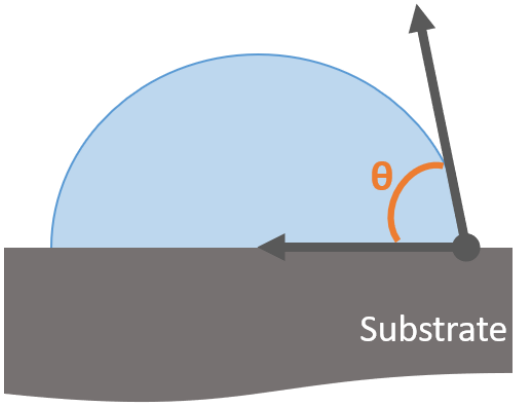

Figure III.12. Schematic illustration of surface free energies and the contact angle between the liquid and the surface sample. Adapted from [37].

The wettability of the anodic surfaces was evaluated by the sessile drop test. Static contact angles were measured at RT with an OCA20 Plus optical contact angle measuring system (DataPhysics, Germany), in view of Milli-Q ultrapure water. A droplet of 2 µL of water was suspended on the surface using a micro-syringe (Hamilton 500 µL syringe) with a dosing rate of 1 µL/s. Water contact angle (θ_w) measurements were performed nine times per surface.

3.2.5 *In vitro* characterization

To characterize the surface cells' responses concerning to cytotoxicity, adhesion and proliferation, as well as antibacterial activity, the samples were previously sterilized at dry heat (180 °C, 2 h).

Moreover, all the results were statistically analyzed. Statistically significant differences ($p < 0.05$) between the various groups were measured using two-ways analysis of variance (one-way ANOVA) and Turkey's multiple comparison tests. All statistical analysis was carried out using the GraphPad Prism 6 statistical software package. All the data are expressed as mean ± standard deviation (SD).

3.2.5.1 Biological evaluation

3.2.5.1.1 Bioactivity: apatite-inducing ability assay

The bone-bonding ability of a material surface translates its bioactivity that can be evaluated by apatite-inducing ability method. Therefore, this method is based on the immersion of the material in SBF, with a ions' concentration similar to those of human blood plasma, during a determined period of time and the examination of the apatite formation on the material surface, being useful for prediction the *in vivo* bone bioactivity of a material, qualitatively and quantitatively, before animal testing [39].

The modified samples were immersed in 40 mL of SBF under static conditions at 36.5°C and 120 rpm, for a period of time to evaluate their apatite-inducing ability (28 days). The SBF solution was prepared according to Kokubo and Takadama approach [39] by dissolving NaCl, $NaHCO_3$, KCl, $K_2HPO_4.3H_2O$, $MgCl_2.6H_2O$, $CaCl_2$ and Na_2SO_4 in distilled water and buffered at pH 7.4 at 36.5 °C with and appropriate amount of HCl. The ions concentration of SBF are nearly equal to those of human blood plasma at 36.5 °C. After soaked, the samples were removed from SBF after 7, 14 and 28 days, cleaned with distilled water and dried in a desiccator. The experiment was performed in triplicate for each sample group. Scanning electron microscopy (SEM, Nova NanoSEM 200 microscope, FEI) was used to study and evaluate the presence of calcium phosphates.

3.2.5.1.2 Cell culture

All cell cultures were performed in a laminar flow hood under appropriated aseptic conditions. The cell line MG-63 derives from the human juxtacortical osteosarcoma diagnosed in the distal diaphysis of the left-femur of a fourteen years-old male [40, 41]. These cells have a rapid cell growth without demonstrating contact inhibition, resulting in the formation of aggregates [40]. Additionally, MG-63 cells were defined as immature osteoblast phenotype and undergoes temporal development in long term cultures [42]. All the following experiments described in this subchapter were performed using MG-63 cells between cell passage (P-95). In biology cell passage translates the number of times that cells were split and enable to growth *in vitro* [43].

For the *in vitro* cytocompability evaluation, human osteoblast-like MG-63 cells linage was maintained in alpha minimum essential medium (α-MEM, Gibco) supplemented with 10% v/v heat-inactivated fetal bovine serum (FBS, Gibco), 1% v/v penicillin streptomycin (10.000 units/mL penicillin and 10.000 μg/mL streptomycin, Gibco) and 1% v/v amphotericin B (250 μg/mL, Gibco). Incubation was carried out in a humidified atmosphere of 95% air and 5% CO_2 at 37°C. Prior cells seeding, material samples were pre-incubated in 6-well plates with phosphate buffer saline (PBS, Sigma-Aldrich) for three time points (4 h, 24 h and 7 days) at 37°C. After leaching, each leachate was collected for a falcon and preserved in the freezer. Subsequently, the samples were pre-incubated with complete medium for 30 minutes at 37°C. Then, the medium was removed, and the cells were seeded on the samples at a density of $9x10^4$ cells/mL. Three wells with cells seeded without sample were used as positive control and wells with samples in culture medium were the blanks. Thereafter, the culture plates were incubated for 1, 3, 7, 10 and 14 days.

3.2.5.1.3 Cell adhesion: DNA content approach

The adhesion behaviour of a population of cells on a new surface determines the material biocompatibility. One technique used for study attachment events of a population of cells is the wash assay. The cells are cultured under static conditions, followed by cell washing before adhesion analysis (DNA count). After one or more washings, only the cells adhered to the substrate remain. The adhered cells are analysed for further quantitative assays such as quantification of DNA content [44].

DNA content was measured using the Quant-iTTM PicoGreenTM dsDNA assay kit (Invitogen) according to the manufacturer's instructions. Initially, materials' samples were washed with PBS and the cell lysate were obtained by placing the samples at 37 °C for 1 h with ultrapure water, subsequently frozen at -80 °C for 1 h and finally thawed at RT to lyse all the cells membranes adhered on the materials' surface. Each cell lysate was incubated with PicoGreen reagent, in the dark, for 5 minutes and the fluorescence intensity was measured with a microplate reader (Synergy HT, BioTek) at 530 and 590 nm excitation and emission, respectively, and expressed as relative fluorescent units (RFU). The experiment was performed in triplicate for each material group.

3.2.5.1.4 Cell viability assays

i. Resazurin reduction assay

Cell viability translates the number of metabolic active cells (live cells) that can reduce resazurin (blue color) into resorufin product (pink color and fluorescent). Resazurin is a cell permeable redox indicator used to monitor viable cells along time that is dissolved in physiological buffers, causing a deep blue colored solution, and is directly introduced to cell cultures. The quantity of resorufin produced is proportional to the number of viable cells which is quantified using a microplate fluorometer equipped with a 560 nm excitation/ 590 nm emission filter set. The most important advantages of resazurin reduction are the price, homogenous format and is highly sensitivity [45].

To evaluate the cellular metabolic activity, cells were incubated with complete medium and 10 %v/v resazurin (Resazurin sodium salt, Sigma-Aldrich R7017) for 3 h at 37 °C. Finally, the fluorescence was recorded using a 560 nm excitation/590 nm emission filter set on a microplate reader (SynergyMix, Biotek) with Gen5 1.09 Data Analysis Software. Results are expressed as RFU, for each time point. The experiment was performed in triplicate for each group. Before SEM analysis, samples preparation was performed by the fixation of the cells with 1.5% v/v glutaraldehyde (diluted in cacodylate, 25% solution, TAAB laboratories equipment Ltd) for 15 minutes and hydration with cacodylate (Sodium cacodylate

trihydrate,98%, Sigma-Aldrich). Then, fixed cells were dehydrated sequentially in graded ethanol solutions (50%, 70%, 90% and 100% v/v) for 15 minutes each and hexamethyldisilane (70% and 100% v/v, HMDS, Sigma-Aldrich) series.

ii. MTT reduction assay

The MTT (3-(4,5-dimethylthiazol-2-yl)-2,5-diphenyltetrazolium bromide) is also used to quantify cellular metabolic activity being an indicator of cell viability, proliferation and cytotoxicity. This is also a colorimetric assay based on the reduction of the yellow tetrazolium salt to purple formazan crystals by live cells, which contain NAD(P)H-dependent oxidoreductase enzymes, and thus the number of surviving cells is determined indirectly by MTT dye reduction. The amount of MTT-formazan produced can be quantified measuring the absorbance at 500-600 nm using a multi-well spectrophotometer. While this method is quick and easy, it is not as sensitive as the resazurin assay and the cells became non-viable [43].

Osteoblast metabolic activity was also evaluated using MTT reduction assay. Briefly, cell culture was performed in 96-well plate at a density of $3x10^4$ cells/mL, incubated in a mixture of concentrated complete medium (α-MEM, 20% v/v FBS, 2% v/v penicillin streptomycin and 2% v/v amphotericin B) and obtained leachate of each time point, for 1, 4 and 7 days at 37°C. A well without any leachate was used as positive control. After each culture time point, 10% of 3-(4,5-Dimethylthiazol-2-yl)-2,5-diphe-nyltetrazolium bromide dye (MTT, Sigma-Aldrich) was added to each well and the plates were incubated for 2 h at 37°C. Finally, the MTT solution was discarded, and the formed formazan crystals were dissolved with dimethyl sulfoxide (DMSO, 99.9%, Fisher Chemical) for 15 minutes at RT, followed by absorbance measurement at 550 nm. Five samples per group were used.

iii. Fluorescence microscopy

The absorption and subsequence re-radiation of light by the specimen is the result of a physical phenomenon described as fluorescence. Fluorescence microscopy is based on the irradiation of a specimen with the desired and specific band of wavelengths following by the separation of the much weaker emitted fluorescence from the excitation light. This technique is an essential tool in biology and biomedical sciences that makes possible to identify cells and sub-microscopic cellular components as well as reveals the presence of a single molecule. Applying multiple fluorescence labeling, different probes can simultaneously identify several targets [46].

After 24 h of culture, the culture medium and leachate mixtures were discarded, and each well was washed with heated-sterile PBS. Then, the mitochondria specific tracking dye, MitoSpy (500 nM,

MitoSpyTM Red CMXRos, XX, BioLegend), was added and the plate was incubated for 40 minutes at 37°C. At 24 h, for F-actin visualization, the cultures were washed with PBS fixed with 3.7% paraformaldehyde (Sigma-Aldrich) and stained. Finally, cells membranes were permeabilized with 0.1% Triton-X100 for 15 minutes at RT. And non-specific proteins were blocked with 1% bovine serum albumin (BSA) for 30 minutes (broth Sigma-Aldrich). Cell cytoskeleton filamentous actin (F-actin) was stained with Alexa Fluor 488 (1:100 in 1% BSA, Alexa Fluor R 488 phalloidin) for 30 minutes followed by nuclei staining with Hoechst 33342 (10 μg/mL, Enzo) for 15 minutes. Images of fluorescent-labelled cells and nanoparticles were obtained by using the Celena S digital imaging system (Logos Biosystems).

3.2.5.2 Antibacterial activity

3.2.5.2.1 Cell culture

Most microbiologic works require pure cultures or bacteria clones, which contains only one single type of bacteria. As bacteria can live anywhere, the culture and subculture steps must be performed in aseptically conditions to avoid bacterial or fungal contaminations. The most effective way to isolate a single type of bacteria is the streak plate method, which consists in spreading the bacteria over the nutritive medium, such as over the surface of an agar plate, using an inoculation loop handle. Single bacteria cell reproduces during incubation period forming colonies. Each colony represents the descents of a single bacteria cell and, consequently, the colony's cells are clones [47].

To study antibacterial activity of porous Ta_2O_5 samples, changes in the growth of *Staphylococcus aureus* (ATCC 25923) bacteria was investigated. The cultures containing the bacteria were inoculated into 50 mL of fresh tryptic soy broth (TSB, Liofilchem) in order to obtain an initial suspension of 106 colony forming units (CFU) mL^{-1}. The porous Ta_2O_5 samples with and without C layer and/ or ZnO nanoparticles and pure Ta (control material) were added to the 6-well plate and incubated in a constant temperature shaker at 37 °C and 150 rpm. A well without any sample was used as positive control. Negative controls were obtained by incubating the samples in TSB.

3.2.5.2.2 Bacteria viability assays

i. Colony Forming Units (CFU)

The bacteria cell number determination is the most fundamental procedures in microbiology. The widely used gold standard method is colony forming units (CFU). As one colony cannot result from a single bacterium but in fact from a fragment of a bacteria strain or bacteria aggregation, the counts are reported as CFU. The CFU method has two main advantages, the capacity for count the number of bacteria using

dilutions, if too many, or concentrations if too few, and second only viable bacteria are counted excluding dead bacteria debris. On the other hand, the major disadvantage is that clamps. Moreover, CFU results are obtained after 24 h, the counting CFU is time-consuming and labor-sensitive. The Food Drugs and Administration (FDA) recommends the count per plate with only 25 to 250 colonies. Therefore, to ensure that the counts are in this range, the inoculum is diluted several times in a process called as serial dilution (Figure III.13) [47, 48].

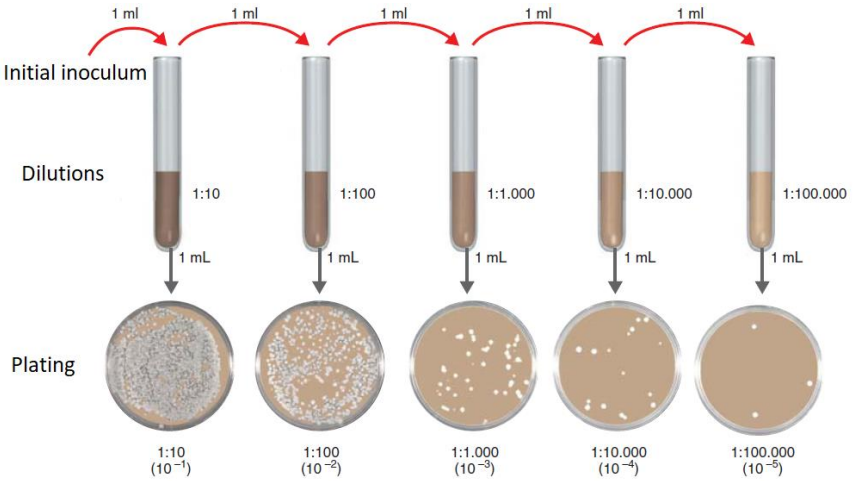

Figure III.13. Example of a serial dilution from the initial inoculum and CFU counting [47].

In this work, to determine the colony counts (CFU/mL), a serial dilution (from 10^{-1} to 10^{-7}) of *S. aureus* was performed. For the first dilution, 20 µL of the initial inoculum was added to 180 µL of PBS. After resuspension, 20 µL from this initial dilution (10^{-1}) was pipette to 180 µL of PBS (second dilution 10^{-2}), and so on (Figure III.14). After the preparation of the serial dilution, 20 µL of the latest three dilutions (10^{-5}, 10^{-6} and 10^{-7}) was pipette onto nutrient agar (brain heart infusion broth, BHI, and agar, Liofilchem) plates, from the less to the more concentrated dilution. The experiment was performed in triplicate for each group.

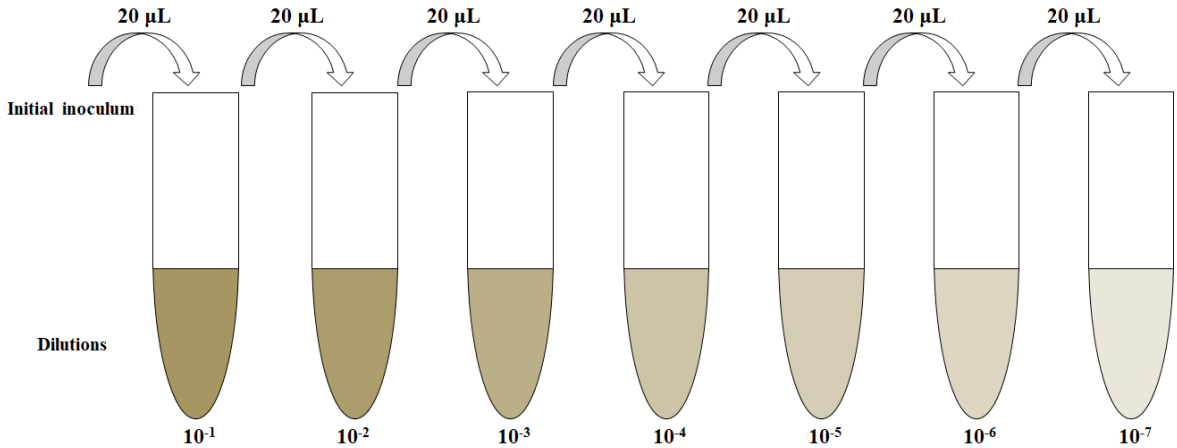

Figure III.14. Serial dilution from the initial *S. aureus* inoculum performed for CFU counting.

ii. Optical density (OD)

Another common method used to estimate bacterial load is turbidimetry or optical density (OD) which is used to evaluate the turbidity in order to monitor the bacteria growth since as the bacteria proliferate in a liquid medium this medium becomes more turbid or opaque. The instrument used to measure the OD is the spectrophotometer where the light that pass through the bacterial suspension achieving the detector. The turbidity variation or OD is proportional to the solids in solution. The increase of bacteria cells decreases the intensity of light that achieve the detector, and this light alteration is recorded in the spectrophotometer in an absorbance logarithmic scale named as optical density. However, this method is not able to distinguish live bacteria from dead bacteria or even particles [47, 48].

After 24 h of bacteria culture incubation, the bacteria suspension, from each well, was collected and the planktonic bacteria were quantified by OD at 600 nm using a microplate reader (SynergyMix, Biotek) with Gen5 1.09 Data Analysis Software. The experiment was performed in quadruplicate for each group.

iii. Resazurin assay

Bacteria cell number can also be determined based on metabolic features, such as resazurin reduction assay, already described on subchapter 3.2.5.1.4i. This method is based on the reduction of non-fluorescent resazurin to fluorescent resorufin by active bacteria [49]. Resazurin reduction test have been used to determine bacteria chemical cytotoxicity and minimum inhibitory concentration for antibiotics [49, 50].

The metabolic activity was evaluated adding 10% v/v resazurin with 200 μL TSB extracted from each sample to 96-well plate. After 3 h of incubation at 37°C, the fluorescence was measured using a microplate reader (excitation: 530 nm and emission; 590 nm). The experiment was performed in quadruplicate for each group. Additionally, the samples were carefully washed twice with saline solution to remove non-adherent bacteria, and the metabolic activity of sessile bacteria was assessed by resazurin method: 200 μL TSB with 10% resazurin were added to each well and incubated for 3 h at 37 °C. After incubation, the fluorescence was recorded. The experiment was performed in triplicate for each group. At the end of incubation, for further adhesion and morphologic bacteria characterization by SEM, the sessile bacteria were first fixed by 1.5% v/v glutaraldehyde for 15 minutes and remained in cacodylate. Then, the samples were dehydrated in a graded series of ethanol solutions for 10 minutes each, sequentially, followed by dying in the hexamethyldisilane ethanol solution series.

3.3 References

[1] S. E. Kim, J. H. Lim, S. C. Lee, S. C. Nam, H. G. Kang, and J. Choi, "Anodically nanostructured titanium oxides for implant applications," *Electrochimica Acta,* vol. 53, pp. 4846-4851, 2008.

[2] J. M. Macak, H. Tsuchiya, A. Ghicov, K. Yasuda, R. Hahn, S. Bauer*, et al.*, "TiO2 nanotubes: Self-organized electrochemical formation, properties and applications," *Current Opinion in Solid State and Materials Science,* vol. 11, pp. 3-18, 2007.

[3] T. J. Webster and C. Yao, "Anodization: A promising nano-modification technique of titanium-based implants for orthopedic applications," in *Surgical Tools and Medical Devices*, ed, 2016.

[4] R. S. Namur, K. M. Reys, and C. E. B. Marino, "Growth and Electrochemical Stability of Compact Tantalum Oxides Obtained in Different Electrolytes for Biomedical Applications," *Materials Research,* vol. 18, pp. 0-6, 2015.

[5] S. A. Alves, S. B. Patel, C. Sukotjo, M. T. Mathew, P. N. Filho, J. P. Celis*, et al.*, "Synthesis of calcium-phosphorous doped TiO2 nanotubes by anodization and reverse polarization: A promising strategy for an efficient biofunctional implant surface," *Applied Surface Science,* vol. 399, pp. 682-701, 2017.

[6] S. C. Han, J. M. Doh, J. K. Yoon, G. H. Kim, J. Y. Byun, S. H. Han*, et al.*, "Highly Ordered Self-Organized TiO2 Nanotube Arrays Prepared by a Multi-Step Anodic Oxidation Process," vol. 15, pp. 493-499, 2009.

[7] R. P. Antony, T. Mathews, S. Dash, A. K. Tyagi, and B. Raj, "X-ray photoelectron spectroscopic studies of anodically synthesized self aligned TiO2 nanotube arrays and the effect of electrochemical parameters on tube morphology," *Materials Chemistry and Physics,* vol. 132, pp. 957-966, 2012.

[8] A. R. Ribeiro, F. Oliveira, L. C. Boldrini, P. E. Leite, P. Falagan-Lotsch, A. B. R. Linhares*, et al.*, "Micro-arc oxidation as a tool to develop multifunctional calcium-rich surfaces for dental implant applications," *Materials Science and Engineering C,* vol. 54, pp. 196-206, 2015.

[9] A. B. Novaes, S. L. S. de Souza, R. R. M. de Barros, K. K. Y. Pereira, G. Iezzi, and A. Piattelli, "Influence of implant surfaces on osseointegration," *Brazilian Dental Journal,* vol. 21, pp. 471-481, 2010.

[10] S. A. Alves, A. L. Rossi, A. R. Ribeiro, J. Werckmann, J. P. Celis, L. A. Rocha*, et al.*, "A first insight on the bio-functionalization mechanisms of TiO2 nanotubes with calcium, phosphorous and zinc by reverse polarization anodization," *Surface and Coatings Technology,* vol. 324, pp. 153-166, 2017.

[11] S. Alves, "A new concept of bio-multifunctional nanotubular surfaces for dental implants : tribocorrosion resistant , antibacterial and osteogenic," 2017.

[12] T. W. Clyne and S. C. Troughton, "A review of recent work on discharge characteristics during plasma electrolytic oxidation of various metals," *International Materials Reviews,* vol. 64, pp. 127-162, 2019.

[13] C. J. Tavares, "Caracterização estrututal e mecânica de multicamadas de TiN/ZrN depositadas por PVD," 1997.

[14] C. F. Almeida Alves, S. V. Calderón, D. Dias, and S. Carvalho, "Influence of Oxygen content on the electrochemical behavior of Ta1-xOx coatings," *Electrochimica Acta,* vol. 211, pp. 385-394, 2016.

[15] C. F. Almeida Alves, A. Cavaleiro, and S. Carvalho, "Bioactivity response of Ta1-xOx coatings deposited by reactive DC magnetron sputtering," *Materials Science and Engineering C,* vol. 58, pp. 110-118, 2016.

[16] C. Chaneliere, J. C. Autran, R. A. B. Devine, and B. Balland, "Tantalum pentoxide (Ta2O5) thin films for advanced dielectric applications," *Materials Science and Engineering,* vol. 22, pp. 269-322, 1998.

[17] F. Shi, "Introductory Chapter: Basic Theory of Magnetron Sputtering," ed, 2018.

[18] M. Braun, "Magnetron Sputtering Technique," ed: Springer-Verlag London, 2015, pp. 2929-2949.

[19] C. F. A. Alves, "Desenvolvimento de revestimentos nanoestruturados para implantes osteointegrados," Master, Physics Department, University of Minho, 2013.

[20] M. de Assumpção Pereira-da-Silva and F. A. Ferri, "1 - Scanning Electron Microscopy," in *Nanocharacterization Techniques*, A. L. Da Róz, M. Ferreira, F. de Lima Leite, and O. N. Oliveira, Eds., ed: William Andrew Publishing, 2017, pp. 1-35.

[21] C. A. E. S. W. C. Richard Brundle, *Encyclopedia of materials characterization*, First edit ed.: Butterworth-Heinemann, 1992.

[22] M. Ohring, *Materials Science of Thin Films*, Second Edt ed.: Academic Press, 2002.

[23] P. Echlin, *Handbook of Sample Preparation for Scanning Electron Microscopy and X-Ray Microanalysis*, 2009.

[24] N. Yao, *Focused ion beam systems: basics and applications*: Cambridge University Press, 2007.

[25] B. Bharat, *Handbook of Nanotechnolgy*, Second edi ed.: Springer, 2017.

[26] S. Mourdikoudis, R. M. Pallares, and N. T. Thanh, "Characterization techniques for nanoparticles: comparison and complementarity upon studying nanoparticle properties," *Nanoscale,* vol. 10, pp. 12871-12934, 2018.

[27] B. W. David, C Barry Carter, *Transmission Electron Microscopy, A Textbook for Materials Science*, Second Edi ed. vol. 53: Springer Science & Business Media, 2012.

[28] (2020, 2020-03-23). *Scanning transmission electron microscope (STEM) image*. Available: https://www.jeol.co.jp/en/words/emterms/search_result.html?keyword=scanning%20transmission%20electron%20microscope%20(STEM)%20image

[29] (2020, 2020-03-23). *High-angle annular dark-field scanning transmission electron microscopy*. Available: https://www.jeol.co.jp/en/words/emterms/search_result.html?keyword=HAADF-STEM

[30] P. D. Ngo, "Energy Dispersive Spectroscopy," L. C. Wagner, Ed., ed Boston, MA: Springer Science & Business Media, 1999, pp. 205-215.

[31] J. F. Moulder, W. F. Stickle, P. E.'Sobol, and K. D. Bomben, *Handbook of X-ray Photoelectron Spectroscopy*, 1992.

[32] I. S. Tilinin, A. Jablonski, and W. Werner, "Quantitative surface analysis by Auger and x-ray photoelectron spectroscopy," *Progress in surface science,* vol. 52, pp. 193-335, 1996.

[33] C. J. Powell and A. Jablonski, "Progress in quantitative surface analysis by X-ray photoelectron spectroscopy: Current status and perspectives," *Journal of Electron Spectroscopy and Related Phenomena,* vol. 178, pp. 331-346, 2010.

[34] C. B. Boss and K. J. Fredeen, *Concepts, Instrumentation and techniques in Inductively Coupled Plasma Optical Emission Spectrometry*, Third edit ed.: PerkinElmer, Inc., 2004.

[35] J. Epp, "X-Ray Diffraction (XRD) Techniques for Materials Characterization," ed: Elsevier Ltd, 2016, pp. 81-124.

[36] F. Rupp, R. A. Gittens, L. Scheideler, A. Marmur, B. D. Boyan, Z. Schwartz*, et al.*, "A review on the wettability of dental implant surfaces I: Theoretical and experimental aspects," *Acta Biomaterialia,* vol. 10, pp. 2894-2906, 2014.

[37] Hernando S. Salapare III, Ma. Gregoria Joanne P. Tiquio, and H. J. Ramos, "RF Plasma Treatment of Neptune Grass (Posidonia oceania): A Facile Method to Achieve Superhydrophylic Surfaces for Dye Adsorption from Aqueous Solutions," K. L. Mittal, Ed., First edit ed: John Wiley & Sons, 2015, pp. 305-329.

[38] R. A. Gittens, L. Scheideler, F. Rupp, S. L. Hyzy, J. Geis-gerstorfer, Z. Schwartz*, et al.*, "A review on the wettability of dental implant surfaces II : Biological and clinical aspects," *Acta Biomaterialia,* vol. 10, pp. 2907-2918, 2014.

[39] T. Kokubo and H. Takadama, "How useful is SBF in predicting in vivo bone bioactivity?," *Biomaterials,* vol. 27, pp. 2907-2915, 2006.

[40] H. Heremans, A. Billiau, J. J. Cassiman, J. C. Mulier, and P. d. Somer, "In vitro cultivation of human tumor tissues II. Morphological and virological characterization of three cell lines," *Oncology,* vol. 35, pp. 246-252, 1978.

[41] A. Billiau, V. G. Edy, H. Heremans, J. Van Damme, J. Desmyter, J. A. Georgiades*, et al.*, "Human interferon: mass production in a newly established cell line, MG 63," *Antimicrobial Agents and Chemotherapy,* vol. 12, pp. 11-15, 1977.

[42] E. M. Czekanska, M. J. Stoddart, R. G. Richards, and J. S. Hayes, "In search of an osteoblast cell model for in vitro research," *European Cells and Materials,* vol. 24, pp. 1-17, 2012.

[43] R. I. Freshney, *Culture of Animal Cells, A Manual of Basic Techniques*, fifth edit ed.: John Wiley & Sons, Inc, 2005.

[44] A. A. Khalili and M. R. Ahmad, "A Review of cell adhesion studies for biomedical and biological applications," *International Journal of Molecular Sciences,* vol. 16, pp. 18149-18184, 2015.

[45] G. Sittampalam, N. Coussens, M. Arkin, D. Auld, C. Austin, B. Bejcek*, et al.*, *Assay Guidance Manual*: Sciences, Eli Lilly & Company and the National Center for Advancing Translational, 2020.

[46] M. Davidson. (2020-03-29). *Introduction to Fluorescence Microscopy*. Available: https://www.microscopyu.com/techniques/fluorescence/introduction-to-fluorescence-microscopy

[47] C. L. C. Tortora, R. F. Berdell, and J. Gerard, "Crescimento Microbiano," 12th editi ed: Armet Editora Ltda, 2017, pp. 149-171.

[48] R. Hazan, Y. A. Que, D. Maura, and L. G. Rahme, "A method for high throughput determination of viable bacteria cell counts in 96-well plates," *BMC Microbiology,* vol. 12, pp. 1-1, 2012.

[49] J. O'Brien, I. Wilson, T. Orton, and F. Pognan, "Investigation of the Alamar Blue (resazurin) fluorescent dye for the assessment of mammalian cell cytotoxicity," *European Journal of Biochemistry,* vol. 267, pp. 5421-5426, 2000.

[50] S. D. Sarker, L. Nahar, and Y. Kumarasamy, "Microtitre plate-based antibacterial assay incorporating resazurin as an indicator of cell growth, and its application in the in vitro antibacterial screening of phytochemicals," *Methods,* vol. 42, pp. 321-324, 2007.

CHAPTER IV– Review about tantalum nanostructures achieved by anodization and micro-arc oxidation

4 Introduction

In this chapter a literature review about tantalum nanostructures achieved by anodization and micro-arc oxidation with a biomedical final application is presented. The surface properties of the Ta_2O_5 nanostructure, such as morphological, chemical, physical and structural, are introduced and discussed. Moreover, based on the literature, a description of the mechanisms of both electrochemical processes is also provided.

4.1 Tantalum nanostructures obtained by anodization and micro-arc oxidation processes

During the past years, as nanostructured surfaces (nanoporous or nanotubular structures) combine the functional properties of the material and a well-controlled nanoscale architecture, they have attracted much attention due to a wide range of possible applications, such as biomedical devices, catalysis, (micro)electronics, energy, photonics [1, 2] and sensors [3]. Inorganic nanoporous structures, like metal oxides, are also promising as components in heterojunction solar cells, photocatalytic water splitting, fuel cells, molecular filtration and bioengineering [1, 2].

Tantalum oxide (Ta_2O_5) has been attracting attention and it has been widely used in several applications according to its specific properties since it is a multifunctional material [4]. Nanostructured Ta_2O_5 films have high dielectric strength which make them useful in various applications, such as storage capacitors and resistors in electronic [5, 6] and microelectronic industries [6-8]. Also, it shows an excellent corrosion [4, 9, 10] and abrasion [11] resistance and thus, it is used as protective coating in electronic devices, biomedical instruments [9, 10, 12, 13] and for chemical equipment (e.g., optical devices) [14]. Moreover, Ta_2O_5 has a wide band gap and therefore exhibits a high photocatalytic activity under UV radiation [3]. Ta_2O_5 has a high melting point [4] and thermal stability [2] and it seems to be promising for capacitors [15]. Ta-based materials (nitrides, oxynitrides) have been suggested as good option for photochemical [3, 16, 17] and MOS devices [18], as well as SiO-Ta_2O_5 films for optical and memory devices [1, 19, 20]. Because of its biocompatibility and bioinert behaviour [21], Ta_2O_5 is also a suitable material for bioengineering implants application [9, 12, 22-25].

Nanostructured Ta_2O_5 film can be fabricated electrochemically by a low-cost and easily scale-up method [26,27] called anodization which provides ease of control over the size and configuration of structure [26]. The process can work in low voltages, so-called anodization assisted by electric field, or it can be

carried out at higher voltages above the Ta_2O_5 breakdown potential (around 200 V [27]), so-called micro-arc oxidation (MAO), also known as plasma electrolytic oxidation (PEO).

4.2 Ta_2O_5 nanostructures obtained by anodization assisted by electric field

In anodization process, a potential is applied between the anode (metallic surface) and the cathode (counter electrode such as graphite, platinum, lead), transferring charges and ions and subsequently an oxide layer is formed. This process allows for the production of a controllable thickness of the protective oxide layer [28]. Moreover, depending on the process parameters, anodization can modify the roughness in order to obtain either compact layer either micro/nano-porous with controlled nanotubular and/or nanolayer structures besides chemical surface modification [28–30]. Working in potentiostatic mode, the electrolyte composition and concentration, the temperature, the applied potential and the process duration are adjusted according to the desired morphology, physical and chemical properties [20,28,31,32]. The most studied anodized metal is aluminum (Al) and the growth of self-ordered porous alumina layers [27] was proposed by Masuda and Fukuda [33]. More recently, well-ordered nanoporous or nanotubular structures, under optimized electrochemical conditions, have been reported for other valve metals, like titanium (Ti), zirconium (Zr), niobium (Nb), tungsten (W) and tantalum (Ta) [27,34]. Hence, those metals have become more attractive due to their potential use as catalysts, catalyst supports for fuel, electronic devices, waveguides, biological purposes, photoelectrochemical applications, among others [27, 35–37]. In case of Ta, the presence of fluoride ions (F^-) is necessary in the electrolyte since the growth of the Ta_2O_5 nanostructures is a result of the competition between electrochemical oxide formation and the chemical dissolution of oxide by F^- ions [27, 30, 31, 38–40]. Most literature has studied Ta anodization using electrolytes composed of hydrofluoric acid (HF) as source of F^- ions [2, 17, 19, 35, 40–42] to obtain nanostructured surfaces, however only very few studies were focusing on Ta anodization in HF-free electrolytes. Nanotubular [2, 3, 9, 17, 35], nanoporous [19, 40, 43] and dimples [2, 41, 42] Ta_2O_5 anodic layers were obtained by anodization using an electrolyte mixture of sulphuric acid (H_2SO_4) and HF. Different additives were studied in the mentioned electrolyte acid-mixture, such as ethylene glycol (EG) [16, 44, 45], dimethyl sulfoxide (DMSO) [44] and glycerol [45], achieving nanotubes. Lately, it was reported Ta anodization with an electrolyte mixture of H_2SO_4, water and ammonium fluoride (NH_4F) [22] and with glycerin [46] fabricating a nanotubular structure revealing, after annealing, a great potential as a highly efficient photoanode [22] and photoactivity [46]. Porous Ta_2O_5 nanostructures have been also achieved using organic electrolytes, such as glycerol and NH_4F [5] with addition of $(NH_4F)_2SO_4$ [18, 21] and EG [18], and most recently was reported a mixture of EG and NH_4F [47] with phosphoric

acid (H_3PO_4) and water [4]. Due to their high surface area, nanoporous surfaces are terrific candidate materials for electronic and sensor devices [5, 19, 22, 43] and, after a thermal treatment to become crystalline, they improve the photo-response making them suitable for photoelectrochemical devices [21] and photocatalysts [4] as well as for rapid and sustainable for Li storage in micro-batteries [47]. Interestingly, uniform ordered Ta_2O_5 nanoporous were also obtained using a F-free electrolyte, composed by glycerol and dipotassium phosphate, held at 180 °C [23]. However, most of the papers reports the development of Ta_2O_5 free-standing nanoporous membranes by anodization using an acid electrolyte mixture of H_2SO_4 and HF [3, 17, 25, 44, 48] (with additives such as EG or DMSO [9]), which make them potentially useful in electrolytic capacitors [9], photocatalysts [3, 25], molecular filtration membranes, Bragg-like sensor and dielectric spacers [25], platform for devices with sensing functions [48] and nanolithography templates [25]. Moreover, these membranes can also be transferred to non-Ta substrates, such as Si wafers or glass slides, having a great interest in sensor, optical and catalysis applications [9, 25]. Curiously, some studies related to free-standing titanium oxide membranes prepared by anodization in an EG electrolyte with small amounts of NH_4F and H_2O were found [49–55].

4.2.1 The mechanism of anodization assisted by electric field process

The development of nanostructures (nanotubes, nanopores, dimples) by anodization in a fluoride-containing electrolyte is based on an electric field-assisted dissolution mechanism that involves three main stages: 1) metallic surface oxidation forming an anodic layer by recombination of Ta^{5+}, O^{2-} and OH^- ions moving under the action of the electric field; 2) local chemical dissolution of Ta_2O_5 by fluoride ions and pore formation [28, 29]; 3) oxidation and dissolution reactions reach an equilibrium ensuring the pores/tubes growth [1, 30]. If the F^- ions concentration decreases, and the water increases, the anodic layer stabilizes, decreasing the dissolution and increasing the passivation.

Initially, the electric field is not uniform due to the surface asperities where the preferential dissolution occurs (Figure IV.1-a) [27, 31]. The F^- ions attack the oxide layer and dissolve it by pitting corrosion [32]. Thus, the first pits are formed in the first seconds of the electrochemical process (Figure IV.1–b), leading to a more uniform electric field caused by the polishing effect. Consequently, then the ordered nanopores structures are formed (Figure IV.1–c) [2, 21, 33]. During anodization, F^- ions continuously react with the oxide layer being incorporated in the outer part of the anodic layer [2, 33, 34], forming TaF_7^{2-} (Eq. IV.1 and IV.2) [29, 32].

$$\mathbf{2Ta + 5H_2O \rightarrow Ta_2O_5 + 10H^+ + 10e^-} \qquad \text{Eq. IV.1}$$

$$Ta_2O_5 + 14F^- + 10H^+ \rightarrow 2[TaF_7^{2-}] + H_2O \quad \text{Eq. IV.2}$$

These metal-fluoride complexes (TaF_7^{2-}) are responsible for the growth and shape of the nanostructures. The F^- ions has higher migration velocity comparing with O^{2-} ions, and consequently, the F^- ions migrate from the outer part of the anodic layer to the inner part, leading to the formation of nanotubes due to its water solubility (Figure IV.1–d) [31]. On the other hand, the water-solubility of the metal-fluoride complexes can promote the nanotubes release during the rinse of the samples with water, leaving behind a surface with ordered dimple-shaped morphology (Figure IV.1-e) [27].

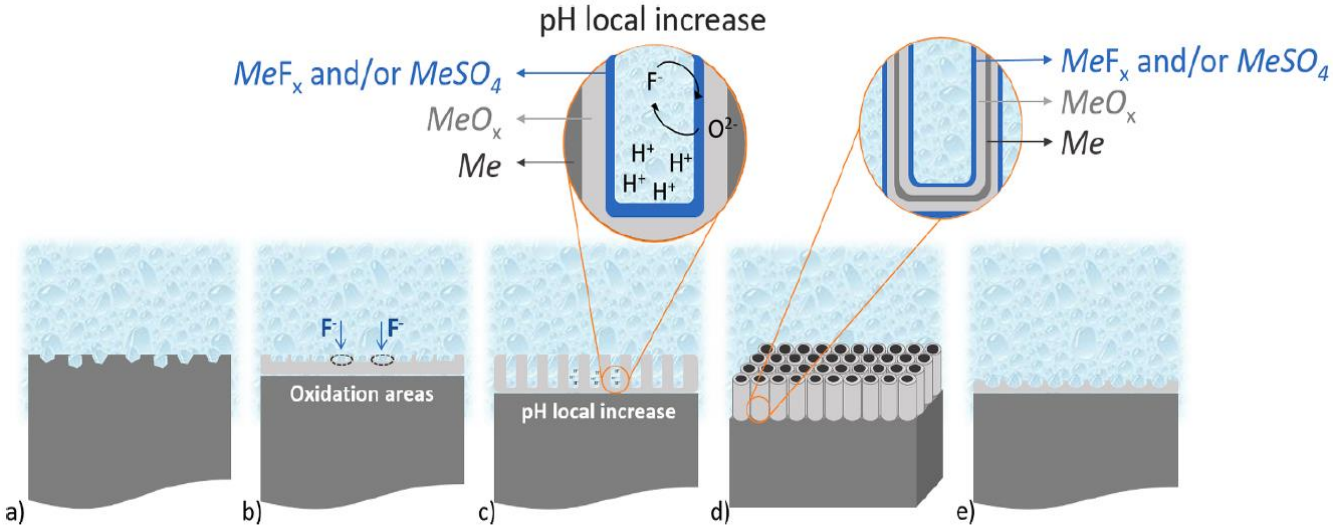

Figure IV.1. Schematic representation of the nanopore-nanotube assembly' mechanism: (a) Surface with pits before anodization; (b) Dissolution of the Ta_2O_5 anodic layer [27].

The growth of nanostructures from the asperities in the Ta surface occurs in all directions due to the hemispherical spread of the electric field, leading to a hemispherical shape of oxide layer structure [27].

4.2.2 Anodized Ta_2O_5 nanostructures for biomedical applications

Although there is a wide range of studies of anodization of tantalum in literature, there is a very limited number of published investigations of anodized tantalum for biomedical applications. Table IV.1 displays the papers on anodized Ta surfaces and the information is divided into the two reported morphologies related to biocompatibility: nanoporous and nanotubular structures (Figure IV.2-A). Formation of tubes from pore structures is observed by the bottom of a close-packed hexagonal pore layer that is gradually converted into round tubes (Figure IV.2-B) [35]. This formation, illustrated in Figure IV.2-C, is caused by selective dissolution of fluoride-rich layers and etching at preferential points by H_2O in the electrolyte. The top-view transition from pore to tube structures is illustrated in Figure IV.2-D.

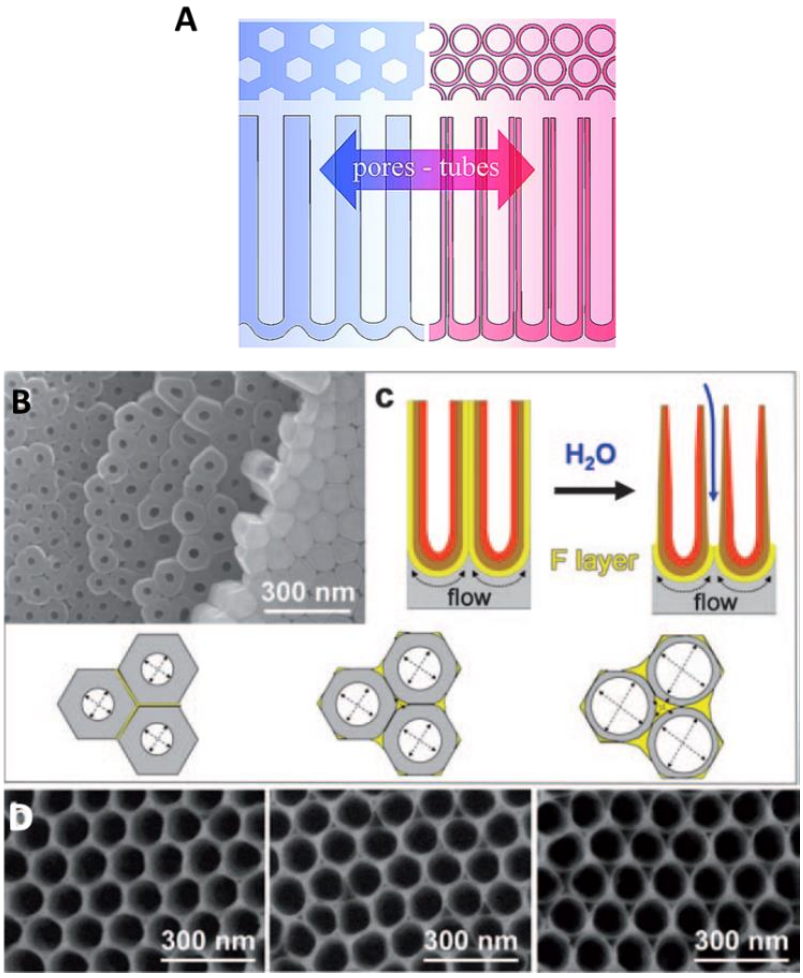

Figure IV.2. A) Morphological representation of pores and tubes [36]. B) SEM bottom view of a nanotube layer cracked off from the metal substrate [35]. C) Representation of the formation of a tubular morphology. D) Transition from a porous to tubular structure (left to right)

Table IV.1. Review table of the different type of anodized Ta nanostructures under different conditions for biomedical applications.

Type of nanostructures	Electrolyte	Working conditions	Time (min)	Distance between cathode and anode (cm)	Temperature (ºC)	Pre-treatment	Applications	References
Nanopores	1:9 (vol/vol) HF (38-40%): H_2SO_4 (95-97%)	30 V	5 -20	4	RT	Ultrasonic clean in acetone, ethanol and DI water for 15 min, and dry in air at RT.	Biomedical	[37]
Nanotubes	4.9 wt.% HF + H_2SO_4	10- 40 V			20	Ultrasonic clean in acetone, isopropanol, ethanol and water.	Biomedical	[38]
	5.5 mL HF + 223 mL H_2SO_4	15 V	90 s			Ultrasonic clean in acetone, ethanol and DI water for 10 min, and dry in air at 80 °C.	Endosseous implant	[39]
	1:9 (vol/vol) HF (48%) : H_2SO_4 (98%) + 5 vol.% DMSO	15 V	20		22	Clean with acetone and rinse with DI water	Orthopedic and dental implants	[26]

4.2.2.1 Morphological characterization of anodized Ta_2O_5 surface

4.2.2.1.1 Porous Ta_2O_5 layers

The most investigated electrolyte to produce Ta_2O_5 porous layers is composed by sulphuric acid (H_2SO_4) and hydrofluoric acid (HF).

Ta anodization using an electrolyte mixture of 9:1 (vol/vol) H_2SO_4 + HF at 30 V for 5 to 20 minutes formed porous Ta_2O_5 layers (Figure IV.3-a-e) [37]. The average of pore diameter increased with the increase in anodization duration (Figure IV.3-f). In agreement with SEM analysis, BET analyses confirmed the presence of micropores and mesopores on the anodized Ta_2O_5 surfaces. The nanophase roughness and surface area (assessed by AFM) increased with the anodization duration, on the other hand the microphase roughness (assessed by profilometer) decreased. These results demonstrated that the anodized nanoporous Ta_2O_5 layer has a smoother surface in the micrometer scale compared to untreated Ta. Contrarily, anodization process raised the nanophase roughness and surface area due to the nanopores formation, which properties are related to the improvement of cell-surface interaction. The current density-time was recorded to understand the formation mechanism of the porous Ta_2O_5 showing four distinct regions (Figure IV.3-g). In region "a", the current density decreases sharply due to the formation of the compact tantalum oxide layer, reaching the current's minimum in region "b", when the first pits are formed that will further grow to pores with different orientations. Then, in region "c", the current density increases that is caused by the dissolution reactions of the F^- ions, which migrate further into the barrier leading to pores' formation. The current's maximum is reached followed by a decreased tendency (region "d"), towards to reach an equilibrium between oxide formation and oxide dissolution reactions. However, the authors stated that the sample with the smallest pores' diameter (NPT25) produced by 5 minutes of anodization (regions "a", "b" and part of "c") was in fact multiple layers of stacked nanopores rather than a single nanoporous layer [37].

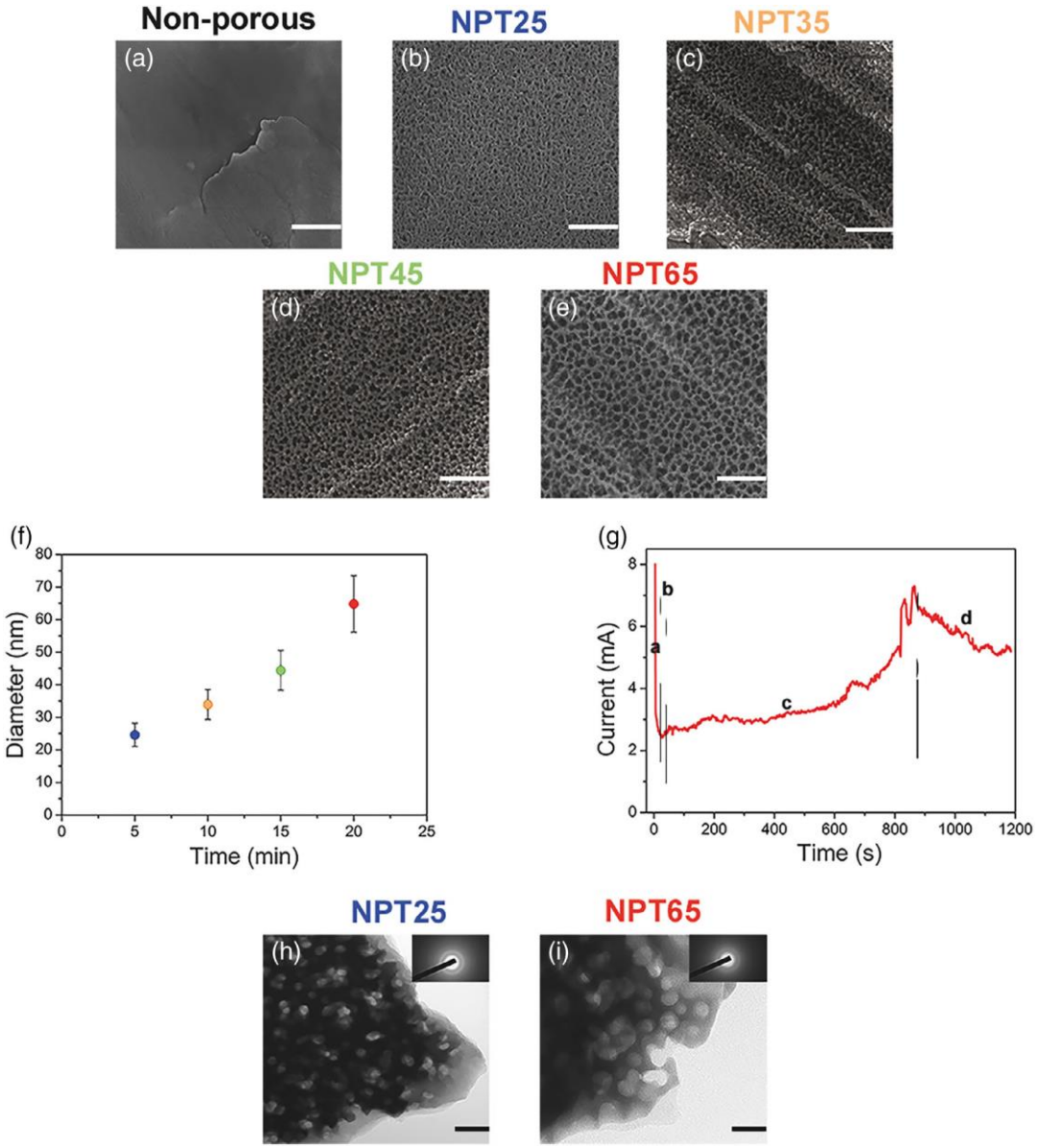

Figure IV.3. SEM micrographs of (a) nonporous tantalum and nanoporous tantalum oxide surfaces obtained by (b) 5, (c) 10, (d) 15 and (e) 20 minutes of anodization. Scale bars are 500 nm. (f) Increase in the average pore size of nanoporous tantalum oxide surfaces with increased anodization duration. (g) Current-time graph obtained during anodization of tantalum. Bright-field transmission electron microscopy (TEM) images of (h) NPT25 and (i) NPT65 samples. Insets show selected area electron diffraction (SAED) patterns of these samples. Scale bars for (h) and (i) are 50 nm [37].

4.2.2.1.2 Nanotubular Ta_2O_5 layers

Defined nanotubular Ta_2O_5 structures were obtained by anodization using an electrolyte mixture of 4.9 wt.% HF + H_2SO_4 at a range from 10 to 40 V (Figure IV.4-A and B). The nanotube diameters were proportional to the applied voltage, increasing from 20 to 90 nm (Figure IV.4-A) [38]. Using the same electrolyte composition at 15 V for 90 s, Ta surface was anodized and annealed at 500 °C for 2 h achieving a highly ordered tantalum oxide nanotube arrays with a diameter of around 20 nm and around 920 nm of length [39].

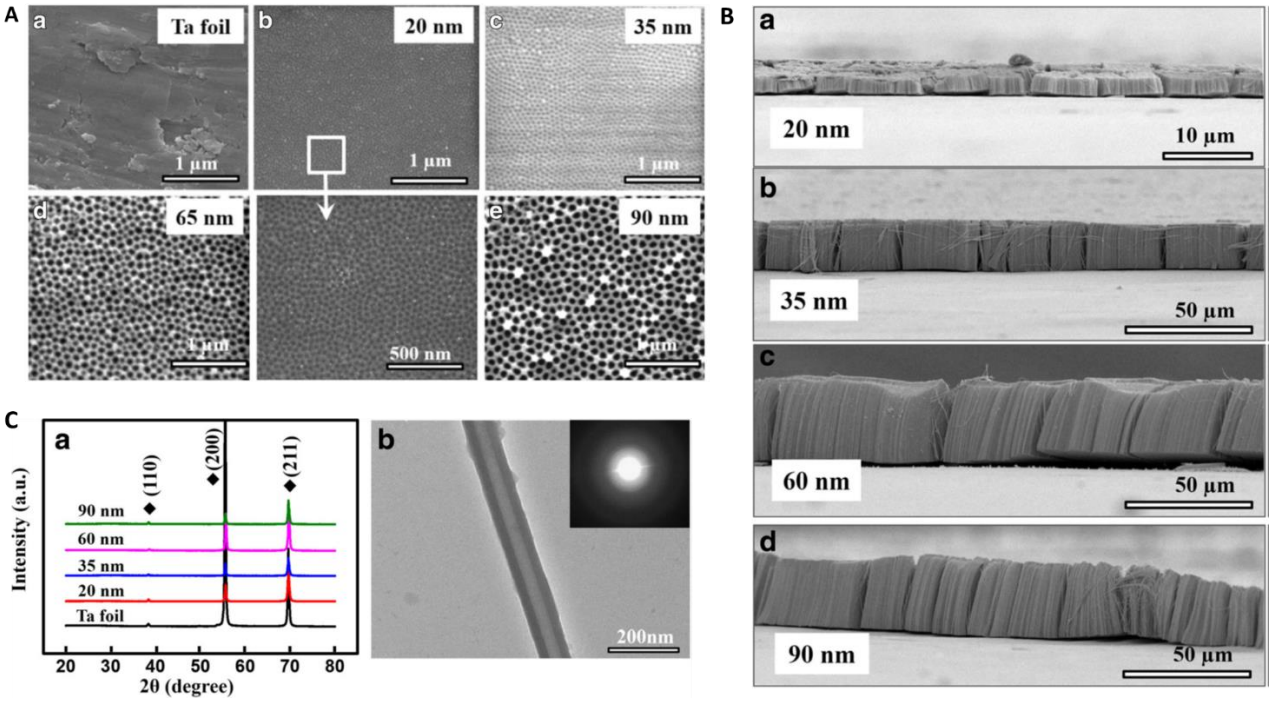

Figure IV.4. SEM micrographs showing the A) surface morphology and B) the cross-section of a- the untreated Ta foil and TaO_x nanotubes with diameters b-20 nm, c- 35 nm, d- 65 nm and e- 90 nm. C) Crystalline characterization by a- XRD spectra of the untreated and treated Ta surfaces; b- TEM micrograph of one anodized TaO_x nanotube with 90 nm of diameter (in inset is the correspondent diffraction pattern) [38].

The effect of addition of small volume of dimethyl sulfoxide (DMSO) to the electrolyte mixture of HF and H_2SO_4 was investigated in the nanotubular morphology development [26]. The increase of the applied voltage leaded to an increase of the length of vertically oriented nanotube arrays.

4.2.2.2 Anodized Ta_2O_5 surface chemical composition and wettability

The XPS results revealed that the outmost layers of the nanotubular tantalum oxide is mostly composed by Ta, O, C and S [39]. However, the authors did not mention the presence or not of F element. Moreover, Ta 4f spectra of pure Ta had two chemical states: 25.7 eV and 27.5 eV ascribed to Ta_2O_5 and 20.5 eV and 22.3 eV in the metallic state, while only one chemical state appeared after anodization and annealing treatments: 25.7 and 27.5 eV in the Ta_2O_5 state. On the other hand, Uslu *et al.* [37] demonstrated that the XPS spectrum of the untreated Ta had only the characteristics peaks of metallic Ta: $Ta4f_{7/2}$ and $Ta4f_{5/2}$ at 21.6 and 23.5 eV, respectively, while the Ta4f and O1s spectra of the anodized surfaces confirmed the formation of Ta_2O_5 layer.

Anodized Ta_2O_5 nanotubes were hydrophilic because the contact angles are smaller than 90° (and 60°) for both water [38, 39] and culture medium liquids [38]. The contact angle decreased with the increasing nanotube diameter to 35 nm, although for higher diameters the contact angle started increasing [38].

The wettability behaviour of these nanotubular structures was based on Wenzel's law, which ascribes a smaller contact angle as a result of the surface roughness, as the water fill the grooves below the droplet. Zeng *et al.* [38] determined the geometric roughness of the Ta_2O_5 nanotube surfaces by the physical surface area of nanotubes per unit of projected area (Figure IV.5). The geometric roughness factor G can be calculated by the following equation, assuming that the nanotubes' surfaces are smooth:

$$G = \left(4\pi L \frac{D + W}{\sqrt{3}(D + 2W)^2}\right) + 1$$

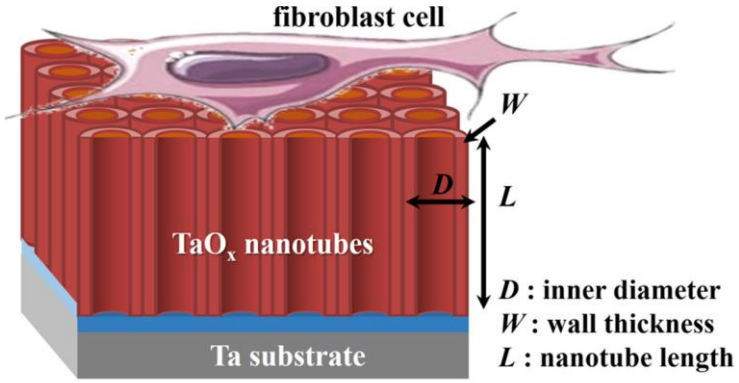

Figure IV.5. Schematic diagram of an idealized nanotubular structure with inner diameter D, wall thickness W, and nanotube length L [38].

In agreement to the Wenzel's model, smaller diameter nanotubes have higher geometric roughness factor and thus better hydrophilicity, with the exception of the 20 nm-diameter nanotubes that revealed an unclear nanotubular morphology (Figure IV.4-B) with the smallest geometric roughness and the poorest hydrophilicity [38]. Similar trend of water contact angles was observed with the increasing of the anodized Ta_2O_5 pore diameter, as the surface had a hydrophilic character for 25 and 35 nm pore diameters while for 45 and 65 nm diameter were hydrophobic [37]. However, the authors used the Cassie-Baxter model to explain this behaviour on rougher surface, which defends that the water molecules are not in complete contact with the surface, only with the peak points of the surface, due to the air molecules entrapment in the surface cavities.

Anodized Ta_2O_5 nanotubes after annealing also shows a hydrophilic behaviour with a water contact angle around 30.5 ° and a consequently increase of surface energy to 68.6 mJ/m^2 when compared to untreated Ta (33.6 mJ/m^2) [39].

4.2.2.3 Structural analysis of anodized Ta_2O_5 surface

Anodized Ta_2O_5 nanopores/nanotubes crystallinity was assessed by XRD and TEM characterization. TEM micrographs confirmed formation of nanoporous morphologies of anodized Ta and the SAED patterns in

inset showed that the Ta_2O_5 had an amorphous structure (Figure IV.3-h and i) [37]. The diffraction patterns of the XRD spectra were ascribed to the Ta substrate, suggesting that the Ta_2O_5 nanotubes was probably amorphous (Figure IV.4-C and Figure IV.6) [38, 39]. The TEM micrograph of the 90 nm- diameter Ta_2O_5 nanotube peeled-off revealed a well-defined nanotubular structure (Figure IV.4-C-b) as well as the diffraction pattern in the inset confirmed that the nanotubes are indeed non-crystalline [38]. The XRD pattern of the anodized Ta_2O_5 nanotube surface after annealing (Figure IV.6) showed the appearance of Ta_2O_5 diffraction peaks with quite low intensity, which can be related to the short length of the Ta_2O_5 nanotubes [39].

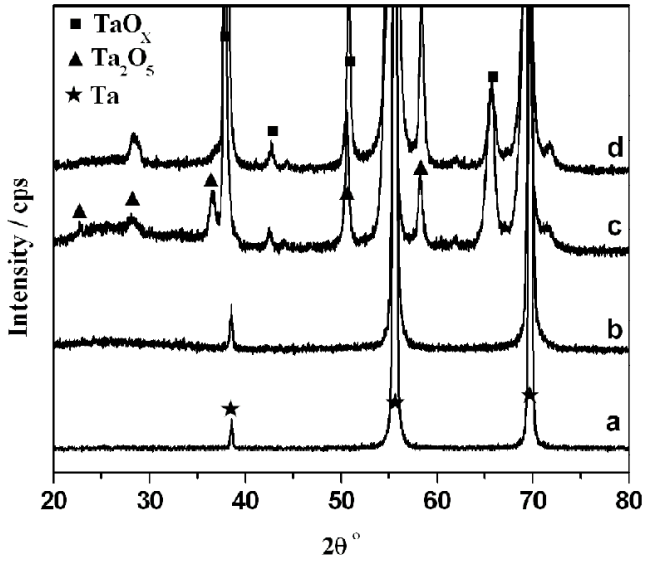

Figure IV.6. XRD spectra of a) pure Ta, b) anodized Ta, c) anodized Ta after annealing and d) pure Ta after annealing at 550 °C for 2 h [39].

4.2.2.4 *In vitro* biocompatibility of anodized Ta_2O_5 surface

To evaluate cell behaviour in response to untreated-Ta and Ta_2O_5 nanostructures, cell adhesion and proliferation, protein adsorption were assessed by several authors [26, 37-39], using different cell lines.

MTT results for fibroblasts cells cultured on Ta_2O_5 nanoporous surfaces with two different pore diameters, 25 and 65 nm, and untreated Ta surfaces, demonstrated that after 1 day of culture the anodized surface had more adherent cells than untreated Ta (Figure IV.7-a). At the third day of culture, the 25 nm-diameter pores surface showed higher cellular density than the other surface. The same behaviour was observed after 5 days of cell culture, as the anodized surfaces improve cell proliferation than untreated Ta, and lower pore diameter had the best biological behaviour. Both fluorescence microscopy (Figure IV.7-b-d) and SEM images (Figure IV.7-e-g) are in agreement to the MTT results. The anodized surface with 25 nm pore size displayed the best biological response because it was the more hydrophilic surface [37].

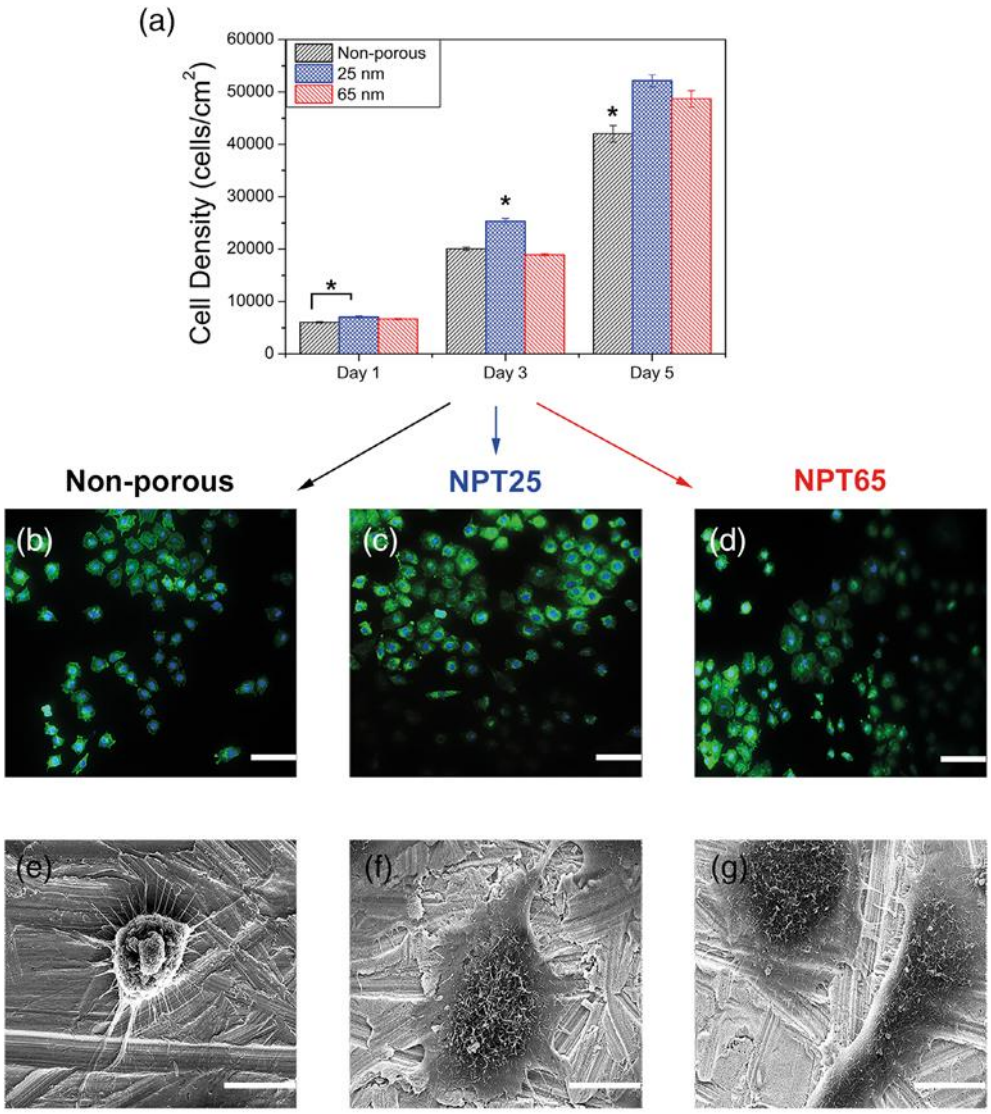

Figure IV.7. Fibroblast density on tantalum samples up to 5 days *in vitro*. Actin (green) and nuclei (blue) stained images of fibroblasts cultured on (b) nonporous, (c) NPT25, and (d) NPT65 samples. Scale bars are 50 μm. SEM micrographs of fibroblasts cultured on (e) nonporous, (f) NPT25, and (g) NPT65 samples. Scale bars are 10 μm [37].

Similarly, fibroblast cell adhesion to Ta_2O_5 nanotubes was characterized by fluorescence microscopy (Figure IV.8) and SEM [38]. The fibroblasts revealed an excellent adherence with an elongated flatted morphology, although both untreated Ta foil and 90 nm-diameter Ta_2O_5 nanotubular surface showed less adherent cell. The 35 nm-diameter Ta_2O_5 nanotubular surface had the largest cell coverage area. In agreement, cell proliferation evaluated by the WST-assay was higher in the 35 nm-diameter Ta_2O_5 nanotubular surface. Thus, the cells responses demonstrate a wettability-dependent behaviour, since the more hydrophilic nanotubular surface shows better cell adhesion and proliferation [38], in agreement with the biological responses on Ta_2O_5 nanoporous surfaces [37].

Significantly more fibronectin and BSA proteins were adsorbed on nanotubular Ta_2O_5 surfaces than on untreated Ta surfaces. This improvement can be correlated to the surface nanoscale topography and

hydrophilicity [39]. The improved fibronectin adsorption on the anodized Ta surface suggests that the Ta_2O_5 nanotube layer can enhance osteoinductivity of pure Ta and promote osteogenesis of the Ta implant. The MTT assay demonstrates that rabbit bone mesenchymal stem cells (rBMSCs) attach and spread significantly better on nanotubular Ta_2O_5 surfaces than on untreated Ta surface. Additionally, the expression of Osterix, alkaline phosphatase (ALP), Collagen-1 and Osteocalcin at Ta_2O_5 nanotube surfaces was significantly higher, in comparison with the untreated Ta, suggesting that the Ta_2O_5 surfaces have a great potential to induce rBMSCs differentiation to osteoblasts, to promote rBMSCs differentiation, matrix formation and mineralization and to accelerate rBMSCs matrix protein production and early osteogenesis, respectively. The fluorescence microscopy analysis demonstrated that the rBMSCs cells cultured on untreated Ta had a more rounded morphology and less in number than those on the nanotubular Ta_2O_5 surfaces [39], in line with the results of fibroblast culture [38]. Hence, Ta_2O_5 nanotube layers enhance the hydrophilicity and surface energy of pure Ta, which properties are consistent with the improvement of protein adsorption and cell behaviour on a nanotubular surface [39].

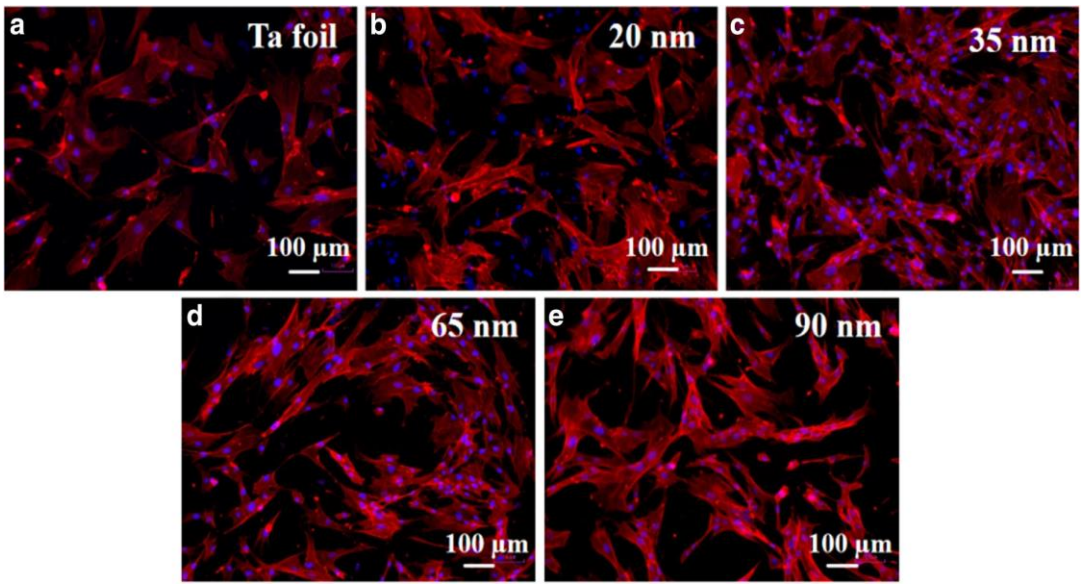

Figure IV.8. Fluorescence microscopy images of the fibroblast cell attachment on the a- Ta foil and self-organized TaOx nanotubes with diameters of b- 20, c- 35, d- 65, and e- 90 nm, respectively. The red fluorescence indicates cytoskeletal protein actin filament, and the blue fluorescence indicates nuclei [38].

Using a smooth Ta surface with passive oxide as control, human fetal osteoblasts were cultured on these surfaces and on Ta_2O_5 nanotubes surface. Fluorescence microscopy images of osteoblasts after one day of culture suggested that cells were viable, and the cellular adhesion was very similar on both surfaces. After 4 days of culture, the cells on Ta_2O_5 nanotube arrays stood out showing higher cell spreading and cell communication as well as the presence of multi-nucleated cells was noticed. These results suggest that the nanotubular surface provides a favorable nano-environment for osteoblast development. The MTT assay indicated that the cells were healthy and viable on nanotube arrays than on smooth oxide surfaces.

Cell differentiation was assessed by ALP activity. Higher ALP levels were observed on the nanotubular surfaces. Correlated results were obtained for calcium content on nanotubular surface, suggesting a favorable interface for cell differentiation and matrix production. Furthermore, during the differentiation phase the cells showed a spreading morphology on nanotubular surface with some cluster formation (Figure IV.9-B), covering the most of the surface, while the majority of the osteoblast were spherical on the smooth tantalum oxide surface (Figure IV.9-A), demonstrating that the nanotopography induces the characteristic phenotypic behaviour of osteoblasts.

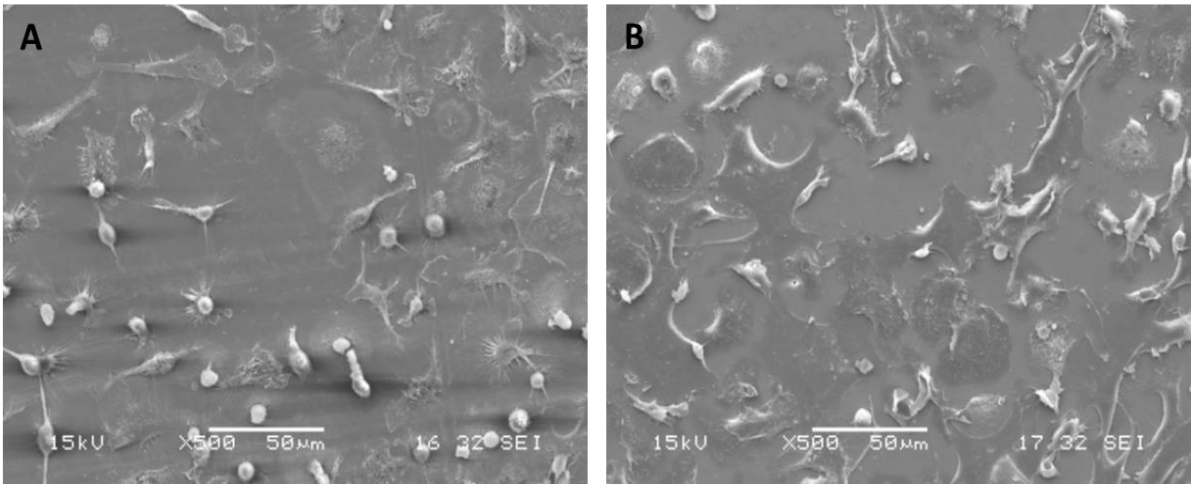

Figure IV.9. SEM micrographs of osteoblastic cells on smooth tantalum oxide (a) and tantalum oxide nanotube arrays (b) after 2 weeks of culture [26].

4.2.2.5 Mechanical and corrosion resistance of anodized Ta_2O_5 surface

After anodization and annealing at 550 °C for 2 h, the anticorrosion of Ta is significantly improved in the culture medium containing 10% PBS due to the nanotubular oxide layer formed on the surface of the Ta substrate [39]. Thus, a Ta_2O_5 nanotubes implant surface may hardly cause cytotoxicity, allergy and chronic inflammation, suggesting a good biocompatibility.

4.3 Ta_2O_5 nanostructures obtained by micro-arc oxidation

4.3.1 Micro-arc oxidation (MAO)

Micro-arc oxidation (MAO) technique, also known as plasma electrolytic oxidation (PEO), originates from anodization but is distinguished by employing higher voltage [40-42]. When the applied voltage is high enough (higher than the breakdown potential of the oxide layer), a dielectric breakdown occurs through the thickness of the growing oxide layer. A large number (cascade) of micro-discharges distributed over the surface is formed [40], and consequently a plasma formation initiates, leading to a series of complex electrochemical, plasma and thermo-chemical reactions, under high temperature and pressure (Figure

IV.10) [25, 43, 44]. The electric field through the oxide (passive layer band gap) increases, and if the applied voltage reaches the breakdown level, i.e., dielectric strength of the oxide, the discharge occurs Figure IV.10-A) [40, 45]. This discharge is initiated by the electron flow from the electrolyte to the substrate, crossing through the passive layer, initially in particular areas (the micro defects of the passive layer), leading to plasma formation and growth [40, 43]. The resultant plasma contains species from the substrate (metallic cations - Me^{x+}), the electrolyte (cations - C^{+}, and anions - A^{-}, OH^{-}) and the growing oxide layer, as well as O_2 gas, which resulted from the ionization of water molecules (Figure IV.10-B). The O_2 molecules can combine with metal cations from the substrate in the plasma. As the plasma cools during its collapse, if the thermodynamic driving forces are greater than the (re)formation of water, the formation of oxide occurs when the temperature becomes relatively low, depending on the metal and its concentration. Simultaneously, at the moment of a discharge, a bubble of water vapour is formed, which rapidly expands (near the plasma in contact with the electrolyte) due to the heat flow. Also, the electric resistance rises, the discharge stops and the bubble shrinks (Figure IV.10-B) [40, 46]. The new oxide condenses, and is quickly redistributed within the layer structure, erupting into “volcanic craters”. The layer then solidifies and a disordered microstructure architecture is created (Figure IV.10-C). The substrate cycle process in progress is continuously consumed at the site of the discharge by evaporating into the plasma and the oxide is gradually formed at the vicinity [40], growing simultaneously inward and outward from the original metal surface [42], with a continuous reconstruction throughout its thickness (Figure IV.10-D). Thus, several phenomena take place during a MAO process for the metal oxidation: the melting and vaporization of the metallic substrate, the melting of the oxide layer, the initiation and sustainment of the plasma, the water vaporization, the electrical heating of the electrolyte and finally the metal to oxide conversion [40]. The developed oxide is broadly classified into two layers, as a porous outer layer and a compact inner layer (Figure IV.10-D) [42]. The discharge’s characteristics change as the oxide thickness increases. This demonstrates that there is a tendency for the discharge to become more energetic and more disperse in time and space [40, 46-48], which increases the duration of the process [41]. Also, oxygen liberation at the anode occurs at a high anodic current due to the oxidation of water or oxide ions [42]. The lifetime of a discharge cascade is terminated when the oxide reaches enough thickness, in that specific site, presenting a higher electrical resistance than in the vicinity.

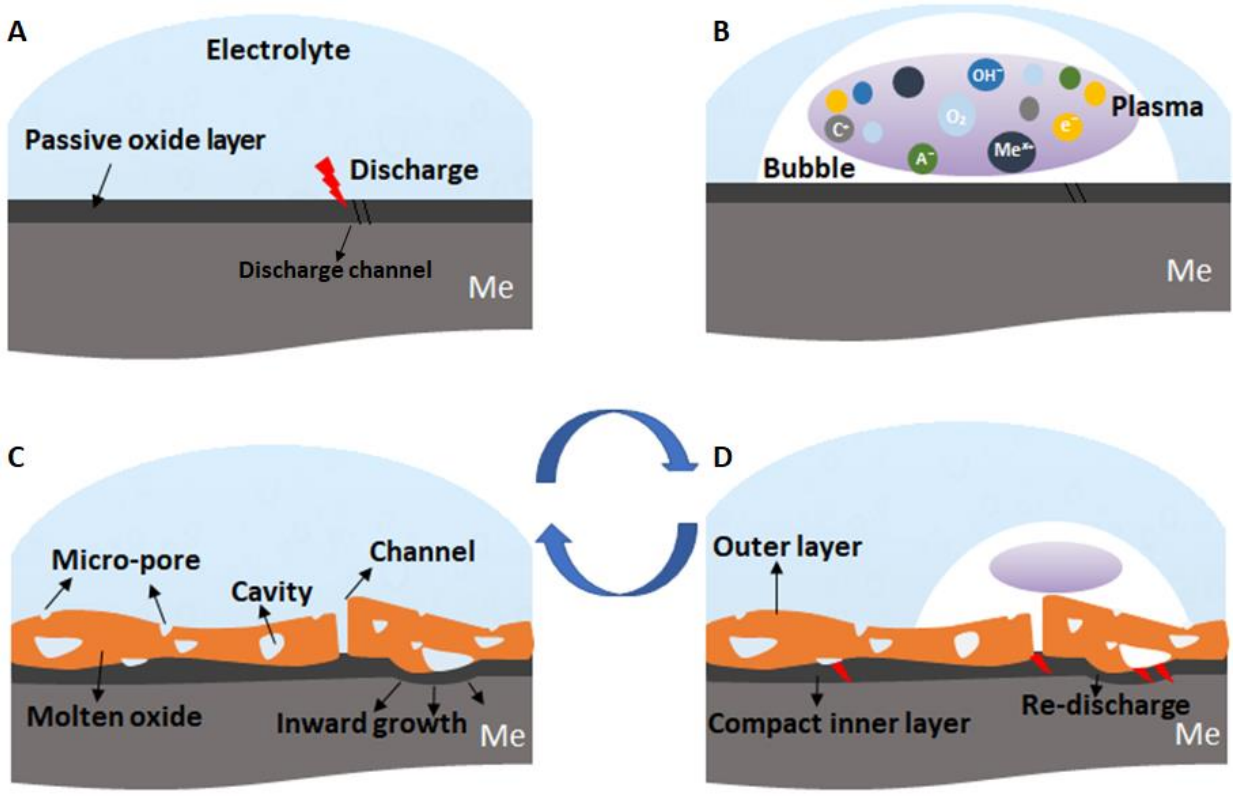

Figure IV.10. The grow mechanism of MAO oxide layer.

The MAO step-up and procedure are relatively similar to anodization, although oxidation occurs when there is a combination of metal and oxygen atoms or ions within the discharge plasma (as it cools and collapses) instead of a continuous transport of ions through the electrolyte and within a thin oxide layer [40]. During MAO, with anodic polarization, the electron flow through the oxide layer is limited by the relative slow rate of the arrival OH^- ions, through the electrolyte under the influence of the applied potential (Figure IV.11). Like in anodization, electrolyte composition, which is even aqueous and alkaline, influences the discharge ignition since it must be conductive, and may influence the chemical reactions of ionized species as well as the metallic substrate oxidation [40, 49].

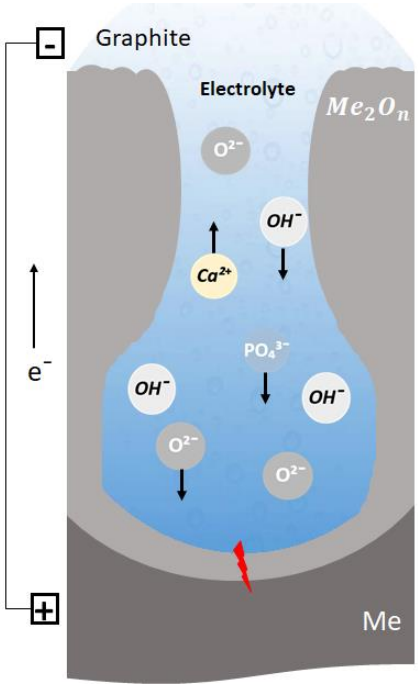

Figure IV.11. Transport phenomena taking place during MAO process.

This mechanism allows the production of thick oxide layers which often results in a harder and more crystalline structure due to large amounts of heat released by the discharges [40, 41]. The maximum thickness is not dependent on the applied voltage but is reached at stable discharges [40]. Additionally, the MAO process allows for the formation of durable and well-adherent coatings on many metals (e.g., Ti, Mg, Zr and Ta) [25, 40], as well as for the creation of surfaces with a wide range of colors and textures [40]. Also, the resulting oxide layer has relatively high levels of porosity [40], and it can be enriched with components from the electrolyte (Figure IV.11) [25]. The MAO oxide layer can benefit of mechanical stability, such as reduced stiffness and Young's modulus, conferring sliding, corrosion and fatigue resistance. MAO enables the development of functional surfaces for biomedical applications. In fact, this process provides the formation of porous structures, raising the specific area which allows a strong bonding to the bone. Furthermore, incorporation of species from the electrolyte, as calcium (Ca) and phosphorous (P), enhances the bioactivity [40]. All these surface features can be tailored by the applied voltage, anodic current density and electrolyte composition and concentration, like in anodizing [25]. It is lso important to highlight that MAO process, like anodization, is quite well industrially accepted.

4.3.2 Understanding the microdischarge phenomena during MAO process

The MAO process in a Ta surface can be divided into three distinct stages as displayed in Figure IV.12-A and B [41, 47, 50, 51]. In the first seconds of a galvanostatic mode (Figure IV.12-A), the voltage sharply increases in a short time, which is defined as the first stage of the MAO process. It is similar to conventional anodization and a compact oxide layer is formed. The electric field strength for a given current density remains constant during the anodic growth and the ionic current is two or three orders of magnitude larger than the electronic component. The voltage increases with the anodic layer thickness in order to maintain the electric field strength constant [41, 47, 50]. In this stage, galvanoluminescence is not observed. During the electrolytic oxidation, electrons are injected into the conduction band of the anodic layer, which are accelerated by the electric field producing avalanches by an ionization mechanism [50]. When the electronic current avalanche reaches a critical value, the dielectric breakdown occurs, which is reflected by an apparent deflection from linearity of V-t curve and appearance of small sparks. The compact layer thickening is terminated, starting a so-called breakdown voltage (second stage) [41, 47, 50] which activates a rapid increase of galvanoluminescence intensity [50]. The breakdown is triggered by local heating effects caused by highly localized processes taking place at macro and micro-defects in the oxide (electrolyte-filled fissures, micropores, flaws) [41, 47]. The voltage keeps increasing continually, but the voltage-time slope decreases, and a large number of bright spots (microdischarges) appear over the whole surface. The slope decreases as a consequence of the relatively low voltage required to maintain the same total current density, due to the fact that the electron's current density is independent from the anodic layer thickness. Further, the third stage is reached when the voltage is relatively constant, with a voltage-time slope near zero, since the total current density is practically independent of the anodic layer thickness, as the fraction of electronic current density in total current density becomes dominant [41, 47]. When a constant potential is applied in the MAO process, the same three stages are observed (Figure IV.12-B) [45]. According to the Ohm's law, for this situation the first stage is characterized by a sharp decrease of the current density that corresponds to the moment in which the surface oxidation forms the anodic layer. Then in the second stage, the current density continually decreases, but with a lower slope, corresponding to the breakdown and the beginning of sparking. Finally, the current density is nearly constant.

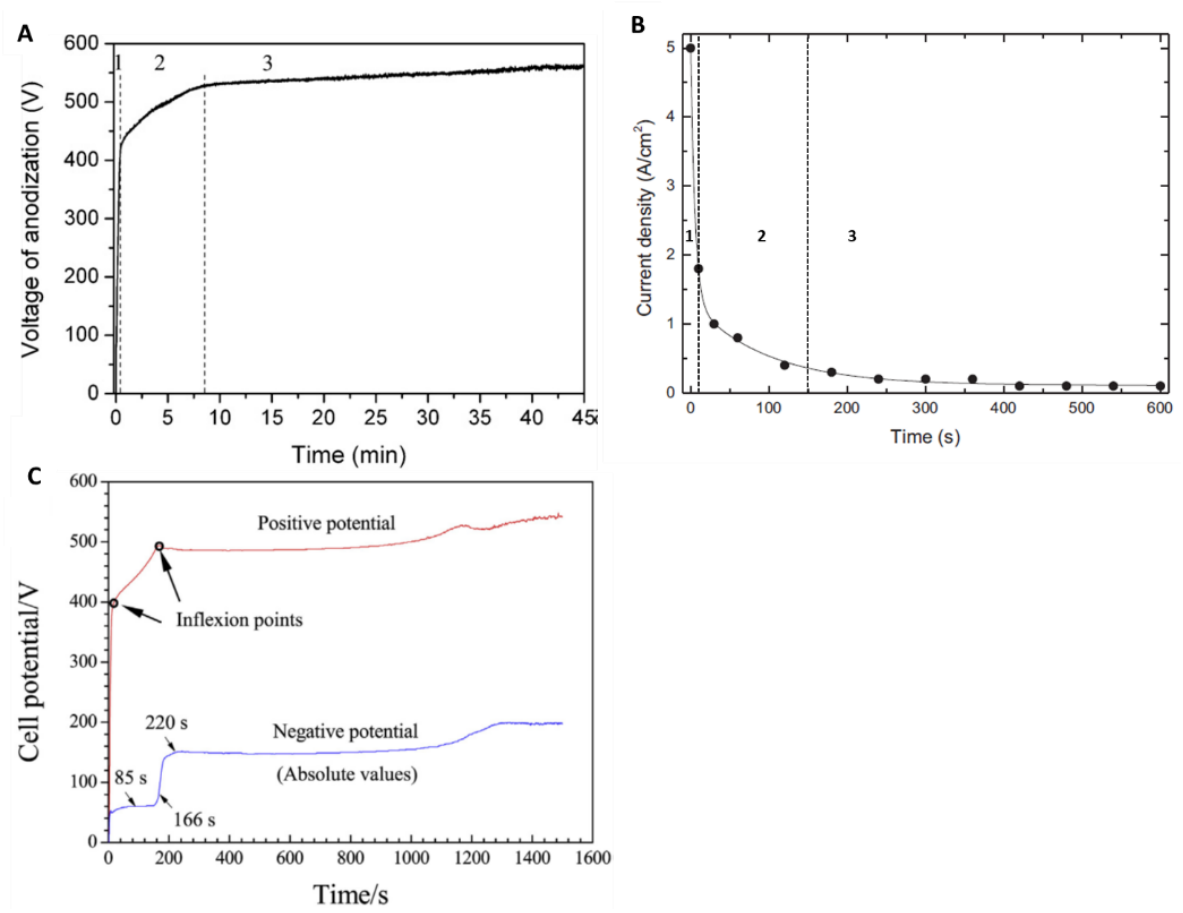

Figure IV.12. A) Typical voltage-time curve recorded during a MAO process carried out in a galvanostatic mode [41] and B) typical current-density curve at potentiostatic mode [45]. C) Cell potential-time responses during MAO treatment [52].

Throughout a MAO process, carried out in AC mode using a silicate electrolyte to modify a Ta surface, the cell potential-time responses (Figure IV.12-C) displays an increase of the positive potential whilst the anodic layer grows (also called barrier layer) until the first inflection occurs, when fine sparks initiate and the breakdown commences [52]. Then, the potential rises slower when there is a second inflection that indicates that the sparks are more intense. In agreement, the negative potential increases during the growth of the barrier layer reaching a plateau, followed by a potential escalation coincident with the second inflection in the anodic potential. Then, the potential increases slowly as the anodic potential.

The recorded voltage-time (during the galvanostatic mode as first step) and the current density-time curves (the second step the process was switched for potentiostatic mode when as the desired voltage was achieved) are strongly influenced by the electrolyte composition, such as increasing the electrolyte conductivity, by adding the calcium formate ($Ca(HCOO)_2$) or the magnesium acetate ($Mg(CH_3COO)_2$) to calcium hypophosphite ($Ca(H_2PO_2)_2$). There are more charge carries in the solution, thus the resistive behaviour decreases less, and larger and more intense sparks appear at lower voltages, creating more larger pores, increasing the current density [25, 53]. In fact, the third region is better discerned for 0.1

and 0.5 M K_2SiO_3 since for the most concentrated electrolyte (1 M K_2SiO_3) voltage oscillations are verified, which is related to the necessary time to reach the maximum voltage of 400 V as it is dependent on the K_2SiO_3 concentration (such as that to more concentrated electrolytes more time is required).

Hence, it is possible to summarize that the stages of the MAO process are dependent on the electrolyte composition and concentration but are also independent on the operation mode (DC or AC).

In literature, there are two models to explain the formation of sparks. The first suggests that the appearance of spark discharge comes as a consequence of the dielectric breakdown of the oxide in a strong electric field. The second considers spark discharges as gas discharges occurring in micropores of the oxide, since the formation phase in micropores is induced by the initial dielectric breakdown of the barrier layer in the bottom of the micropores. The results reported in a study of a MAO-treated Ta surface at 70 mA/cm^2 using H_3PO_4 electrolyte indicate that both models can be distinguished during the MAO treatment. In the second stage, the first model neither ionic nor atomic lines are observed in the luminescence spectrum suggesting that at the beginning of spark discharging there is a continuum radiation (Figure IV.13-d). In the third stage, when the electric field reaches a critical value and the electronic current is high enough to cause gas discharge occurrence in the micropores, strong emission ionic and atomic emission lines appear, ascribed to O_2 (Figure IV.13-a) and H_2 species (Figure IV.13-b and c), in agreement with the second model [50].

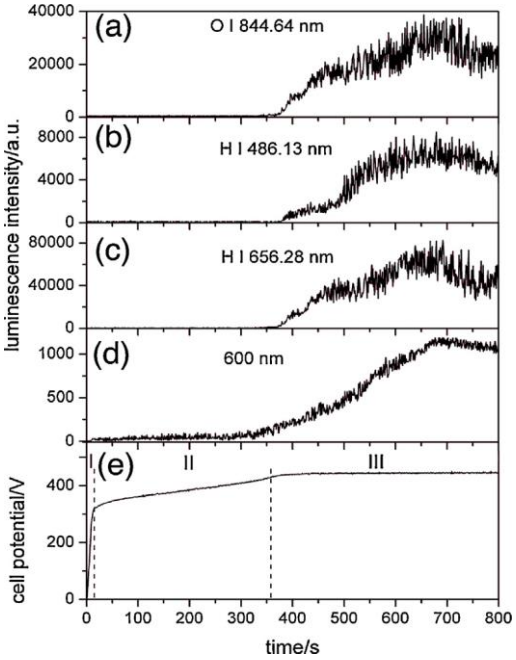

Figure IV.13. The temporal variation of the luminescence intensity of a) oxygen and b-c) hydrogen lines, d) continuum radiation at 600 nm, and e) cell potential [50].

The anodic pulses are responsible for multiple electrode processes such as anodic layer formation and oxygen evolution, while the cathodic pulses lead to hydrogen evolution. The gas bubbles contain hydrogen and oxygen, both generated electrochemically and by dissociation of water molecules [52]. In this sense, some investigations have been carried out to understand the behaviour of gas bubbles and sparks formation recording real-time images during the MAO process.

The real-time images (Figure IV.14) demonstrate that first the bubbles cover the surface and while their density decreases, short microdischarges start to uniformly distribute over the whole surface, which decreases in number and increases in diameter and intensity with increasing time and voltage. For more concentrated electrolytes, the sparks start at lower voltages [51].

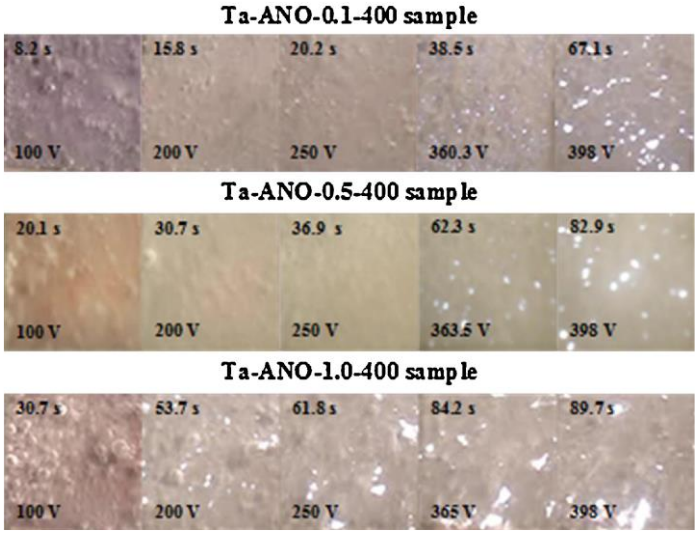

Figure IV.14. Real-time images of the MAO process of Ta (10 mm × 10 mm) [51].

Another study carried out at 70 mA/cm^2 using tungstosilicic acid (0.001 M $H_4SiW_{12}O$) [47], shows different stages of the process with distinct microdischarge characteristics in the real-time images. Initially an intensive gas formation is observed after the first few seconds of the process (Figure IV.15-a). After 20 s, small microdischarges start to be visible followed by bubble evolution (Figure IV.15-b). During the MAO process, as mentioned before, the size of the microdischarges becomes larger in a reduced number (Figure IV.15-c-f). In addition, the spatial density of the microdischarges reaches the maximum after about 2.5 minutes, which is substantially reduced during the next 5 min, achieving a plateau. In agreement, the surface fraction under active discharge sites also has a maximum of about 5% after 2.5 minutes, which continually decreases with time. Thus, relatively small discharges occur during the MAO process. The behaviour of the microdischarges is related to the number of microdischarge sites through which higher anodic current is able to pass, since the number of pores decreases while their size increases with the MAO duration. The optical emission spectroscopy, used to detect the presence of self-absorption for Balmer lines in MAO spectra, displays a strong line ascribed to H_α while other two weaker Balmer lines

associated to H_β and H_γ. The analysis of the H_β line shape indicates the presence of two types of discharges with a relatively low electron number density (Ne) of 0.9×10^{15} cm^{-3} and 2.2×10^{16} cm^{-3}, respectively, due to the high melting temperature of Ta (comparing with Al that have 3 types of microdischarges). This prevents formation of metallic plasma in microchannels though the oxide layer.

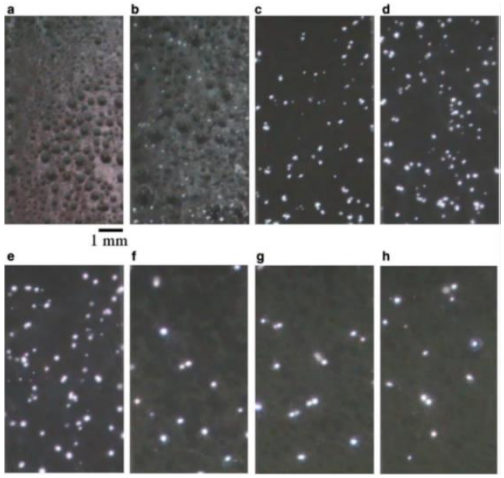

Figure IV.15. Real-time images of the MAO process of Ta using tungstosilicic acid electrolyte at a) 10 s, b) 20 s, c) 1 min, d) 3 min, e) 5 min, f) 15 min, g) 30 min and h) 45 min [47].

In a bipolar pulsed current MAO process, the Ta surface presents an initial purple interference colour of a thin anodic layer in first few seconds. This is accompanied by the presence of gas that consists of electrochemically generated hydrogen produced during the cathodic polarization and possible oxygen created over the anodic polarization (Figure IV.16-a) [52]. Then, the whole surface has numerous white and fine sparks, that reduces in number and increases in intensity, turning to an orange hue (Figure IV.16-b-g). Also, a more energetic gas evolution and a wider dispersion of bubbles into the electrolyte arise in the presence of strong discharges.

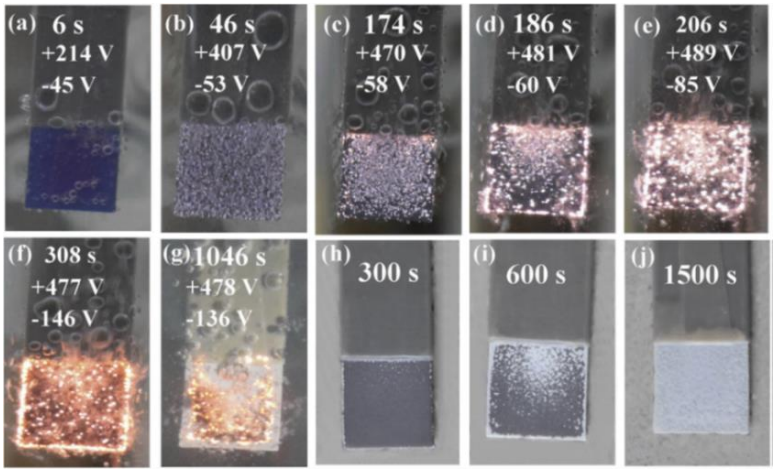

Figure IV.16. (a–g) Real-time images during MAO of Ta (10 mm × 10 mm) with corresponding positive and negative potentials indicated using a silicate electrolyte. (h–j) Optical images for the coatings formed for 300, 600 and 1500 s, respectively [52].

4.3.3 Formation mechanism of Ta_2O_5 anodic layer

Initially, the oxide layer grows at the Ta/oxide and oxide/electrolyte interfaces as result of migration of O^{2-}, OH^- and Ta^{5+} ions across the oxide, assisted by a strong electric field. Consequently, a small amount of electrolyte is incorporated into the oxide at the oxide/electrolyte interface. The main chemical reaction at metal/oxide interface is defined by Eq. IV.3, while the reaction at oxide/electrolyte interface is defined by Eq. IV.4 and the overall reaction in Eq. IV.5 [41].

$$Ta \rightarrow Ta^{5+} + 5e^- \quad \text{Eq.IV.3}$$

$$4H_2O - 4e^- \rightarrow O_2 \uparrow + 4H^+ + 2H_2O \quad \text{Eq.IV.4}$$

$$2Ta^{5+} + 5H_2O - 10e^- \rightarrow Ta_2O_5 + 10H^+ \quad \text{Eq.IV.5}$$

According to the measurements of the total thickness (t), outward growth thickness (t_{out}) and inward growth thickness (t_{in}) (Figure IV.17-A) on the cross-sectional SEM micrographs, during the MAO process, the variation in the total growth rate (V) of the anodic thickness (Figure IV.17-B) indicates that the growth process of MAO-layers can be divided into three distinct periods [54]. In first minute of MAO, a dramatic increase in the total thickness occurs as well as in the total growth rate V of the anodic layer, so that the outward growth rate (V_{out}) is much superior than the inward growth rate (V_{in}). Thus, the outward growth rate dominates the anodic growth at this stage. In the second stage, the total thickness increases more slowly and the total growth rate declines abruptly.

The descending tendency of the outward growth rate is faster than of the inward growth rate. Consequently, the outward growth behaviour slows down, whereas the inward growth is kept. In the final stage, the total thickness continues increasing slightly and the total growth rate drops gradually. The outward growth rate continues decreasing gradually and the inward growth rate continuously increasing, as the downward tendency of the outward growth rate is still the fastest. In fact, in this period, the increment of outward growth thickness is lower than the increment of the inward growth thickness, indicating that the inward growth has higher contribution to the total thickness in the final stage. Interestingly, similar growth behaviour was observed for MAO treatment at a lower voltage.

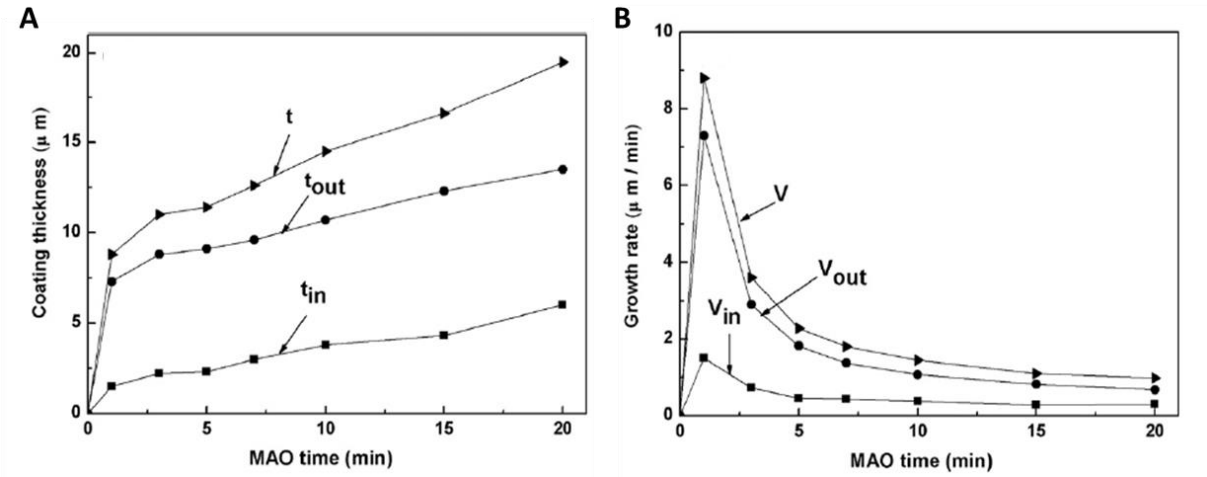

Figure IV.17. A) Total thickness t, outward growth thickness t_{out} and inward growth thickness and B) total growth rate V, outward growth rate V_{out} and inward growth rate V_{in} of the 450 V MAO-treated anodic layer with MAO time [54].

During the MAO process, sparks or plasma micro-discharges in an aqueous solution are responsible for an ionized gaseous media from the solution on the metallic surface through the plasma chemical interactions. Thus, discharge zones and heat-affected zones are generated, playing both a role as adsorption centers, supplying conditions for adsorption of the solute anions by the anodic layer. Hence, under a strong electric field, the anions diffuse from the electrolyte to the metal/oxide interface reaching the metal cations to form a ceramic layer; while the cations diffuse from the metallic surface to the oxide/electrolyte interface and react with anions to form the anodic layer. In the first stage of the MAO process, there are numerous fine sparks over the whole surface, providing a number of adsorptive zones for anions (such as O^{2-} and PO_4^{3-}) to enter the oxide layer, and plasma-chemical reactions for the cations (like Ta^{5+} and Ca^{2+}) are compounded into the layer, thus the outward growth dominates this phase. With the treatment time, the number of sparks decreases and their size increases, the diffusion and electron migration are blocked by the increasing of the anodic layer thickness. The inward migration of anions from the electrolyte to the metal/oxide interface is easier than Ta^{5+} from the metallic substrate to the oxide/electrolyte interface. Thus, the inward growth gradually plays an important role in growth behaviour at latter stages.

To better understand the ionic incorporation into the anodic layer, a study of MAO-treated Ta surface using a mixture of copper nitrate ($Cu(NO_3)_2$) and calcium nitrate ($Ca(NO_3)_2$) in H_3PO_4 was performed [55]. The morphology achieved is neither porous nor flat (Figure IV.18-A) and its top surface is mainly composed by calcium phosphates, such as $CaHPO_4$ and/ or $Ca_3(PO_4)_2$, and copper phosphates. Through the GDOES profile (Figure IV.18-B) in relation to the erosion time (not directly through the depth as it is difficult to precisely estimate it on rough and porous surfaces), the authors propose a new model of the

MAO-treated Ta surface composed by three sublayers. The top one (0-40 s) is enriched by P, copper (Cu), oxygen (O), nitrogen (N) and hydrogen (H), with a small content of Ta and Ca. The second one that corresponds to the erosion time between 40 to 80 s contains Ca, Cu and O. The third sublayer is divided into four different zones. The first, from 80 to 125 s, is enriched with Ca, Cu and O, with a depletion of Ta and H, and an increasing trend of P is recorded, while a decreasing trend of N is observed. At 125 to 150 s (second zone), the P content achieves a maximum with an increase of Ta and H, while Ca, Cu, O and N have a tendency to decrease. Then, between 150 and 270 s, a maximum signal of H is detected, while Ta continues increasing and the others decreasing. After 270 s, all signals decrease, except Ta. In sum, the Ca and Cu are distributed practically over the whole volume of the anodic layer.

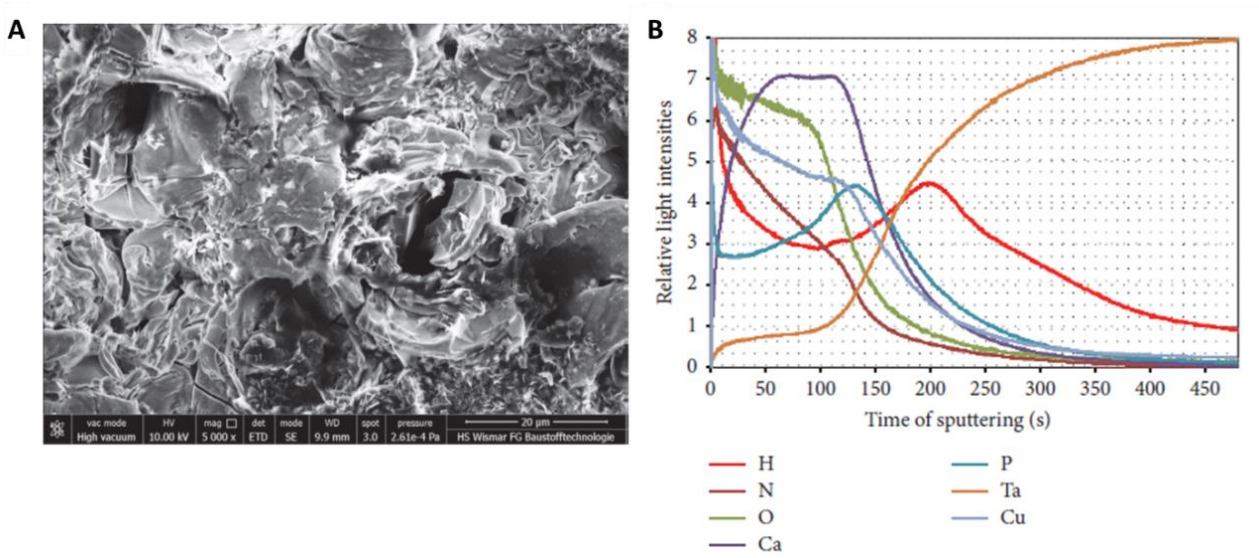

Figure IV.18. A) Surface morphology of MAO-treated Ta surface. B) Relative light intensities of tantalum, phosphorus, calcium, copper, oxygen, and nitrogen of PEO coating formed on tantalum obtained by GDOES method [55].

4.3.4 Tantalum surfaces treated by MAO for biomedical applications

MAO is a process strongly studied on Ti surfaces, however there are very few published papers on Ta surfaces. Table IV.2 displays papers on MAO-treated Ta surfaces and it is divided into the two morphologies that can be obtained: porous and non-porous structures. As mentioned before, the MAO process develops a non-uniform and non-homogenous porous structures, but it can also form non-porous surfaces, such as a compact oxide layer with some pores and/or discharge channels [56], cracks, “alveolar”, “pancakes” features.

In fact, a recent review paper about Ta modification by MAO was found. In this paper, the authors try to relate electrolyte composition and applied voltage with the morphology achieved and the possible growth mechanism [57]. However, the authors do not explore the published results.

Although the studies of Ta surfaces modified by MAO are scarce, most of them are based on the formation of porous structures which allows incorporation of Ca and P species from the electrolyte developing functional surfaces for biomedical applications (Table IV.2) [40].

Table IV.2. Review table of the different type of Ta nanostructures after MAO treatment under different conditions for biomedical applications.

Type of nanostructures	Electrolyte	Working conditions	Time (s)	Temperature (ºC)	Pre-treatment	Applications	References
Porous	0.2 M CaA + 0.02 M β-GP	AC: V_+= 350, 400, 450, 480 V, V_-=70V, 100 Hz, duty ratio of 25%	600	20	Polished with abrasive papers; ultrasonically cleaned in acetone, ethanol and DI water	Biomedical	[58]
		AC: V_+=470 V, V_-=100V, 100 Hz, duty ratio of 26%	60-1200	20	Polish with abrasive papers; ultrasonically cleaned in acetone, ethanol, DI water	Orthopedic implants	[54]
			300			Biomedical	[59]
		AC: V= 250 - 480 V, 100 Hz, duty ratio of 40%	300, 600, 900 and 1800	30	Polish with abrasive papers; ultrasonically cleaned in acetone, ethanol and DI water; dried at 60 °C	Orthopedic implants	[60]

		AC: 160 – 300 V	60-300	RT	Washed in DI water; ultrasonic clean in acetone; cleaned in ethanol and air-jet dried	Dental implants	[61]
		AC: 350, 450 and 500 V, 100Hz, duty cycle 60%	60-600s	25-60	Sonicated in acetone, isopropyl alcohol and DI water baths	Biomedical	[45]
	A: 0.35 – 0.7 M CaA B: 0.7 M CaA + 0.04-0.08 M β-GP C: 0.7 M CaA + 0.08 M β-GP + 0.01 – 0.1 M MgA	DC: 150 – 200 V	1800	RT	Ultrasonic clean in benzine and ethanol for 5 min each; rinsed in DI water and dried in air	Dental implants	[62]
	0.35 M CaA + 0.12 M β-GP	DC: 200 V	1800	RT	Ultrasonically cleaned in ethanol and DI water for 5 min each	Dental implants	[63]
	(0.5, 0.1, 1.0 M) K_2SO_3 + 5 g/dm^3 KOH	DC: 0.1 A/dm^2 up to 100, 200 or 400 V	120		Etching in 1 M HF and 4 M H_2SO_4 ; cleaned in DI water and	Orthopedic implants	[51]

					ultrasonically in propanol and DI water		
	A: 0.5 M $Ca(H_2PO_2)_2$ 0.5 M $Ca(H_2PO2)_2$ + 1.15 M $Ca(HCOO)_2$ C: 0.5 M $Ca(H_2PO_2)_2$ + 1.15 M $Mg(HCOO)_2$ D:0.5 M $Ca(H_2PO_2)_2$ + 1.5 M $Mg(HCOO)_2$	DC: 150 mA/cm^2 up to 200, 300, 400 or 500 V	300		Polished with abrasive paper; etching in 4 M H_2SO_4 and 1M HF; ultrasonically cleaned in DI water	Biomedical	[25]
	A: 0.5 M $Ca(H_2PO_2)_2$ B: 0.5 M $Ca(H_2PO_2)_2$ + 1.15 M $Ca(HCOO)_2$ C: 0.5 M $Ca(H_2PO_2)_2$ + 1.15 M $Mg(HCOO)_2$	DC: 150 mA/cm^2 up to 200, 300 or 400 V					[53]
Non-porous	A: Na_2SiO_3+ KOH B: Na_3PO_4+KOH	AC: 0.085 A/cm^2	1200	30		Biomedical	[56]
	300 g $Ca(NO_3)_2$ + 300 g $Cu(NO_3)$ in 1 L of 85% H_3PO_4	DC: 450 V	180	20	Polish with abrasive papers	Biomedical	[55]

	10 g/L $NaSiO_3.9H_2O$ + 1 g/L KOH	AC: j^+ = 0.22 A/cm^2, j^- = 0.11 A/cm^2, 100 Hz, duty cycle 20%	1500		Polish with abrasive papers; degreased in ethanol and rinsed in DI water; dried at warm air	Biomedical	[52]

4.3.4.1 Morphological and wettability characterization of MAO-treated Ta_2O_5 surface

The most reported electrolyte composition is a mixture of 0.2 M calcium acetate (CaA) and 0.02 M β - disodium glycerolphosphate (β-GP) as precursors of Ca and P, respectively (Table IV.2). The micro-porous, with diameters ranging from 1 to 5 μm, are distributed over the surface [45, 59, 60] and are related to the preferential growth and the dielectric breakdown of the oxide layer with the evolution of oxygen and aqueous vapour [54]. The amount of pores decreases while the size of the pores increases with MAO time (Figure IV.19-C) [54], as consequence of the proximity of small discharge channel connectors [60]. On the other hand, the growth of cluster structures occurs when increasing the applied voltage (450 and 500 V), and therefore covers the pores (Figure IV.20) [45]. However, at 450 and 480 V another study reports that the size of the pores increases while the number of pores decreases with the increase of the applied voltage (Figure IV.19-A) [58]. The difference in the MAO process between both studies is the duty cycle and the surface polishing as pre-treatment (Table IV.2). Recent papers [62, 63] report the Ta surface treatment by MAO using identical electrolyte composition but with higher concentration at 200 V achieving a porous morphology similar to the previously discussed. Although not as significant as that induced by increasing CaA concentration, when β-GP is added to the electrolyte, increasing its concentration the porosity is enhanced, while the roughness and wettability significantly increase. Adding MgA in the electrolyte, any amendment of surface morphology and roughness are noticed, but the water contact angle raises [62].

In agreement with the morphological results of MAO-treated surfaces, which uses an electrolyte mixture of CaA and β-GP, when the electrolyte used is composed of $Ca(H_2PO_2)_2$ and $Ca(HCOO)_2$ or $Mg(CH_3COO)_2$, the diameter of the pores and surface roughness increase with increasing the applied voltage [25]. For more conductive electrolytes, a rougher pore size is created and up to 500 V dendritic structures are formed, which are correlated to the more energetic sparks that generate these morphologies due to partial evaporation of the electrolyte combined with thermal and plasma effects. In this study, the surface wettability does not show a linear tendency. The authors explain this behaviour by assuming that some surface features can be ascribed by the Cassie-Baxter state. In these cases, the pores are so small that they do not allow the water droplet to easily penetrate them, forming air pockets. The surface, therefore, presents a hydrophobic behaviour. For higher applied voltages, the pores are large enough for an easier water penetration, and a Wenzel surface state can be achieved. Also, the authors attribute the hydrophobicity increase to morphological changes on the surfaces and not to chemical modifications. The anodic layer has pores in its internal layer and the thickness revealed to be potential and electrolyte-

dependent, since the Mg-enriched electrolyte is responsible for the thickness's decrease which increases with the electrolyte concentration [25]. This may be related to the lower standard potential of Ca with respect to Mg or due to counter ions used in their respective salts [53].

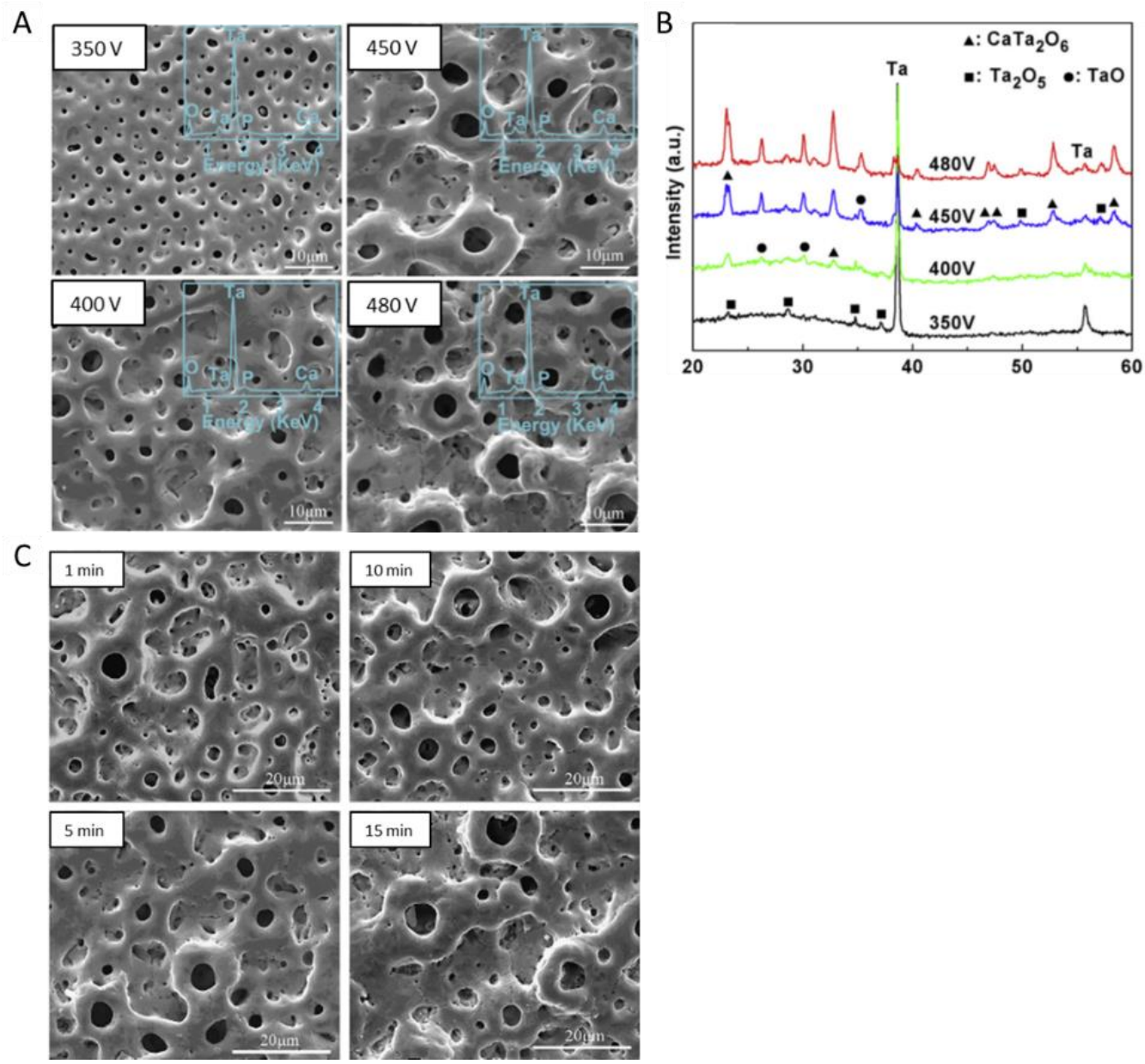

Figure IV.19. Surface morphologies of Ta2O5 treated by MAO A) at different applied potentials with EDS spectra inset, scale bar 10 μm, B) the respective XRD patterns [58] and C) MAO process at 450 V for different process durations [54], scale bar 20 μm.

The anodic layer shows a uniform thickness and with no discontinuity at the oxide layer/substrate interface [54, 59], with a compact inner region and a porous outer region [45]. However, for an electrolyte mixture of $Ca(H_2PO_2)_2$ and $Ca(HCOO)_2$ or $Mg(CH_3COO)_2$, the anodic layer structure reveals to be dependent on the applied voltage [53]. In this case, the structure can be divided into two or three sublayers: the outer porous layer; the inner barrier layer at the substrate/oxide interface; and, at 400 V, a third

intermediate sublayer is observed when the outer layer is denser than this highly porous intermediate layer (Figure IV.21). This structure can be formed due to solidification and oxidation of the molten substrate during MAO process.

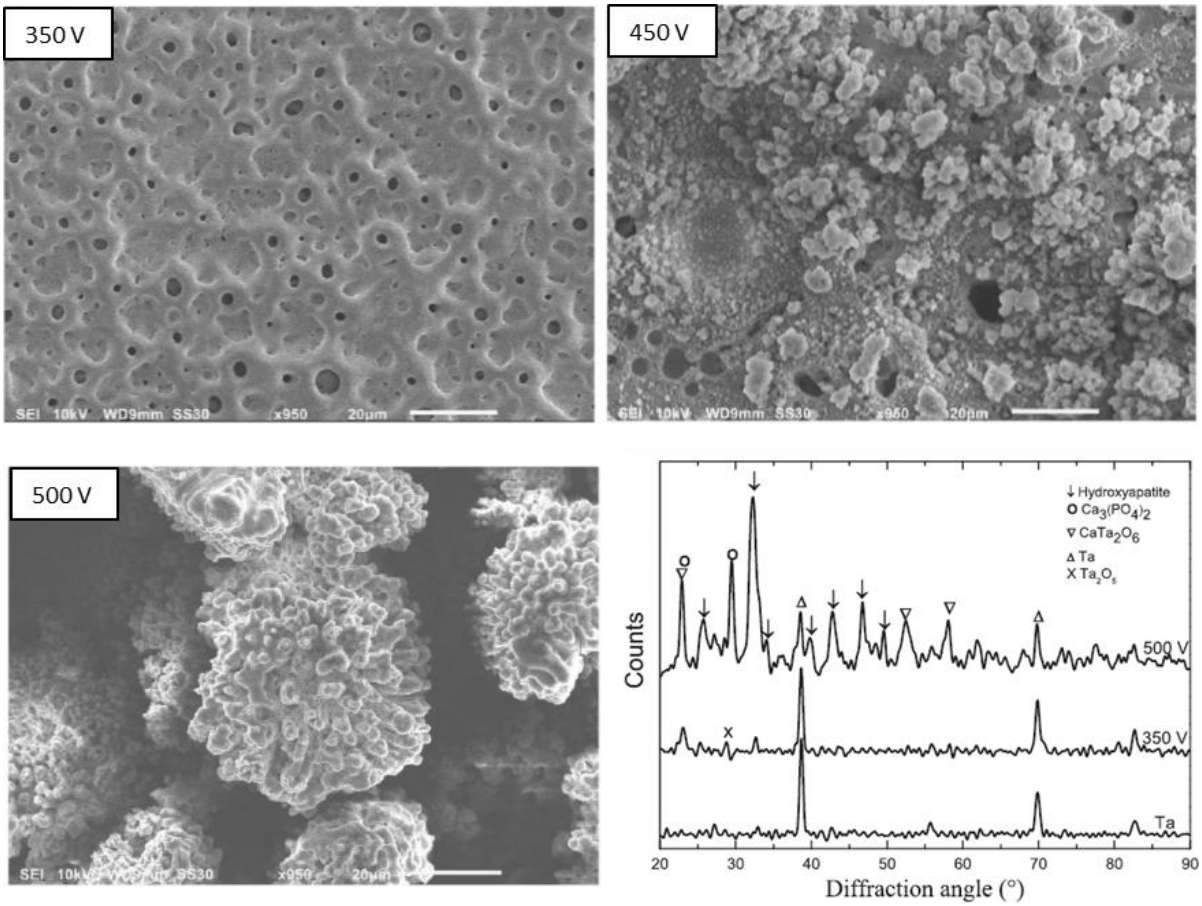

Figure IV.20. Surface morphologies of Ta_2O_5 treated by MAO at different applied potentials [45], scale bar 20 μm, and XRD patterns for untreated Ta and MAO-treated Ta at 350 and 500 V.

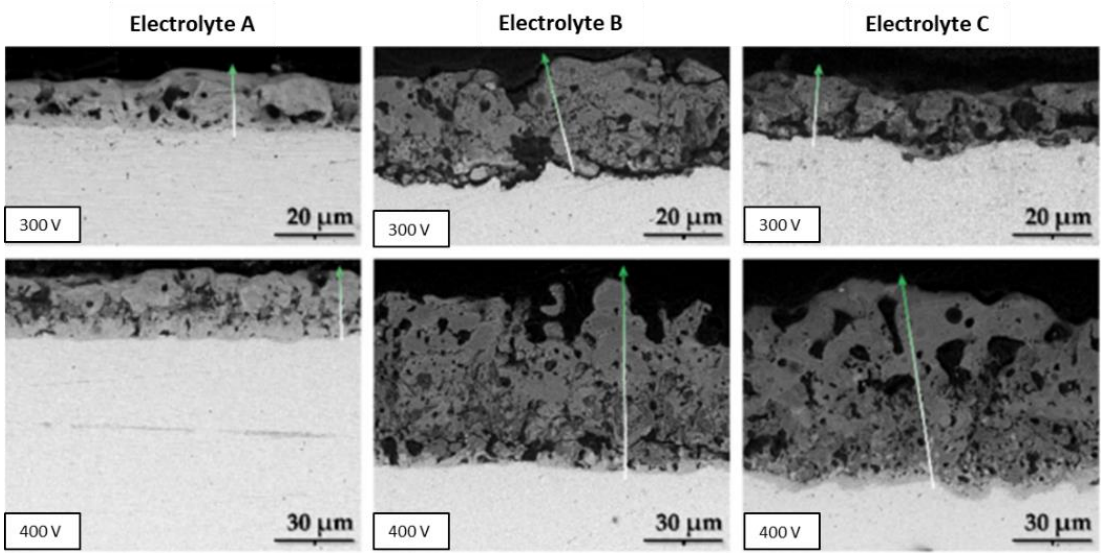

Figure IV.21. SEM cross-sectional images of the MAO-treated Ta surfaces obtained from different electrolyte composition and at different limiting voltages [53].

The layer thickness increases with the applied voltage and with the electrolyte concentration (that is responsible for exerting less resistance to the current flow, intensifying the process [53]), as described in the MAO-treated Ta surfaces under different conditions [25, 45, 51, 58], as well as increasing with the MAO duration [45, 54]. Furthermore, surface roughness increases with MAO treatment mainly for higher applied voltages [25, 45, 61]. The presence of minor cracks on the surface is reported by Zhao *et al.* [60]. This is related to the thermal stress caused by the high temperature generated by the discharges during the MAO process.

Other than the Ca-enriched electrolytes, silicate and phosphate solutions are also commonly used in MAO treatments (Table IV.2). MAO-treated Ta surfaces, using an electrolyte mixture of different concentrations of potassium silicate (K_2SiO_3) and potassium hydroxide (KOH), show a porous structure when the applied voltage was above the dielectric potential [51]. The surface roughness, the thickness of the oxide layer and the diameter of the pores, are dependent on the concentration of the electrolyte and the applied voltage. In fact, the increase in K_2SiO_3 concentration or the applied voltage, will produce thicker and rougher surfaces with larger pores (Figure IV.22). Furthermore, the surface wettability displays to be dependent on the applied voltage since with increasing the voltage the contact angle strongly decreases and the surface becomes hydrophilic.

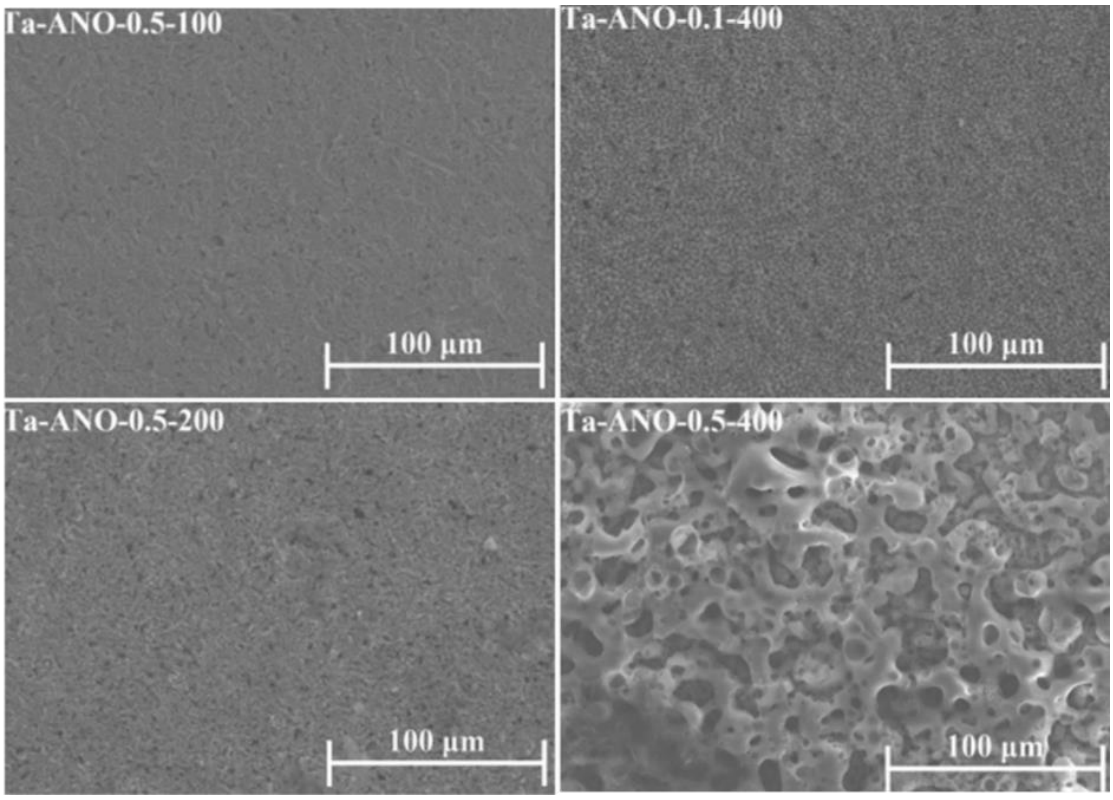

Figure IV.22. Surface morphologies of Ta_2O_5 prepared by MAO under different conditions: 0.5 M K_2SiO_3 at a range of 100 to 400 V, and 0.1 M K_2SiO_3 at 400 V [51].

MAO-treated Ta surfaces (on a polyurethane foam), using an electrolyte mixture of sodium metasilicate (Na_2SiO_3) or trisodium phosphate (Na_3PO_4) and KOH were submitted to an alkaline treatment to evaluate the effect on the surface bioactivity [56]. The authors report that the surface shows more pores after the MAO treatment (Figure IV.23-B and E), which are completely different from those previously reported. However, the pores (or holes) are already observed on the untreated surface (Figure IV.23-A and B), wherefore, this achieved Ta surface is here considered as non-porous surface. Additionally, many cracks in the boundary grains are observed before and after the MAO treatment. With the alkaline (NaOH) treatment, where the samples were soaked in NaOH at 60 °C for 24 h, more holes are observed (Figure IV.23-C and F) when compared with both untreated Ta and MAO-treated Ta surfaces and cracks are still detected.

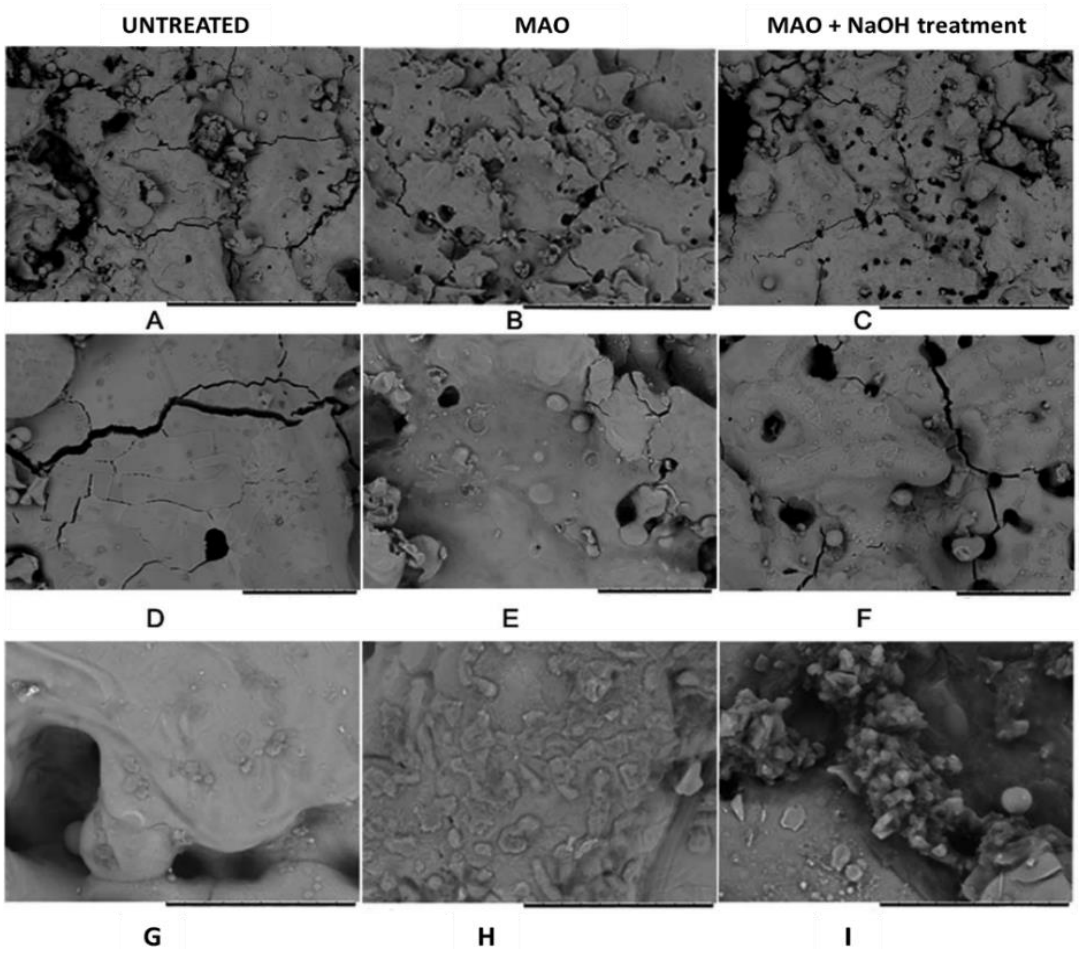

Figure IV.23. Surface morphologies of (A and D) untreated Ta surface, (B and E) Ta_2O_5 prepared by MAO using the phosphate solution and (C and F) with NaOH treatment.; (G-I) after SBF soaking. Scale bars (A-C) 200 μm and (D-F) 30 μm (G-I) 20 μm [56].

The Ta surface modified by MAO under bipolar constant pulsed current density using a silicate electrolyte shows transitional morphologies depending on the treatment time [52]. An initial nodular morphology is observed (Figure IV.24-A and E) and then smooth pancakes are formed around the nodules (Figure IV.24-B and F), which become dominants (Figure IV.24-C). These morphological features are identical to those

previously reported in the MAO treatment using H_3PO_4 electrolyte [50]. Increasing the MAO time, several coral reef features (with a dendritic morphology and nodular branches) arise, and the pancakes are still evident between the coral reef which are non-uniformly distributed (Figure IV.24-D and G) [52]. The presence of the coral-reef increases the thickness of the anodic layer.

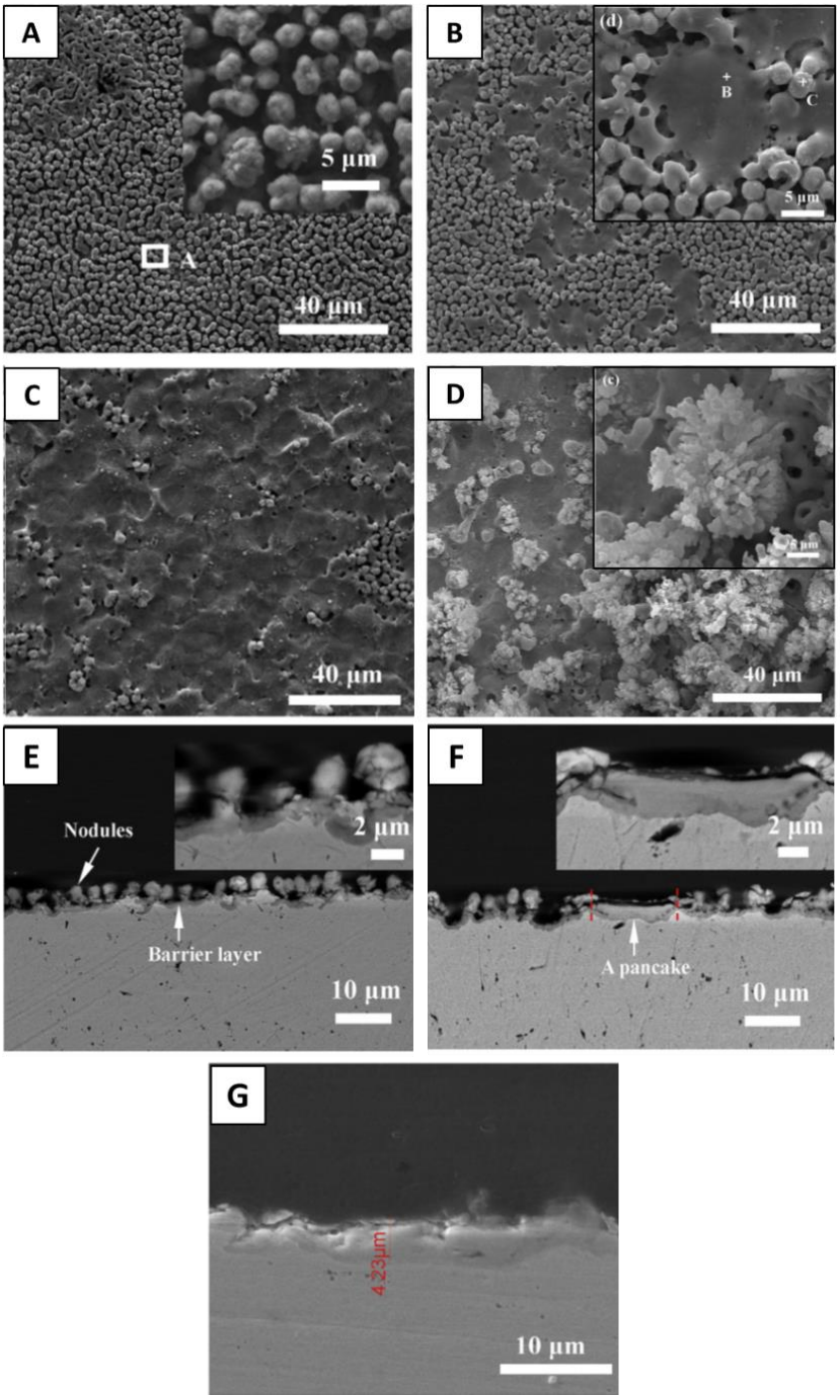

Figure IV.24. Surface morphologies of MAO-treated Ta surface using a silicate electrolyte in a bipolar pulsed current for A) 120 s, B) 140 s, C) 180 s and D) 600 s. SEM cross-sectional images after E) 120 s, F) 157 s and G) 600s [52].

These morphological transitions are coincident with the transient in cell-potential. Before the escalation of the negative potential (Figure IV.25 – left), the surface is characterized by a nodules features and fine

sparks and hydrogen evolution over the whole surface (Figure IV.24-A and E, Figure IV.16-b). Then, the first transition occurs (Figure IV.25 – right), leading to an escalation in the overpotential for hydrogen evolution and an increase of sparking intensity (change of spark colour and gas generation), which originates the pancakes due to material solidification from the quenching discharges, such as nodular material (Figure IV.24-B, C and F, Figure IV.16-c-h). The sparking intensification results from a gradual thickening of the pancake covering the surface defects, resulting in a current concentrating in fewer favored regions for dielectric breakdown. The second transition, and a further increase of the overpotential, arises more slowly and coincides with the formation of coral-reef features accompanied by an increase of the anodic potential associated to the growth of the barrier layer, involving anodic and thermal oxidation of the Ta substrate (and molten ejection of Ta_2O_5) caused by the stronger discharges and high temperature.

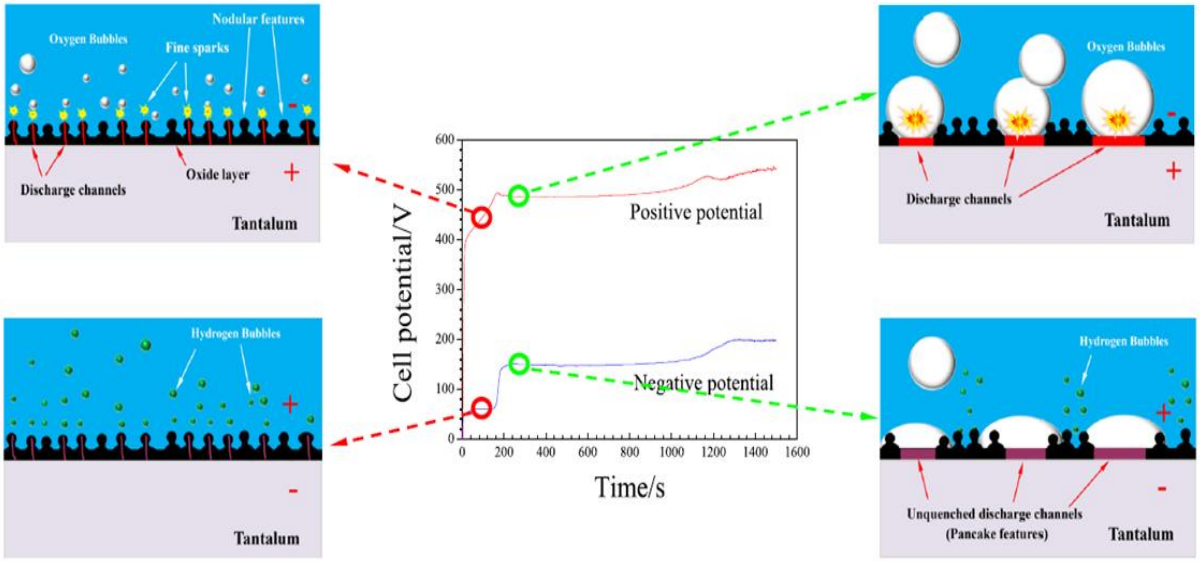

Figure IV.25. Schematic illustration of the anodic layer morphology, discharge behaviour and gas emission on Ta before and after the first escalation of the negative potential [52].

4.3.4.2 MAO-treated Ta_2O_5 surface chemical composition

For certain applications it is desired to dope the anodic layer with specific elements in order to tailor specific properties. In this regard, incorporation of Ca and P elements onto the oxide layer have been demonstrated, which increases with the increase of the MAO time and the applied potential (Figure IV.19-A in insets) [45, 54, 58, 60-62] , as well as increasing the electrolyte concentration [62, 63]. Increasing β-GP concentration in the electrolyte, a boost of Ca incorporation is noted, besides the P incorporation is increased. This anodic layer doping is related to the phenomena of sparks generation and the local increase of temperature, which directly depends on the electrolyte composition/concentration. Moreover, Ca and P concentrations are larger on the surface [62]. In addition, P is only observed in the bulk when

the MAO treatment voltage is higher than 450 V as well as for times higher than 180 s. When the applied potential is increased, electrophoresis is more important and contributes to the increase of the P containing the species' density near the substrate which, combined with the large available energy provided by the microarcs, increases the rate of complex reactions, leading to the formation of calcium phosphates and hydroxyapatite (HAp) [45]. Indeed, the electrolyte ions enter into the anodic layer via diffusion and electrophoresis, to the extent that Ca^{2+} mainly arrives through diffusion, while P (in form of PO_4^{3-}) moves by electrophoresis along the discharge channels [60]. Additionally, the presence of sodium (Na) and magnesium (Mg) is reported by Goulart *et al.* [61]. The authors relate this fact to the salt deposition during the MAO treatment. Although not explained by the authors, these contaminations can be justified by the chemical composition of β-GP as a precursor of Na, but Mg contamination does not have any evident source. Also, the authors only report the presence of P on the surface modified at a higher voltage because they do not take into consideration that both Ta M and P Kα peaks are overlapped (which can be qualitatively compared to the untreated Ta surface).

Additionally, for all solution mixtures of $Ca(H_2PO_2)_2$ and $Ca(HCOO)_2$ or $Mg(CH_3COO)_2$, the relative amount of elemental species increases with a decrease of Ta content. In fact, P content remains practically static while the Ca and Mg contents increase with the applied potential. Also, the addition of Mg decreases the incorporation content of Ca [25]. Additionally, the results show that the concentration of the electrolyte species is higher in the outer region of the anodic layer [53].

For the MAO process using a free Ca and P electrolyte the amount of Si incorporated into the anodic layer, which increases with the K_2SiO_3 concentration, was observed [51]. Also, potassium concentration increases towards the surface oxide. The XRD patterns are associated to the metallic Ta and Ta_2O_5, and by XPS the presence of silica/silicate deposits are confirmed, and the silica is the dominant component. Using another silicate electrolyte (Na_2SiO_3) in bipolar pulsed current, the different morphologies achieved along the MAO process show different chemical compositions [52]. The nodules are constituted by Ta, O and Si, while the pancakes are only Ta and O, and the coral-reefs are silicon-rich.

4.3.4.3 Structural analysis of MAO-treated Ta_2O_5 surface

The phase composition is another key material property that is influenced by MAO process.

On the diffractograms of Ta surfaces treated with CaA and β-GP, crystalline phases of orthorhombic Ta_2O_5 and both bcc and tetragonal-Ta (from the substrate) are visible[62, 63] . When the applied voltage is higher than 350 V, crystalline Ta_2O_5 and TaO phases are detected as well as the predominant related to

the crystalline calcium tantalate ($CaTa_2O_6$) [54, 58-60] (Figure IV.19-B, Figure IV.27-g(i)). No other crystalline phase is generated increasing the MAO time [54]. On the other hand, for higher applied potential (500 V), new peaks associated to cubic $CaTa_2O_6$, $Ca_3(PO_4)_2$ and hexagonal HAp (the predominant phase) are observed (Figure IV.20) [25, 45]. These results reveal that MAO process can successfully produce a crystalline HAp layer on Ta without any pre- and post-treatment [45]. Also, the presence of diffraction lines related to HAp appears after heat treatment [59]. These results are corroborated by XPS analysis, attributing the Ca 2p peaks at 347.1 eV to $CaTa_2O_6$ and 350.7 eV to $Ca_3(PO_4)_2$. The P 2p peak at 133.3 eV confirms the $Ca_3(PO_4)_2$ [54, 58, 59, 62]. Wang *et al.* [54, 58, 59] reveal that Ca is mostly compounded into $CaTa_2O_6$ and a residual Ca compound with P to form a small amount of $Ca_3(PO_4)_2$. In contrast, using an electrolyte only composed by CaA, orthorhombic $CaTa_2O_6$ phase is noticed but it is no further detected when β-GP and MgA are added, meaning that, probably Ca bound to them [62]. On the other hand, after the surface annealing at 800 °C, the amorphous phase disappears and a newly formed crystal phase $CaTa_4O_{11}$ arises [58].

The formation of calcium tantalate can be described by the reactions of Ca^{2+} ions with the Ta_2O_5 previously developed by the substrate oxidation, under high temperature generated by the microarcs [45], Eq. IV.6.

$$\boldsymbol{Ta_2O_5 + Ca^{2+} + \ +O^{2-} \rightarrow CaTa_2O_6} \qquad \text{Eq.IV.6}$$

However, when a great amount of Ta_2O_5 is crystallized and then reacts with Ca^{2+} and O^{2-} in the anodic layer $CaTa_4O_{11}$ is formed, Eq. 7 [58].

$$\boldsymbol{2Ta_2O_5 + Ca^{2+} + \ +O^{2-} \rightarrow CaTa_4O_{11}} \qquad \text{Eq.IV.7}$$

When higher voltages are applied, the amorphous phase converts to crystalline Ta_2O_5 and reacts directly with $CaTa_2O_6$, Eq. IV.8 [58].

$$\boldsymbol{Ta_2O_5 + CaTa_2O_6 \rightarrow CaTa_4O_{11}} \qquad \text{Eq.IV.8}$$

Heat treatment (HT) of MAO-modified Ta surfaces induces the formation of HAp. After 0.5 h of heat treatment short nanorods, containing Ca and P, are nucleated into the porous layer (Figure IV.26-a1 and a2). Increasing the HT duration, the nanorods became larger and more evident, covering the micro-porous surface (Figure IV.26-b1 and b2) and, after 24 h, the nanorods turns to parallel HAp nanofibers (Figure IV.26-d1 and d2). Thus, these results might be explained by the tendency to migrate out of the Ca^{2+} and PO_4^{3-} ions incorporated onto the oxide layer during the heat treatment, since the intensity of the $CaTa_2O_6$ diffraction peaks decreases, whereas the Ta_2O_5 increases. This shows the possible conversion of partial

$CaTa_2O_6$ to Ta_2O_5, due to the loss of Ca^{2+}, which will react with the PO_4^{3-} ions present on the surface, forming calcium phosphates. Consequently, the HAp diffraction peaks start appearing. As well as this, it was possible to observe that the MAO-treated surface has the highest ions concentration release, which decreases with HT time as more HAp is formed (that has low solubility) and less ions are in the oxide layer [59].

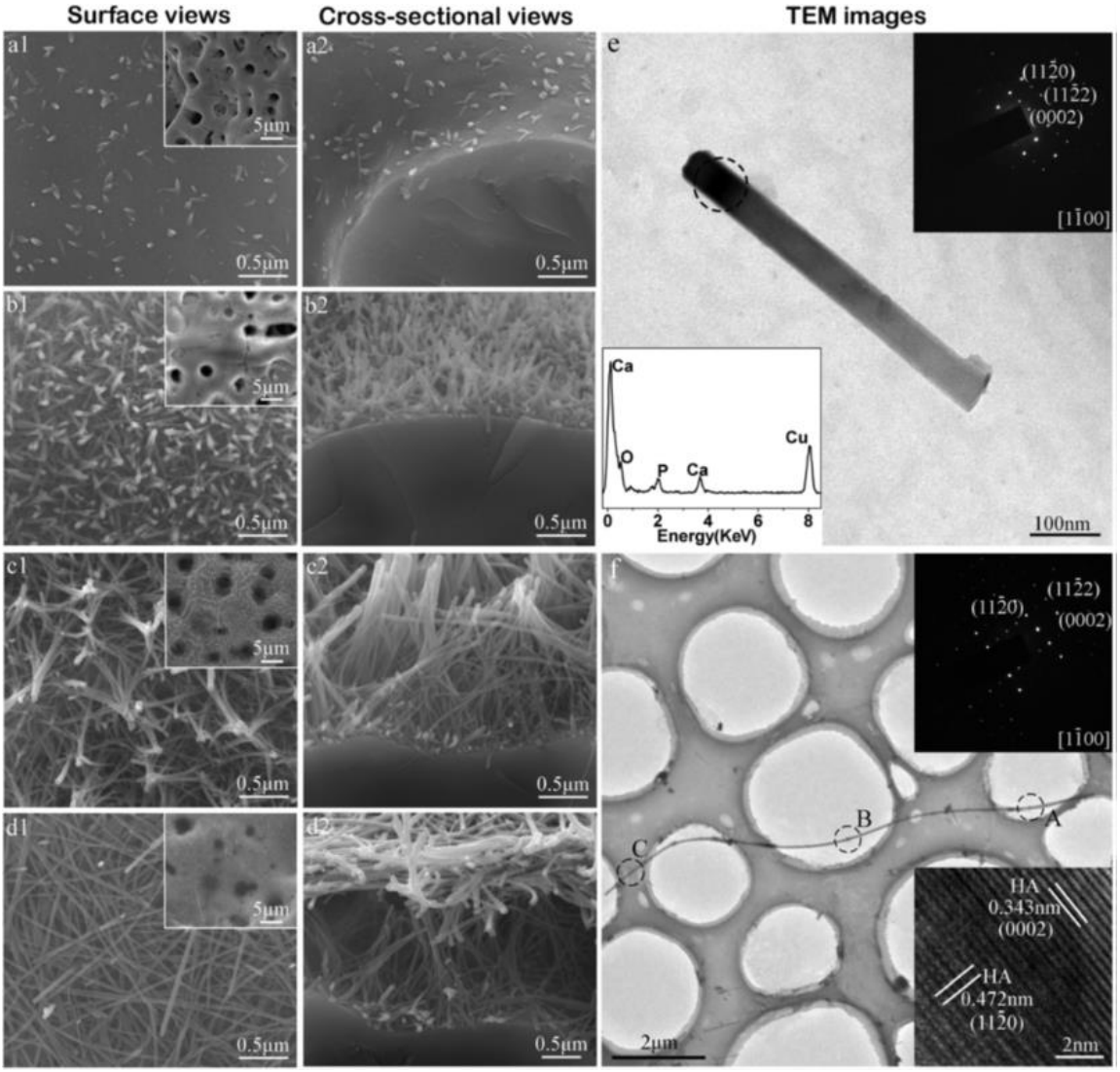

Figure IV.26. (a1–d1) Surface and (a2–d2) cross-sectional SEM images of the outermost parts of the internal walls of macropore, taken from the centrally fractured MAO-treated Ta_2O_5 surface after HT for (a1, a2) 0.5, (b1, b2) 3, (c1, c2) 6 and (d1, d2) 24 h, respectively. (e) TEM image of the nanorod scratched from the surface heated for 3 h, the top inset showing the SAED pattern, and the bottom inset showing the EDS spectrum taken from the dotted-circle marked area on the nanorod. (f) TEM image of the nanofiber scratched from the surface heated for 24 h, the top inset showing the SAED pattern, and the bottom inset showing the HRTEM image taken from area B [59].

It is interesting to note that MAO process using an electrolyte of $Ca(H_2PO_2)_2$ at 500 V leads to a formation of an amorphous oxide layer, but when the calcium formate is added to the electrolyte, several new peaks arise that are ascribed to $Ca_3(PO_4)_2$, $Ca_5(PO_4)_3(OH)$ and $CaTa_2O_6$. On the other hand, when magnesium acetate is introduced, the peaks are assigned to $Ca(PO_3)_2.2H_2O$, $Ca_2P_2O_7$, $Ca_4Mg_5(PO_4)_6$ and $MgCO_3$, and

thus the surface crystallinity is totally modified [25]. The presence of phosphates and carbonates is corroborated by the XPS results, although the authors do not justify the presence of nitrogen (N) and silica (Si) on the survey.

4.3.4.4 MAO-treated Ta_2O_5 surface bioactivity and biological responses

MAO-treated Ta surfaces have been widely developed to be used in biomedical devices, tailoring its surface to manipulate both bioactivity and biological responses. In this concern, MAO-treated CaP-enriched Ta surfaces at 350 and 450 V were characterized regarding their apatite-inducing ability by the bioactivity assay, which consists in the sample's immersion in simulated body fluid (SBF) for different time-points. New spherical-like particles are indeed detected after 42 days of immersion on Ta surface MAO-treated at 350 V. After 48 days these particles cover the whole surface. In subsequence to annealing, only after a period of 24 days are the first particles detected and after 30 days, they cover the complete surface. When treated at 450 V the deposited particles are detected at 32 days and cover the surface at 40 days (Figure IV.27-a-c). The FTIR spectra of this surface before and after SBF immersion confirm the presence of phosphates on the oxide layer but also demonstrate that this apatite is carbonated after immersion in SBF (Figure IV.27-h). The XRD patterns show new diffraction peaks ascribed to apatite after immersion in SBF, revealing that the spherical-like particles are assembles of tiny apatite crystals (Figure IV.27-g). After annealing, an immersion of 9 days is enough for the apatite formation (Figure IV.27-d-f) [58]. In MAO treatment at 470 V, the spherical particles are observed after 22 days of immersion in SBF, and after 28 days the surface is completely covered. Once more, the HT accelerates the apatite formation [59].

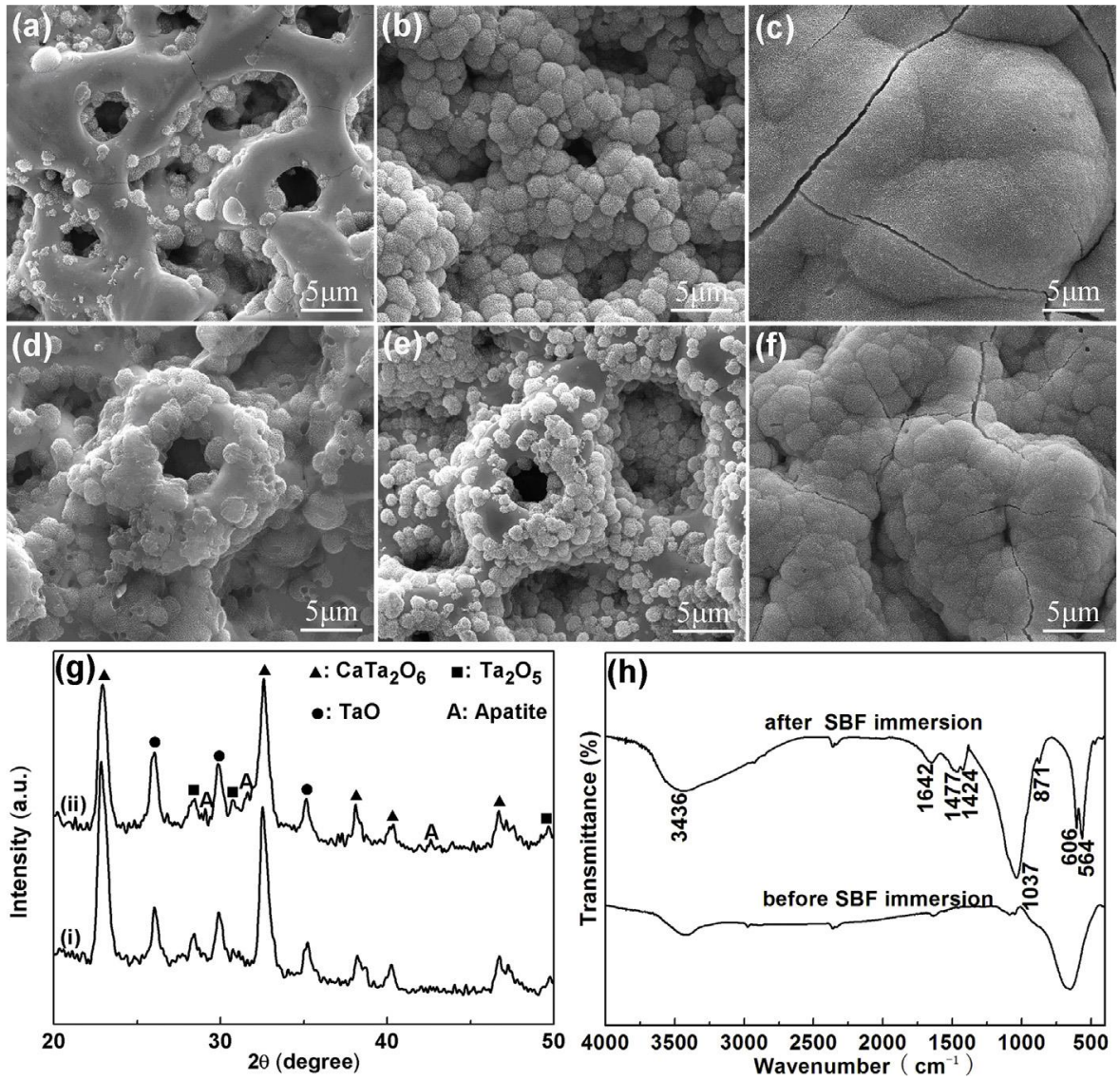

Figure IV.27. Surface morphologies of Ta_2O_5 modified by MAO at 450 V after immersion in SBF for (a) 32, (b) 36 and (c) 40 days; surface morphologies of the Ta_2O_5 modified by MAO annealed at 800◦C formed at 450 V after immersion in SBF for (d) 9, (e) 12 and (f) 18 days; (g) XRD patterns of the MAO-treated surface formed at 450 V before (i) and after (ii)immersion in SBF for 40 days; (h) FTIR spectra of the MAO-treated surface formed at 450 V before and after immersion in SBF for 40 days[58].

In sum, the apatite-inducing ability can be greatly improved increasing the applied voltage, heat treatments (annealing) and by the presence of a $CaTa_2O_6$-based layer with well-crystallized HAp nanorods/nanofibers as well as the presence of crystalline $CaTa_4O_{11}$ [58, 59]. However, the authors [58] describe the atomic arrangement of $CaTa_4O_{11}$ as a crystal structure suitable for the epitaxial nucleation of apatite crystals, whereas the structure of $CaTa_2O_6$ (200) hardly match to the apatite structure (0004) (Figure IV.28). Moreover, a better apatite-inducing ability is attributed to more enriched Ta_2O_5 layers with Ca and P and also to a more crystalline phase and less amorphous phase formed [58].

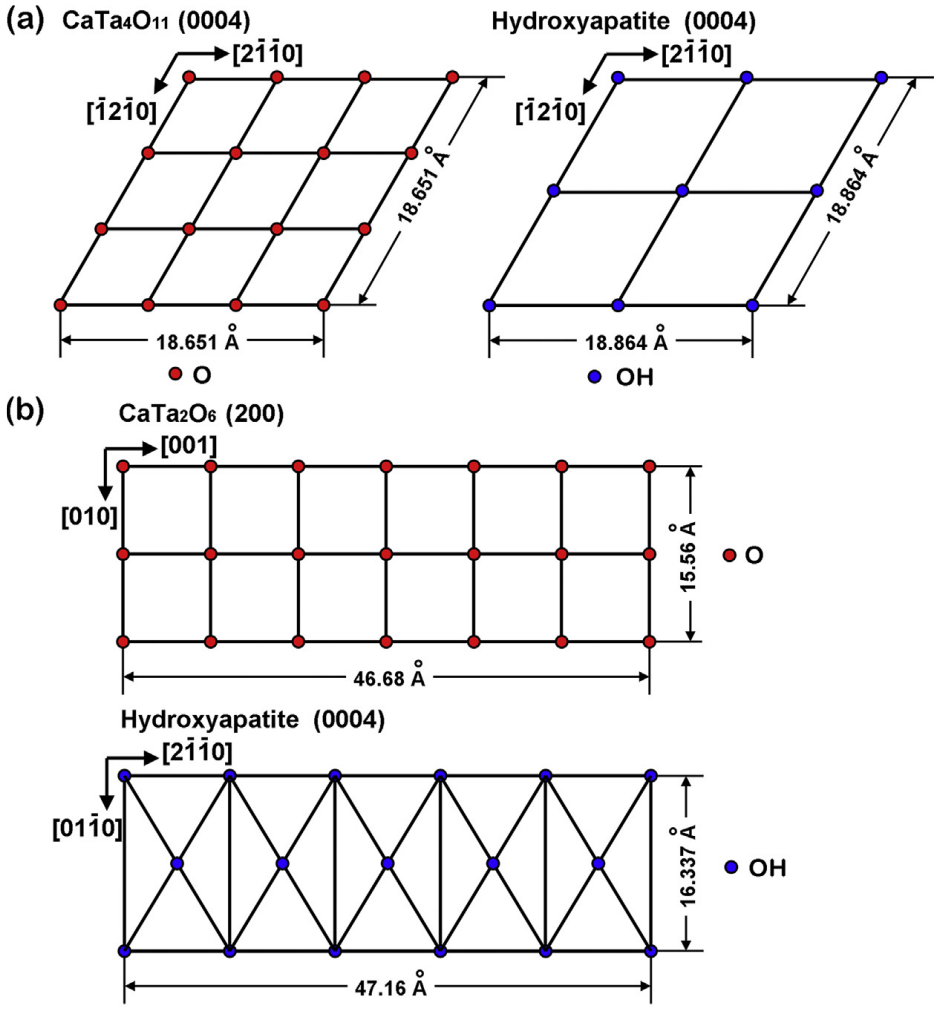

Figure IV.28. (a) Schematic diagram of the arrangement of oxygen atoms on the $CaTa_4O_{11}$(0004) crystal plane and the arrangement of OH group on the apatite (0004) crystal plane. (b) Schematic diagram of the arrangement of oxygen atoms on the $CaTa_2O_6$(200) crystal plane and the arrangement of OH group on the apatite (0004) crystal plane. It shows the micro-matching structure between $CaTa_2O_6$(200) and apatite (0004) [58].

A porous Ta_2O_5 surface enriched with Ca and P is not toxic for osteoblastic cells, supporting the cells' adhesion and proliferation [45, 62, 63], as well as enhancing the ALP levels, in comparison to both positive control and an untreated-Ta surface. This confirms the surface ability in maintaining the cells' phenotype (inducing the conversion of osteoblasts to bone) [45]. Both protein adsorption and cell adhesion are enhanced by MAO modification [59, 62] and further HAp nanorods/nanofibers. However, HAp nanofibers resulting from longer times of HT show a reduced number of the focal adhesion and collage secretion, inducing cell apoptosis responses [59], although the authors do not present a possible explanation for this cell behaviour. In a recent study [62], the authors state that surface properties have a great impact on cell responses, mainly surface chemical composition and wettability, since cell adhesion and gene expressions results are significantly better in the rougher surface with hydrophilic behaviour, with amorphous calcium phosphates, with higher Ca content on the surface and a Ca/P ratio near the hydroxyapatite value.

Furthermore, after soaked in SBF for one week, MAO-treated Ta surfaces (using an electrolyte mixture of Na_2SiO_3 or Na_3PO_4 and KOH and submitted to an alkaline treatment) displayed more spherical-particles precipitation (Figure IV.23-H) than on the untreated Ta surface (Figure IV.23-G), which are significantly more on the surface submitted to both MAO and NaOH treatments (Figure IV.23-I) [56]. In agreement, the samples treated by MAO and/or NaOH treatment reveal diffraction peaks ascribed to apatite, with the exception of the Ta untreated surface, maybe due to the small size and concentration of particles, and an increase peak height in Ca 2p and P 2p in XPS spectra. Besides the strong diffraction lines of Ta, the authors describe the presence of diffraction peaks of Ta_2O_5 and sodium tantalates that are neither represented nor observed in the XRD patterns. In biological characterization, the MTT assay display a reduction of viable cells for the MAO-treated surfaces, from 24 h to 72 h of cell culture, revealing some cytotoxic effect whereas the surface treated by both MAO and NaOH soaking shows biocompatibility. According to the authors, this cytotoxicity can be related with the free ions dissolved from the substrate, or with complex toxic organic species from the foam or with reactive oxygen species (ROS) and reactive nitrogen species involved in cell death. After 24 h of culture, cells show adherent protrusions, which are much larger after 72 h and spread over the whole surface, where some calcium crystals are observed. However, it is not clear which surface is used as cell culture substrate. Moreover, neovascularization and new bone ingrowth occurs after 4 and 12 weeks, respectively, confirming the modified Ta surface as suitable option for biomedical applications.

4.3.4.5 Mechanical and corrosion resistance of MAO-treated Ta_2O_5 surface

In another area of knowledge, MAO-treated Ta surfaces exhibit interesting properties for mechanical and corrosion applications, which are highly dependent on the layer porosity.

In what these concerns, the porous Ta_2O_5 anodic layer adheres firmly to Ta substrate with cohesive strength [54] and a long-term adhesive strength stability that decreases with the increase of applied voltage [58] and HT (which is attributed to the migration of Ca^{2+} and PO_4^{3-} ions out) [58, 59], concluded by scratch tests. Contrarily, Sowa *et al.* [25], that use a DC regime in the MAO process, report that the adhesion strength is improved with the increasing voltage.

The OCP and potentiodynamic polarization measurements demonstrate that the corrosion properties are improved with the MAO treatment [51]. However, increasing the applied potential does not further improve the Ta corrosion resistance, as the sample is treated at 200 V with the best corrosion performance, for an electrolyte composed by K_2SiO_3 [51]. A more recent paper carries out a deeply

corrosion resistance investigation of the modified Ta surfaces using different electrolytes mixtures of $Ca(H_2PO_2)_2$ and $Ca(HCOO)_2$ or $Mg(CH_3COO)_2$ with an applied potential range from 200 to 400 V (Table IV.2) [53]. By electrochemical impedance spectroscopy, the total resistance of the biomaterial/electrolyte interface in corrosion environment is determined. The results demonstrate that the untreated Ta surface is characterized by a single time constant that can be ascribed with a parallel RC connection (Figure IV.29-a), instead of the MAO-treated Ta surfaces have at least two-time constants. The RC circuit is based on a resistance of the electrolyte between the reference electrode capillary tip and the sample (RS) and the parallel resistance (Rb) and capacitance (Qb) of the passive barrier layer on the flooded Ta surface. Ta surfaces treated by MAO at 200 and 300 V show two well-separated time constants (Figure IV.29-b), where the extra time constant is translated by the RO (electrolyte resistance in the pores of the outer oxide layer) and QC (total capacitance of the anodic layer) pair. For MAO treatments at 400 V, the impedance data are dependent on the electrolyte composition. The electrolytes composed by calcium hypophosphite (electrolyte A) and with calcium formate (electrolyte B) have a more complicated spectrum with an almost linear region in the low frequencies, that can suggest that diffusion can play a crucial part in limiting the corrosion rate of treated Ta surfaces. Thus, the correspondent circuits have an additional Warburg impedance (W) (Figure IV.29-c) to improve the fitting of the low-frequency part. The authors conclude that the main factor that determines the overall corrosion resistance of MAO-treated Ta surfaces is the resistance of the barrier sublayer (Rb), since the best corrosion resistance occurs at low voltages. When the voltage is low enough, the intense sparking is absent, resulting in the development of a thin and porous anodic layer. Independently of the voltage of MAO process, no evidence of pitting corrosion or oxide breakdown is observed in potentiodynamic polarization measurements. In fact, the higher polarization resistance is observed for the more resistive layers, even in more porous layers.

The electrochemical measurements of Ta MAO-treated under bipolar AC constant current density in absence of anodic sparks indicate that the overpotential for hydrogen evolution has an ohmic dependence of the current density due to the resistance of the anodic layer and electrolyte. The overpotential is enhanced by anodic discharges, which is proposed to be due to the oxygen gas generated during anodic discharges that impede ionic migration during subsequent cathodic polarization [52].

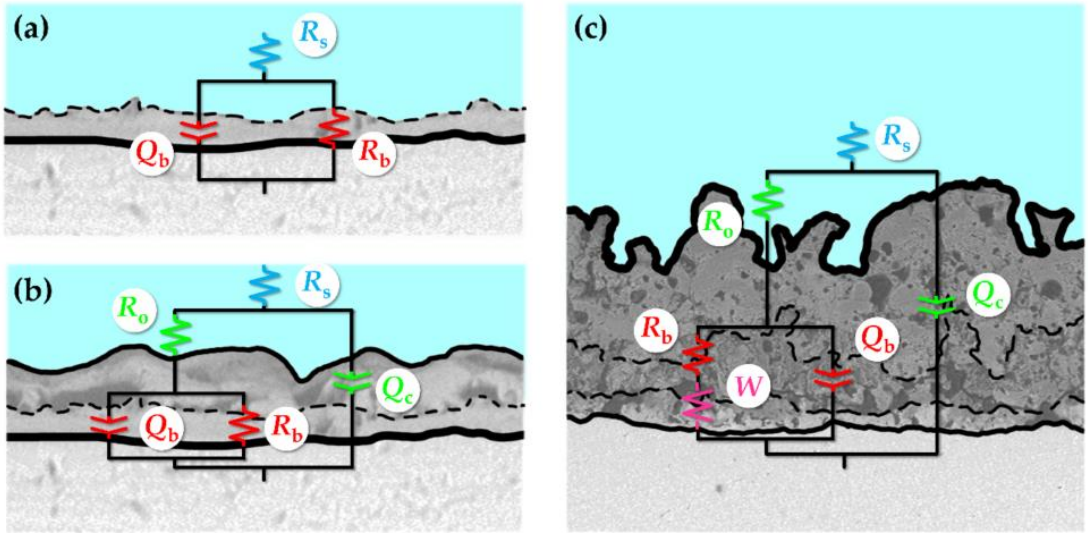

Figure IV.29. Equivalent electrical circuits used for fitting of the impedance spectra of (a) the untreated Ta surface; (b) the MAO samples that showed 2-time constants, and (c) those that exhibited 2-time constants with a linear constant-phase region [53].

4.4 Conclusion

After anodization using a HF-containing electrolyte, nanoporous/nanotubular Ta_2O_5 layers significantly improve the anticorrosion, hydrophilicity, surface energy of pure Ta, promoting the protein adsorption and biological responses (adhesion, proliferation and differentiation), suggesting that Ta_2O_5 enhance the Ta surface biocompatibility and osteoinductivity of Ta, particularly in Ta_2O_5 nanostructures with small pore/tube diameters.

MAO is effectively a more complicated process that embraces different reactions at the same time and different stages characterized by specific sparks, gas bubbles and consequent surface morphology, during time process. Ta surfaces modified by MAO are reported in a few numbers of papers, but globally all of them agree on the surface properties achieved according to the anodizing parameters. Most of the papers report biomedical applications as their main goal, and for that a Ca and P-enriched electrolyte is mostly used to embed these species on the outer porous layer, and if the applied voltage is high enough or if a heat treatment is used as post-treatment, crystals of calcium phosphates are detected which, combined with the presence of calcium tantalate, significantly enhance the surface bioactivity and consequently the biological responses. Moreover, the Ta_2O_5 layer shows a great adhesion as well as good corrosion properties. Thus, Ta_2O_5 nanostructures developed by both electrochemical anodization assisted by electric field and MAO have a very good perspective of biological applications.

4.5 References

[1] S. Minagar, C. C. Berndt, and C. Wen, "Fabrication and characterization of nanoporous niobia, and nanotubular tantala, titania and zirconia via anodization," Journal of Functional Biomaterials, vol. 6, pp. 153-170, 2015.

[2] H. A. El-Sayed and V. I. Birss, "Controlled interconversion of nanoarray of Ta dimples and high aspect ratio Ta oxide nanotubes," Nano Letters, vol. 9, pp. 1350-1355, 2009.

[3] R. V. Gonçalves, P. Migowski, H. Wender, D. Eberhardt, D. E. Weibel, F. C. Sonaglio, et al., "Ta2O5 nanotubes obtained by anodization: Effect of thermal treatment on the photocatalytic activity for hydrogen production," Journal of Physical Chemistry C, vol. 116, pp. 14022-14030, 2012.

[4] H. Yu, S. Zhu, X. Yang, X. Wang, H. Sun, and M. Huo, "Synthesis of Coral-Like Tantalum Oxide Films via Anodization in Mixed Organic-Inorganic Electrolytes," PLoS ONE, vol. 8, pp. 6-11, 2013.

[5] W. Wei, J. M. Macak, and P. Schmuki, "High aspect ratio ordered nanoporous Ta2O5 films by anodization of Ta," Electrochemistry Communications, vol. 10, pp. 428-432, 2008.

[6] C. Christensen, R. De Reus, and S. Bouwstra, "Tantalum oxide thin films as protective coatings for sensors," Journal of Micromechanics and Microengineering, vol. 9, pp. 113-118, 1999.

[7] J. Y. Zhang and I. W. Boyd, "Thin tantalum and tantalum oxide films grown by pulsed laser deposition," Applied Surface Science, vol. 168, pp. 234-238, 2000.

[8] C. Chaneliere, J. L. Autran, R. A. B. Devine, and B. Balland, "Tantalum pentoxide (Ta2O5) thin films for advanced dielectric applications," Materials Science and Engineering R: Reports, vol. 22, pp. 269-322, 1998.

[9] G. Xu, X. Shen, Y. Hu, P. Ma, and K. Cai, "Fabrication of tantalum oxide layers onto titanium substrates for improved corrosion resistance and cytocompatibility," Surface and Coatings Technology, vol. 272, pp. 58-65, 2015.

[10] M. Sarraf, B. A. Razak, B. Nasiri-Tabrizi, A. Dabbagh, N. H. A. Kasim, W. J. Basirun, et al., "Nanomechanical properties, wear resistance and in-vitro characterization of Ta2O5 nanotubes coating on biomedical grade Ti–6Al–4V," Journal of the Mechanical Behavior of Biomedical Materials, vol. 66, pp. 159-171, 2017.

[11] W. Chen, Q. Tu, H. Wu, C. Zhao, X. Yao, W. Fan, et al., "Study on morphology evolution of anodic tantalum oxide films in different using stages of H2SO4/HF electrolyte," Electrochimica Acta, vol. 236, pp. 140-153, 2017.

[12] R. S. Namur, K. M. Reys, and C. E. B. Marino, "Growth and Electrochemical Stability of Compact Tantalum Oxides Obtained in Different Electrolytes for Biomedical Applications," Materials Research, vol. 18, pp. 0-6, 2015.

[13] W. Wei, J. M. Macak, N. K. Shrestha, and P. Schmuki, "Thick Self-Ordered Nanoporous Ta2O5 Films with Long-Range Lateral Order," Journal of The Electrochemical Society, vol. 156, pp. K104-K104, 2009.

[14] I. V. Sieber and P. Schmuki, "Porous Tantalum Oxide Prepared by Electrochemical Anodic Oxidation," Journal of The Electrochemical Society, vol. 152, pp. C639-C639, 2005.

[15] Q. Lu, S. Mato, P. Skeldon, G. E. Thompson, D. Masheder, H. Habazaki, et al., "Anodic film growth on tantalum in dilute phosphoric acid solution at 20 and 85°C," Electrochimica Acta, vol. 47, pp. 2761-2767, 2002.

[16] Y. Kado, R. Hahn, C. Y. Lee, and P. Schmuki, "Strongly enhanced photocurrent response for Na doped Ta3N5-nano porous structure," Electrochemistry Communications, vol. 17, pp. 67-70, 2012.

[17] Z. Su, S. Grigorescu, L. Wang, K. Lee, and P. Schmuki, "Fast fabrication of Ta2O5 nanotube arrays and their conversion to Ta3N5 for efficient solar driven water splitting," Electrochemistry Communications, vol. 50, pp. 15-19, 2015.

[18] K. Lee and P. Schmuki, "Highly ordered nanoporous Ta2O5 formed by anodization of Ta at high temperatures in a glycerol/phosphate electrolyte," Electrochemistry Communications, vol. 13, pp. 542-545, 2011.

[19] A. Zaffora, D. Y. Cho, K. S. Lee, F. Di Quarto, R. Waser, M. Santamaria, et al., "Electrochemical Tantalum Oxide for Resistive Switching Memories," Advanced Materials, vol. 29, pp. 1-6, 2017.

[20] S. Singh, M. T. Greiner, and P. Kruse, "Robust inorganic membranes from detachable ultrathin tantalum oxide films," Nano Letters, vol. 7, pp. 2676-2683, 2007.

[21] H. A. El-Sayed and V. I. Birss, "Controlled growth and monitoring of tantalum oxide nanostructures," Nanoscale, vol. 2, pp. 793-798, 2010.

[22] D. Cristea, I. Ghiuţă, and D. Munteanu, "Tantalum based materials for implants and prosthesis applications," Bulletin of the Transilvania University of Braşov, vol. 857, 2015.

[23] C. F. Almeida Alves, A. Cavaleiro, and S. Carvalho, "Bioactivity response of Ta1-xOx coatings deposited by reactive DC magnetron sputtering," Materials Science and Engineering C, vol. 58, pp. 110-118, 2016.

[24] Y. Liu, C. Bao, D. Wismeijer, and G. Wu, "The physicochemical/biological properties of porous tantalum and the potential surface modification techniques to improve its clinical application in dental implantology," Materials Science and Engineering C, vol. 49, pp. 323-329, 2015.

[25] M. Sowa, M. Woszczak, A. Kazek-Kęsik, G. Dercz, D. M. Korotin, I. S. Zhidkov, et al., "Influence of process parameters on plasma electrolytic surface treatment of tantalum for biomedical applications," Applied Surface Science, vol. 407, pp. 52-63, 2017.

[26] T. Ruckh, J. R. Porter, N. K. Allam, X. Feng, C. A. Grimes, and K. C. Popat, "Nanostructured tantala as a template for enhanced osseointegration," Nanotechnology, vol. 20, p. 045102, 2008/12/18 2008.

[27] C. A. Alves, P. Ferreira, L. Marques, and S. Carvalho, "Passivation and dissolution mechanisms in ordered anodic tantalum oxide nanostructures," Applied Surface Science, vol. 513, p. 145575, 2020.

[28] S. A. Alves, S. B. Patel, C. Sukotjo, M. T. Mathew, P. N. Filho, J. P. Celis, et al., "Synthesis of calcium-phosphorous doped TiO2 nanotubes by anodization and reverse polarization: A promising strategy for an efficient biofunctional implant surface," Applied Surface Science, vol. 399, pp. 682-701, 2017.

[29] H. A. El-Sayed, C. A. Horwood, A. D. Abhayawardhana, and V. I. Birss, "New insights into the initial stages of Ta oxide nanotube formation on polycrystalline Ta electrodes," Nanoscale, vol. 5, pp. 1494-1498, 2013.

[30] J. M. Macak, H. Tsuchiya, A. Ghicov, K. Yasuda, R. Hahn, S. Bauer, et al., "TiO2 nanotubes: Self-organized electrochemical formation, properties and applications," Current Opinion in Solid State and Materials Science, vol. 11, pp. 3-18, 2007.

[31] A. Ghicov and P. Schmuki, "Self-ordering electrochemistry: A review on growth and functionality of TiO2 nanotubes and other self-aligned MOx structures," Chemical Communications, pp. 2791-2808, 2009.

[32] H. El-Sayed, S. Singh, and P. Kruse, "Formation of Dimpled Tantalum Surfaces from Electropolishing," Journal of The Electrochemical Society, vol. 154, pp. C728-C728, 2007.

[33] N. K. Allam, X. J. Feng, and C. A. Grimes, "Self-Assembled Fabrication of Vertically Oriented Ta2O5 Nanotube Arrays , and Membranes Thereof , by One-Step Tantalum Anodization," Chem. Mater., vol. 20, pp. 6477-6481, 2008.

[34] K. Lee, A. Mazare, and P. Schmuki, "One-Dimensional Titanium Dioxide Nanomaterials: Nanotubes," Chemical Reviews, vol. 114, pp. 9385-9454, 2014.

[35] P. Roy, S. Berger, and P. Schmuki, "TiO2 Nanotubes: Synthesis and Applications," Angew. Chem. Int, vol. 50, pp. 2904-2939, 2011.

[36] S. Berger, H. Tsuchiya, and P. Schmuki, "Transition from Nanopores to Nanotubes: Self-Ordered Anodic Oxide Structures on Titanium–Aluminides," Chemistry of Materials, vol. 20, pp. 3245-3247, 2008/05/01 2008.

[37] E. Uslu, H. Öztatlı, B. Garipcan, and B. Ercan, "Fabrication and cellular interactions of nanoporous tantalum oxide," Journal of Biomedical Materials Research Part B: Applied Biomaterials, vol. 108, pp. 2743-2753, 2020.

[38] Y.-J. Zeng, S.-C. Twan, K.-W. Wang, H.-H. Huang, Y.-B. Hsu, C.-Y. Wang, et al., "Enhanced biocompatibility in anodic TaOx nanotube arrays," Nanoscale Research Letters, vol. 12, pp. 1-8, 2017.

[39] N. Wang, H. Li, J. Wang, S. Chen, Y. Ma, and Z. Zhang, "Study on the Anticorrosion, Biocompatibility, and Osteoinductivity of Tantalum Decorated with Tantalum Oxide Nanotube Array Films," ACS Applied Materials & Interfaces, vol. 4, pp. 4516-4523, 2012/09/26 2012.

[40] T. W. Clyne and S. C. Troughton, "A review of recent work on discharge characteristics during plasma electrolytic oxidation of various metals," International Materials Reviews, vol. 64, pp. 127-162, 2019.

[41] M. Petković, S. Stojadinović, R. Vasilić, and L. Zeković, "Characterization of oxide coatings formed on tantalum by plasma electrolytic oxidation in 12-tungstosilicic acid," Applied Surface Science, vol. 257, pp. 10590-10594, 2011.

[42] M. Rizwan, R. Alias, U. Z. Zaidi, R. Mahmoodian, and M. Hamdi, "Surface modification of valve metals using plasma electrolytic oxidation for antibacterial applications: A review," Journal of Biomedical Materials Research - Part A, vol. 106, pp. 590-605, 2018.

[43] Y. Zhang, Y. Wu, D. Chen, R. Wang, D. Li, C. Guo, et al., "Micro-structures and growth mechanisms of plasma electrolytic oxidation coatings on aluminium at different current densities," Surface and Coatings Technology, vol. 321, pp. 236-246, 2017.

[44] Y. Cheng, T. Wang, S. Li, Y. Cheng, J. Cao, and H. Xie, "The effects of anion deposition and negative pulse on the behaviours of plasma electrolytic oxidation (PEO)—A systematic study of the PEO of a Zirlo alloy in aluminate electrolytes," Electrochimica Acta, vol. 225, pp. 47-68, 2017.

[45] R. F. Antonio, E. C. Rangel, B. A. Mas, E. A. R. Duek, and N. C. Cruz, "Growth of hydroxyapatite coatings on tantalum by plasma electrolytic oxidation in a single step," Surface and Coatings Technology, vol. 357, pp. 698-705, 2019.

[46] W. Tu, Y. Cheng, X. Wang, T. Zhan, J. Han, and Y. Cheng, "Plasma electrolytic oxidation of AZ31 magnesium alloy in aluminate-tungstate electrolytes and the coating formation mechanism," Journal of Alloys and Compounds, vol. 725, pp. 199-216, 2017.

[47] S. Stojadinović, J. Jovović, M. Petković, R. Vasilić, and N. Konjević, "Spectroscopic and real-time imaging investigation of tantalum plasma electrolytic oxidation (PEO)," Surface and Coatings Technology, vol. 205, pp. 5406-5413, 2011.

[48] F. G. Oliveira, A. R. Ribeiro, G. Perez, B. S. Archanjo, C. P. Gouvea, J. R. Araújo, et al., "Understanding growth mechanisms and tribocorrosion behaviour of porous TiO2 anodic films containing calcium, phosphorous and magnesium," Applied Surface Science, vol. 341, pp. 1-12, 2015.

[49] K. R. Shin, Y. G. Ko, and D. H. Shin, "Effect of electrolyte on surface properties of pure titanium coated by plasma electrolytic oxidation," Journal of Alloys and Compounds, vol. 509, pp. S478-S481, 2011.

[50] S. Stojadinović, N. Tadić, and R. Vasilić, "Luminescence of oxide films during the electrolytic oxidation of tantalum," Electrochimica Acta, vol. 152, pp. 323-329, 2015.

[51] M. Sowa, A. Kazek-k, R. P. Socha, G. Dercz, J. Michalska, and W. Simka, "Modification of tantalum surface via plasma electrolytic oxidation in silicate solutions," Electrochimica Acta, vol. 114, pp. 627-636, 2013.

[52] Y. Cheng, Q. Zhang, Z. Zhu, W. Tu, Y. Cheng, and P. Skeldon, "Potential and morphological transitions during bipolar plasma electrolytic oxidation of tantalum in silicate electrolyte," Ceramics International, vol. 46, pp. 13385-13396, 2020.

[53] M. Sowa and W. Simka, "Electrochemical impedance and polarization corrosion studies of tantalum surface modified by DC Plasma electrolytic oxidation," Materials, vol. 11, 2018.

[54] C. Wang, F. Wang, and Y. Han, "Structural characteristics and outward-inward growth behavior of tantalum oxide coatings on tantalum by micro-arc oxidation," Surface and Coatings Technology, vol. 214, pp. 110-116, 2013.

[55] K. Rokosz, T. Hryniewicz, P. Chapon, S. Raaen, and H. R. Z. Sandim, "XPS and GDOES characterization of porous coating enriched with copper and calcium obtained on tantalum via plasma electrolytic oxidation," Journal of Spectroscopy, vol. 2016, 2016.

[56] H. Gao, Y. F. Jie, Z. Q. Wang, H. Wan, L. Gong, R. C. Lu, et al., "Bioactive tantalum metal prepared by micro-arc oxidation and NaOH treatment," Journal of Materials Chemistry B, vol. 2, pp. 1216-1224, 2014.

[57] A. Fattah-alhosseini, M. Maryam, and D. Kazem Babaei, "Influence of Electrolyte Composition and Voltage on the Microstructure and Growth Mechanism of Plasma Electrolytic Oxidation (PEO) Coatings on Tantalum: A Review," Analytical & Bioanalytical Electrochemistry, vol. 12, pp. 517-535, 2020.

[58] C. Wang, F. Wang, and Y. Han, "The structure, bond strength and apatite-inducing ability of micro-arc oxidized tantalum and their response to annealing," Applied Surface Science, vol. 361, pp. 190-198, 2016.

[59] C. Wang, Z. Fan, and Y. Han, "Formation and osteoblast behavior of HA nano-rod/fiber patterned coatings on tantalum in porous and compact forms," Journal of Materials Chemistry B, vol. 2, pp. 5442-5454, 2015.

[60] Q. M. Zhao, G. Z. Li, H. L. Yang, and X. F. Gu, "Surface modification of biomedical tantalum by micro-arc oxidation," Materials Technology, vol. 32, pp. 90-95, 2017.

[61] M. A. P. C. Goularte, G. F. Barbosa, N. C. da Cruz, and L. M. Hirakata, "Achieving surface chemical and morphologic alterations on tantalum by plasma electrolytic oxidation," International Journal of Implant Dentistry, vol. 2, 2016.

[62] C. F. Almeida Alves, L. Fialho, S. M. Marques, S. Pires, P. Rico, C. Palacio, et al., "MC3T3-E1 cell response to microporous tantalum oxide surfaces enriched with Ca, P and Mg," Materials Science and Engineering: C, vol. 124, p. 112008, 2021.

[63] L. Fialho, L. Grenho, M. H. Fernandes, and S. Carvalho, "Porous tantalum oxide with osteoconductive elements and antibacterial core-shell nanoparticles: A new generation of materials for dental implants," Materials Science and Engineering: C, vol. 120, p. 111761, 2021.

CHAPTER V - Development of porous tantalum oxide by anodization assisted by electric field

The following chapter is partially based on the results published in:

1. L. Fialho, C. F. Almeida Alves, L. S. Marques, and S. Carvalho, "Development of stacked porous tantalum oxide layers by anodization," Applied Surface Science, vol. 511, p. 145542, 2020.

5 Introduction

Highly ordered nanostructured surfaces are well-known to improve and promote osseointegration due to mimic the bone properties [1] and also to avoid infections due to antibacterial properties [2]. There are several nanofeatures, such as nanopores and nanotubes. In fact, the bone matrix morphology is similar to a nanoporous structure [3, 4]. Thus, the manipulation of osseointegration process is possible developing metal nanostructures with homogenous pores patterns and uniform pore diameters [5]. Anodization is a low-cost electrochemical process used to produce a nanoporous structures, controlling the uniformity of pores distribution and pores diameters [6, 7]. However, the formation of ordered nanoporous oxide layers is mostly reported using hydrofluoric acid in the electrolyte composition, which is clearly now considered a chemical product with very high risk to human health and to the environment.

On this concern, this chapter is focused on the production of Ta_2O_5 nanoporous surfaces by anodization assisted by electric field using an HF-free electrolyte composed of ethylene glycol, water and ammonium fluoride (NH_4F). Different anodization parameters, such as electrolyte concentration, applied potential and duration of the process were deeply studied in order to understand how they are related to the achieved morphology. Additionally, two-step anodization was investigated and compared with one-step anodization regarding the improvement of the porous nanopatterns. The surface morphology of each sample was investigated by SEM and correlated with the respective current density-time curve behavior. The sample with the more uniform porous nanostructure was characterized in terms of elemental and chemical composition and crystalline structure.

To better briefly illustrate the experimental procedure, a diagram is shown in Figure V.1.

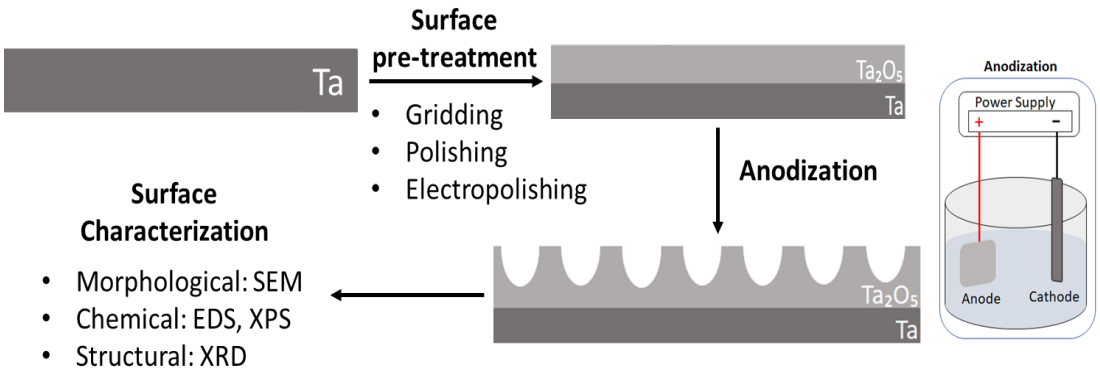

Figure V.1. Diagram of experimental procedure.

5.1 Materials and Methods

5.1.1 Surface pre-treatment

Squares of high-pure tantalum sheet (Testbourne, 99.5%, thickness 0.5 mm) of 400 mm^2 were used as substrates and named Ta. Firstly, the samples were grinded with a series of silicon carbide (SiC) sandpapers such as P500, P800, P1200 and P2500 (Carbimet, Buehler), followed by a polishing cloth with diamond paste (Diamond Suspension 3 and 6 μm, Struers) mixed with lubricant fluid (DP-Lubricant Blue, Struers) until achieving a mean roughness of 5 nm (mirror finish). All samples were ultrasonically cleaned in acetone for 15 minutes, 10 minutes in ethanol and 5 minutes in distilled (DI) water. Afterwards, an electrochemical treatment was performed to smooth the samples' surface (mean roughness of 3.7 nm) using a two-electrode set-up where a Ta sample and graphite rod served as the working and counter electrodes, respectively, with 1.8 cm^2 area exposed to 1 M H_2SO_4 (Sulphuric Acid 98%, Biochem, Chemopharma). Both electrodes were connected to a DC power supply (Agilent Technologies N5751A, 300V/2.5A/750W, LXI, USA). A constant voltage of 25 V was applied for 10 minutes with a working distance of 3 cm. The electrolyte was continuously stirred at room temperature (RT). These samples were called by Ta-pol.

5.1.2 Development of nanostructures

The nanostructures were obtained by anodization using the two-electrode set-up previously described. Ta-pol samples were used as working electrodes, while a graphite rod was used as a counter electrode. Both electrodes were immersed in an electrolyte composed of EG (Ethylene Glycol anhydrous 99.8%, Sigma-Aldrich), 3 vol.% DI water and a variable concentration of NH_4F (Ammonium Fluoride 98%, Sigma-Aldrich). For presentation purposes, the solvent mixture of EG and DI water was named as ES (electrolyte solution). The distance between the working and counter electrodes was fixed to 1.5 cm. The applied potential used was 40 or 60 V from 20 to 60 minutes. Also, two-step anodization was performed in which both steps were carried out under the same conditions. There was a time gap of 20 minutes between the first and the second step. At the end of this procedure, surfaces were gently rinsed with DI water and dried at RT. Anodized samples were named as Ta-anod$x$ (x=1, 2, 3, ... 7). All the detailed anodizing parameters are shown in Table V.1.

5.2 Study of the effect of electrochemical conditions on the Ta surface morphology

The Ta substrates (Figure V.2-A) were pre-treated by mechanical polishing in order to achieve a smoother surface (Figure V.2-B). Further electrochemical treatment (Figure V.2-C) promotes a more uniform oxidized surface. This oxide layer can minimize the stress mismatch between this pre-oxide and the further anodic layer.

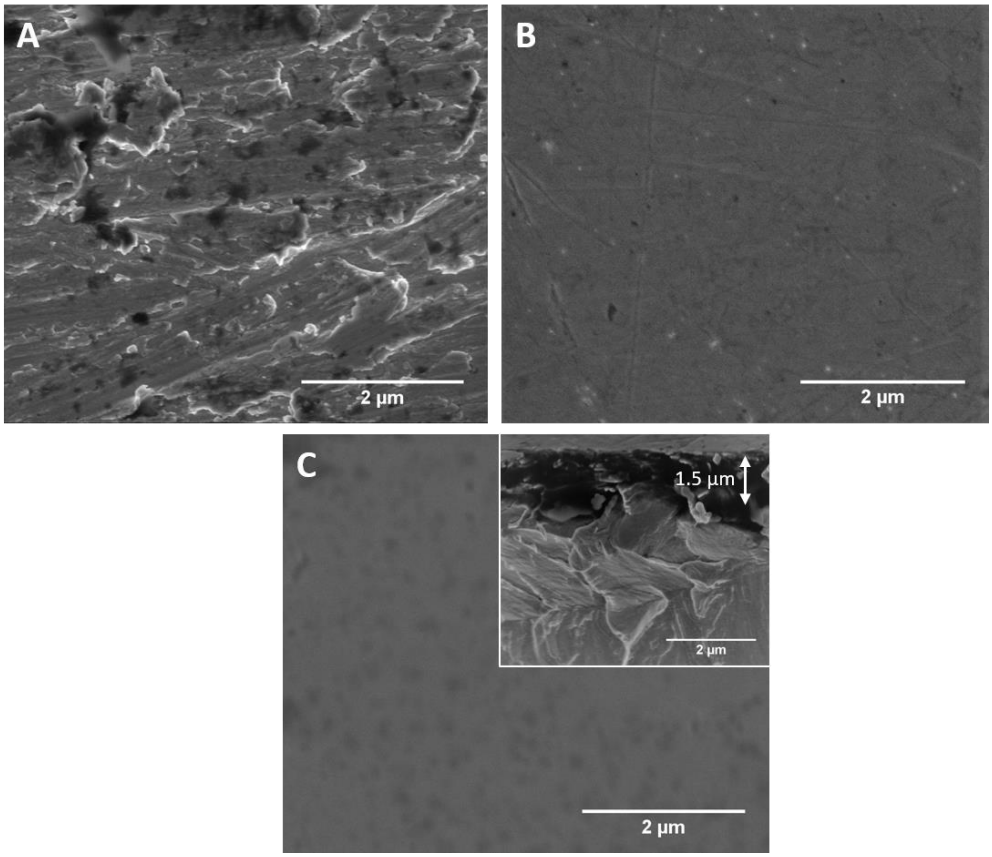

Figure V.2. Top-view FEGSEM micrographs of (a) Ta sheet and (b) Ta polished surface and (c) Ta surface after electrochemically pre-treatment, named Ta-pol sample.

One-step anodization was performed at 40 V using an electrolyte of 2.4 wt.% NH_4F in ES for 20 minutes (Ta-anod1 in Table V.1). The current density-curve can provide further information about the surface morphology evolution during the anodizing treatment [8]. The current density-time curve under these conditions (Figure V.3-A: red dot line) shows an initial decaying stage (see in the inset) followed by a gradual increase with time until the end of the procedure. As observed in Figure V.4-A, an anodic layer with only few small isolated pores was achieved.

Table V.1. Anodizing parameters: applied potential, electrolyte (composition and concentration) and process duration.

Sample	Anodization approach	Potential (V)	Electrolyte	Duration (min)
Ta-anod1	1-step	40	2.4 wt.% NH_4F + ES	20
Ta-anod2	1-step	60	0.3 wt.% NH_4F + ES	20
Ta-anod3	1-step	60	0.6 wt.% NH_4F + ES	20
Ta-anod4	1-step	60	1.2 wt.% NH_4F + ES	20
Ta-anod5	2-step	60	1.2 wt.% NH_4F + ES	60 (20 minutes stop) + 60
Ta-anod6	1-step	60	1.2 wt.% NH_4F + ES	60
Ta-anod7	1-step	60	2.4 wt.% NH_4F + ES	20

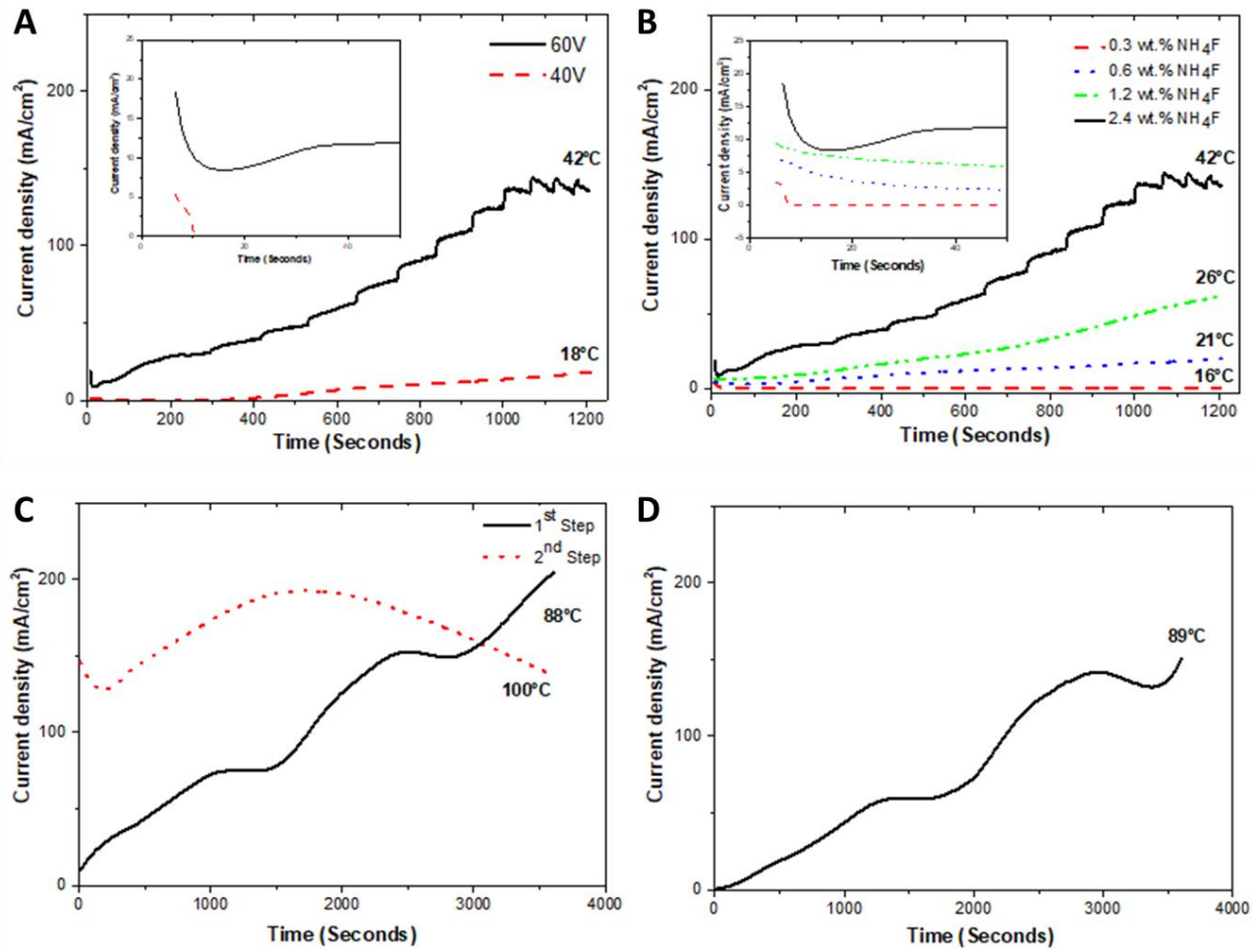

Figure V.3. Current density-time curves of several anodization assays: (a) Ta-anod1 and Ta-anod7 samples, (b) Ta-anod2, Ta-anod3, Ta-anod4 and Ta-anod7, (c) Ta- anod5 obtained by two-step and (d) Ta-anod6 obtained by one-step anodization under the same conditions.

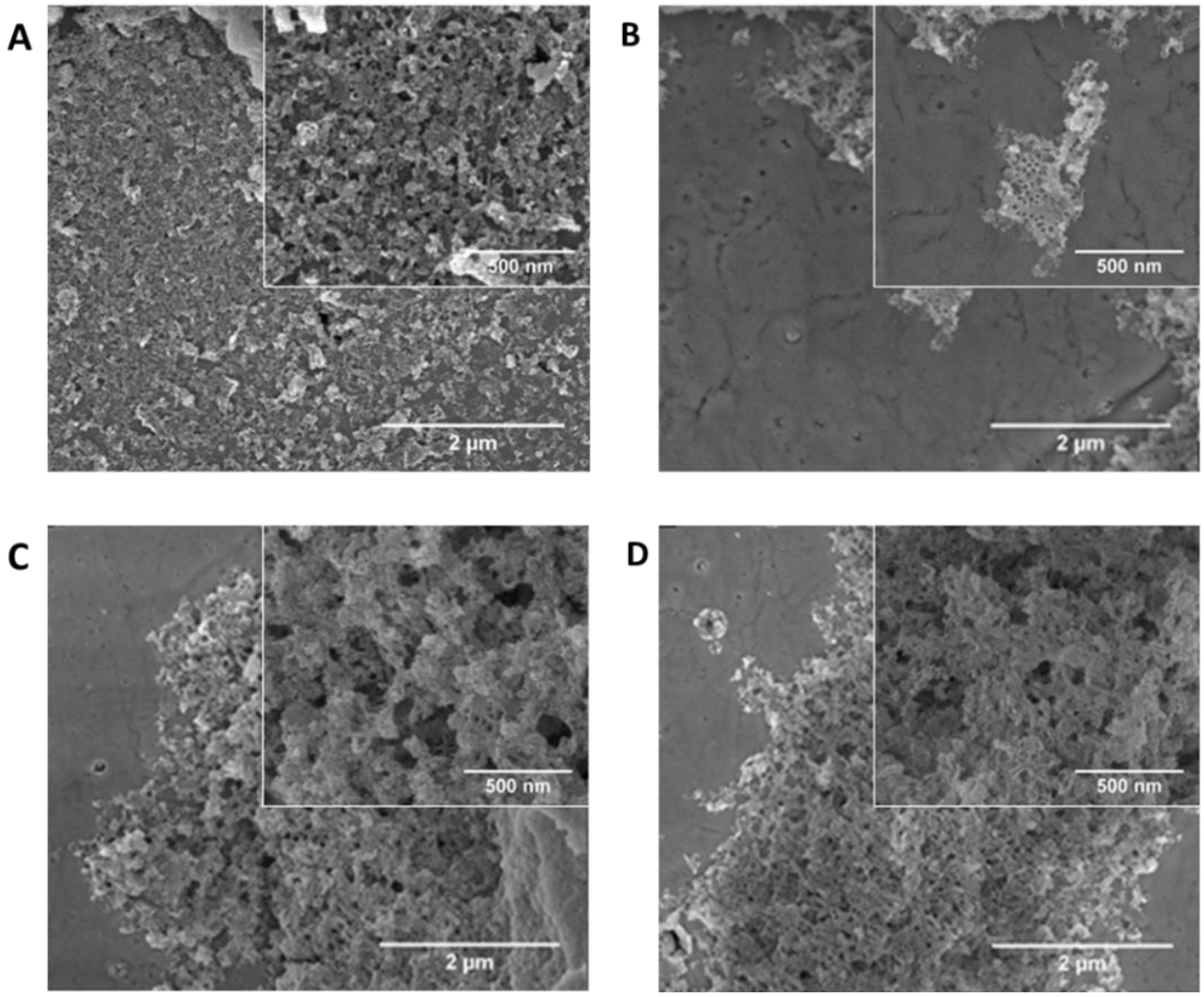

Figure V.4. Top-view FEGSEM micrographs for Ta anodized samples using an electrolyte solution with mixture of SE and A) 2.4 wt.% NH_4F (Ta-anod1) at 40 V for 20 minutes, B) 0.3 wt.% NH_4F (Ta-anod2), C) 0.6 wt.% NH_4F (Ta-anod3) and D) 1.2 wt.% NH_4F (Ta-anod4) at 60 V for 20 minutes.

Typically, three stages can be identified in the current density curve (Figure V.5). First, an initial exponential decay related to the build-up of a resistive compact oxide layer (Figure V.5-stage I) through Ta hydrolysis at the electrolyte/metal interface, according to Eq. IV.1.

The current density reaches a minimum value, which is believed to reflect the onset of electric field-enhanced dissolution of oxide film, leading to the generation of the first small pits . This stage is followed by an increase of current as the surface area increases when the pores extend and multiply due to the high dissolution rate of Ta_2O_5 in fluoride-containing solutions, according to Eq. IV.2 [9] (Figure V.5–stage II).

Finally, in the last stage it reaches a steady value [10], indicating that the oxide formation and dissolution reactions are in equilibrium [11, 12].

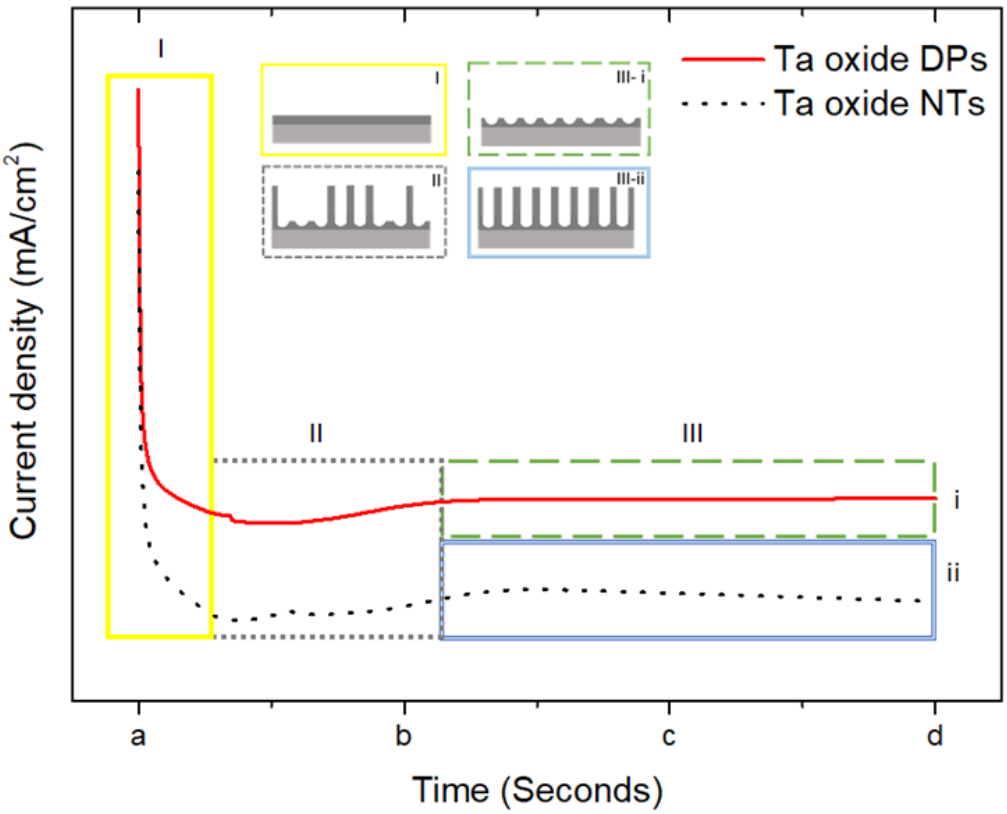

Figure V.5. Illustration of current density-time response during Ta anodization with the typical three stages: I) compact oxide layer formation, II) pores formation and extension, III) steady-state with i) dimples (DP) formation or ii) nanotubes (NTs) formation.

Several authors attribute different meanings to this third stage: a decrease in current density with time indicates stable nanotubular or porous Ta oxide formation, as illustrated in Figure V.5-stage III-ii, whereas a steady-state current or very slow increase is related to the oxide ordered nanostructure instability resulting in Ta dimpled surface morphology - Figure V.5-stage III-i [8]. On the other hand, El-Sayed *et al.* [9] proposed a new interpretation of current-time data, showing that pores are already formed in the first few milliseconds of anodization. In our case, the current density slightly increased in the second stage never reaching the third stage, and neither pore nor dimple development was clearly observed.

As the formation of pores could be enhanced by the applied electric field [6], the increase of the applied potential could provide a more uniform porous distribution at Ta surface [13]. Taking this in mind, the potential was raised from 40 to 60 V for different NH_4F concentrations. Firstly, in order to prevent current-density increase in the second stage, which is being associated with nanostructures instability, and in order to have a more controllable process, 0.3 wt.% NH_4F on the electrolyte was investigated (Ta-anod2 in Table V.1). Under these conditions, only two stages were registered in current density-time curve: a drop of current density and a long steady-state (Figure V.3-B). This current density-time curve behaviour was a characteristic of the formation of compact oxide in fluoride-free electrolytes [14]. Nevertheless, the

morphology obtained presented small islands of oxide with tiny pits above the compact oxide layer (Figure V.4-B), due to a low concentration of fluoride ions on the electrolyte and consequently a low dissolution rate.

Therefore, the NH_4F amount was increased to 0.6 wt.% (Ta-anod3 in Table V.1), however this concentration was still not enough to form a homogenous porous anodic layer (Figure V.4-C). Once again, the obtained morphologies indicate that the balance between the oxidation and the dissolution rate are not favorable, creating an irregular oxide layer with few evidences of pore formation. When NH_4F content reached 1.2 wt.% (Ta-anod4), the curve tended to increase promptly with time (Figure V.3-B), however no ordered nanostructured oxide layer was achieved (Figure V.4-D). In fact, it should be noticed that the presence of Ta oxide formed during the pre-treatment (Ta-pol sample) made it difficult to dissolve/pit the oxide surface demanding for stronger anodizing conditions (higher potential and/or more concentrated electrolytes) to dissolve/pit it.

Two-step anodization is recommended in literature as a better approach to reach well-ordered nanostructures [15, 16], as well as it helps to avoid mechanical damage and improve structural uniformity of the ordered nanostructures [7]. The first step will create nucleation pits by the growth of pores that will, in a second step, induce the growth of well-ordered pores or tubes [15-17]. Interestingly, for Ti anodization the development of the top layer (also called as sacrificial layer) was recorded in the first step and, 5 minutes later after its conclusion, the second step anodization started to grow the bottom layer (the desired layer) and a high-aspect-ratio titania nanostructure was obtained [18]. Thus, with the purpose of achieving a more uniform and homogeneous nanostructure, the previous hypothesis was tested (Ta-anod5 in Table V.1). In order to enhance the development of the nanopores, the anodization time was increased to 60 minutes with a time gap of 20 minutes between the first and the second step. As seen in Figure V.6-A, the nanostructures developed under two-step anodization did not exhibit a uniform and well-ordered structure, however some pores were formed. A lower magnification image (Figure V.6-A inset) shows the presence of cracks and overlapping layers. This non-uniform morphology could be related to the abnormal current density behaviour (Figure V.3-C). In regard to the formation of multi-layered titania nanotubes using a two-step anodization by switching the voltage from high to low (from the first to second step) neither cracks nor overlapping layers were reported [18]. Thus, to confirm this hypothesis, one-step anodization was performed under similar parameters (sample Ta-anod6 in Table V.1). As shown in Figure V.6-B, the overall morphology of the anodic layer was quite improved exhibiting a more uniform surface without visible cracks. However, it is possible to observe in Figure V.6-B (inset) pores with smaller

diameters (red streak circle) in the interior of larger pores (white circle) meaning that a bimodal porosity was achieved.

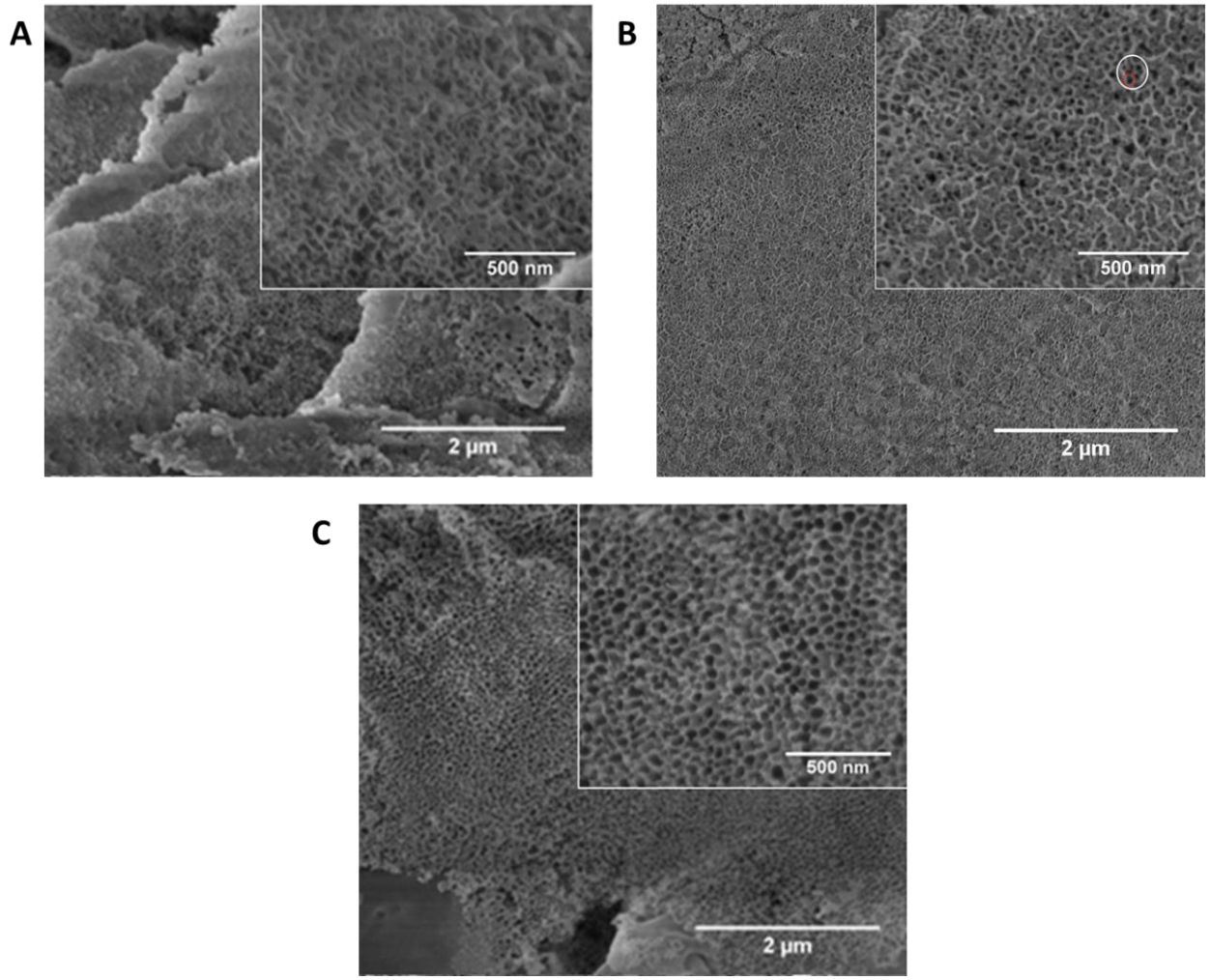

Figure V.6. Top-view FEGSEM micrographs of the Ta nanostructured surface using an electrolyte with 1.2 wt.% NH_4F in SE at 60V by (a) two-steps anodization for 60 minutes each (Ta-anod5), (b) one-step anodization for 60 minutes (Ta-anod6) – the white circle indicates a representative larger pore and the red streak circle as the smaller pore; (c) one-step anodization using 2.4 wt.% NH_4F in ES electrolyte for 20 minutes (Ta-anod7).

In general terms, the two-step anodization produced patchy anodic layers with less-ordered nanostructured surfaces in comparison to one-step anodization, reason why the two-step approach was not further considered in this study.

The obtained morphology of sample Ta-anod6 could suggest that, under these conditions, the process duration of 20 minutes (Ta-anod4 sample) was not enough to develop a nanostructured anodic film with nanostructure. Thus, the more obvious option would be increasing the process duration, however this is not feasible, since the current over 60 minutes was too high, showing a rapid increase (see Figure V.3-C and D). Thereby, in order to increase the dissolution rate with controllable current density, one-step anodization was performed for 20 minutes, raising the concentration of NH_4F to 2.4 wt.% on ES (Ta-anod7

in Table V.1). Under these conditions, it was possible to obtain a more uniform porous structure (Figure V.6-C). In Figure V.3-A (or B) the current density-time curve of Ta-anod7 sample shows a long second stage, exhibiting a continuous increase in current density with fast periodic oscillations, but not reaching a steady-state. Subsequently, the increase of current density is associated with the accelerated dissolution of the anodic layer, due to the higher concentration of NH_4F.

An increase in electrolyte temperature, related to the current flow through the oxide layer, was noticed, which further accelerates chemical dissolution, due to the enhancement of chemical reaction rates. The increase in electrolyte temperature leads not only to an unstable balance between oxide formation/dissolution kinetics, explaining the continuous increase of current density, but also to an increase in ion diffusion in electrolyte, while at the same time introduces turbulence in the mass transport. A similar behaviour of electrolyte temperature was previously observed in Ta anodization performed under RT, recording some oscillations in current density curve in the third stage which was attributed to an increase in the solution conductivity as the solution temperature increased 3 °C in 10 minutes, for a higher HF concentration in the electrolyte [8]. Despite the similar temperature behaviour, it is not possible to compare the overall current density-time curves experimentally obtained in this study with those reported in literature since the current densities recorded are almost one hundred times of order of magnitude superior. Only the curve behaviour for the initial times (Figure V.3-A and B insets) is in the same order of magnitude.

The high current density could also lead to acidification of the electrolyte and it can be accompanied by abundant gas production, due to water hydrolysis [6, 13], Eq. V.1:

$$2H_2O \rightarrow O_2 + 4H^+ + 4e^- \qquad \text{Eq. V.1}$$

In this sense, the pH of the electrolyte was measured before and after anodization, 5.6 and 4.8, respectively. Anodizing for a longer time could contribute to the acidic dissolution and consequently induce a merging of the neighboring pores [19, 20]. The joint action of all these factors explains the observed random nanoporous morphology due to disordered growth of porous in the oxide layer [21].

An interesting feature in current density is the presence of fast current oscillations for high NH_4F concentration, as shown in Figure V.3-A (or B). These oscillations started to occur in the second stage and could be the result of the breakdown on the oxide-metal interface. In literature, current (or voltage) oscillations are reported during anodization of semiconductors, as Si [22], and metals, as Ti [23-26] or Al [20], and numerous models were suggested. For Si and Ti voltage oscillations were ascribed to the

alternating stages of anodic oxide growth and lifting-off, while in the case of Al, the current oscillations were attributed to the oxidation process controlled by electrolyte diffusion through the pore combined with the local heat generation, due to the exothermic nature of the oxidation reaction.

Therefore, as a more uniform porous structure was achieved, the sample produced by one-step anodization under 60 V with an electrolyte of 2.4 wt.% NH_4F in ES for 20 minutes, will be further characterized (Ta-anod7 sample).

5.3 Phase composition

XRD analyses were carried out in order to understand the evolution of the structure caused by the topographic/morphologic and chemical modifications of the Ta substrate during anodization. Figure V.7 presents the diffraction patterns for Ta sheet before any treatment, Ta-pol and Ta-anod7. The main crystalline phases identified are α-Ta: body-centered cubic (bcc) (ICDD card n. 00-004-0788) and β-Ta: tetragonal (ICDD card n. 00-025-1280).

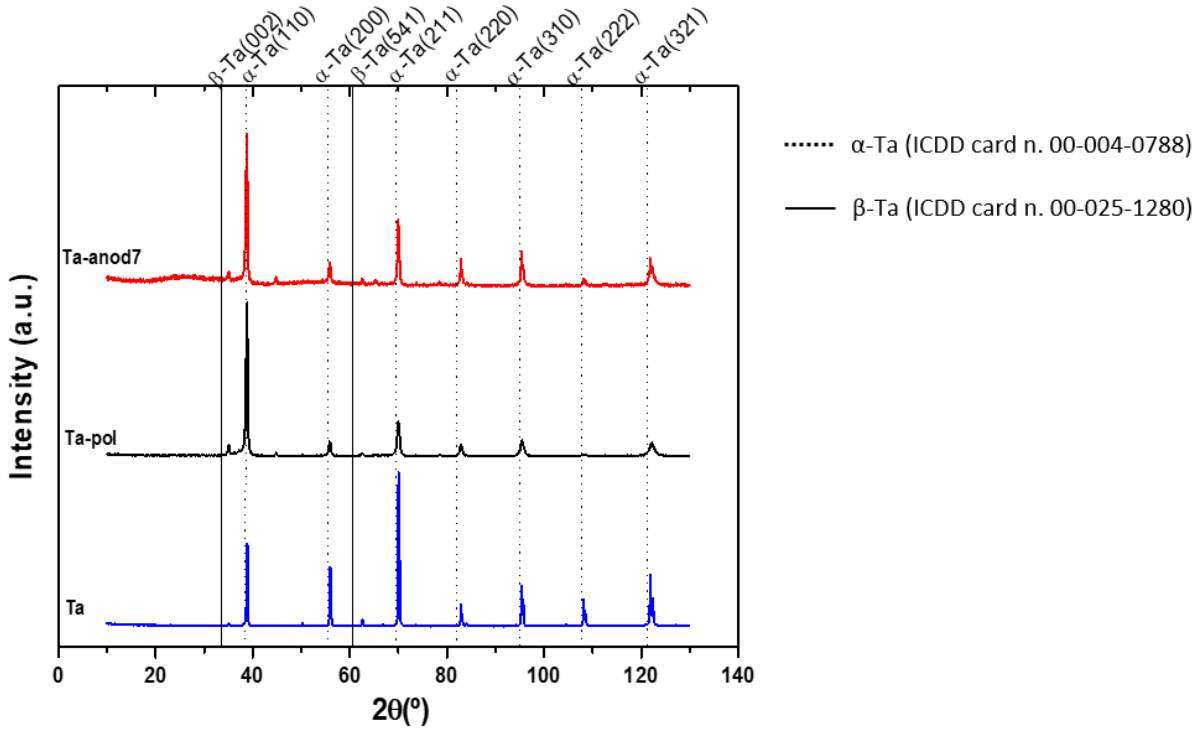

Figure V.7. XRD diffractograms of Ta sheet without any treatment (Ta - blue row); Ta with pre-treatment (Ta-pol - black row) and Ta anodized (Ta-anod7 - red row).

Ta sheet presented a mixture of both α-Ta and β-Ta phases. The presence of α-Ta and β-Ta phases in both Ta-pol and Ta-anod7 samples was related with the crystalline composition of the base material, Ta sheet. The absence of any further diffraction peaks indicates that the Ta_2O_5 anodic layer is amorphous, barely being observed in Ta-anod7 pattern for lower angles which is consistent with previous studies [27].

Similar results were also observed by Momeni et. al [28] where Ta anodized exhibited a diffraction peak of Ta substrate and after annealing at 400 °C the sample revealed new diffraction peaks, with a low intensity of crystalline Ta_2O_5. Moreover, Gonçalves *et al.* [29] demonstrated that only thermal treatment above 750 °C results in crystalline structure formation with the appearance of Ta_2O_5 orthorhombic phase. Also, it was evident that the dissolution rate has an important influence on the sheet orientations. Before any treatment, the presentation of a preferential orientation in the [211] direction by Ta sheet was noticed. After the electrochemical process, the [211] direction was consumed and a preferential [110] direction arose. The results revealed that the high atomic packing for {211} planes allowed a higher dissolution rather than the {110} planes, which revealed more resistance to be consumed during anodization.

5.4 Chemical composition

The EDS spectra acquired from Ta-pol and Ta-anod7 are shown in Figure V.8-A and B, respectively, which shows that with the surface pre-treatment, Ta element, such as a residual amount of Carbon (C) and some Oxygen (O) were detected, due to the tantalum oxidation expected by electrochemical treatment. After the anodization process, beyond the mentioned elements, Fluorine (F) was also detected on the surface of the Ta-anod7 with an increasing of O content, which was likely related with the increase of the thickness of the anodic layer.

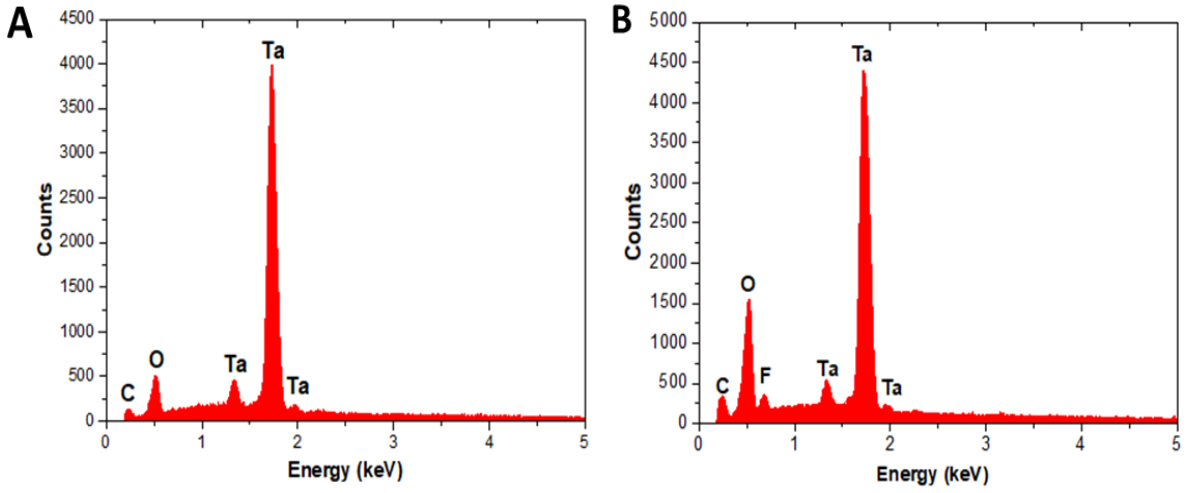

Figure V.8. EDS spectra of A) Ta-pol and B) Ta-anod7 samples.

Considering that the EDS technique analyses the composition of the materials in depth, so as to have a more reliable and accurate measurement of the surface chemical composition, the XPS analysis was performed on both sample surfaces. Figure V.9-A displays both surveys and quantitative results are summarized in Table V.2. Chemical quantification by XPS revealed an O and Ta content close of composition reported for Ta_2O_5 [30]. The qualitative chemical composition of both surfaces is similar,

except for the fact that in Ta-pol sulphur (S) contamination, which came from the electrochemical treatment with H_2SO_4, was detected. These findings can indicate that S element is present on the top layer of the oxide or its content is low, and, because of that, it was only detected by XPS and not by EDS. This contamination was also noticed by Namur *et al.* [31] in compact Ta_2O_5 obtained in 1 M H_2SO_4 anodization. In Ta-anod7, the F peak appeared due to the used electrolyte during the anodizing process. Moreover, Ta 4f doublet (Figure V.9-B) corresponded to Ta^{5+} in Ta_2O_5 [32-34] for both Ta-pol and Ta-anod7 samples with peak binding energies for Ta $4f_{7/2}$ at 26.3 eV and 26.5 eV, respectively, and the metallic state was not detected (the Ta^0 $4f_{7/2}$ peak would be detected at 21.5 eV [34]), indicating an efficient anodization process. While the dissolution reaction is continuously occurring, a fluoride-rich Ta_2O_5 layer builds-up at the metal/oxide interface and remains on the surface after oxide film detachment [35]. Indeed, a binding energy peak around 685 eV, which corresponds to F 1s, was detected. Its presence has been reported on Ti nanostructured surfaces obtained by anodization with a mixture of EG, H_2O and NH_4F electrolyte, being attributed to adsorbed F^- ions [36-38]. It is thus reasonable to assume that the F 1s peak detected corresponds to F^- ions absorbed on Ta_2O_5. Furthermore, it is possible that fluoride-rich layer is dissolved after the lift-off, resulting in the re-precipitation of a pill-off layer onto the growing porous oxide layer.

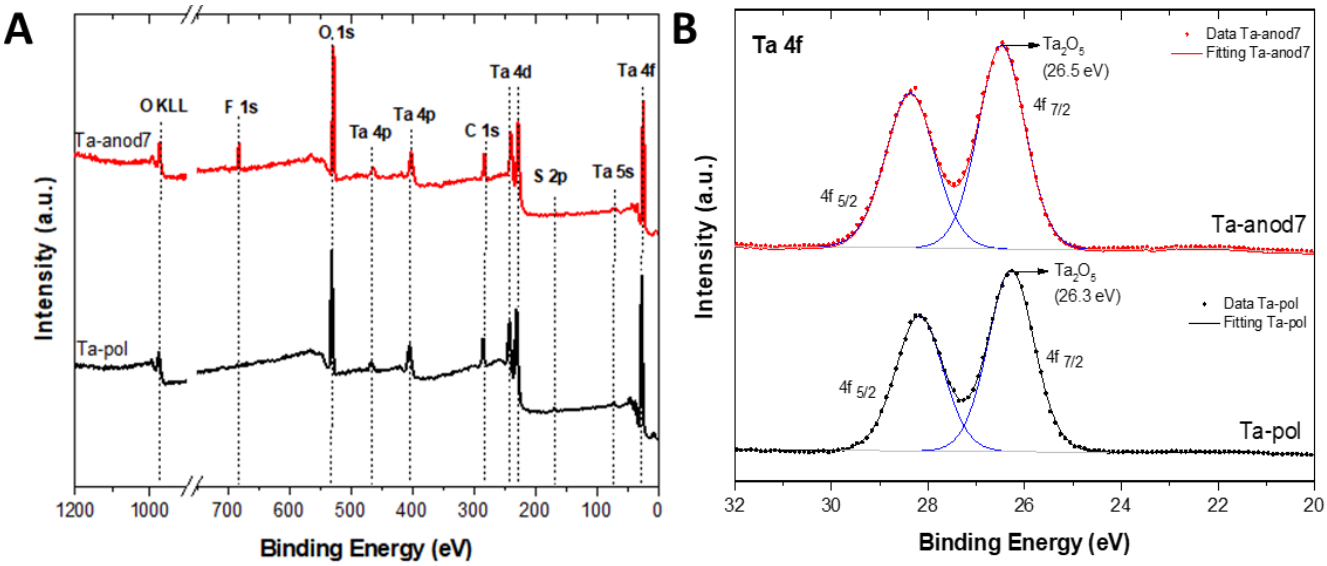

Figure V.9. A) Survey XPS data of Ta-pol (black row) and Ta-anod7 (red row) and the respective B) Ta 4f deconvoluted spectra.

Table V.2. Chemical composition of Ta-pol and Ta-anod7 samples recorded by XPS.

Sample	Chemical composition (at. %)		
	Ta 4f	O 1s	F 1s
Ta-pol	27.0	73.0	-
Ta-anod7	17.9	73.0	9.1

5.5 Partial conclusions

This study has shown the possibility of developing a nanostructure on Ta oxide layer using an HF-free electrolyte composed only of an organic solvent, EG, and water. The addition of a different content of NH_4F affected the nanostructure and current density-time curve recorded during the anodizing process. A more concentrated electrolyte led to a strong increasing current density and a uniform porous Ta_2O_5 surface was obtained. However, these anodization conditions ascribed to a more unstable variation of the current density with time, and a different behaviour of the typical anodization current-time curve with a magnitude 100 times higher than the conventional/published. Under these conditions, the electrochemical oxide dissolution was stronger, leading to a strong electrolyte temperature increase, and consequently to an unbalance between dissolution and oxide formation rates, preventing the current density from achieving the steady-state. Furthermore, two-step anodization efforts to reach a well-ordered porous structure of the oxide layer did not show any morphology improvement compared with one-step anodization under similar anodizing conditions. By one-step anodization, increasing the NH_4F concentration, a quite organized and homogenous porous nanostructure was formed.

5.6 References

[1] L. Zhang and T. J. Webster, "Nanotechnology and nanomaterials: promises for improved tissue regeneration," *Nano today,* vol. 4, pp. 66-80, 2009.

[2] E. P. Ivanova, J. Hasan, H. K. Webb, G. Gervinskas, S. Juodkazis, V. K. Truong*, et al.*, "Bactericidal activity of black silicon," *Nature Communications,* vol. 4, p. 2838, 2013/11/26 2013.

[3] T. Gong, J. Xie, J. Liao, T. Zhang, S. Lin, and Y. Lin, "Nanomaterials and bone regeneration," *Bone Research,* vol. 3, p. 15029, 2015/11/10 2015.

[4] L. Zhu, D. Luo, and Y. Liu, "Effect of the nano/microscale structure of biomaterial scaffolds on bone regeneration," *International Journal of Oral Science,* vol. 12, pp. 1-15, 2020.

[5] G. Ryan, A. Pandit, and D. P. Apatsidis, "Fabrication methods of porous metals for use in orthopaedic applications," *Biomaterials,* vol. 27, pp. 2651-2670, 2006.

[6] I. V. Sieber and P. Schmuki, "Porous Tantalum Oxide Prepared by Electrochemical Anodic Oxidation," *Journal of The Electrochemical Society,* vol. 152, pp. C639-C639, 2005.

[7] W. Wei, J. M. Macak, N. K. Shrestha, and P. Schmuki, "Thick Self-Ordered Nanoporous Ta2O5 Films with Long-Range Lateral Order," *Journal of The Electrochemical Society,* vol. 156, pp. K104-K104, 2009.

[8] H. A. El-Sayed and V. I. Birss, "Controlled growth and monitoring of tantalum oxide nanostructures," *Nanoscale,* vol. 2, pp. 793-798, 2010.

[9] H. A. El-Sayed, C. A. Horwood, A. D. Abhayawardhana, and V. I. Birss, "New insights into the initial stages of Ta oxide nanotube formation on polycrystalline Ta electrodes," *Nanoscale,* vol. 5, pp. 1494-1498, 2013.

[10] W. Wei, J. M. Macak, and P. Schmuki, "High aspect ratio ordered nanoporous Ta2O5 films by anodization of Ta," *Electrochemistry Communications,* vol. 10, pp. 428-432, 2008.

[11] J. M. Macak, H. Tsuchiya, A. Ghicov, K. Yasuda, R. Hahn, S. Bauer*, et al.*, "TiO2 nanotubes: Self-organized electrochemical formation, properties and applications," *Current Opinion in Solid State and Materials Science,* vol. 11, pp. 3-18, 2007.

[12] S. Minagar, C. C. Berndt, and C. Wen, "Fabrication and characterization of nanoporous niobia, and nanotubular tantala, titania and zirconia via anodization," *Journal of Functional Biomaterials,* vol. 6, pp. 153-170, 2015.

[13] I. Sieber, H. Hildebrand, A. Friedrich, and P. Schmuki, "Initiation of tantalum oxide pores grown on tantalum by potentiodynamic anodic oxidation," *Journal of Electroceramics,* vol. 16, pp. 35-39, 2006.

[14] P. Roy, S. Berger, and P. Schmuki, "TiO2 Nanotubes: Synthesis and Applications," *Angew. Chem. Int,* vol. 50, pp. 2904-2939, 2011.

[15] J. M. Macak, S. P. Albu, and P. Schmuki, "Towards ideal hexagonal self-ordering of TiO2 nanotubes," *Physica Status Solidi - Rapid Research Letters,* vol. 1, pp. 181-183, 2007.

[16] H. Masuda and K. Fukuda, "Ordered Metal Nanohole Arrays Made by a Two-Step Replication of Honeycomb Structures of Anodic Alumina," *Science (New York, N.Y.),* vol. 268, pp. 1466-1468, 1995.

[17] S. Singh, M. T. Greiner, and P. Kruse, "Robust inorganic membranes from detachable ultrathin tantalum oxide films," *Nano Letters,* vol. 7, pp. 2676-2683, 2007.

[18] X. Wang, S. Zhang, and L. Sun, "A Two-step anodization to grow high-aspect-ratio TiO2 nanotubes," *Thin Solid Films,* vol. 519, pp. 4694-4698, 2011.

[19] T. Aerts, T. Dimogerontakis, I. De Graeve, J. Fransaer, and H. Terryn, "Influence of the anodizing temperature on the porosity and the mechanical properties of the porous anodic oxide film," *Surface and Coatings Technology,* vol. 201, pp. 7310-7317, 2007.

[20] B. W. Lee, J.-c. Kim, and U. Go, "Spontaneous Current Oscillations during Hard Anodization of Aluminum under Potentiostatic Conditions," *Advance functional Materials,* vol. 20, pp. 21-27, 2010.

[21] A. Ghicov and P. Schmuki, "Self-ordering electrochemistry: A review on growth and functionality of TiO2 nanotubes and other self-aligned MOx structures," *Chemical Communications,* pp. 2791-2808, 2009.

[22] V. Parkhutik, J. Curiel-Esparza, M. C. Millan, and J. Albella, "Spontaneous layering of porous silicon layers formed at high current densities," *Physica Status Solidi (A) Applications and Materials Science,* vol. 202, pp. 1576-1580, 2005.

[23] S. Chen, M. Liao, P. Yang, S. Yan, R. Jin, and X. Zhu, "Simulation of anodizing current-time curves and the morphology evolution of TiO2 nanotubes obtained in phosphoric electrolytes," *RSC Advances,* vol. 6, pp. 84309-84318, 2016.

[24] L. V. Taveira, J. M. Macak, K. Sirotna, L. F. P. Dick, and P. Schmuki, "Voltage Oscillations and Morphology during the Galvanostatic Formation of Self-Organized TiO2 Nanotubes," *Journal of The Electrochemical Society,* vol. 153, pp. 137-143, 2006.

[25] W. Z. Shen, "Controllable current oscillation and pore morphology evolution in the anodic growth of TiO2," *Nanotechnology,* pp. 1-12, 2011.

[26] J. M. Macak, K. Sirotna, and P. Schmuki, "Self-organized porous titanium oxide prepared in Na2SO4/NaF electrolytes," *Electrochimica Acta,* vol. 50, pp. 3679-3684, 2005.

[27] W. Chen, Q. Tu, H. Wu, C. Zhao, X. Yao, W. Fan*, et al.*, "Study on morphology evolution of anodic tantalum oxide films in different using stages of H2SO4/HF electrolyte," *Electrochimica Acta,* vol. 236, pp. 140-153, 2017.

[28] M. M. Momeni, M. Mirhosseini, and M. Chavoshi, "Fabrication of Ta2O5 nanostructure films via electrochemical anodisation of tantalum," *Surface Engineering,* vol. 0844, pp. 160226022403003-160226022403003, 2015.

[29] R. V. Gonçalves, P. Migowski, H. Wender, D. Eberhardt, D. E. Weibel, F. C. Sonaglio*, et al.*, "Ta2O5 nanotubes obtained by anodization: Effect of thermal treatment on the photocatalytic activity for hydrogen production," *Journal of Physical Chemistry C,* vol. 116, pp. 14022-14030, 2012.

[30] M. Sowa, M. Woszczak, A. Kazek-Kęsik, G. Dercz, D. M. Korotin, I. S. Zhidkov*, et al.*, "Influence of process parameters on plasma electrolytic surface treatment of tantalum for biomedical applications," *Applied Surface Science,* vol. 407, pp. 52-63, 2017.

[31] R. S. Namur, K. M. Reys, and C. E. B. Marino, "Growth and Electrochemical Stability of Compact Tantalum Oxides Obtained in Different Electrolytes for Biomedical Applications," *Materials Research,* vol. 18, pp. 0-6, 2015.

[32] J. Y. Zhang and I. W. Boyd, "Thin tantalum and tantalum oxide films grown by pulsed laser deposition," *Applied Surface Science,* vol. 168, pp. 234-238, 2000.

[33] P. M. Ranjith, M. T. Rao, S. Sapra, I. I. Suni, and R. Srinivasan, "On the Anodic Dissolution of Tantalum and Niobium in Hydrofluoric Acid," *Journal of The Electrochemical Society,* vol. 165, pp. C258-C269, 2018.

[34] R. Simpson, R. G. White, J. F. Watts, and M. A. Baker, "XPS investigation of monatomic and cluster argon ion sputtering of tantalum pentoxide," *Applied Surface Science,* vol. 405, pp. 79-87, 2017.

[35] H. A. El-Sayed and V. I. Birss, "Controlled interconversion of nanoarray of Ta dimples and high aspect ratio Ta oxide nanotubes," *Nano Letters,* vol. 9, pp. 1350-1355, 2009.

[36] S. A. Alves, S. B. Patel, C. Sukotjo, M. T. Mathew, P. N. Filho, J. P. Celis*, et al.*, "Synthesis of calcium-phosphorous doped TiO2 nanotubes by anodization and reverse polarization: A promising strategy for an efficient biofunctional implant surface," *Applied Surface Science,* vol. 399, pp. 682-701, 2017.

[37] S. C. Han, J. M. Doh, J. K. Yoon, G. H. Kim, J. Y. Byun, S. H. Han*, et al.*, "Highly Ordered Self-Organized TiO2 Nanotube Arrays Prepared by a Multi-Step Anodic Oxidation Process," vol. 15, pp. 493-499, 2009.

[38] R. P. Antony, T. Mathews, S. Dash, A. K. Tyagi, and B. Raj, "X-ray photoelectron spectroscopic studies of anodically synthesized self aligned TiO2 nanotube arrays and the effect of electrochemical parameters on tube morphology," *Materials Chemistry and Physics,* vol. 132, pp. 957-966, 2012.

CHAPTER VI - Incorporation of osteoconductive elements in the anodic porous tantalum by reverse polarization and/or anodization

The following chapter is partially based on the results published in:

1. L. Fialho and S. Carvalho, "Surface engineering of nanostructured Ta surface with incorporation of osteoconductive elements by anodization," Applied Surface Science, vol. 495, p. 143573, 2019.
2. L. Fialho, C. F. Almeida Alves, L. S. Marques, and S. Carvalho, "Development of stacked porous tantalum oxide layers by anodization," Applied Surface Science, vol. 511, p. 145542, 2020.

6 Introduction

The structure of bone is mainly constituted by inorganic component, composed of HAp, and a minor part of organic component, mostly composed of collagen. HAp is a crystalline complex of calcium phosphate, $Ca_{10}(PO_4)_6(OH)_2$, but has origin from amorphous calcium phosphate [1]. Thus, the major components of enamel and dentine are Ca and P, followed by a minor content of Mg and Na [2]. Thereby, the main attempt of this chapter was to mimic the natural bone chemical composition through the surface biofunctionalization with elements natively present in natural bone, ensuring the bone-like structure at micro/nanoscale achieved in the previous CHAPTER V.

For this purpose, two different approaches were proposed: anodization assisted by electric field and RP followed by anodization, under different anodizing conditions (applied potential, times and electrolyte). After the first anodization step to attain a porous morphology (Ta-anod7 surface sample developed in CHAPTER V), the approaches were used for surface biofunctionalization (i.e. enrich the anodic layer with osteoconductive elements) using an electrolyte mixture of calcium acetate (CaA), β-glycerolphosphate (β-GP) and magnesium acetate (MgA) to incorporate Ca, P and Mg, respectively, on the Ta_2O_5 nanostructured surface with a Ca/P ratio on the surface as close as possible to the theoretical natural hydroxyapatite (HAp) value of 1.67 [3, 4]. The obtained surfaces were characterized by SEM and EDS to understand the effect of each anodizing condition on the surface morphology and chemical composition, respectively. Additionally, the surfaces that showed the best commitment between morphologic structure and Ca/P ratio were investigated by XPS, XRD, AFM and sessile drop test to evaluate the influence of the biofunctionalization step on the surface properties, as well as their cross-section morphology.

To better briefly illustrate the experimental procedure, a diagram is shown in Figure VI.1.

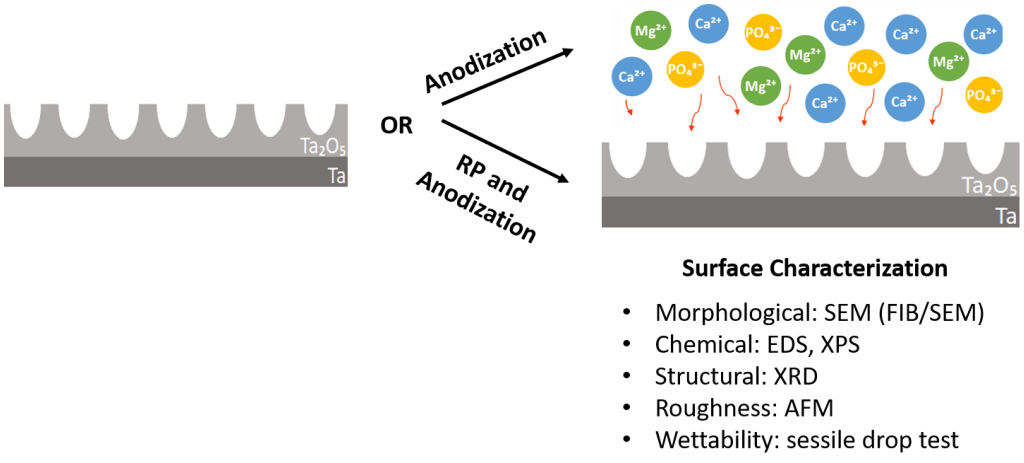

Figure VI.1. Diagram of experimental procedure.

6.1 Materials and Methods

6.1.1 Biofunctionalization of the nanostructured surface with Ca, P and Mg

Nanostructured Ta surfaces, Ta-anod7, were functionalized by reverse polarization (RP) and/or anodization in order to incorporate initially Ca and P species in the structure. Previous samples were used as the working electrode and the graphite rod was the counter electrode. In the first approach a constant voltage of 100 V was applied for 30 minutes. In a second approach a RP was applied to promote the incorporation of the bioactive species. In this step, the Ta-anod sample became the cathode and the graphite rod the anode. In this step, a constant voltage of 20 V for 10 and 20 seconds as parameters were used. After that, the polarity of the electrodes was turned over again to perform the anodizing process during 30 minutes for a constant potential (100V). For both approaches, both electrodes were immersed in an electrolyte mixture of CaA (calcium acetate 99%, Biochem, Chemopharma) as Ca precursor and β-GP (β-glycerolphosphate disodium salt pentahydrate 98%, Sigma-Aldrich) as P precursor with different concentrations. The treatment parameters are displayed in Table VI.1. The specimens were called Ta-CaP*n* (*n*= 1, 2, ..., 4). The chemical composition of the obtained specimens Ta-CaP*n* estimated by EDS is displayed in Table VI.2. Also, MgA (magnesium acetate 99%, Biochem, Chemopharma) as Mg precursor was added to the previous electrolyte mixture varying its concentration and changing the applied potential. These conditions are presented in Table VI.3. The obtained samples were labeled as Ta-CaPMg*n* (*n*= 1, 2, ..., 5). The chemical composition of the obtained specimens Ta-CaPMg*n* estimated by EDS is displayed in Table VI.4. Thereafter, the samples were gently rinsed in DI water and dried at RT.

6.2 Understanding the biofunctionalization by RP and/or anodization regarding the morphology and chemical composition

Using a Ta_2O_5 porous nanostructured (Ta-anod7) sample as substrate, the incorporation of Ca and P was firstly performed by two different approaches and with different electrolyte concentrations (Table VI.1).

Figure VI.2 shows the morphology of each sample achieved with the conditions presented in Table VI.1. As can be observed, sample Ta-CaP1 (Figure VI.2-A) had a different morphology than Ta-anod7 (Figure V.6-C), as it presents different levels of porosity (at micro and nano-pores scale). On the other hand, Ta-CaP2 (Figure VI.2-B) produced by RP followed by anodization promoted a quite well uniform morphology. Increasing the β-GP concentration on the electrolyte mixture, samples Ta-CaP3 and Ta-CaP4 (Figure VI.2-C and D) morphologies did not reveal a significant modification compared to Ta-anod7 (Figure VI.2-A).

Table VI.1. Different parameters for Ca and P incorporation on Ta-anod7 surfaces by both biofunctionalization approaches: reverse polarization or/and anodization.

Sample	Approach	Voltage (V)	Duration (min)	Electrolyte
Ta-CaP1	Anodization	100	30	0.18 M CaA + 0.06 M β-GP
Ta-CaP2	Reverse polarization	20	10 s	
	Anodization	100	30	
Ta-CaP3	Anodization	100	30	0.18 M CaA + 0.12 M β-GP
Ta-CaP4	Reverse polarization	20	10 s	
	Anodization	100	30	

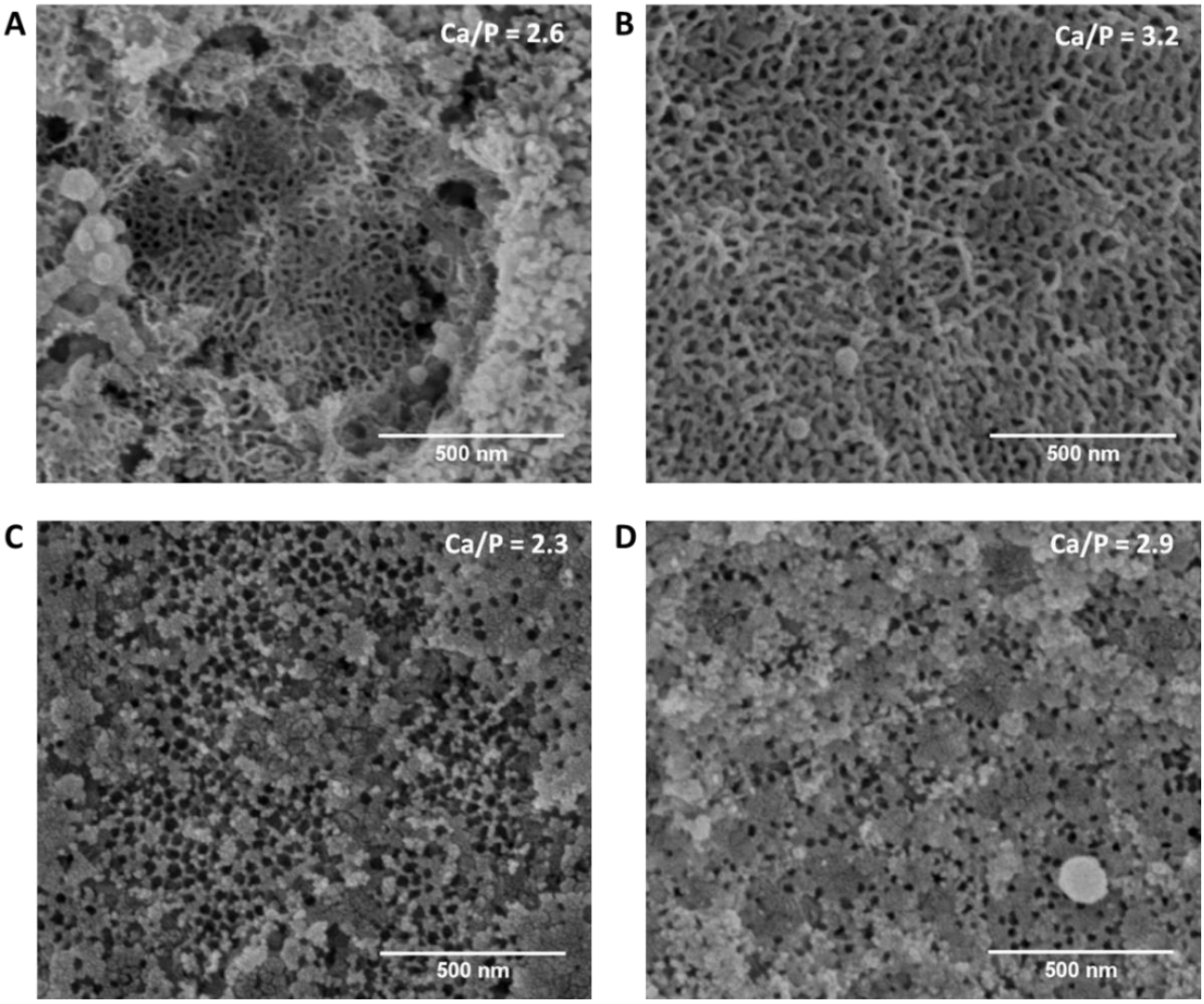

Figure VI.2. Top-views FEGSEM micrographs of Ta anodized samples with incorporation of Ca and P ions for different anodizing parameters: A) Ta-CaP1, B) Ta-CaP2, C) Ta-CaP3 and D) Ta-CaP4. Corresponding Ca/P ratio is represented in each inset.

Table VI.2 displays the chemical composition of the osteoconductive elements recorded by EDS analysis of each sample. For lower concentrated electrolyte, no significant incorporation of P on the surface samples was observed. Increasing electrolyte concentration, both approaches (RP and/or anodization) showed a higher ions incorporation, mainly Ca. An additional element also contributed to the chemical composition: sodium (Na) from β-GP.

Table VI.2. Chemical composition of Ca, P and Na elements determined by EDS of Ta anodized samples, as well as Ca+Na)/P and Ca/P ratios.

Sample	Chemical composition (at. %)			(Ca+Na)/P	Ca/P
	Ca	P	Na		
Ta-CaP1	2.1	0.8	0.8	3.6	2.6
Ta-CaP2	3.2	1.0	0.8	4.0	3.2
Ta-CaP3	8.8	3.8	1.2	2.6	2.3
Ta-CaP4	9.7	3.3	2.3	3.6	2.9

Beyond the osteoconductive elements incorporation goal, another purpose was to attain the Ca/P ratio on the surface as close as possible to the theoretical natural hydroxyapatite (HAp) value of 1.67 [3, 4]. (Ca+Na)/P and Ca/P ratios are represented in Table VI.2. Although its Ca/P ratio was higher than the HAp value, Ta-CaP3 was the sample that presented a better commitment between morphological and chemical modification onto the Ta-anod7 surface.

Besides Ca and P, the incorporation of Mg is also desired. To investigate the effect of MgA in oxide morphology and ions incorporation (Ca, P and Mg), anodization procedures were performed using 0.18 M CaA, 0.12 M β-GP with different contents of MgA in DI water. Table VI.3 shows the new procedure parameters.

Table VI.3. Reverse polarization or/and anodization parameters for Ca, P and Mg incorporation onto nanostructured Ta substrates.

Sample	Approach	Voltage (V)	Duration (minutes)	Electrolyte
Ta-CaPMg1	Anodization	100	30	0.18 M CaA + 0.12 M β-GP + 0.1 M MgA
Ta-CaPMg2	Reverse polarization	20	20 s	
	Anodization	100	30	
Ta-CaPMg3	Anodization	80	30	
Ta-CaPMg4	Anodization	80	30	0.18 M CaA + 0.12 M β-GP + 0.08 M MgA
Ta-CaPMg5	Reverse polarization	20	20 s	
	Anodization	80	30	

For the same anodizing parameters (applied voltage and process duration), Ta-CaPMg1 and Ta-CaPMg2, the addition of Mg to the electrolyte showed a significant impact on morphology (Figure VI.3-A and B), since some agglomerates are observed on both surfaces. The morphology achieved for low potential was similar to the previous samples (Figure VI.3-C). With regard to less concentrated electrolyte, decreasing the MgA concentration to 0.08 M, Ta-CaPMg4 surface, no morphological changes were noticed (Figure VI.3-D) when compared with Ta-CaP3 (Figure VI.2-C). However, with the RP approach, Ta-CaPMg5 sample (Figure VI.3-E) resulted in a porous structure completely covered by spherical nanoparticles.

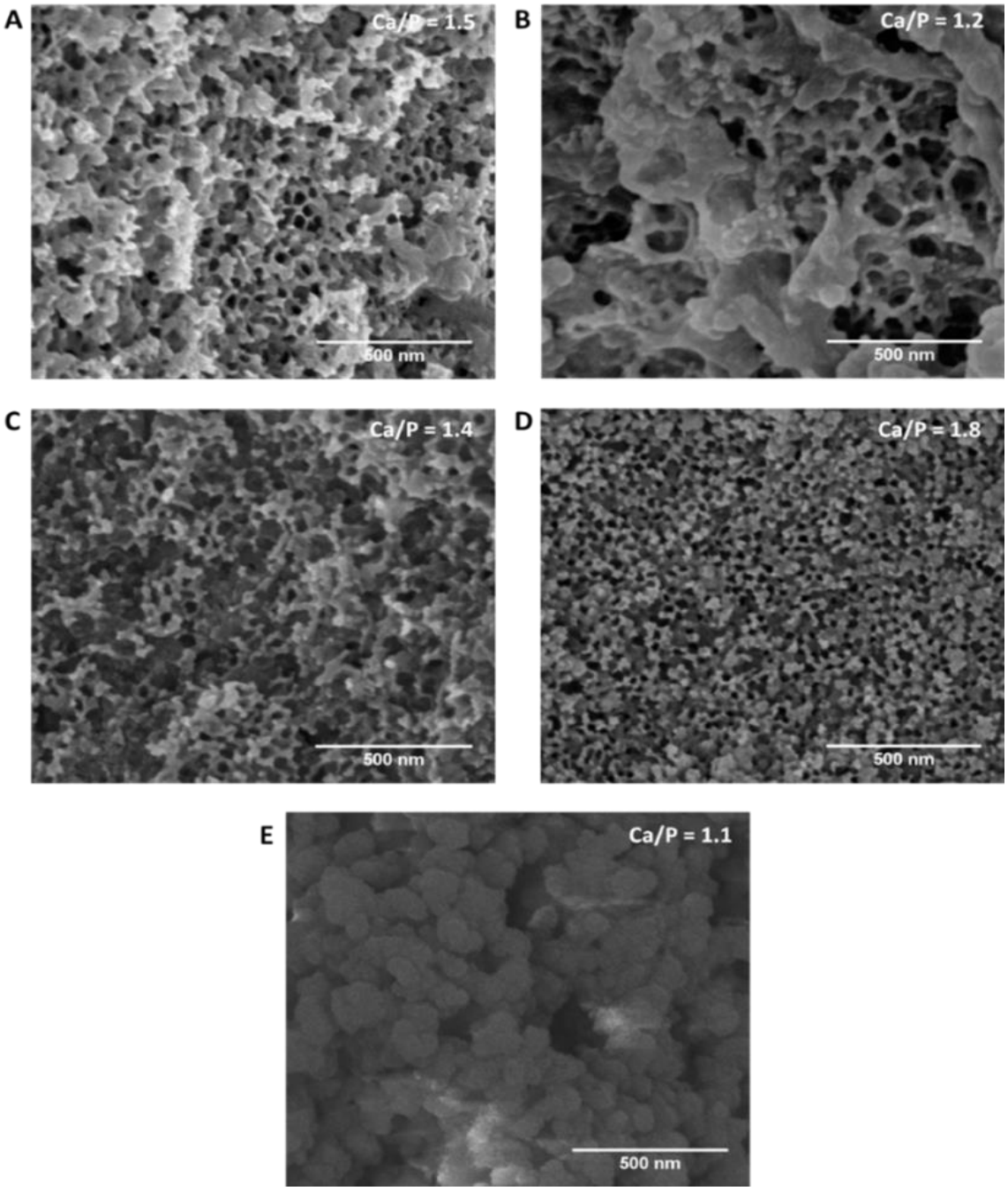

Figure VI.3. Top-views FEGSEM micrographs of Ta anodized samples with incorporation of Ca, P and Mg ions for different anodizing parameters: A) Ta-CaPMg1, B) Ta-CaPMg2, C) Ta-CaPMg3, D) Ta-CaPMg4 and E) Ta-CaPMg5. Corresponding Ca/P ratio is represented in each inset.

A surface with the osteoconductive elements was achieved in all samples (Table VI.4). Nonetheless, the chemical modification was affected due to the Mg incorporation consequently changing the Ca and P contents on the sample surfaces and (Ca+Na+Mg)/P and Ca/P ratios. Moreover, all samples presented Na in their chemical composition, being significantly high in the Ta-CaPMg5 sample. This last sample presented the highest ions' incorporation, and its porous structure was disguised by spherical nanoparticles that coalesced and covered the nanostructure (Figure VI.3-E). The authors Chen et. al [5] detected, after TiO_2 surfaces immersion on SBF, circular nanoparticles of CaP [14] that could be related to nucleation and growth of apatite (and/or HAp) [2, 6, 7]. In light to these results, it is highly probable that these spherical nanoparticles on the Ta-CaPMg5 surface could correspond to calcium phosphates (apatite) [8], although only the diffraction patterns ascribed to Ta were observed in the surface diffractogram (ANNEX III).

Table VI.4. Chemical composition of Ca, P, Na and Mg elements by EDS of Ta anodized samples, as well as (Ca+Na+Mg)/P and Ca/P ratios.

Sample	Chemical composition (at. %)				(Ca+Na+Mg)/P	Ca/P
	Ca	P	Na	Mg		
Ta-CaPMg1	6.0	4.0	4.6	2.8	3.4	1.5
Ta-CaPMg2	3.7	3.1	1.0	7.4	3.9	1.2
Ta-CaPMg3	5.1	3.6	4.6	2.6	3.4	1.4
Ta-CaPMg4	5.3	3.0	1.4	1.1	2.6	1.8
Ta-CaPMg5	6.2	5.5	5.6	7.4	3.5	1.1

The porous structure was formed, as observed in Figure V.6-C. Overall, the biofunctionalization by both approaches showed typically porous morphology (Figure VI.2 and Figure VI.3).

By anodization process with an electrolyte composed by CaA, β-GP and MgA it was possible to incorporate the osteoconductive elements Ca, P and Mg, respectively, on the nanostructured surface (Table VI.2 and Table VI.4). Cathodic polarization has been pointed out as responsible for the positive charged ions incorporation, namely Ca^{2+}, Mg^{2+} and Na^{+} [9, 10], on the anodic surface (Figure VI.4-A). On the other hand, during anodization negative charged ions are directed to the sample surface (Figure VI.4-B). Thus, it would be expected that combing RP with anodization, cations incorporation would be enhanced compared to the anodization approach. In fact, the RP approach promoted the incorporation of positive charged ions increasing (Ca+Na)/P, (Ca+Na+Mg)/P ratios (Table VI.2 and Table VI.4, respectively). The mechanism

for the cation's incorporation in conventional anodization (Ta surface as anode) is related with ion's diffusion, assisted by the electric field, through the electrolyte to the oxide layer.

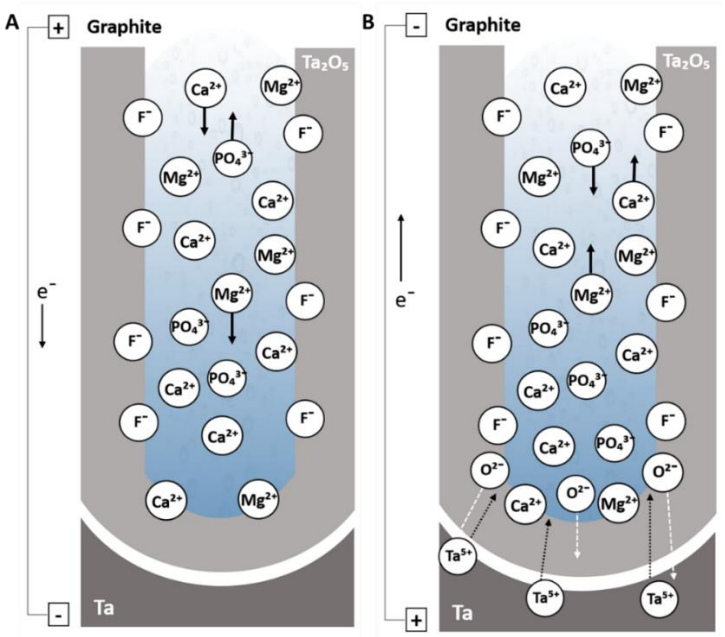

Figure VI.4. The schematic illustration of biofunctionalization mechanisms on Ta_2O_5 porous by A) cathodic polarization and B) anodization.

The ions content changed mainly with the electrolyte (composition and concentration) and the adopted approach (RP and/or anodization). Increasing β-GP concentration in the electrolyte mixture, in both approaches was observed that P content increased and promoted Ca incorporation. When Mg is presented on the electrolyte, the incorporation of cations (Ca^{2+} and Mg^{2+}) is competitive since a decrease on Ca incorporation was noticed whereas the Mg content on the surface increased. As it was already explained, the RP approach (Ta surface as cathode) clearly promoted the incorporation of cations (Ca^{2+}, Mg^{2+} and Na^{+}) in a competitive way. For instance, in most of the cases, the presence of Na became more noticeable on the anodic surface with Mg incorporation, compromising the Ca incorporation. It is important to highlight that Na^{+} ions came from β-GP ($C_3H_7Na_2O_6P{\cdot}5H_2O$).

As the purpose was to incorporate Ca, P and Mg ions achieving a Ca/P ratio more approximated to HAp without compromising the porous structure, samples Ta-CaP3 and Ta-CaPMg4 were chosen for further characterization.

6.3 Characterization of biofunctionalized Ta nanostructure

6.3.1 Structural and chemical analysis

XRD analysis was carried out in order to understand the evolution of the crystalline structure caused by the topographic/morphologic and chemical modifications on the Ta substrate. Figure VI.5 presents the

diffraction patterns for anodized Ta (Ta-anod7), and anodized Ta enriched with Ca and P (Ta-CaP3) and Mg (Ta-CaPMg4). The main crystalline phases identified were α-Ta: body-centered cubic (bcc) (ICDD card n. 00-004-0788) and β-Ta: tetragonal (ICDD card n. 00-025-1280), with a predominant α-Ta phase. It was evident that no changes on the crystalline structure was recorded for the chemical and morphological surfaces modification, as no evidence of crystalline Ta_2O_5 (ICDD car n. 01-025-0922) neither HAp (calcium phosphate) were noticed (ICDD card n. 00-055-0592). Firstly, anodized Ta_2O_5 only shows a crystalline structure when the surface is treated by annealing [11, 12] and thus the formed oxide layer was amorphous [13]. Calcium phosphate was not detected by XRD suggesting amorphous nature [14-17].

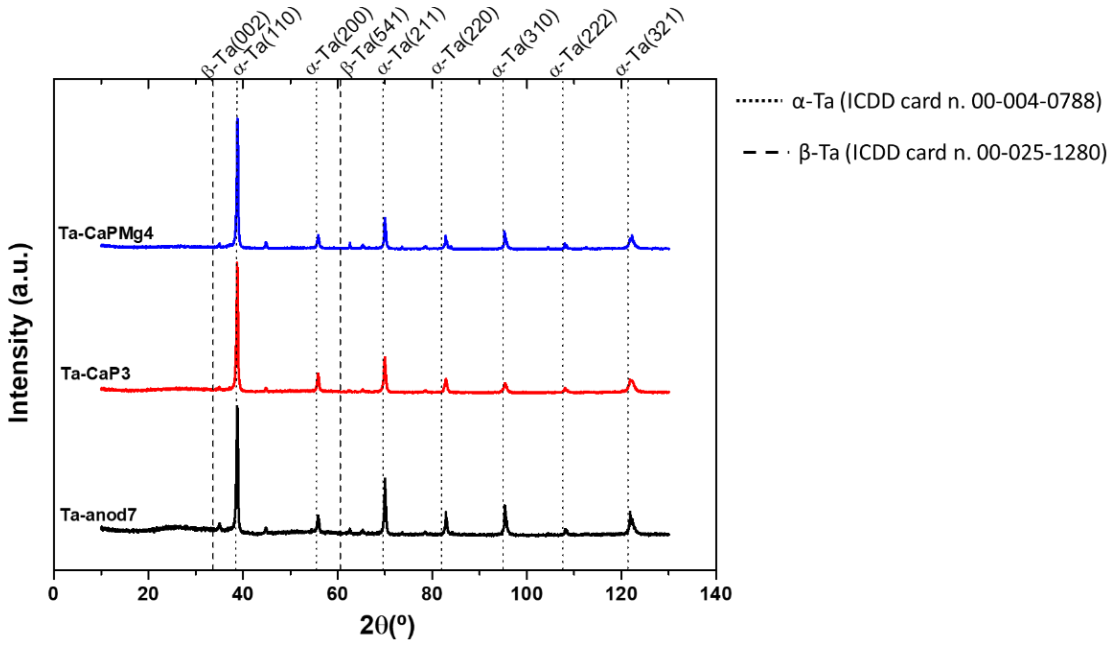

Figure VI.5. XRD patterns of Ta-anod7, Ta-CaP3 and Ta-CaPMg4 samples.

The binding states and quantification of chemical elements detected on biofunctionalized and/or nanostructured Ta surfaces were studied by XPS. With these purposes, individual spectra of each element detected were deconvoluted into their components using a product of Lorentzian-Gaussian functions. The effect of the electric charge was corrected by the reference of the C 1s peak at 285 eV and a Shirley background was used for electron background correction. The XPS individual spectra of the detected elements, as well as the information obtained from deconvolution with reference to the possible chemical compound assigned to it on Ta-anod7, Ta-CaP3 and Ta-CaPMg4 are displayed in Figure VI.6,Figure VI.7 and Figure VI.8, respectively.

After the first anodization (Ta-anod7 sample – nanostructured surface), Ta, O, C and F elements were detected by EDS (Figure V.8-B and Figure V.9-A) and XPS (Figure VI.6). First, Ta and O elements came from the Ta_2O_5 anodic layer. The fluoride species (F^- from the electrolyte) had the ability to dissolve the oxide layer to form pores or tubes, being adsorbed on the nanostructure. After the biofunctionalization

step, Ca, P were detected on Ta-CaP3 by EDS (Table VI.2) and XPS (Figure VI.7), and also Mg on Ta-CaPMg4 (Table VI.4 and Figure VI.8).

The possible chemical compounds formed on the Ta nanostructured surface were depicted by XPS analysis. On the porous structure (Ta-anod7), C 1s main peak deconvolution (Figure VI.6-A) had three peaks related to the carbon chemical states. The asymmetric peak at 285 eV corresponded to C-C bond [9], the peaks at 286.49 eV and 288.80 eV could be related to C-O and C=O bonds, respectively, which can be assigned to a very thin contamination layer. Similar anodization process was carried out on Ti substrates and these last peaks were associated to the hydroxyl group (C-OH) and carboxyl groups (O=C-OH) [18]. The deconvolution of Ta 4f (Figure VI.6-C) displayed the correspondent doublet with Ta $4f_{7/2}$ at 26.48 eV (Ta $4f_{5/2}$ at 28.38 eV) related to the Ta^{5+} state from Ta_2O_5 [19-21], having a spin orbital splitting of 1.9 eV, in agreement with the literature [20]. It was confirmed by O 1s deconvoluted spectrum (Figure VI.6-B) with the peak at 530.55 eV [22] indicating the main contribution was coming from Ta_2O_5. In addition, the other two O 1s peaks at 531.69 eV and 532.81 eV could support the presence of hydroxyl and carboxyl groups, respectively [9]. Moreover, Figure VI.6-D depicts the F 1s spectrum with a single peak at 684.68 eV which could be assigned as the adsorbed fluoride ions on Ta_2O_5 [9, 18], incorporated into the anodic layer due to the dissolution assisted by electric field.

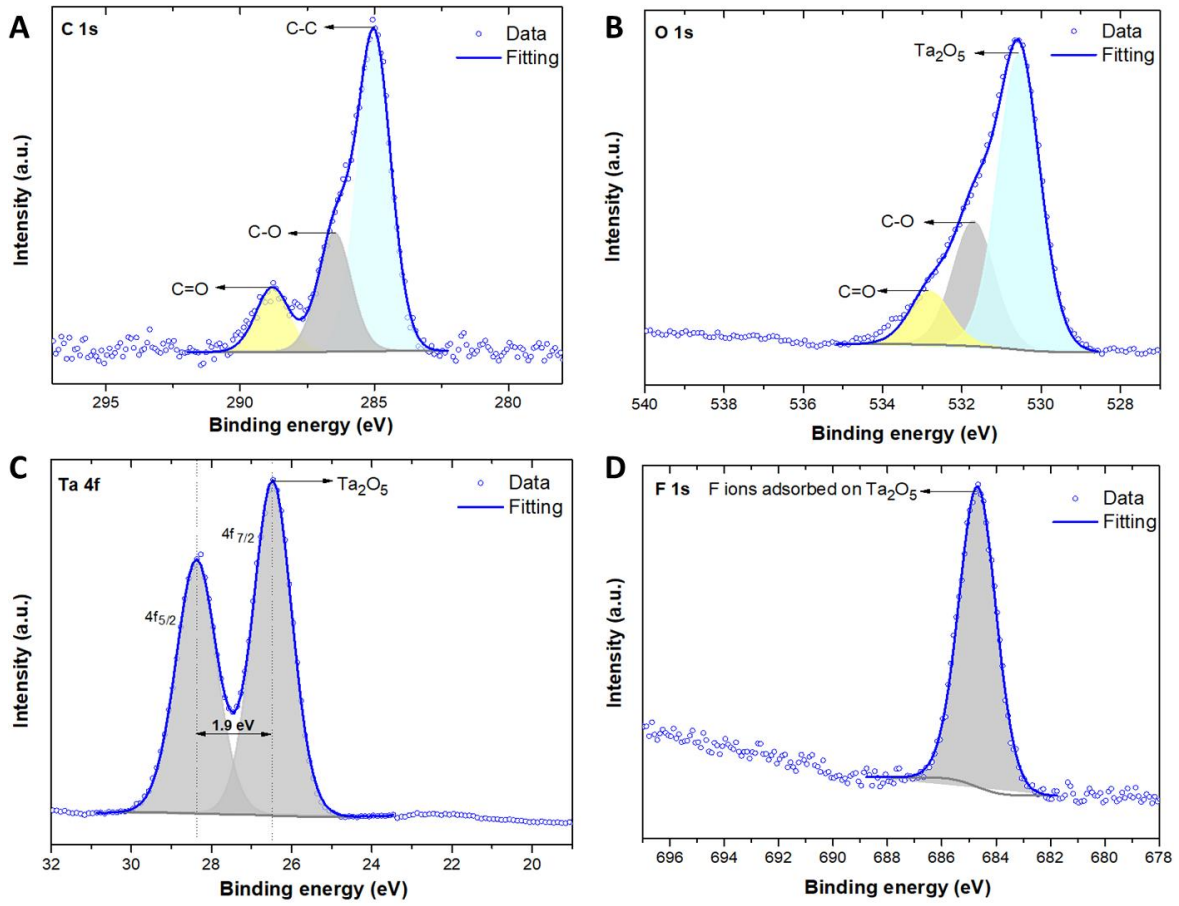

Figure VI.6. XPS spectra of deconvoluted A) C 1s, B) O 1s, C) Ta 4f and D) F 1s elements detected on Ta-anod7 surface.

Figure VI.7 shows the XPS spectra of the biofunctionalized Ta-CaP3 surface sample, only for new findings. Indeed, the incorporation of Ca and P elements can induce the surface biofunctionalization. C 1s spectrum (Figure VI.7-A) exhibits three peaks at 285 eV (C-C), 286.74 eV (C-O), 288.44 eV (C=O), binding energies as previously discussed, and a new peak at 289.25 eV which could correspond to $CaCO_3$ [23-25]. The O 1s, Ca $2p_{3/2}$ and Ca $2p_{1/2}$ core levels for $CaCO_3$ were found at 532.58 eV (Figure VI.7-B), 347.62 eV and 351.12 eV (Figure VI.7-C), with a spin-orbit splitting of 3.5 eV, respectively [25, 26]. The Ca $2p_{3/2}$ doublet peaks at 348.08 eV (Ca $2p_{1/2}$ at 351.58 eV) suggested the Ca was on the second stage of oxidation (Ca^{2+}) [27] that could be assigned to $Ca_3(PO_4)_2$ (Figure VI.7-D). The P $2p_{3/2}$ doublet at 133.48 eV and P $2p_{1/2}$ at 134.35 eV [26], with a spin-orbit splitting of 0.87 eV [28], Figure VI.7-D, could confirm this assessment. Furthermore, the O 1s binding energy at 531.59 eV corroborating the presence of $Ca_3(PO_4)_2$ [25, 26].

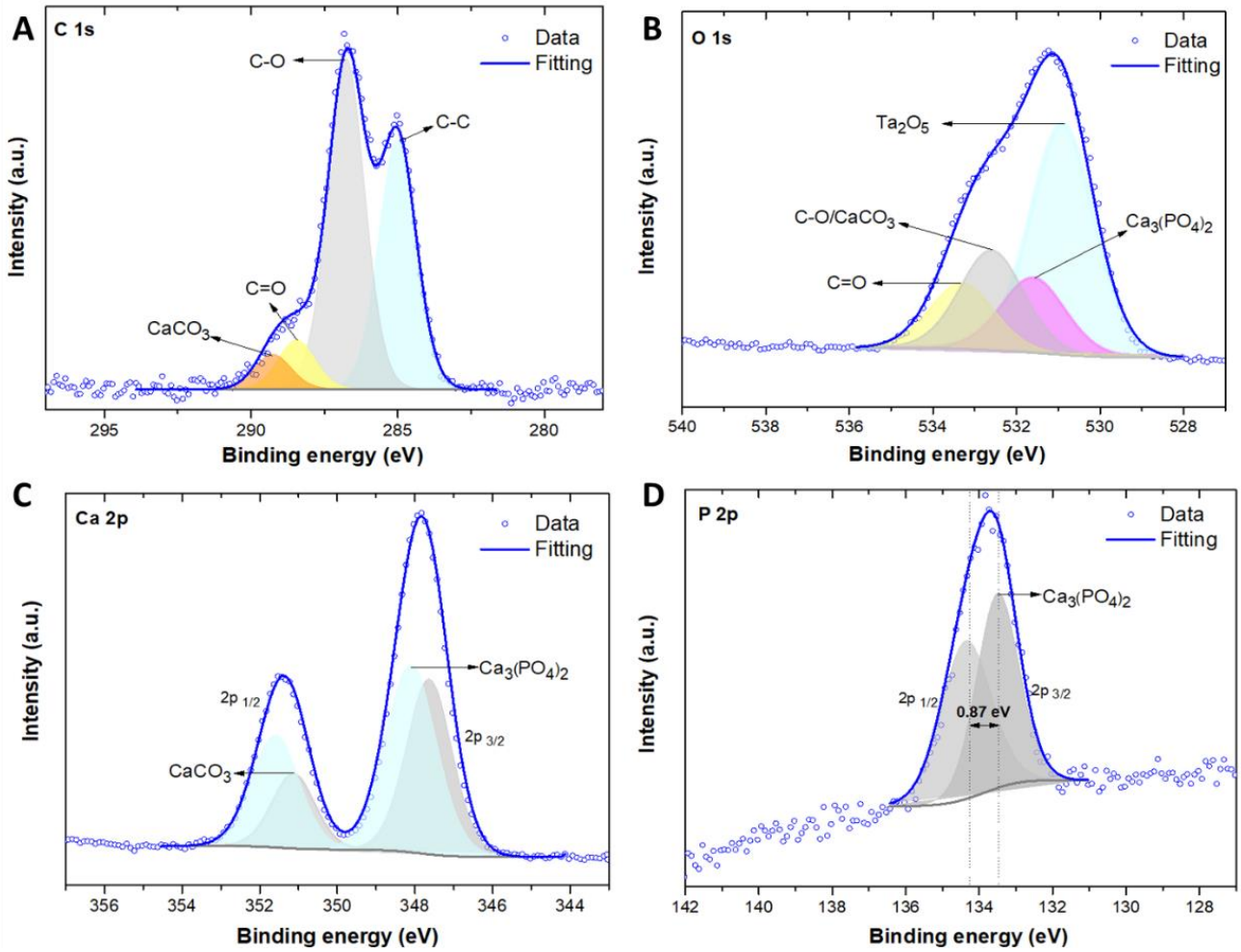

Figure VI.7. XPS spectra of deconvoluted A) C 1s, B) O 1s, C) Ca 2p and D) P 2p elements detected on Ta-CaP3 surface.

With addition of Mg specie to the chemical composition (Ta-CaPMg4 sample), the XPS analysis was similar to the previous one (Ta-CaP3). As a new finding, Mg 1s spectrum had the main peak at 1304.02

eV (Figure VI.8-B) which could be related to the MgO component [29], which was supported by O 1s spectrum with a new peak at 532.89 eV binding energy (Figure VI.8-A) [30, 31].

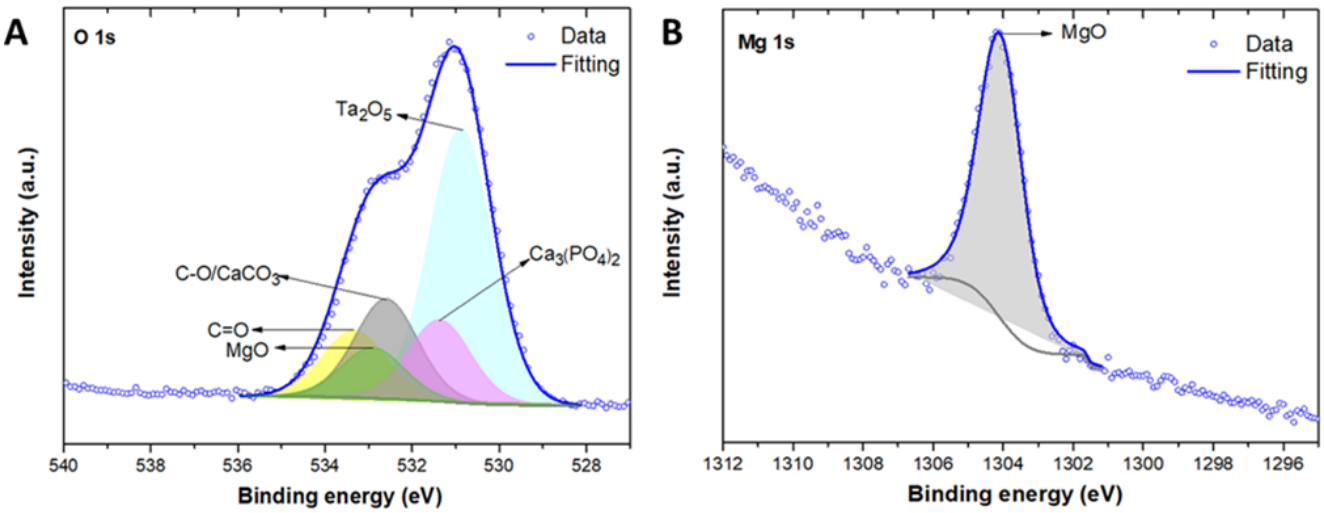

Figure VI.8. XPS spectra of deconvoluted A) O 1s and B) Mg 1s elements detected on Ta-CaPMg4 surface.

Moreover, in Ta 4f spectra (Figure VI.6-C), any peak at 27.8 eV [32] related to TaF_5 was detected [33]. Also the peak at 24.8-25.8 eV corresponding to sodium tantalate [34] was also not detected, even though no evidence of Na on Ta-CaP3 neither Ta-CaPMg4 surveys was recorded. As Na presence was only detected by EDS, this can mean that this element is not in the top surface, but deeper.

Chemical composition of each biofunctionalized surface obtained by XPS is represented in Table VI.5. The amount of Ca, P and Mg were calculated from the corresponding peak areas divided by the appropriated relative sensitivity factors (2.62 for Mg, 0.486 for P and 1.83 for Ca). The ratio of calcium to phosphorous, Ca/P, estimated by XPS is also included. The Ca/P ratio of sample Ta-CaP3 is 2.0, higher than the stochiometric HAp ratio, but with Mg addition to the anodic layer (nanostructured surface) the ratio decreased to 1.4, due to competitive incorporation between Ca^{2+} and Mg^{2+}. These ratios clearly could be associated with the amorphous tricalcium phosphate (ATP: $Ca_3(PO_4)_2$) with a Ca/P ratio around 1.5 [3, 25, 26] which is in agreement with the XPS results. This ATP can be considered as a potential agent in remineralization for dental applications [35].

Table VI.5. Chemical composition of biofunctionalized samples Ta-CaP3 and Ta-CaPMg4 obtained from XPS analysis.

Sample	Chemical composition (at. %)			Ca/P
	Ca 2p	P 2p	Mg 2p	
Ta-CaP3	15.1	7.5	-	2.0
Ta-CaPMg4	13.5	9.6	4.9	1.4

XPS sputtering was performed on both biofunctionalized samples in order to understand the chemical composition distribution with depth. Figure VI.9 shows the surface concentration of Ta 4f, O 1s, F 1s, Ca 2p and P 2p trend, Ta-CaP3 (Figure VI.9-A), and also Mg 2p, Ta-CaPMg7 (Figure VI.9-B), for three etching times (0, 120 and 600 seconds). Concentration of O on the surface decreased with time in contrast to an increasing Ta concentration. F and Ca concentration did not present a significant variation with depth whereas Mg and P decreased with sputter time. The composition of the elements obtained after XPS sputtering of biofunctionalized surfaces (Figure VI.9) demonstrated first that a certain amount of F could be detected throughout the oxide layer [32] as well as Ca. On the other hand, Mg content slightly decreased but P almost disappear, indicating that all osteoconductive elements were incorporated in the porous structure, except P which was mostly detected on top surface. Consequently, calcium phosphates may be present on top surface and calcium carbonates deeper.

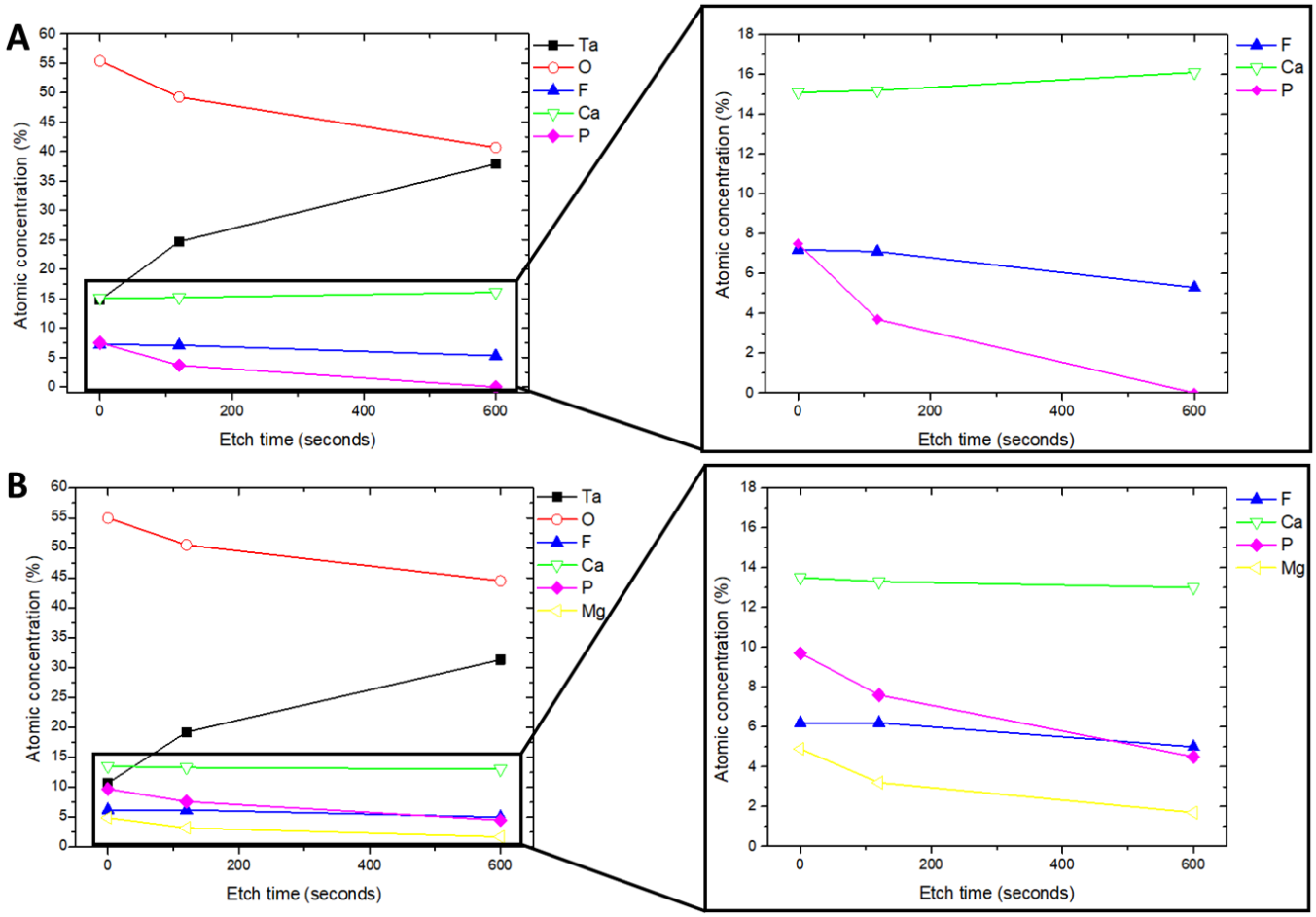

Figure VI.9. XPS depth-profile of nanostructured Ta_2O_5 biofunctionalized by the incorporation of A) Ca and P, Ta-CaP3 sample and B) Ca, P and Mg, Ta-CaPMg4 sample.

6.3.2 Wettability and roughness assessment

Wettability is an important surface property of biomaterials that can greatly influence cell behavior at the biomaterial-host interface. This analysis followed the Van Oss approach [36] to characterize the

hydrophilicity or hydrophobicity of samples surfaces. According to that, Van Oss considered that a surface with a contact angle above 65° is hydrophobic and, consequently, below this value is hydrophilic.

The wettability measurement essays are displayed in Figure VI.10. The contact angles measured for Ta was 69 ± 4°, indicating, according to Vogler [37], that the surface showed a moderate hydrophobic character. With the pre-surface treatment the contact angle value decreases slightly to 56 ± 2° and the surface became hydrophilic. After anodization, the hydrophilicity of the surface was enhanced as shown by the significant decrease in the water contact angle (11 ± 2°). With the incorporation of bioactive agents, the θ_w increased slightly for both Ta-CaP3 and Ta-CaPMg4 surfaces: 19 ± 4° and 14. ± 1°, respectively.

The roughness values, Sa and Sq, are displayed in Figure VI.10 and Table VI.6. Once the surface pre-treatment (polishing and electropolishing) had as goal the uniformization of the Ta surface, Ta-pol presented a significantly lower values of Sa and Sq than Ta (Ta sheet), as expected. Overall, rougher surfaces were developed by anodization process, more pronounced for biofunctionalized samples (with the incorporation of bioactive agents). This roughness increment can be related to the spherical nanoparticles [8].

The relationship between surface wettability and roughness for each morphological and chemical treatment is represented in Figure VI.10. It was evident that after anodization, with and without biofunctionalization, the surface became rougher while hydrophilicity behavior increased significantly.

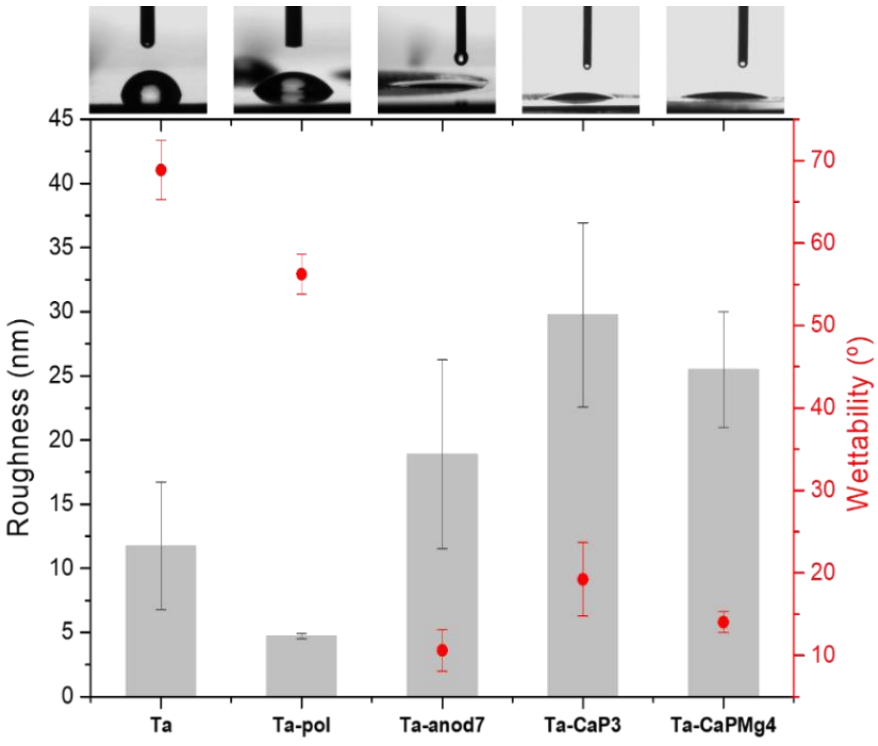

Figure VI.10. Relationship between roughness (column plot) and wettability (scatter plot) for each surface modification, with each wetting behavior in view on Lilli-Q ultrapure water.

Table VI.6. Average and root mean square roughness of the Ta, Ta-pol, Ta-anod7, Ta-CaP3 and Ta-CaPMg4 surfaces.

Sample	Roughness ± SD (nm)	
	Sa	Sq
Ta	11.8 ± 5.0	15.1 ± 6.0
Ta-pol	4.7 ± 0.2	5.7 ± 0.1
Ta-anod7	18.9 ± 7.4	23.0 ± 8.8
Ta-CaP3	29.8 ± 7.2	38.9 ± 8.1
Ta-CaPMg4	25.5 ± 4.7	27.9 ± 6.4

Surface wettability is influenced by the surface roughness and chemistry. In the present work, the hydrophilicity was achieved by mechanical and electrochemical polishing and enhanced by anodization treatment and biofunctionalization. As observed by the photos of sessile test measurements (Figure VI.10-top), water drops completely spread when reached the surface, for the three anodized samples (with and without biofunctionalization), recording contact angles near the superhydrophilicity limit, θ_w <10° [38, 39]. The hydrophilic surface behavior could be attributed to presence of OH^- groups adsorbed on surfaces [9, 40] once these hydroxyl groups were identified on XPS O 1s spectra (Figure VI.6-B, Figure VI.7-B and Figure VI.8-A). Moreover, a higher surface roughness presented a lower water contact angle (higher hydrophilicity), Figure VI.10, due to the strong capillary adsorption effect [13], enhanced by the surface roughness [38]. According to several studies, nano-scale topography improved surface wettability [38, 41, 42], and the surfaces can have more electron-acceptor sites to encourage osteoblasts [43]. These topographic and hydrophilic features enhance the cell-material interaction [6, 39, 40, 44], and therefore, combining a nanostructured surface and a hydrophilic behavior, protein adsorption can be improved such as to induce an early blood coagulation [39]. In addition, higher surface hydrophilicity can stimulate hard and soft tissues integration with the implant, accelerating the healing and early osseointegration. However, the optimal degree of hydrophilicity for best biological and clinical outcomes remains unclear, mostly regarding superhydrophilicity favored by several hydrophilic implant systems [45]. Controversially, a moderate hydrophobic behavior was reported as a condition for an optimal cell adhesion [40], although *in vivo* studies failed to demonstrated higher osseointegration using hydrophobic surfaces implants [6]. Hence, nowadays, there is still no agreement regarding the surface wettability in the enhancement of osseointegration.

6.3.3 Oxide structure and thickness

In order to study the morphology of the produced anodic layer, the cross-section of the samples Ta-anod7 and Ta-CaPMg4 were analyzed (Figure VI.11). The anodic nanostructure layer consists in multiple thin and porous layers instead of a columnar structure with pores. Moreover, the thickness of the anodic layer of Ta-anod7 sample was around 5.3 µm (Figure VI.11-A) which, according to literature, fits in the range 4-16 µm of Ta porous layer thickness under different electrochemical conditions using electrolytes with NH_4F [46]. However, Ta-CaPMg4 surface thickness is around 2.3 µm (Figure VI.11-C). This difference in the oxide thickness can be related to the loss of thin anodic layers during biofunctionalization procedure in an aqueous electrolyte. Identical multiple layers morphology were obtained by Ta anodization for 120 minutes in 1 M H_2SO_4 and 3.3 wt.% NH_4F at 20 V, showing that every layer exhibited a closed bottom, but no further explanation was discussed [38]. In literature, multiple thin discontinuous porous layers on Ta substrate formed by one-step anodization have been associated with the requirement of a lower water content (or a higher fluoride concentration) in the electrolyte to achieve this morphology [46]. H. Yu *et al.* [47] reported a coral-like nanoporous structure formation of sensitive water-content, which was only obtained when the dissolution rate was not enough to form pores/ pits on the surface indicating a concentration of fluoride ions. However, for Ti-based materials, it was demonstrated that a minimum content of water in EG electrolyte was necessary to obtain a well-ordered titania nanostructure, which should not exceed a critical limit, otherwise the local pH condition was affected and formation of ridges on the ordered nanostructure were present [48]. Apart from the electrolyte concentration, formation of thin oxide Ta multilayers could be related to higher potentials and a high dissolution current [32]. When the applied voltage is too high, loosely-connected layers are formed [46].

As previously discussed in CHAPTER V, the current density-time curve recorded - Figure V.3-A (or B) - does not exhibit neither a typical behaviour nor typical values (higher than literature). The voltage (current) oscillatory behaviors during anodization in the case of Ti or Si have been attributed to a cyclic process of growth and detachment of anodic oxides forming a stack of oxide layers [49, 50]. For Si, the mechanism proposed for layer detachment is based on accumulation of mechanical stress at the oxide/Si interface that further triggers isotropic etching of multiple pores. For Ti anodization, they were ascribed to periodical undermining of the ordered nanotubular layer when the voltage exceeded certain values. Moreover, stress effects related to the mismatch of the oxide and substrate, which could lead to cracking at the metal/oxide interface, were previously reported in Ta anodization [32]. In fact, in the present study, a previous oxide layer was formed as pre-treatment (Figure V.2-C) and, in this way, anodization-starting point had already oxidized the surface with similar properties. Thus, it is not completely evident that this stress mismatch

effect in the interface is the main factor for the delamination process because the layer stacking is still observed in the sample anodized after pre-treatment.

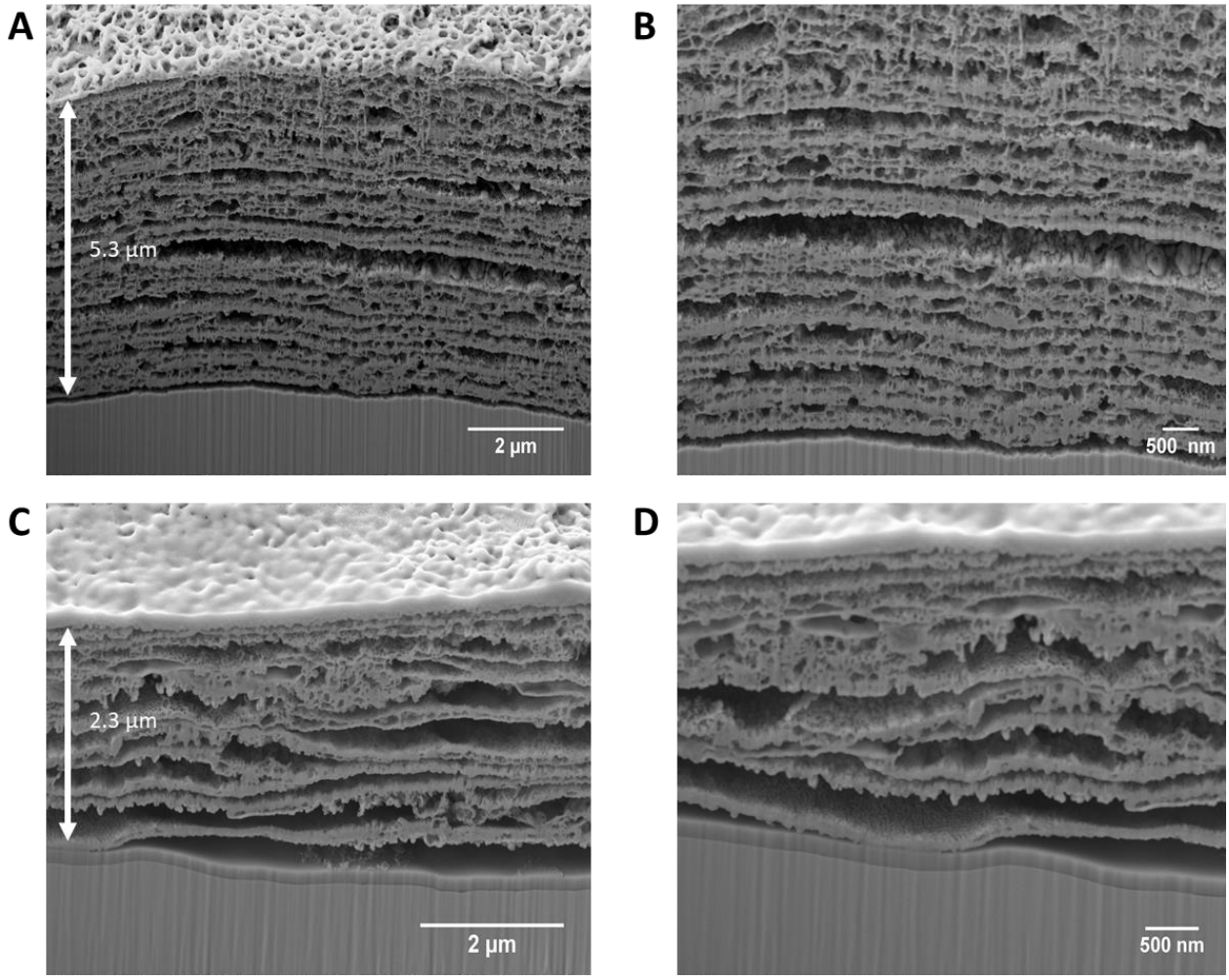

Figure VI.11. SEM images of the FIB cross-sections of Ta-anod7 and Ta-CaPMg4 sample at A) and C) lower and with B) and D) higher magnification, respectively.

Apart from the multiple thin anodic layers (Figure VI.11), a continuous interface between Ta substrate and the anodic layer is clearly observed. This is likely to be a hollow space, indicating a lift-off of the anodic layer from the substrate. Similar interface was reported in Ti anodization, which had a hollow space between Ti and titania ordered nanostructure [10]. A mechanism has been proposed for anodic layer detachment in Ti anodization, namely water assisted dissolution of the fluoride-rich layer in the interface of metal/oxide. It has been widely accepted that this layer, enriched with fluoride formation, can be ascribed to the twice migration rate of F^- comparing with O^{2-} ions for aqueous electrolytes [51]. Thus, the interfacial hollow space could be related to the dissolution of the fluoride-rich layer after immersion in containing-water solutions [10], for instance during the rinsing of the samples with distilled water. Likewise, a tantalum-fluoride complex could be formed (Eq. IV.2) [52], resulting in the build-up of a fluoride-rich layer (likely TaF_5) at Ta/ Ta_2O_5 interface which could cause the detachment of the anodic layer form the Ta surface [53, 54].

The observed layering effect is surprisingly similar with that of regular oscillations of anodic potential during Si anodization in very diluted HF [55]. The periodic formation of porous layers and their lift-off from the substrate was explained, in terms of periodic change of intensity and anisotropy of electrochemical dissolution reaction and accumulation of mechanical stress within growing Ta_2O_5 layer. The layering of the growing film might be associated with fluctuations of local current density at the pore bottoms related to the accumulation and release of gas bubbles from the surface of the sample. The gas bubbles growing at the surface, mask part of the surface, preventing the increase or even reducing the local current density. When the bubble leaves the surface, current density in the pores jumps back to steady-state level with a simultaneous change of the intensity of electrochemical reactions contributing to the formation of a porous layer. The accumulation of gas bubbles at the pores can develop a very high internal pressure, which is able to provoke a collapse of the porous layer and trigger the lift-off of the mechanically stressed Ta_2O_5 oxide layer.

Therefore, the most reliably possible explanation must be related to the gas formation and evolution as the main mechanism responsible for triggering the layer's delamination and especially for the gaps between them, due to the high internal gas pressure developed.

The morphological and topographic features of the surface play a crucial role in the implant-tissue interaction and consequently in osseointegration [4]. The natural bone tissue shows a non-uniform porosity due to the existence of cortical (compact) and trabecular bones (porous). Also, bone tissue responses are mostly determined by processes controlled at the nanoscale level [56]. Although the bone chemical composition was mimicked, the bone-like structure was not achieved due to the thin and porous multi-layers morphology makes these surfaces unsuitable for biomedical applications, in particular for dental implant surfaces.

6.4 Partial Conclusions

The current study was concerned with the biofunctionalization of Ta_2O_5 porous structure in containing Ca, P and Mg ions electrolytes by RP and/ or anodization under different limiting voltages. The aim was to find suitable anodizing conditions to incorporate these osteoconductive elements without compromising the porous bone-like structure achieved by the first anodization step. The obtained results can be detailed as following:

- Micro/nano-porous structure similar to bone morphology was formed by anodization using an acid-free fluoride-containing electrolyte;
- Surfaces enriched with Ca, P and Mg was attained using RP followed anodization and only anodization, promoting formation of an amorphous tricalcium phosphate (ATP: $Ca_3(PO_4)_2$);

- RP approach enhanced positive charged ions (Ca^{2+}, Mg^{2+} and Na^{+}) incorporation;
- Formation of amorphous calcium phosphates was observed on biofunctionalized surfaces, and the Mg addition brought the Ca/P ratio close to the stochiometric HAp theoretical value;
- Decrease of roughness and the water contact angle were achieved by mechanical and electrochemical polishing;
- Anodization treatment and biofunctionalization lead to a strongly increase of both roughness and hydrophilicity.

All these surface characteristics achieved have potential for remineralization of dental implants and consequently to promote osseointegration process. However, FIB/SEM cross-sectional images revealed a multi-layered structure, consisting in a stacking of thin porous layers, due to the accumulation of gas bubbles at the pores that develop very high internal pressure and which are able to provoke a collapse of the porous layer and trigger the lift-off of the mechanically stressed Ta_2O_5 oxide layer. Thus, this approach was not appropriate to mimic the bone structure and consequently the samples are not reliable options for biomedical applications. Therefore, an alternative methodology had to be adopted.

6.5 References

[1] U. K. Nandeesh and N. B, "Physiology of Bone Formation, Remodeling, and Metabolism." vol. 9783642024, ed, 2012, pp. 1-1046.

[2] H. Pan, X. Zhao, B. W. Darvell, and W. W. Lu, "Apatite-formation ability - Predictor of "bioactivity"?," *Acta Biomaterialia,* vol. 6, pp. 4181-4188, 2010.

[3] B. Wopenka and J. D. Pasteris, "A mineralogical perspective on the apatite in bone," *Materials Science and Engineering C,* vol. 25, pp. 131-143, 2005.

[4] C. Wang, F. Wang, and Y. Han, "The structure, bond strength and apatite-inducing ability of micro-arc oxidized tantalum and their response to annealing," *Applied Surface Science,* vol. 361, pp. 190-198, 2016.

[5] J. Chen, Z. Zhang, J. Ouyang, X. Chen, and Z. Xu, "Bioactivity and osteogenic cell response of TiO2 nanotubes coupled with nanoscale calcium phosphate via ultrasonification-assisted electrochemical deposition," *Applied Surface Science,* vol. 305, pp. 24-32, 2014.

[6] L. Le Guéhennec, A. Soueidan, P. Layrolle, and Y. Amouriq, "Surface treatments of titanium dental implants for rapid osseointegration," *Dental Materials,* vol. 23, pp. 844-854, 2007.

[7] T. Miyazaki, H. M. Kim, T. Kokubo, C. Ohtsuki, H. Kato, and T. Nakamura, "Mechanism of bonelike apatite formation on bioactive tantalum metal in a simulated body fluid," *Biomaterials,* vol. 23, pp. 827-832, 2002.

[8] X. Chen, A. Nouri, Y. Li, J. Lin, P. D. Hodgson, and C. Wen, "Effect of Surface Roughness of Ti , Zr , and TiZr on Apatite Precipitation From Simulated Body Fluid," *Biotechnology and Bioengineering,* vol. 101, pp. 378-387, 2008.

[9] S. A. Alves, S. B. Patel, C. Sukotjo, M. T. Mathew, P. N. Filho, J. P. Celis*, et al.*, "Synthesis of calcium-phosphorous doped TiO2 nanotubes by anodization and reverse polarization: A

promising strategy for an efficient biofunctional implant surface," *Applied Surface Science,* vol. 399, pp. 682-701, 2017.

[10] S. A. Alves, A. L. Rossi, A. R. Ribeiro, J. Werckmann, J. P. Celis, L. A. Rocha*, et al.*, "A first insight on the bio-functionalization mechanisms of TiO2 nanotubes with calcium, phosphorous and zinc by reverse polarization anodization," *Surface and Coatings Technology,* vol. 324, pp. 153-166, 2017.

[11] Y. Kado, R. Hahn, C. Y. Lee, and P. Schmuki, "Strongly enhanced photocurrent response for Na doped Ta3N5-nano porous structure," *Electrochemistry Communications,* vol. 17, pp. 67-70, 2012.

[12] R. V. Gonçalves, P. Migowski, H. Wender, D. Eberhardt, D. E. Weibel, F. C. Sonaglio*, et al.*, "Ta2O5 nanotubes obtained by anodization: Effect of thermal treatment on the photocatalytic activity for hydrogen production," *Journal of Physical Chemistry C,* vol. 116, pp. 14022-14030, 2012.

[13] W. Chen, Q. Tu, H. Wu, C. Zhao, X. Yao, W. Fan*, et al.*, "Study on morphology evolution of anodic tantalum oxide films in different using stages of H2SO4/HF electrolyte," *Electrochimica Acta,* vol. 236, pp. 140-153, 2017.

[14] F. G. Oliveira, A. R. Ribeiro, G. Perez, B. S. Archanjo, C. P. Gouvea, J. R. Araújo*, et al.*, "Understanding growth mechanisms and tribocorrosion behaviour of porous TiO 2 anodic films containing calcium , phosphorous and magnesium," *Applied Surface Science,* vol. 341, pp. 1-12, 2018.

[15] A. C. Alves, F. Oliveira, F. Wenger, P. Ponthiaux, J. P. Celis, and L. A. Rocha, "Tribocorrosion behaviour of anodic treated titanium surfaces intended for dental implants," *J. Phys. D: Appl. Phys.,* vol. 46, pp. 404001-9, 2013.

[16] D. Wei, Y. Zhou, and C. Yang, "Structure, cell response and biomimetic apatite induction of gradient TiO2 -based / nano-scale hydrophilic amorphous titanium oxide containing Ca composite coatings before and after crystallization," *Colloids and Surfaces B : Biointerfaces,* vol. 74, pp. 230-237, 2009.

[17] T. Kokubo, H.-m. Kim, and M. Kawashita, "Novel bioactive materials with different mechanical properties," *Biomaterials,* vol. 24, pp. 2161-2175, 2003.

[18] S. C. Han, J. M. Doh, J. K. Yoon, G. H. Kim, J. Y. Byun, S. H. Han*, et al.*, "Highly Ordered Self-Organized TiO2 Nanotube Arrays Prepared by a Multi-Step Anodic Oxidation Process," vol. 15, pp. 493-499, 2009.

[19] J. Y. Zhang and I. W. Boyd, "Thin tantalum and tantalum oxide films grown by pulsed laser deposition," *Applied Surface Science,* vol. 168, pp. 234-238, 2000.

[20] P. M. Ranjith, M. T. Rao, S. Sapra, I. I. Suni, and R. Srinivasan, "On the Anodic Dissolution of Tantalum and Niobium in Hydrofluoric Acid," *Journal of The Electrochemical Society,* vol. 165, pp. C258-C269, 2018.

[21] R. Simpson, R. G. White, J. F. Watts, and M. A. Baker, "XPS investigation of monatomic and cluster argon ion sputtering of tantalum pentoxide," *Applied Surface Science,* vol. 405, pp. 79-87, 2017.

[22] Y. Masuda, S. Wakamatsu, and K. Koumoto, "Site-selective deposition and micropatterning of tantalum oxide thin films using a monolayer," *Journal of the European Ceramic Society,* vol. 24, pp. 301-307, 2004.

[23] G. C. Gomes, F. F. Borghi, R. O. Ospina, E. O. López, F. O. Borges, and A. Mello, "Nd:YAG (532 nm) pulsed laser deposition produces crystalline hydroxyapatite thin coatings at room temperature," *Surface and Coatings Technology,* vol. 329, pp. 174-183, 2017.

[24] Y. Tsutsumi, D. Nishimura, H. Doi, N. Nomura, and T. Hanawa, "Difference in surface reactions between titanium and zirconium in Hanks' solution to elucidate mechanism of calcium phosphate formation on titanium using XPS and cathodic polarization," *Materials Science and Engineering C,* vol. 29, pp. 1702-1708, 2009.

[25] M. Sowa, M. Woszczak, A. Kazek-Kęsik, G. Dercz, D. M. Korotin, I. S. Zhidkov*, et al.*, "Influence of process parameters on plasma electrolytic surface treatment of tantalum for biomedical applications," *Applied Surface Science,* vol. 407, pp. 52-63, 2017.

[26] B. Demri and D. Muster, "XPS study of some calcium compounds," *Journal of Materials Processing Tech.,* vol. 55, pp. 311-314, 1995.

[27] K. Rokosz, T. Hryniewicz, P. Chapon, S. Raaen, and H. R. Z. Sandim, "XPS and GDOES characterization of porous coating enriched with copper and calcium obtained on tantalum via plasma electrolytic oxidation," *Journal of Spectroscopy,* vol. 2016, 2016.

[28] M. R. Vilar, A. M. Botelho, A. M. Ferraria, Y. Jugnet, D. Peled, and R. Naaman, "Interaction of Self-Assembled Monolayers of DNA with Electrons : HREELS and XPS Studies," *Journal of Physical Chemistry B,* vol. 112, pp. 6957-6964, 2008.

[29] H. Seyama and M. Soma, "X-ray photoelectron spectroscopic study of montmorillonite containing exchangeable divalent cations," *Journal of the Chemical Society, Faraday Transactions 1: Physical Chemistry in Condensed Phases,* vol. 80, pp. 237-248, 1984.

[30] Y. Rao, W. Wang, F. Tan, Y. Cai, J. Lu, and X. Qiao, "Influence of different ions doping on the antibacterial properties of MgO nanopowders," *Applied Surface Science,* vol. 284, pp. 726-731, 2013.

[31] S. Ardizzone, C. L. Bianchi, M. Fadoni, and B. Vercelli, "Magnesium salts and oxide : an XPS overview," *Applied Surface Science,* vol. 119, pp. 253-259, 1997.

[32] I. V. Sieber and P. Schmuki, "Porous Tantalum Oxide Prepared by Electrochemical Anodic Oxidation," *Journal of The Electrochemical Society,* vol. 152, pp. C639-C639, 2005.

[33] H. A. El-Sayed, C. A. Horwood, A. D. Abhayawardhana, and V. I. Birss, "New insights into the initial stages of Ta oxide nanotube formation on polycrystalline Ta electrodes," *Nanoscale,* vol. 5, pp. 1494-1498, 2013.

[34] H. Langhuan, C. Qizhong, Z. Bin, W. U. Xiaojing, G. A. O. Peng, and J. Zibin, "Preparation of Sodium Tantalate with Different Structures and Its Photocatalytic Activity for H 2 Evolution from Water Splitting," *Chinese Journal of Catalysis,* vol. 32, pp. 3-8, 2011.

[35] J. Zhao, Y. Liu, W.-b. Sun, and H. Zhang, "Amorphous calcium phosphate and its application in dentistry," *Chemistry Central Journal,* vol. 5, pp. 40-40, 2011.

[36] C. J. Van Oss, R. J. Good, and M. K. Chaudhury, "The role of van der Waals forces and hydrogen bonds in hydrophobic interactions between biopolymers and low energy surfaces," *J. Colloid Interface Sci.,* vol. 111, pp. 378-390, 1986.

[37] E. A. Vogler, "Structure and reactivity of water at biomaterial surfaces, Adv," *Coll. Interf. Sci.,* vol. 74, pp. 69-117, 1998.

[38] S. Minagar, C. C. Berndt, and C. Wen, "Fabrication and characterization of nanoporous niobia, and nanotubular tantala, titania and zirconia via anodization," *Journal of Functional Biomaterials,* vol. 6, pp. 153-170, 2015.

[39] B. S. Kopf, S. Ruch, S. Berner, N. D. Spencer, and K. Maniura-weber, "The role of nanostructures and hydrophilicity in osseointegration : In-vitro protein-adsorption and blood-interaction studies," pp. 2661-2672, 2015.

[40] L. Bacakova, E. Filova, M. Parizek, T. Ruml, and V. Svorcik, "Modulation of cell adhesion, proliferation and differentiation on materials designed for body implants," *Biotechnology Advances,* vol. 29, pp. 739-767, 2011.

[41] K. Prasad, O. Bazaka, M. Chua, M. Rochford, L. Fedrick, J. Spoor*, et al.*, "Metallic Biomaterials: Current Challenges and Opportunities," *Materials,* vol. 10, pp. 884-884, 2017.

[42] Q. Zheng and C. Lü, "Size effects of surface roughness to superhydrophobicity," vol. 10, pp. 462-475, 2014.

[43] Y. Wang, H. Yu, C. Chen, and Z. Zhao, "Review of the biocompatibility of micro-arc oxidation coated titanium alloys," *Materials and Design,* vol. 85, pp. 640-652, 2015.

[44] F. Rupp, R. A. Gittens, L. Scheideler, A. Marmur, B. D. Boyan, Z. Schwartz*, et al.*, "A review on the wettability of dental implant surfaces I: Theoretical and experimental aspects," *Acta Biomaterialia,* vol. 10, pp. 2894-2906, 2014.

[45] R. A. Gittens, L. Scheideler, F. Rupp, S. L. Hyzy, J. Geis-gerstorfer, Z. Schwartz*, et al.*, "A review on the wettability of dental implant surfaces II : Biological and clinical aspects," *Acta Biomaterialia,* vol. 10, pp. 2907-2918, 2014.

[46] W. Wei, J. M. Macak, and P. Schmuki, "High aspect ratio ordered nanoporous Ta2O5 films by anodization of Ta," *Electrochemistry Communications,* vol. 10, pp. 428-432, 2008.

[47] H. Yu, S. Zhu, X. Yang, X. Wang, H. Sun, and M. Huo, "Synthesis of Coral-Like Tantalum Oxide Films via Anodization in Mixed Organic-Inorganic Electrolytes," *PLoS ONE,* vol. 8, pp. 6-11, 2013.

[48] K. S. Raja, T. Gandhi, and M. Misra, "Effect of water content of ethylene glycol as electrolyte for synthesis of ordered titania nanotubes," *Electrochemistry Communications,* vol. 9, pp. 1069-1076, 2007.

[49] L. V. Taveira, J. M. Macak, K. Sirotna, L. F. P. Dick, and P. Schmuki, "Voltage Oscillations and Morphology during the Galvanostatic Formation of Self-Organized TiO2 Nanotubes," *Journal of The Electrochemical Society,* vol. 153, pp. 137-143, 2006.

[50] V. Parkhutik, J. Curiel-Esparza, M. C. Millan, and J. Albella, "Spontaneous layering of porous silicon layers formed at high current densities," *Physica Status Solidi (A) Applications and Materials Science,* vol. 202, pp. 1576-1580, 2005.

[51] N. K. Allam, X. J. Feng, and C. A. Grimes, "Self-Assembled Fabrication of Vertically Oriented Ta2O5 Nanotube Arrays , and Membranes Thereof , by One-Step Tantalum Anodization," *Chem. Mater.,* vol. 20, pp. 6477-6481, 2008.

[52] H. El-Sayed, S. Singh, and P. Kruse, "Formation of Dimpled Tantalum Surfaces from Electropolishing," *Journal of The Electrochemical Society,* vol. 154, pp. C728-C728, 2007.

[53] H. A. El-Sayed and V. I. Birss, "Controlled growth and monitoring of tantalum oxide nanostructures," *Nanoscale,* vol. 2, pp. 793-798, 2010.

[54] H. A. El-Sayed and V. I. Birss, "Controlled interconversion of nanoarray of Ta dimples and high aspect ratio Ta oxide nanotubes," *Nano Letters,* vol. 9, pp. 1350-1355, 2009.

[55] V. Parkhutik, "Silicon anodic oxides grown in the oscillatory anodisation regime - Kinetics of growth, composition and electrical properties," *Solid-State Electronics,* vol. 45, pp. 1451-1463, 2001.

[56] X. Liu, P. K. Chu, and C. Ding, "Surface modification of titanium, titanium alloys, and related materials for biomedical applications," *Materials Science and Engineering R: Reports,* vol. 47, pp. 49-121, 2004.

CHAPTER VII - Development of a bone-like MAO-treated Ta_2O_5 surface doped with zinc oxide nanoparticles

The following chapter is partially based on the results published in:

1. L. Fialho, L. Grenho, M. H. Fernandes, and S. Carvalho, "Porous tantalum oxide with osteoconductive elements and antibacterial core-shell nanoparticles: A new generation of materials for dental implants," Materials Science and Engineering: C, vol. 120, p. 111761, 2021.
2. C. F. Almeida Alves, L. Fialho, S. M. Marques, S. Pires, P. Rico, C. Palacio, et al., "MC3T3-E1 cell response to microporous tantalum oxide surfaces enriched with Ca, P and Mg," Materials Science and Engineering: C, vol. 124, p. 112008, 2021.

7 Introduction

The morphology of the biofunctionalized Ta_2O_5 anodic layer developed by anodization assisted by electric field was not suitable for biological applications (due to their low adhesion strength). Thus, as alternative approach micro-arc oxidation (MAO) mechanism, electrochemical process derived from anodization, was selected, since it allows simultaneously the development and biofunctionalization of a non-homogenous micro/nano-pores oxide layer enriched with osteoconductive elements [1-5].

In a previous work [6], Ta surface treated by MAO was investigated in order to develop microporous Ta_2O_5 anodic layer enriched with Ca, P and Mg. Firstly, Ta_2O_5 anodic layer enriched with Ca was developed. Secondly, Ca and P were incorporated, and lastly the incorporation of the mixture of Ca, P and Mg. These surfaces were developed having the criteria proposed by Wu *et al.* [7], which reported optimal concentration value of Ca for positive cell response is around 8-9 at.%. The *in vitro* studies demonstrated that these treated surfaces and the control groups (untreated Ta surface and commercial Ti grade 2, named as CP Ti Gr2) were non-toxic. All surfaces show higher spreading area as well as well-defined focal adhesions were found on all samples' surfaces when compared with the positive control. Moreover, MAO-treated surfaces exhibited higher expression of both OPN and IBSP osteogenic markers. Untreated Ta surface exhibited better cells responses (cell adhesion and differentiation) than CP Ti Gr2. On the other hand, MAO-treated Ta surfaces improved cell adhesion comparing with untreated Ta. These differences in cell behaviour are related to an overall synergy of the surface roughness, chemical composition and wettability. The best biological response was verified on the Ta_2O_5 surface composed by amorphous calcium phosphates (lower circularity, better focal adhesions area, higher cell differentiation), which corresponded to the rougher surface (Sa = 233 ± 47 nm) and the lower wettability (61 ± 4 °).

Using this sample (Ta_2O_5 surface enriched with Ca and P) as reference, the investigation reported in this chapter is related to the optimization of the Ca/P ratio similar to the hydroxyapatite value by MAO, excluding the Mg incorporation since no advantage on the biological behavior was detected. In a second step, the deposition of zinc nanoparticles with and without an additional thin carbon layer by DC magnetron sputtering onto the optimized Ta_2O_5 surface was performed. These surfaces were morphological characterized by SEM, the chemical composition and distribution by FTIR, XPS and SEM/EDS mapping, respectively, and crystallinity by XRD. The zinc nanoparticles were characterized by SEM/STEM and TEM. The Zn ions release from the Ta_2O_5 porous structure was assessed by ICP-OES.

To better briefly illustrate the experimental procedure, a diagram is shown in Figure VII.1.

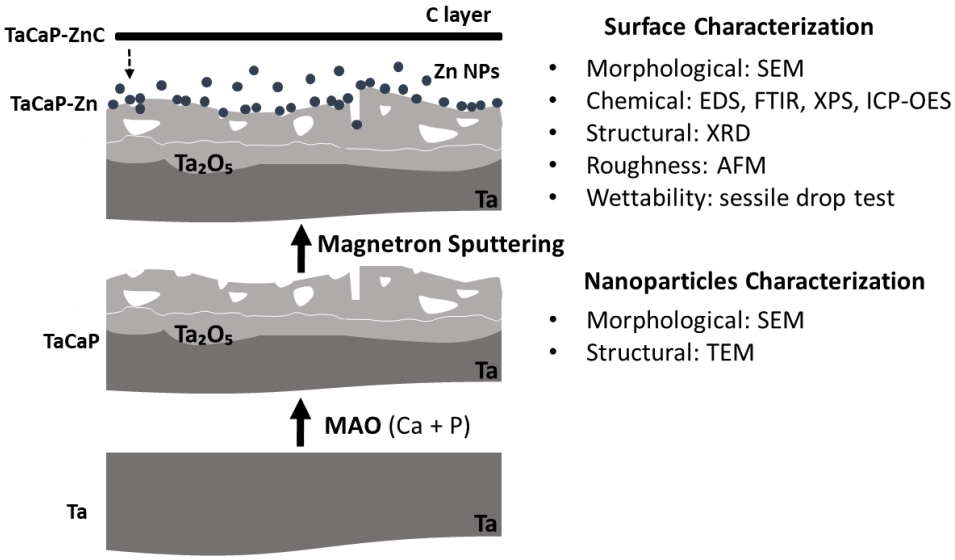

Figure VII.1. Diagram of experimental procedure.

7.1 Optimization of incorporation of Ca/P ratio onto Ta_2O_5 layer by MAO

The reference sample, ultrasonically cleaned in ethanol and distilled water for 5 minutes each (without any further pre-treatment), was repeated by MAO using an electrolyte mixture of 0.7 M CaA and 0.08 M of β-GP at 200 V for 30 minutes using the anodizing two-electrode set-up (previously described in section 5.1.1).The MAO process allows to simultaneously modify the surface morphology, creating micro/nano-pores with non-uniform distribution and non-homogeneous diameters (Figure VII.2-B), as well as the surface chemistry composition by the formation of an oxide layer enriched with Ca and P elements, with a Ca/P ratio of 3.52 (Table VII.1).

The surface optimization by MAO consisted on changing the electrolyte concentrations until reach a Ca/P ratio mimicking the bone chemical composition (Table VII.1). As expected, decreasing the CaA concentration, the incorporation of Ca decreased, and the increase of β-GP concentration enhanced the P content onto the surface. The sample with a Ca/P ratio close to the theoretical value of hydroxyapatite (1.67), mimicking a bone-like structure (Figure VII.2-C and D) and chemical composition (Table VII.1), was named as TaCaP, and used as substrate for the subsequent biofunctional treatment.

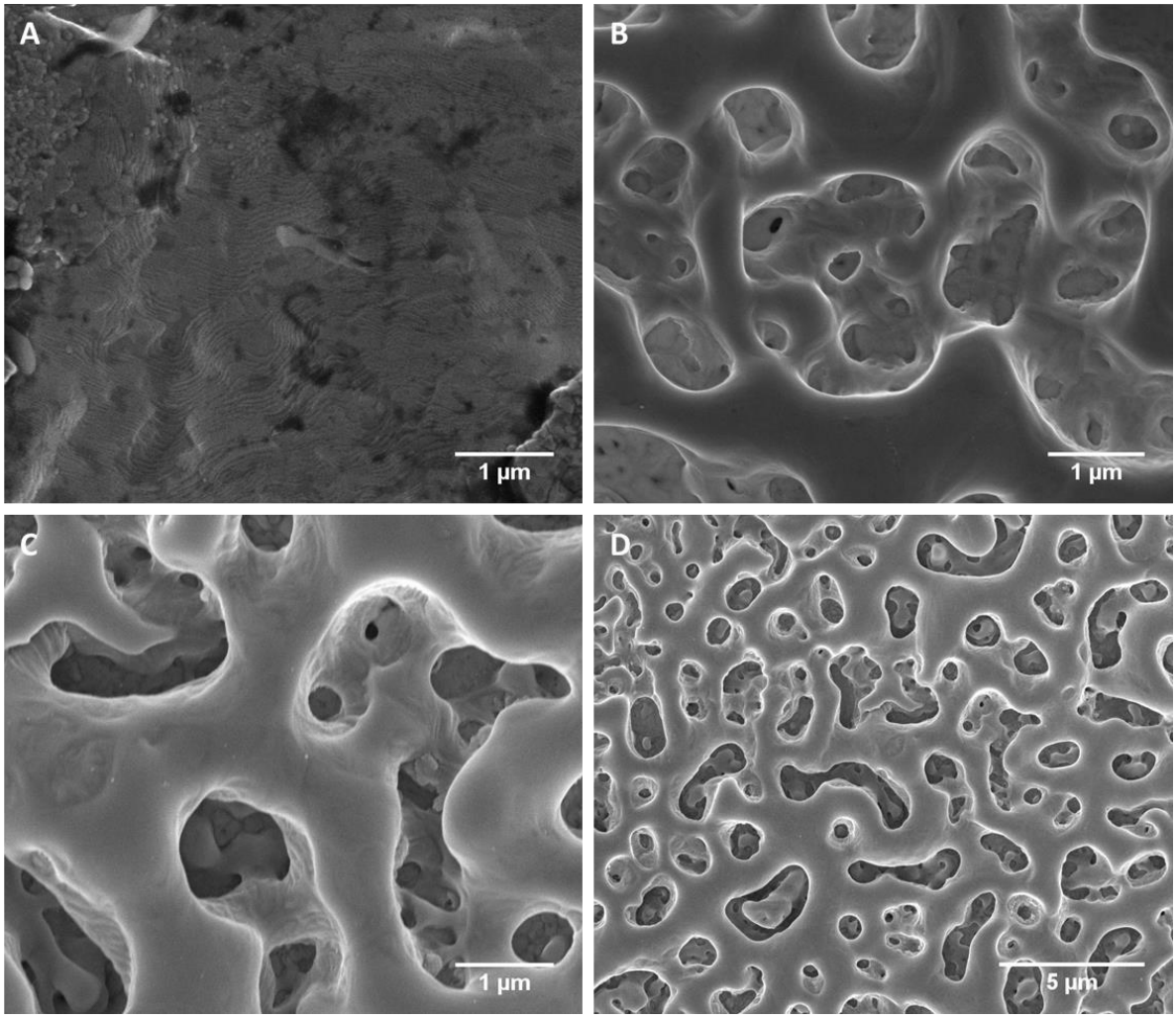

Figure VII.2. Top-views SEM micrographs of the A) untreated Ta, B) Ta_2O_5 enriched with Ca and P used as reference, C) optimized TaCaP surface and D) TaCaP surface at lower magnification.

Table VII.1. Electrolyte composition of MAO treatment and respectively chemical composition of the treated surfaces estimated by EDS.

Sample	Electrolyte composition		Composition (at. %)		Ca/P
	CaA (M)	β-GP (M)	Ca	P	
Reference	0.7	0.08	8.1	2.3	3.52
1	0.35	0.08	6.5	3.1	2.01
TaCaP	0.35	0.12	7.4	4.4	1.68

7.2 Deposition of Zn nanoparticles with or without a thin carbon layer

After the first surface biofunctionalization with a calcium phosphates-enriched porous surface by MAO, the next step was the deposition of Zn nanoparticles onto the TaCaP surface by magnetron sputtering in order to endow the surface with antibacterial behavior. This sample was named as TaCaP-Zn. After nanoparticles' deposition, an additional thin carbon layer was deposited by magnetron sputtering with a plasma composed by Ar and C_2H_2 as source of carbon (TaCaP-ZnC sample). The carbon layer was deposited with the goal to control the zinc ions release from the nanoparticles. The deposition conditions are described in section 3.1.3.

Although spherical nanoparticles coating deposited onto the surface, no obvious differences in the porous microstructure of TaCaP-Zn surface (Figure VII.3-A) were noted with the deposition of Zn nanoparticles comparing to TaCaP surface (Figure VII.2-C and D). However, with the additional deposition of the carbon layer after Zn nanoparticles (sample TaCaP-ZnC), the porosity was marginally mitigated, covering mainly the nano-pores (Figure VII.3-B). This morphological alteration can be related to the dense and smooth appearance of the coating produced with 20 sccm acetylene flux [8].

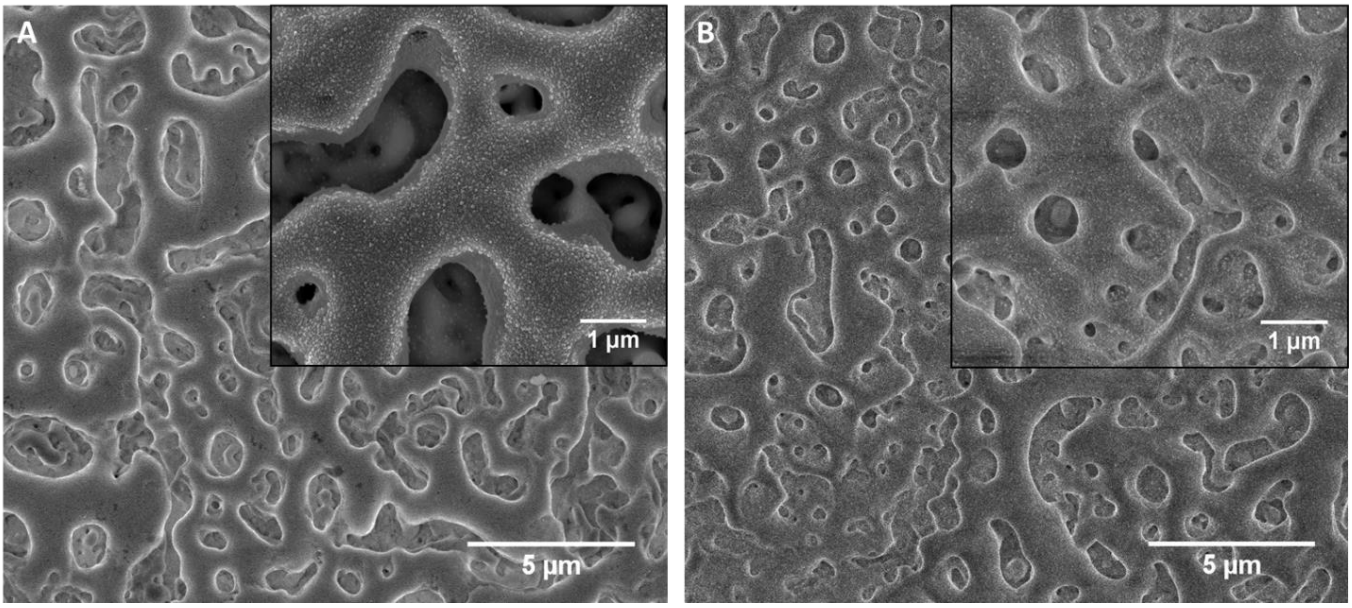

Figure VII.3. Top-views SEM micrographs of the A) TaCaP-Zn and B) TaCaP-ZnC surfaces.

A preliminary characterization of the Zn nanoparticles deposited onto lacey carbon TEM grids was performed by STEM detector and TEM. The results revealed that the nanoparticles had irregular shapes and sizes (Figure VII.4-A), with a Zn core and ZnO shell structure and a thin carbon layer, with a thickness around 1 nm (Figure VII.4-B). Thus, Zn nanoparticles were in fact Zn/ZnO nanoparticles.

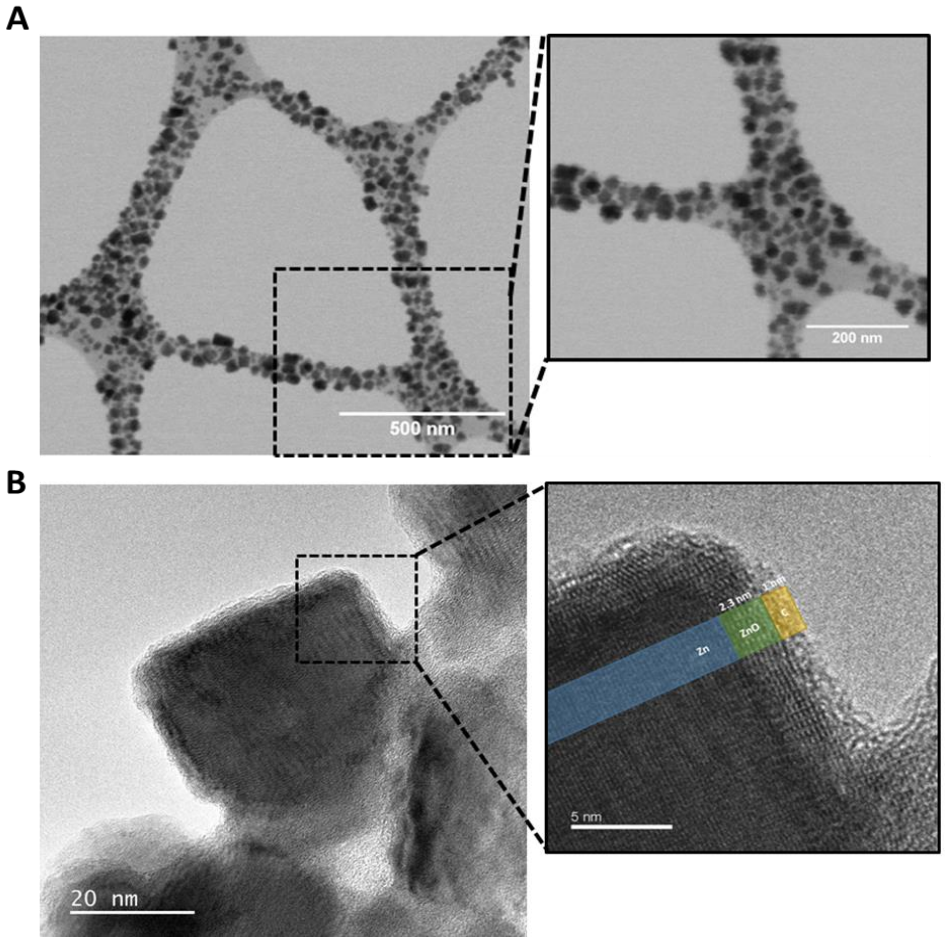

Figure VII.4. A) STEM micrographs of Zn nanoparticles deposited onto carbon lacey grids and B) phase contrast TEM images of a Zn-ZnO core-shell nanoparticle with the additional carbon layer.

The kinetic release of zinc ions (Zn^{2+}) from the nanoparticles has a strong impact on surface biological performance (i.e., surface biocompatibility and antibacterial activity). Thus, the cumulative concentration of Zn^{2+} ions released from both Zn-containing surfaces (TaCaP-Zn and TaCaP-ZnC) by immersing the samples in PBS for 4 h, 1, 3 and 7 days is shown in Figure VII.5. Both samples exhibited similar Zn ions release profile translated as a burst in the first 24 h which tends to stabilize with immersion time. After 4 h, levels of Zn ions were similar for both materials; afterwards, differences in the release profile were noticed, although both samples attained similar values at 7 days of immersion. With TaCaP-Zn, maximum levels were attained at 24 h (0.28 ± 0.02 ppm) remaining constant afterwards. Comparatively, TaCaP-ZnC generates a more controllable time-release profile. At 24 h, levels were lower (0.22 ± 0.02 ppm) and increased slowly through the immersion time (0.24 ± 0.02 ppm, and 0.28 ± 0.03 ppm at days 3 and 7, respectively). This more controlled kinetics release results from the deposited C thin layer, which covers the nanoparticles and consequently delays the ions diffusion and release. The results are in line with those obtained in a previous works [9] describing an initial large amount of Zn release that gradually decreases with immersion time.

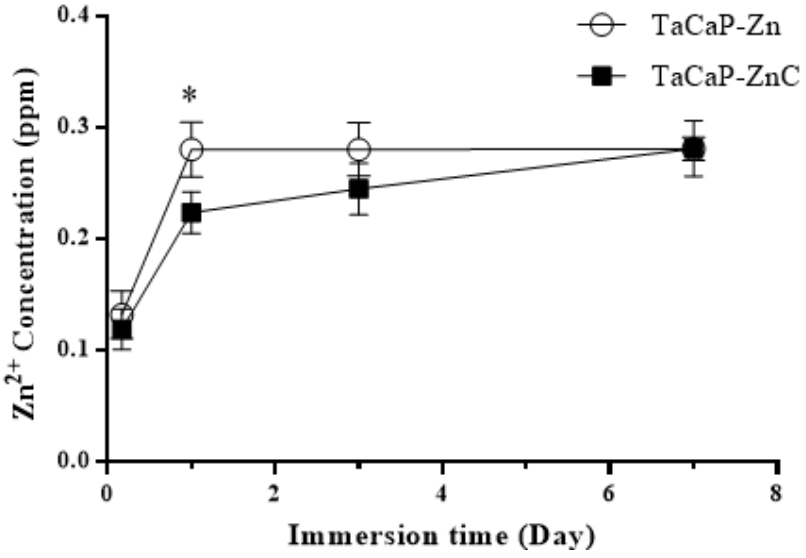

Figure VII.5. Cumulative Zn^{2+} ions release profiles from TaCaP-Zn and TaCaP-ZnC into PBS. * $p \leq 0.05$, for the same time-point.

7.3 Characterization of biofunctionalized surfaces

The developed surfaces were characterized in order to understand if the incorporation of Ca and P promoted the calcium phosphates formation with apatite-like phase as well as if the Zn/ZnO nanoparticles were in a crystalline structure. The overall impact of the surface modifications on the surface roughness and wettability was also studied.

The presence of calcium phosphates was firstly studied by the phosphate-related absorptions registered in the FTIR spectrum of TaCaP surface (Figure VII.6). The spectrum presents absorption bands 600-800 cm^{-1} and 800-1000 cm^{-1} assigned to Ta-O-Ta (of Ta_2O_5) and tantalum suboxides (TaO and TaO_2), respectively [10, 11]. Additionally, the bands located at 560-600 and 1000-1100 cm^{-1} (grey band in Figure VII.6) are ascribed to PO_4^{3-} groups in phosphates and the bands 870-880 and 1460-1530 cm^{-1} to carbonates (CO_2^{3-}) groups [2, 12-15]. Thus, the presence of phosphate-related absorptions corroborates the supposition of the formation of calcium phosphates.

To support the FTIR's results, the presence of CaP onto the porous Ta_2O_5 surface as well as the core-shell structure of the Zn-ZnO nanoparticles were confirmed by XPS analysis. The surveys XPS spectra from the three modified surfaces are displayed in Figure VII.7. The surface of TaCaP sample indicated the presence of several chemical elements: C, O, Ta, Ca and P. However, with the deposition of the Zn/ZnO nanoparticles only C, O and Zn were detected (TaCaP-Zn and TaCaP-ZnC samples), indicating that the first nanometers of the top surface are covered with the nanoparticles preventing the detection of the substrate (TaCaP) chemical elements.

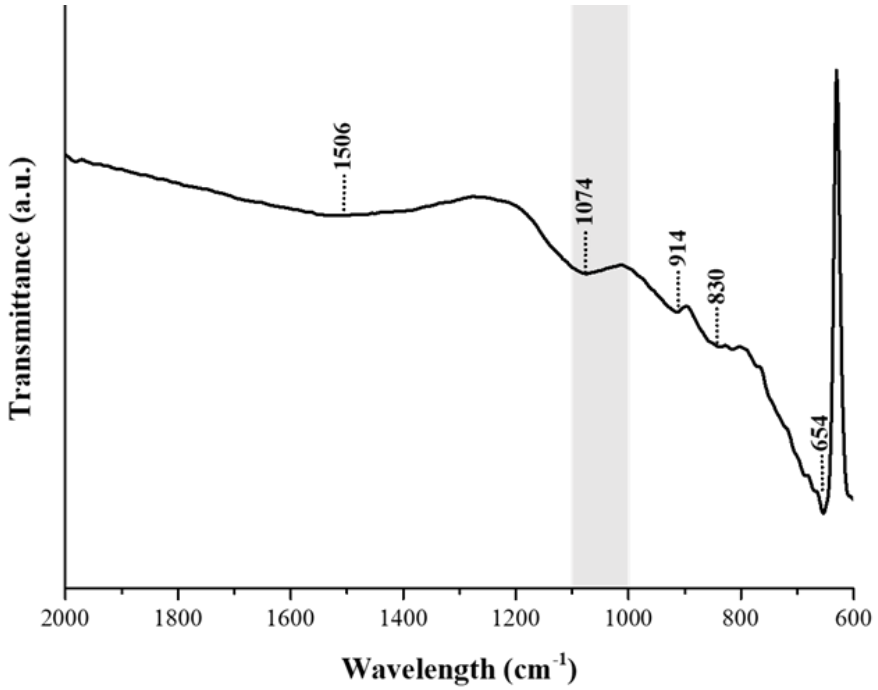

Figure VII.6. FTIR spectrum of TaCaP sample.

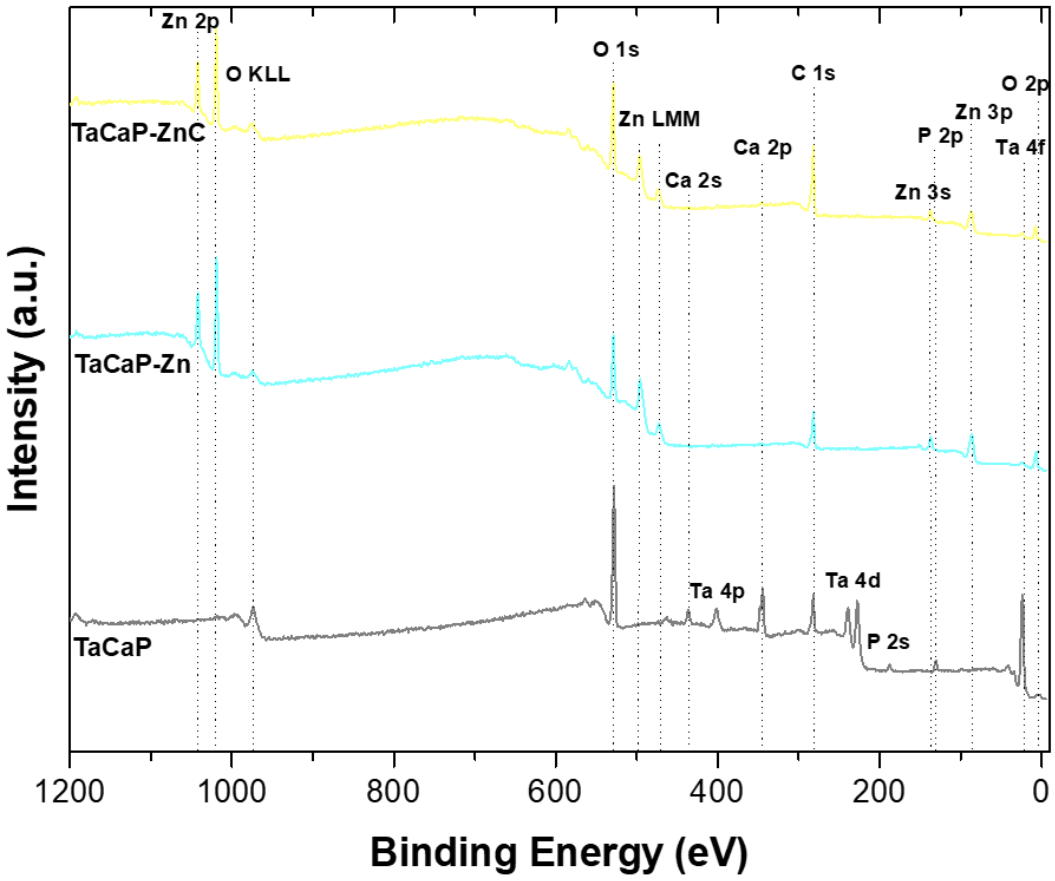

Figure VII.7. Survey XPS data of TaCaP (black row), TaCaP-Zn (light blue row) and TaCaP-ZnC (light yellow row) surface samples.

Each element spectrum was deconvoluted into its components to ensure the curve fitting. The XPS spectra of deconvoluted elements detected on TaCaP surface are shown in Figure VII.8. The C 1s (Figure VII.8-A) was deconvoluted into three peaks at 285 eV, ascribed to C-C bond caused by C contamination [16], at 286.4 eV which can be associated to C-O bonds and at 288.7 eV to C=O bonds [17]. Figure VII.8-C shows the deconvolution of the Ta 4f doublet, presenting two peaks at 26.3 and 28.2 eV which must be attributed to Ta $4f_{7/2}$ and Ta $4f_{5/2}$, respectively, with a spin orbit splitting of 1.9 eV [18-22], indicating the presence of Ta_2O_5 (Ta^{5+} oxidation state). The Ca 2p peak (Figure VII.8-D) displayed two peaks of the doublet Ca $2p_{3/2}$ at 347.4 eV and Ca $2p_{1/2}$ at 350.9 eV (spin orbital 3.5 eV), being assigned to $Ca_3(PO_4)_2$ [2]. The presence of the P 2p peak (Figure VII.8-E) deconvoluted into the doublet at 133.4 and 134.3 eV (spin orbital of 0.87 eV), attributed to PO_4^{3-} groups, supported the $Ca_3(PO_4)_2$ assignment [23]. The O 1s (Figure VII.8-B) exhibited four peaks: 530.5 eV related to the metal oxide Ta_2O_5, 531.3 eV which corroborated the presence of $Ca_3(PO_4)_2$, 531.7 eV ascribed to C-O and 533 eV to C=O, although these two peaks could be also related to species like OH^- and physiosorbed H_2O [3]. Additionally, the at.% of Ca and P was 8.2 and 4.8, respectively, corresponding to a Ca/P ratio of 1.7. This value is closed to the ratio estimated by EDS, which could mean that both chemical elements are uniformly present on the oxide layer thickness. However, a preliminary result of the chemical composition profile of the TaCaP sample (prepared by FIB/SEM and analysed by STEM/EDS) revealed that the P content is higher on the top surface while the Ca element is more uniformly distributed across the oxide layer (ANNEX IV). These results are in agreement with the XPS sputter-profile of the biofunctionalized anodic Ta_2O_5 samples produced by anodization (Figure VI.9). As already discussed in 6.2 subchapter, the involved chemical elements have similar diffusion behavior, assisted by electric field, in incorporation by anodization and MAO, although the incorporation mechanism is different. In fact, some studies of Ta treatment by MAO have attributed the importance of diffusion for the cation's incorporation (i.e., Ca^{2+} ions), while electrophoresis is responsible for anions movement (i.e., PO_4^{3-} ions) [1, 4].

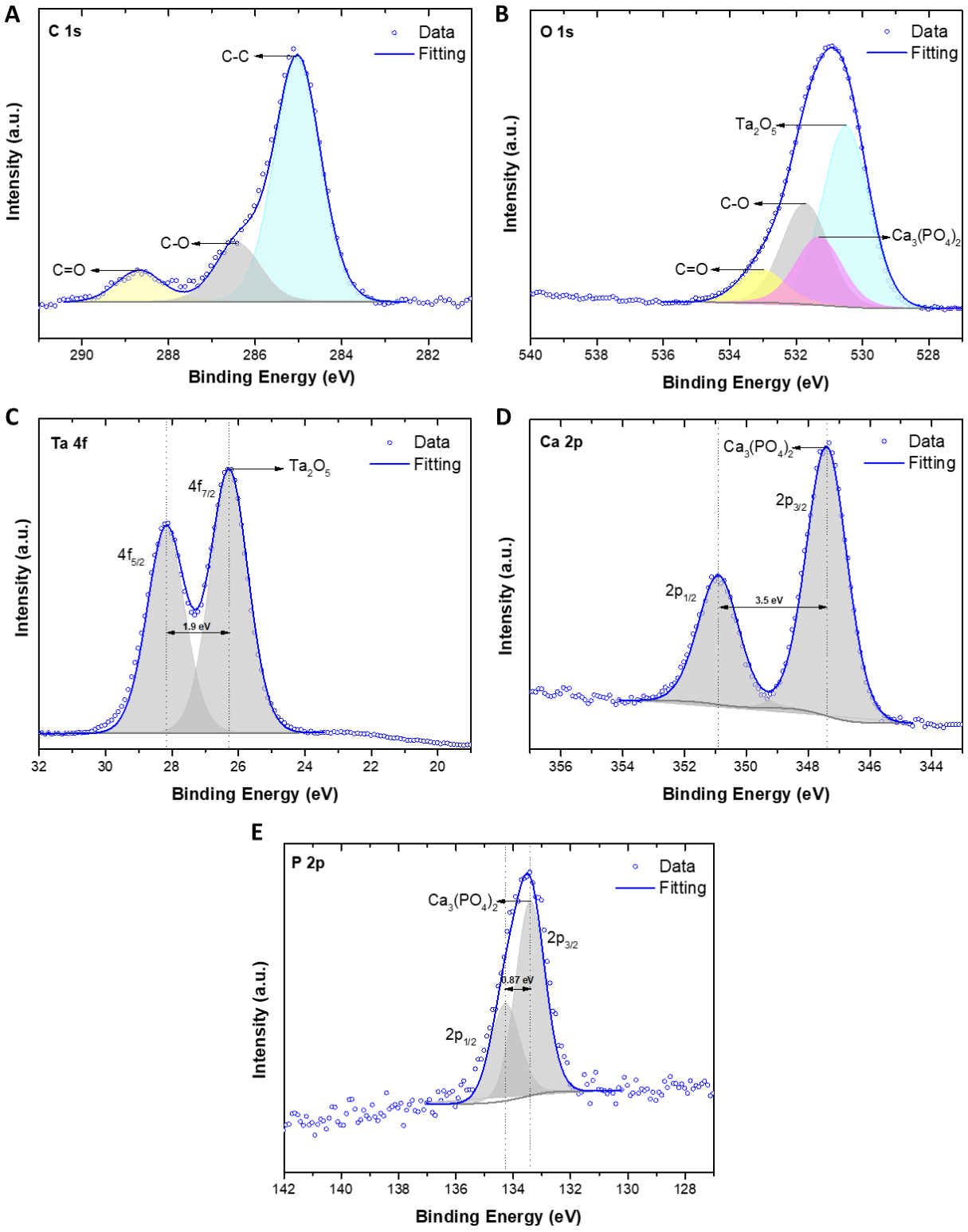

Figure VII.8. XPS spectra of deconvoluted A) C 1s, B) O 1s, C) Ta4f, D) Ca 2p and E) P 2p elements detected on TaCaP surface.

The XPS spectra of deconvoluted elements detected on TaCaP-Zn surface are shown in Figure VII.9. The C 1s spectrum (Figure VII.9-A) presented three peaks at 285, 286.7 and 289 eV corresponding to C-C, C-O and C=O bonds, respectively [24]. The Zn 2p XPS region is shown in Figure VII.9-C. The nanoparticles displayed a doublet at 1021.8 and 1044.9 eV, corresponding to the Zn $2p_{3/2}$ and Zn $2p_{1/2}$, respectively,

with a split spin-orbit of 23.1 eV, that could be assigned to Zn metal [25-28]. Additionally, a second deconvoluted doublet was obtained at 1022.8 and 1045.8 eV (split spin-orbit of 23 eV) which could be attributed to the Zn^{2+} oxidation state, indicating the presence of ZnO [25-29]. The deconvolution of O 1s spectrum (Figure VII.9-B) resulted in three peaks at 530.7, 532.2 and 533.8 eV that should be assigned ZnO, C-O and C=O bonds, respectively [24, 30, 31]. However, the binding energy shifts of the deconvoluted peaks assigned to metallic Zn and ZnO are too close and consequently the interpretation of this XPS spectrum was tricky. Thus, to better distinguish the chemical states of Zn, the principal Zn LMM peak (Auger peak) was also collected since it presents larger chemical shifts compared to Zn 2p. In Figure VII.9-D is represented the spectra of Zn LMM Auger peaks, being assessed more clearly the presence of two Zn compounds. Zn metal had two peaks, as the peak with higher intensity had a kinetic energy around 992 eV, while the peak around 988 eV was ascribed to ZnO [26, 30, 31]. Hence, it was possible to confirm the presence of the core-shell structure of Zn/ZnO nanoparticles.

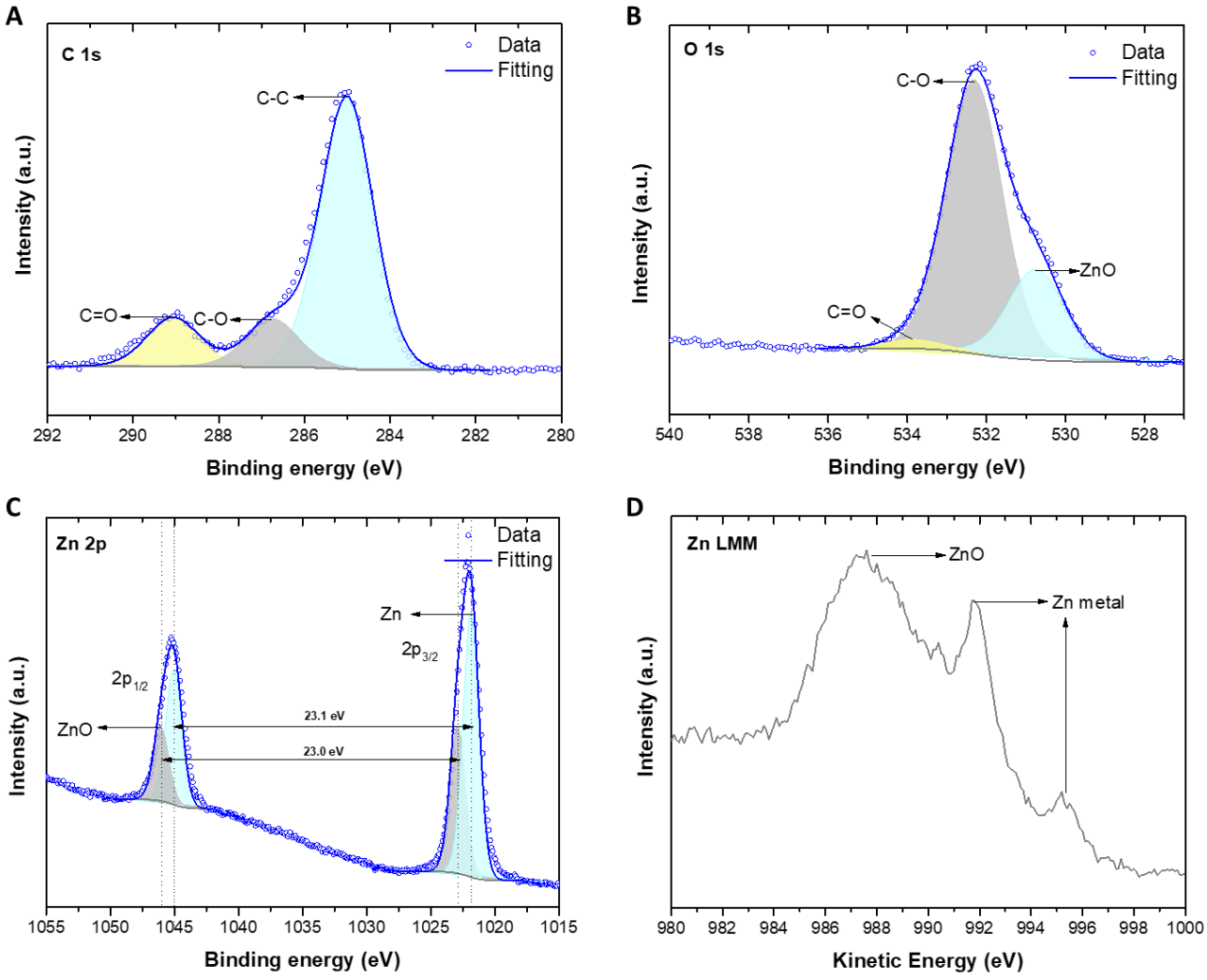

Figure VII.9. XPS spectra of deconvoluted A) C 1s, B) O 1s, C) Zn 2p and elements detected on TaCaP-Zn surface and D) Zn LMM Auger peak.

The XPS spectra of deconvoluted elements on TaCaP-ZnC surface (ANNEX V) had a similar interpretation than TaCaP-Zn. Besides the small binding energy shifts, it is important to highlight an increment of carbon bonds intensity (also observed in Figure VII.7) as a consequence of the non- adventitious thin carbon layer C. The Zn/ZnO core-shell structure was also corroborated by the analysis of both Zn 2p XPS region and Zn LMM Auger peaks.

Complementary, the presence of Zn element on the TaCaP-Zn and TaCaP-ZnC surfaces was assessed by elemental Zn EDS mapping (Figure VII.10), where is possible to observed that the blue dots (Figure VII.10-B and D) are uniformly distributed over both surfaces.

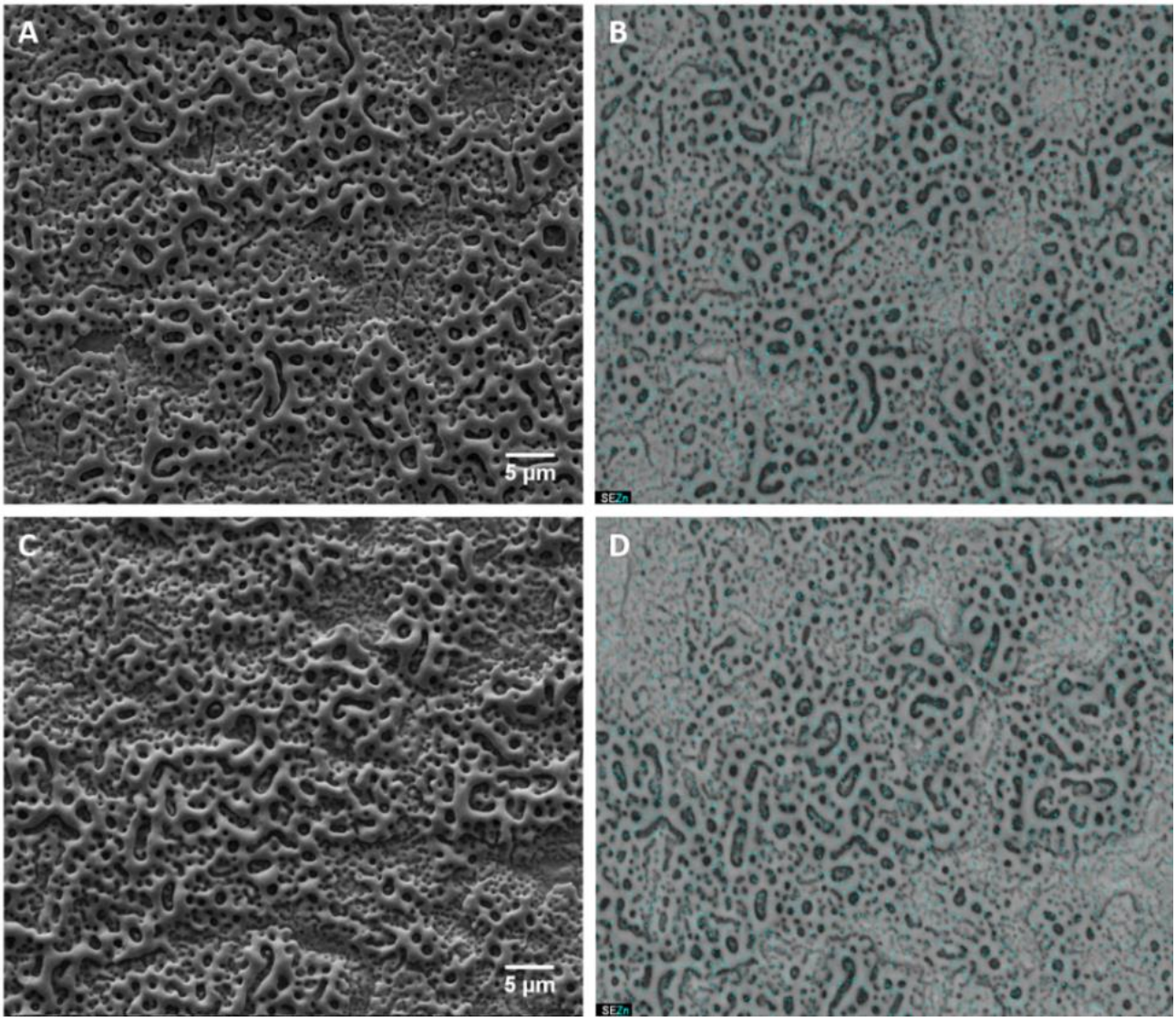

Figure VII.10. Top-views SEM micrographs of the analysed areas of A) TaCaP-Zn and C) TaCaP-ZnC surfaces, and the corresponding EDS mapping distribution (weight %) of the elemental Zn (blue dots) over both surfaces, B) and C) respectively.

XRD analysis were carried out in order to understand the evolution of the structure caused by the topographic, morphologic, and chemical modifications on the Ta substrate during MAO and NPs deposition by magnetron sputtering. Figure VII.11 discloses the diffraction patterns for Ta, TaCaP, TaCaP-Zn and TaCaP-ZnC samples. The main crystalline phases identified are α-Ta: body-centered cubic (bcc) (ICDD card n. 00-004-0788), β-Ta: tetragonal (ICDD card n. 00-025-1280), and Ta_2O_5: orthorhombic (ICDD card n 00-025-0922). Ta sample (without any treatment) had strong diffraction lines related to both α-Ta and β-Ta phases, which are also predominant in all modified samples, as observed in our previous works [32-34]. The MAO treatment formed a partly crystalized oxide Ta_2O_5 layer, in agreement with the XPS results (Figure VII.8-C), although these peaks can be also attributed to β-Ta phase. HAp diffraction peaks were not detected in none of the modified samples. Likewise, the presence of diffraction peaks ascribed to crystalline Ta and Ta_2O_5 when MAO was carried out with an applied potential of 350 V was reported by Antonio *et al.* [1] . However the temperature produced by the microarcs during the MAO process was not enough to form crystalline HAp, and thus amorphous calcium phosphates were probably formed [1]. Indeed, several authors [1, 35] have shown the presence of crystalline calcium phosphates in diffractograms of Ta treated by MAO but applying higher voltage like 500 V, as well as a subsequent heat or UV treatment [36, 37]. In addition, no feature peaks of Zn-containing compounds were detected in both TaCaP-Zn and TaCaP-ZnC XRD patterns, which can be related to the very low concentration of Zn added on the oxide layer surface [38].

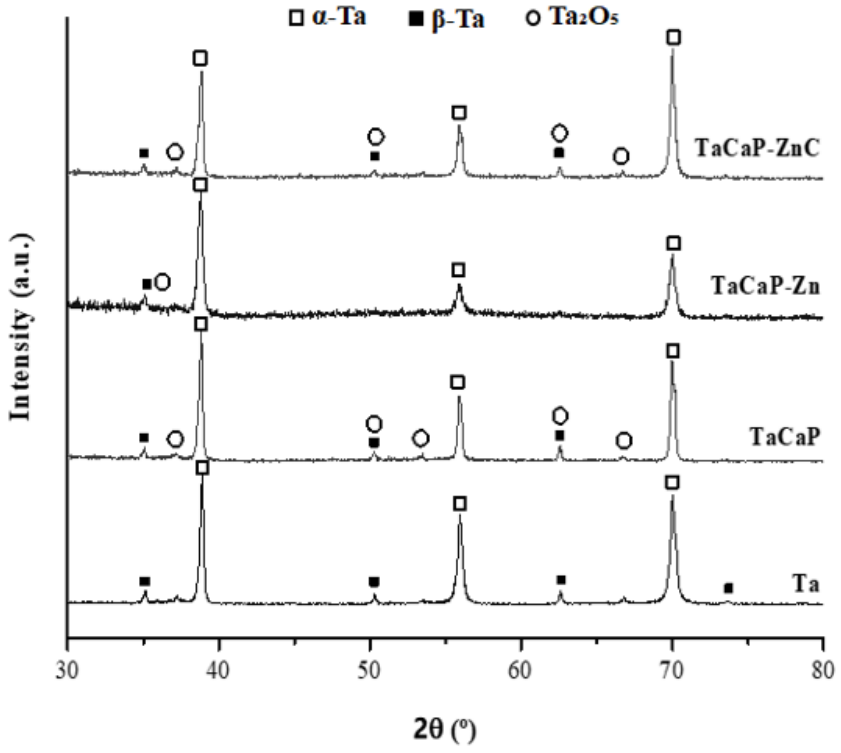

Figure VII.11. XRD patterns of Ta, TaCaP, TaCaP-Zn and TaCaP-ZnC samples.

Moreover, the MAO treatment induced a significant increase on Ta surface roughness (Table VII.2), in line with previous studies [1, 17, 35, 39]. Likewise, the MAO surfaces became slightly rougher with the Zn/ZnO nanoparticles presence (TaCaP-Zn and TaCaP-ZnC). The influence of Zn/ZnO nanoparticles in surface roughness can be related to their growth as island-like growth model (Volmer-Weber mode), as observed previously on carbon substrates [40].

Table VII.2. Surface roughness (Sa and Sq) and water contact angle of Ta, TaCaP, TaCaP-Zn and TaCaP-ZnC samples.

Samples	Roughness ± SD (μm)		Contact angle ± SD (º)
	Sa	Sq	
Ta	0.01±0.005	0.02±0.01	81 ± 10
TaCaP	0.12±0.04	0.14±0.04	72 ± 12
TaCaP-Zn	0.15±0.07	0.18±0.08	127 ± 2
TaCaP-ZnC	0.14±0.04	0.17±0.05	115 ± 2

The water contact angles are also shown in Table VII.2. According to Vogler [41], Ta substrate revealed a hydrophobic character which slightly decreased with MAO treatment, as reported in several works [17, 42, 43]. On the other hand, the water contact angle raised considerably with the subsequent Zn nanoparticles (with or without carbon layer) deposition enhancing the hydrophobic effect. Sowa *et al.* [35] explained the hydrophobicity of MAO-treated surfaces by the morphological effects rather than surface chemistry since surface pores produced at 200 V are small enough (around 2 μm or less) to water droplet (0.2 μL) penetrate them and consequently air pockets can be formed [44]. On the other hand, acting as a hydrophilic component [7, 45], phosphates group can decrease the water contact angle, as well as the presence of OH groups absorbed on the surfaces [16, 46]. On the whole, these results are in line with those obtained by Deng *et al.* [42], wherein MAO treatment, producing a CaP-containing anodic layer, tend to increase the surface roughness and decrease the water contact angle. Additionally, the surface water repellency with Zn nanoparticles (with or without carbon layer) can be modulated by the deposition parameters of Zn NPs which in turn increases the surface roughness and increases the contact angle, due the low affinity of these systems to water, leading to a reduction of water absorption [47]. Likewise,

controlling the deposition parameters of carbon coating, particularly increasing the acetylene flux, the surface hydrophobicity will be enhanced [8].

The obtained surface morphologies (Figure VII.2) are similar to that described by Bai *et al.* [48] in treated titanium, reporting the pores morphology as roughly elliptical shape like a volcanic vent. Although the morphological differences are not evident, it is possible to realize that reference surface (Figure VI.2-B) had larger micropores and more nanoporosity within them compared to the TaCaP surface (Figure VI.2-C). Additionally, it was observed a decrease of the surface roughness (from 233 nm to 120 nm) and increase of wettability (from 61 ± 4 ° to 72 ± 12 °) of the reference and TaCaP surfaces, respectively. These surface properties changes can be ascribed to the MAO conditions, more specifically to the CaA concentration which improve the electrical conductivity of the electrolyte, affecting the breakdown voltage of the anodic layer [7]. Thus, increasing the CaA concentration, the roughness, pore size and porosity degree of the oxide layer will increase, as noticed in the reference sample. The smaller water contact angle of the reference sample than the TaCaP can be related, as already mentioned, with its higher roughness [42].

7.4 Partial Conclusions

Using MAO, a bone-like micro/nano-porosity CaP-containing Ta_2O_5 layer with a biomimetic Ca/P ratio was achieved (TaCaP). The existence of CaP was corroborated by both XPS and FTIR analysis, although no evidence of crystalline apatite was noticed in the XRD pattern, meaning that the CaP formed were amorphous. Zn/ZnO nanoparticles were deposited onto TaCaP samples using DC magnetron sputtering ensuring a homogenous particle distribution (TaCaP-Zn).The core-shell structure of Zn/ZnO nanoparticles was confirmed by TEM and XPS characterization techniques. With both methods, the Ta surface became rougher and more hydrophobic. Finally, the deposition of a thin carbon layer (TaCaP-ZnC) slightly decreased the hydrophobicity and controlled the Zn^{2+} ions release.

7.5 References

[1] R. F. Antonio, E. C. Rangel, B. A. Mas, E. A. R. Duek, and N. C. Cruz, "Growth of hydroxyapatite coatings on tantalum by plasma electrolytic oxidation in a single step," *Surface and Coatings Technology,* vol. 357, pp. 698-705, 2019.

[2] C. Wang, F. Wang, and Y. Han, "The structure, bond strength and apatite-inducing ability of micro-arc oxidized tantalum and their response to annealing," *Applied Surface Science,* vol. 361, pp. 190-198, 2016.

[3] C. Wang, F. Wang, and Y. Han, "Structural characteristics and outward-inward growth behavior of tantalum oxide coatings on tantalum by micro-arc oxidation," *Surface and Coatings Technology,* vol. 214, pp. 110-116, 2013.

[4] Q. M. Zhao, G. Z. Li, H. L. Yang, and X. F. Gu, "Surface modification of biomedical tantalum by micro-arc oxidation," *Materials Technology,* vol. 32, pp. 90-95, 2017.

[5] M. A. P. C. Goularte, G. F. Barbosa, N. C. da Cruz, and L. M. Hirakata, "Achieving surface chemical and morphologic alterations on tantalum by plasma electrolytic oxidation," *International Journal of Implant Dentistry,* vol. 2, 2016.

[6] C. F. Almeida Alves, L. Fialho, S. M. Marques, S. Pires, P. Rico, C. Palacio*, et al.*, "MC3T3-E1 cell response to microporous tantalum oxide surfaces enriched with Ca, P and Mg," *Materials Science and Engineering: C,* vol. 124, p. 112008, 2021/05/01/ 2021.

[7] S.-D. Wu, H. Zhang, X.-D. Dong, C.-Y. Ning, A. S. L. Fok, and Y. Wang, "Physicochemical properties and in vitro cytocompatibility of modified titanium surfaces prepared via micro-arc oxidation with different calcium concentrations," *Applied Surface Science,* vol. 329, pp. 347-355, 2015.

[8] C. Fernandes, S. Calderon V, L. F. Ballesteros, M. A. Cerqueira, L. M. Pastrana, J. A. Teixeira*, et al.*, "Carbon-based sputtered coatings for enhanced chitosan-based films properties," *Applied Surface Science,* vol. 433, pp. 689-695, 2018.

[9] K. Huo, X. Zhang, H. Wang, L. Zhao, X. Liu, and P. K. Chu, "Osteogenic activity and antibacterial effects on titanium surfaces modified with Zn-incorporated nanotube arrays," *Biomaterials,* vol. 34, pp. 3467-3478, 2013.

[10] J. Y. Zhang, B. Lim, and I. W. Boyd, "Thin tantalum pentoxide films deposited by photo-induced CVD," *Thin Solid Films,* vol. 336, pp. 340-343, 1998.

[11] D. Saygin-Hinczewski, K. Koc, I. Sorar, M. Hinczewski, F. Z. Tepehan, and G. G. Tepehan, "Optical and structural properties of Ta2 O5-CeO2 thin films," *Solar Energy Materials and Solar Cells,* vol. 91, pp. 1726-1732, 2007.

[12] A. Salama, M. Neumann, C. Günter, and A. Taubert, "Ionic liquid-assisted formation of cellulose/calcium phosphate hybrid materials," *Beilstein Journal of Nanotechnology,* vol. 5, pp. 1553-1568, 2014.

[13] A. Stoch, W. Jastrzębski, A. Brozek, J. Stoch, J. Szaraniec, B. Trybalska*, et al.*, "FTIR absorption-reflection study of biomimetic growth of phosphates on titanium implants," *Journal of Molecular Structure,* vol. 555, pp. 375-382, 2000.

[14] L. Berzina-Cimdina and N. Borodajenko, "Research of Calcium Phosphates Using Fourier Transform Infrared Spectroscopy," *Infrared Spectroscopy - Materials Science, Engineering and Technology,* 2012.

[15] H. Gheisari, E. Karamian, and M. Abdellahi, "A novel hydroxyapatite -Hardystonite nanocomposite ceramic," *Ceramics International,* vol. 41, pp. 5967-5975, 2015.

[16] S. A. Alves, S. B. Patel, C. Sukotjo, M. T. Mathew, P. N. Filho, J. P. Celis*, et al.*, "Synthesis of calcium-phosphorous doped TiO2 nanotubes by anodization and reverse polarization: A promising strategy for an efficient biofunctional implant surface," *Applied Surface Science,* vol. 399, pp. 682-701, 2017.

[17] M. Sowa, A. Kazek-k, R. P. Socha, G. Dercz, J. Michalska, and W. Simka, "Modification of tantalum surface via plasma electrolytic oxidation in silicate solutions," *Electrochimica Acta,* vol. 114, pp. 627-636, 2013.

[18] J. Y. Zhang and I. W. Boyd, "Thin tantalum and tantalum oxide films grown by pulsed laser deposition," *Applied Surface Science,* vol. 168, pp. 234-238, 2000.

[19] P. M. Ranjith, M. T. Rao, S. Sapra, I. I. Suni, and R. Srinivasan, "On the Anodic Dissolution of Tantalum and Niobium in Hydrofluoric Acid," *Journal of The Electrochemical Society,* vol. 165, pp. C258-C269, 2018.

[20] R. Simpson, R. G. White, J. F. Watts, and M. A. Baker, "XPS investigation of monatomic and cluster argon ion sputtering of tantalum pentoxide," *Applied Surface Science,* vol. 405, pp. 79-87, 2017.

[21] Y. Masuda, S. Wakamatsu, and K. Koumoto, "Site-selective deposition and micropatterning of tantalum oxide thin films using a monolayer," *Journal of the European Ceramic Society,* vol. 24, pp. 301-307, 2004.

[22] N. Benito and C. Palacio, "Nanostructuring of Ta2O5 surfaces by low energy Ar+ bombardment," *Applied Surface Science,* vol. 351, pp. 753-759, 2015.

[23] Z. Q. Yao, Y. Ivanisenko, T. Diemant, A. Caron, A. Chuvilin, J. Z. Jiang*, et al.*, "Synthesis and properties of hydroxyapatite-containing porous titania coating on ultrafine-grained titanium by micro-arc oxidation," *Acta Biomaterialia,* vol. 6, pp. 2816-2825, 2010.

[24] O. Lupan, G. A. Emelchenko, V. V. Ursaki, G. Chai, A. N. Redkin, A. N. Gruzintsev*, et al.*, "Synthesis and characterization of ZnO nanowires for nanosensor applications," *Materials Research Bulletin,* vol. 45, pp. 1026-1032, 2010/08/01/ 2010.

[25] W. M. R. L. E. D. J. F. M. C. D. Wagner, *Handbook of X-ray Photoelectron Spectroscopy: A Reference Book of Standard Data for Use in X-ray Photoelectron Spectroscopy*: Perkin-Elmer, 1979.

[26] T. F. S. Inc. (2021, 19-01-2021). *XPS Interpretation of Zn*. Available: https://xpssimplified.com/elements/zinc.php#aboutthiselement

[27] M. N. Islam, T. B. Ghosh, K. L. Chopra, and H. N. Acharya, "XPS and X-ray diffraction studies of aluminum-doped zinc oxide transparent conducting films," *Thin Solid Films,* vol. 280, pp. 20-25, 1996/07/01/ 1996.

[28] N. T. Mai, T. T. Thuy, D. M. Mott, and S. Maenosono, "Chemical synthesis of blue-emitting metallic zinc nano-hexagons," *CrystEngComm,* vol. 15, pp. 6606-6610, 2013.

[29] B. Zhong, X. Tang, X. Huang, L. Xia, X. Zhang, G. Wen*, et al.*, "Metal–semiconductor Zn/ZnO core–shell nanocables: facile and large-scale fabrication, growth mechanism, oxidation behavior, and microwave absorption performance," *CrystEngComm,* vol. 17, pp. 2806-2814, 2015.

[30] H. Ma, L. Yue, C. Yu, X. Dong, X. Zhang, M. Xue*, et al.*, "Synthesis, characterization and photocatalytic activity of Cu-doped Zn/ZnO photocatalyst with carbon modification," *Journal of Materials Chemistry,* vol. 22, pp. 23780-23788, 2012.

[31] M. S. Xue, W. Li, and F. J. Wang, "Effect of surface ZnO coatings on oxidation and thermal stability of zinc films," *Superlattices and Microstructures,* vol. 48, pp. 213-220, 2010/08/01/ 2010.

[32] L. Fialho and S. Carvalho, "Surface engineering of nanostructured Ta surface with incorporation of osteoconductive elements by anodization," *Applied Surface Science,* vol. 495, pp. 1-13, 2019.

[33] C. F. Almeida Alves, A. Cavaleiro, and S. Carvalho, "Bioactivity response of Ta1-xOx coatings deposited by reactive DC magnetron sputtering," *Materials Science and Engineering C,* vol. 58, pp. 110-118, 2016.

[34] H. Moreira, A. Costa-Barbosa, S. M. Marques, P. Sampaio, and S. Carvalho, "Evaluation of cell activation promoted by tantalum and tantalum oxide coatings deposited by reactive DC magnetron sputtering," *Surface and Coatings Technology,* vol. 330, pp. 260-269, 2017.

[35] M. Sowa, M. Woszczak, A. Kazek-Kęsik, G. Dercz, D. M. Korotin, I. S. Zhidkov*, et al.*, "Influence of process parameters on plasma electrolytic surface treatment of tantalum for biomedical applications," *Applied Surface Science,* vol. 407, pp. 52-63, 2017.

[36] C. Wang, Z. Fan, and Y. Han, "Formation and osteoblast behavior of HA nano-rod/fiber patterned coatings on tantalum in porous and compact forms," *Journal of Materials Chemistry B,* vol. 2, pp. 5442-5454, 2015.

[37] Y. Han, D. Chen, J. Sun, Y. Zhang, and K. Xu, "UV-enhanced bioactivity and cell response of micro-arc oxidized titania coatings," *Acta Biomaterialia,* vol. 4, pp. 1518-1529, 2008.

[38] R. Wang, X. He, Y. Gao, X. Zhang, X. Yao, and B. Tang, "Antimicrobial property, cytocompatibility and corrosion resistance of Zn-doped ZrO2/TiO2 coatings on Ti6Al4V implants," *Materials Science and Engineering C,* vol. 75, pp. 7-15, 2017.

[39] M. Petković, S. Stojadinović, R. Vasilić, and L. Zeković, "Characterization of oxide coatings formed on tantalum by plasma electrolytic oxidation in 12-tungstosilicic acid," *Applied Surface Science,* vol. 257, pp. 10590-10594, 2011.

[40] S. Calderon V, B. Gomes, P. J. Ferreira, and S. Carvalho, "Zinc nanostructures for oxygen scavenging," *Nanoscale,* vol. 9, pp. 5254-5262, 2017.

[41] E. A. Vogler, "Structure and reactivity of water at biomaterial surfaces, Adv," *Coll. Interf. Sci.,* vol. 74, pp. 69-117, 1998.

[42] F. Deng, W. Zhang, P. Zhang, C. Liu, and J. Ling, "Improvement in the morphology of micro-arc oxidised titanium surfaces: A new process to increase osteoblast response," *Materials Science and Engineering C,* vol. 30, pp. 141-147, 2010.

[43] X. Shen, L. Ping, L. Wang, C. Liu, J. Liu, and Z. Deng, "Improving the stability and bioactivity of micro-arc oxidized calcium phosphate / titania porous coatings by high energy shot peening pretreatment," *Ceramics International,* vol. 46, pp. 2041-2048, 2020.

[44] S. P. Rodrigues, C. F. A. Alves, A. Cavaleiro, and S. Carvalho, "Water and oil wettability of anodized 6016 aluminum alloy surface," *Applied Surface Science,* vol. 422, pp. 430-442, 2017.

[45] D. S. W. Benoit, M. P. Schwartz, A. R. Durney, and K. S. Anseth, "Small functional groups for controlled differentiation of hydrogel-encapsulated human mesenchymal stem cells," *Nature Materials,* vol. 7, pp. 816-823, 2008.

[46] L. Bacakova, E. Filova, M. Parizek, T. Ruml, and V. Svorcik, "Modulation of cell adhesion, proliferation and differentiation on materials designed for body implants," *Biotechnology Advances,* vol. 29, pp. 739-767, 2011.

[47] M. Lee, G. Kwak, and K. Yong, "Wettability control of ZnO nanoparticles for universal applications," *ACS Applied Materials and Interfaces,* vol. 3, pp. 3350-3356, 2011.

[48] L. Bai, Z. Du, J. Du, W. Yao, J. Zhang, Z. Weng*, et al.*, "A multifaceted coating on titanium dictates osteoimmunomodulation and osteo / angio-genesis towards ameliorative osseointegration," *Biomaterials,* vol. 162, pp. 154-169, 2018.

CHAPTER VIII - Cytocompatibility and antibacterial activity of MAO-treated Ta_2O_5 doped with zinc oxide nanoparticles

The following chapter is partially based on the results published in:

1. L. Fialho, L. Grenho, M. H. Fernandes, and S. Carvalho, "Porous tantalum oxide with osteoconductive elements and antibacterial core-shell nanoparticles: A new generation of materials for dental implants," Materials Science and Engineering: C, vol. 120, p. 111761, 2021.

8 Introduction

Implant surfaces with cytocompatible and antibacterial properties are extremely desirable for the prevention of implant's infection and the promotion of osseointegration. Thus, the development of stable implant surfaces having both cytocompatibility and antibacterial activity has a scientific and clinical importance. In the previous CHAPTER VII, the combination of MAO, that allowed the production of porous structured surface enriched with Ca and P mimicking bone morphology and chemical composition, and DC magnetron sputtering technique, to deposit Zn/ZnO nanoparticles covered (or not) by a thin carbon layer, to further induce the osteogenic performance and confer antibacterial properties, respectively, was proposed.

Thus, as the proposed the novelty of endowing tantalum-based surfaces with cytocompatibility and antibacterial activity, the main focus of this chapter is to characterize the biological responses of the modified surfaces TaCaP, TaCaP-Zn and TaCaP-ZnC, using the untreated Ta surface as control, regarding to their cytotoxicity, MG-63 cell adhesion (DNA content and cell viability), cell viability and proliferation (by direct and indirect assays). The antibacterial activity of both planktonic and sessile *S. aureus* bacteria was assessed by optical density, CFUs and resazurin viability assay.

To better briefly illustrate the experimental procedure, a diagram is shown in Figure VIII.1.

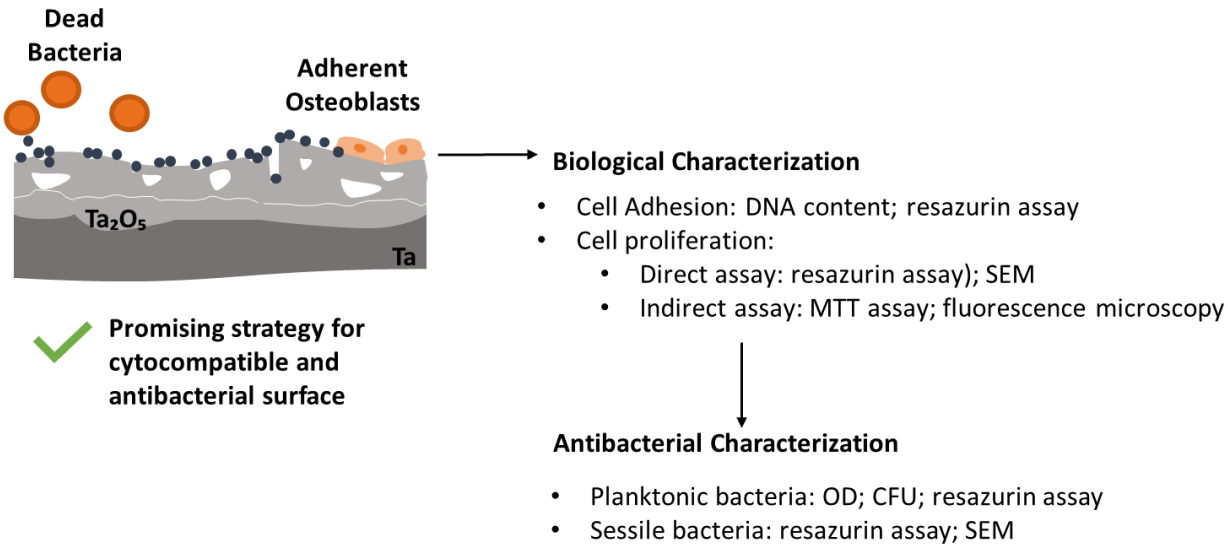

Figure VIII.1. Diagram of experimental procedure.

8.1 Assessment of sterilization resistance

Firstly, all the samples were sterilized as described in 3.2.5 section. As previously stated, an implant surface must be resistant to sterilization processes, thus it is crucial to guarantee that the surfaces are not damaged with the sterilization process and the Zn/ZnO NPs remains on the surface. In this sense, TaCaP-Zn surface was chosen to be characterized by SEM/EDS after sterilization treatment because it is the surface that combined both surface modification by MAO and magnetron sputtering without the carbon layer that would protect the Zn/ZnO nanoparticles release. After sterilization, the nanoparticles were observed on the porous anodic layer (Figure VIII.2-A), and no evident morphologic differences are noticed when compared with the TaCaP-Zn surface before sterilization (Figure VII.3-A). Additionally, Zn is clearly detected by EDS (Figure VIII.2-B), as well as all the chemical elements of the substrate (TaCaP surface), i.e., Ta, O, Ca and P.

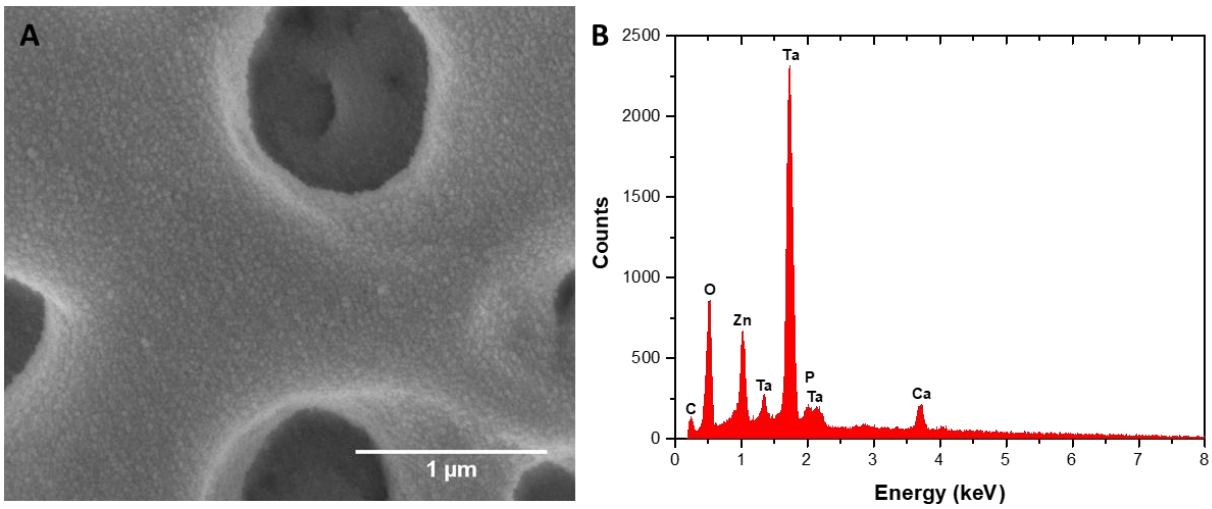

Figure VIII.2. A) SEM micrograph and B) EDS spectrum of TaCaP-Zn surface after sterilization.

8.2 Cytocompatibility of porous Ta_2O_5 samples

8.2.1 Direct assay

8.2.1.1 Cell adhesion

The material samples leached in PBS for 4 h, 24 h and 7 days were seeded with osteoblastic cells, and cell behavior was analysed for cell adhesion. The initial interaction with the material surface is of upmost relevance as it is determinant for the subsequent cell proliferation and function throughout the culture [1]. As such, Figure VIII.3-A presents the results for the DNA content and metabolic activity measured at 24 h after cell seeding on the different Ta substrates, thus providing information concerning the amount

of adherent cells and its viability, respectively. Overall, the initial cell adhesion was strongly improved with surface modification and, for each material, dependent on the leaching/immersion treatment. Ta samples presented the worst performance; DNA content was low in the samples immersed for 4 h and 24 h but increased significantly in those leached for 7 days. Cell adhesion was clearly improved in TaCaP samples (higher DNA content), a behavior most probably associated to the presence of Ca and P on the material surface. Still, a tendency for an increased cell adhesion was verified in the materials immersed for longer times, due to on-going surface events of material leaching/deposition of ionic species resulting in a conditioned surface that favors cell adhesion. Comparatively, a more complex surface behavior is expected during the immersion of the Zn-containing samples in PBS. As mentioned in the previous section, a burst release of Zn ions was observed in the first 24 h, following by a stationary phase (TaCaP-Zn) or a slow increase (TaCaP-ZnC). Thus, on-going release/deposition of Ca, P and Zn-containing species, coming from the material surface and/or the PBS, should be occurring during the immersion period. Thus, the surface topography and chemistry of the samples is expected to change substantially during the PBS immersion. It is interesting to note that cell adhesion on TaCaP-Zn is clearly improved in the samples leached for longer time periods (i.e., 24 h and 7 days). However, coating the TaCaP-Zn samples with a thin C layer clearly had a significant improved effect on cellular adhesion in the 4 h-leached samples and, interestingly, TaCaP-ZnC samples leached for different immersion times (4 h, 24 h, 7 days) presented similar behavior. Compared to TaCaP-Zn, the morphology achieved by the deposited C layer on TaCaP-ZnC samples clearly favored cell adhesion. Further, the slightly more controlled Zn release from these samples is also expected to contribute to the higher cell viability, compared to that on TaCaP-Zn samples.

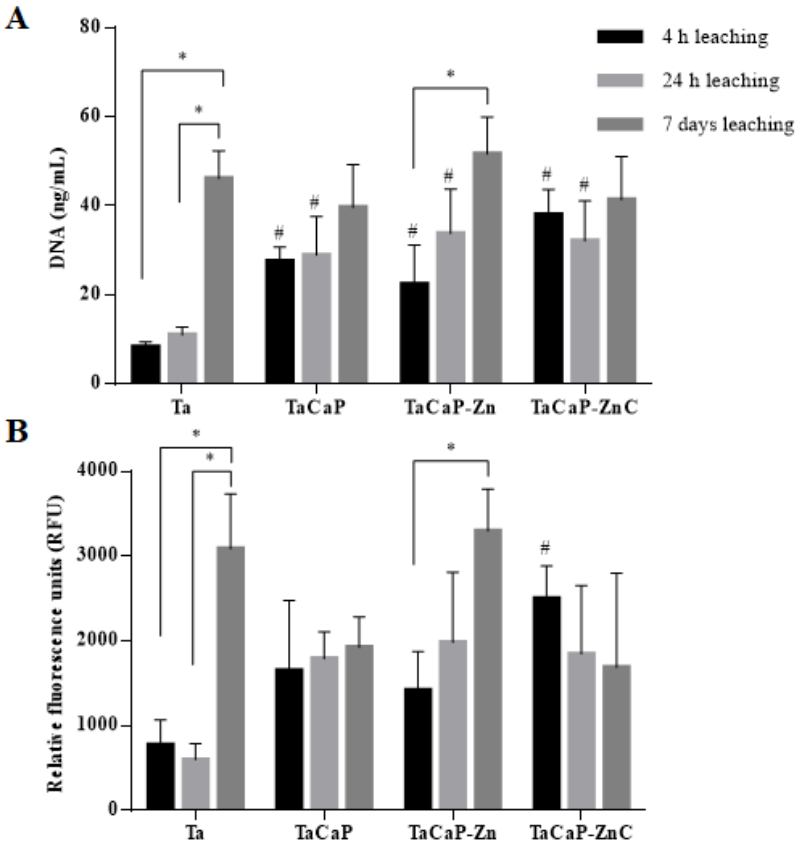

Figure VIII.3. DNA content (A) and metabolic activity (B) of MG-63 osteoblastic cells cultured for 24 h over Ta, TaCaP, TaCaP-Zn and TaCaP-ZnC samples leached in PBS for 4 h, 24 h and 7 days. Significant values as *p ≤ 0.05, compared to leaching time points of the sample; # p ≤ 0.05, compared to the control (Ta surface) for the same leaching time point.

Figure VIII.3-B shows the results for the metabolic activity of the adhered cells. The variation pattern was similar to that observed in the DNA content, either considering the different Ta substrates and the immersion time, clearly proving the viability of the adhered cells for higher leaching times.

As a whole, main differences in the cell adhesion/viability were noted in the samples leached for 4 h, due to the expected higher differences among the materials' surface features. With the higher immersion times, i.e., 24 h and 7 days (especially, the later), the dynamic release/deposition events progressively tend towards an equilibrium approaching the materials' surface properties. Accordingly, no significant differences were observed in the DNA content and cell viability among the materials.

8.2.1.2 Long-term cell metabolic activity

Cell metabolic activity was assessed up to 14 days in the material samples leached for 4 h, 24 h and 7 days (Figure VIII.4), by the Resazurin assay. In all surfaces, values increased throughout the culture time attaining a stationary phase around day 10 (similar values at days 10 and 14). Samples leached for different immersion times presented differences in the pattern of cell viability/growth. Values observed on the samples leached for 4 h are shown in Figure VIII.4-A. Ta samples clearly presented lower values

compared to all materials. TaCaP and TaCaP-Zn surfaces displayed similar cell proliferation tendency, but TaCaP-ZnC stood out mainly after 7 days of cell culture (higher values at days 10 and 14). On the 24 h leached materials, Ta samples also presented the lowest viability/proliferation values, but all modified materials exhibited similar behavior (Figure VIII.4-B). After 7 days leaching, the samples did not show significant differences (Figure VIII.4-C). As mentioned above, the samples' surfaces became morphologically and chemically similar with the immersion time in PBS and consequently cell behavior over the samples get closer. Accordingly, the more notorious differences were registered in the samples subjected to 4 h leaching. This was especially evident in Ta samples, presenting the worst behavior. On the other hand, TaCaP-ZnC samples exhibited the highest amount of adherent cells (highest values on day 1), which translated into a higher viability/proliferation rate.

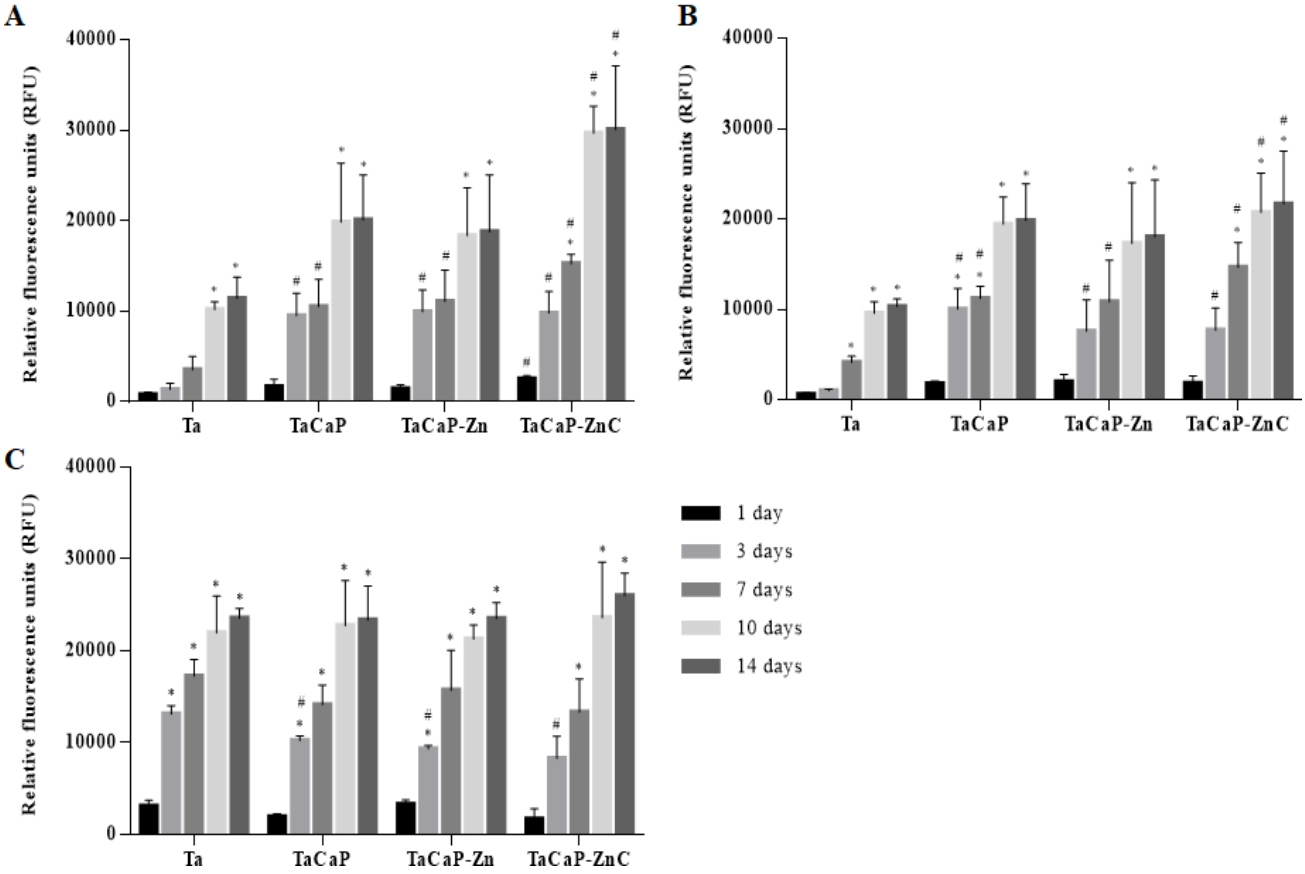

Figure VIII.4. Metabolic activity of MG-63 osteoblastic cells cultured for 14 days over Ta, TaCaP, TaCaP-Zn and TaCaP-ZnC samples leached in PBS for A) 4 h; B) 24 h and C) 7 days. Significant values as *p $\leq$ 0.05, compared to the initial adhesion on the sample; #p $\leq$ 0.05, compared to the control (Ta surface) for the same time point.

8.2.1.3 Cell/material interaction

Material samples cultured for 14 days were observed by SEM (Figure VIII.5-A). Images showed that, as it was observed in the cell viability/proliferation results, the major differences among the materials, particularly between the Ta surface and the modified samples, were observed in the materials leached

for 4 h and 24 h. Thus, the flat Ta surface was only partially covered by cells, contrasting with the modified porous structures exhibiting a dense cell layer. Samples leached for 7 days, including Ta flat surface, were fully covered by cells, in line with the results described in the previous section (Figure VIII.4-C).

The modified materials leached for 4 h were observed at a high magnification (Figure VIII.5-B) allowing a close view of the cells interacting with the samples' morphology. TaCaP and TaCaP-Zn displayed similar behavior, i.e., the cells fully permeating the porous structure. This was also observed in TaCaP-ZnC samples. However, additionally, more complex interactions appeared evident, namely the presence of thin and long cytoplasmic extensions anchoring to the higher protrusion surface structures as well as a dense thin network within the subjacent porous structure. This might explain the better results displayed for TaCaP-ZnC regarding cell adhesion and viability after 24 h culture time (Figure VIII.3), that translated to the higher viability values attained throughout the 14-day culture time, compared to TaCaP and TaCaP-Zn (Figure VIII.4-A).

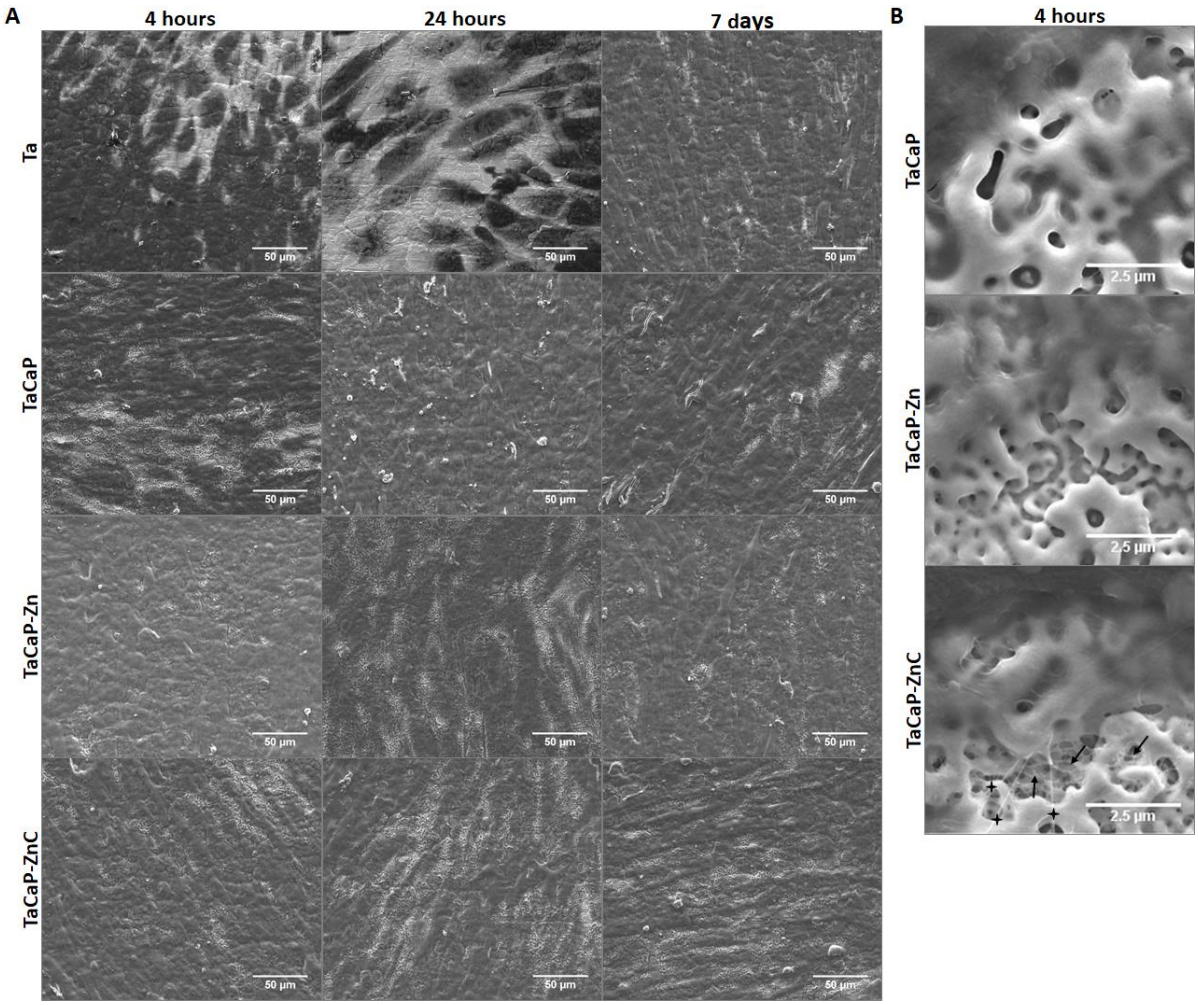

Figure VIII.5. A) Top-views SEM micrographs of MG-63 osteoblastic cells on the samples leached for 4 h, 24 h and 7 days, after culturing for 14 days; scale bar: 50 µm; B) High magnification images of the modified surfaces: thin and long cytoplasmic extensions (cross) and a dense thin network within the subjacent porous structure (arrow); Scale bar: 2,5 µm.

8.2.2 Indirect assay

In the indirect cytocompatibility assay, osteoblastic cells were cultured in the presence of the leachates resulting from the incubation of the material samples in PBS for 4 h, 24 h and 7 days (dilution, 1:2). Cell response was evaluated for cell adhesion, morphology and organization of the F-actin cytoskeleton at 24 h exposure time and for viability/proliferation throughout a 7-day exposure period.

Figure VIII.6-A displays CLSM images of the 24 h-cultures, stained for F-actin cytoskeleton, nucleus and mitochondria. A well-organized cell layer, partially covering the culture surface, was observed in the cultures exposed to the leachates of all materials. Cells presented an elongated morphology with a spread cytoplasm and a defined F-actin cytoskeleton presenting higher staining intensity at the cell membrane which is clearly evidenced in the cell-to-cell interactions. Cells also displayed well-developed nucleus (with easily visible nucleoli) and a perinuclear distribution of the mitochondria. This behavior was similar in all cultures and suggests the presence of healthy cells. A representative high magnification image is shown in Figure VIII.6-B, for the cultures exposed to the leachate from TaCaP-ZnC obtained after 4 h incubation.

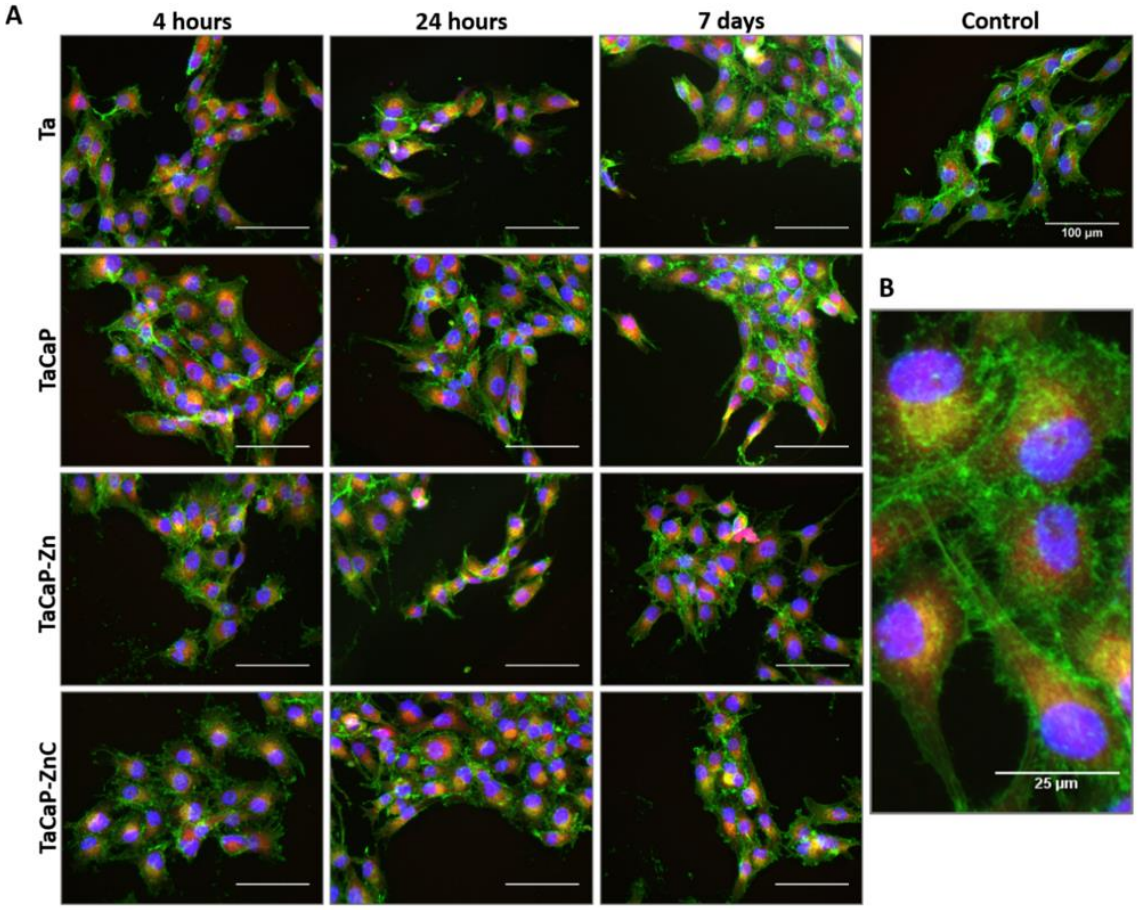

Figure VIII.6. A) Fluorescence images of MG-63 osteoblastic cells after 24 h exposure to the materials leachates resulting from the immersion of the samples for 4 h, 24 h and 7 days. B) High magnification image of the cultures exposed to the leachates (4 h immersion) from TaCaP-ZnC. Staining for F-actin cytoskeleton (green), nucleus (blue) and mitochondria (red). Scale bar: A - 100 µm; B - 25 µm.

Cell metabolic activity was assessed throughout a 7-day exposure to the leachates, Figure VIII.7. In line with the previous results, metabolic activity assessed at 24 h showed quite similar values in the presence of all leachates, and identical to those on control cultures (not exposed to the extracts). The same behavior was observed after 3 days and 7 days exposure. Hence, in the Zn-containing materials, the Zn content/kinetics release was associated with no or minimal cytotoxicity to osteoblastic cells. Zn ions cause dose-dependent effects in cell behavior. At high concentrations, dissolved Zn is known to induce cellular toxicity via production of reactive oxygen species (ROS) and disruption of energy metabolism [2, 3]. Additionally, a study of Song and his co-workers [4] demonstrated that dissolved Zn^{2+} played the main role in toxic effect of ZnO nanoparticles inducing 50% of cell death when the zinc ions concentration was approximately 10 μg/mL, equivalent to 10 ppm [2], which was near to the cytotoxicity of $ZnCl_2$ (IC_{50}=13.33 μg/mL) [4]. In the present work, the concentration of released Zn^{2+} from TaCaP-Zn and TaCaP-ZnC over a period of 7 days was significantly lower than 10 ppm, i.e., lower than 0.3 ppm, as described above (Figure VII.5), which would explain the lack of cytotoxicity of these material leachates.

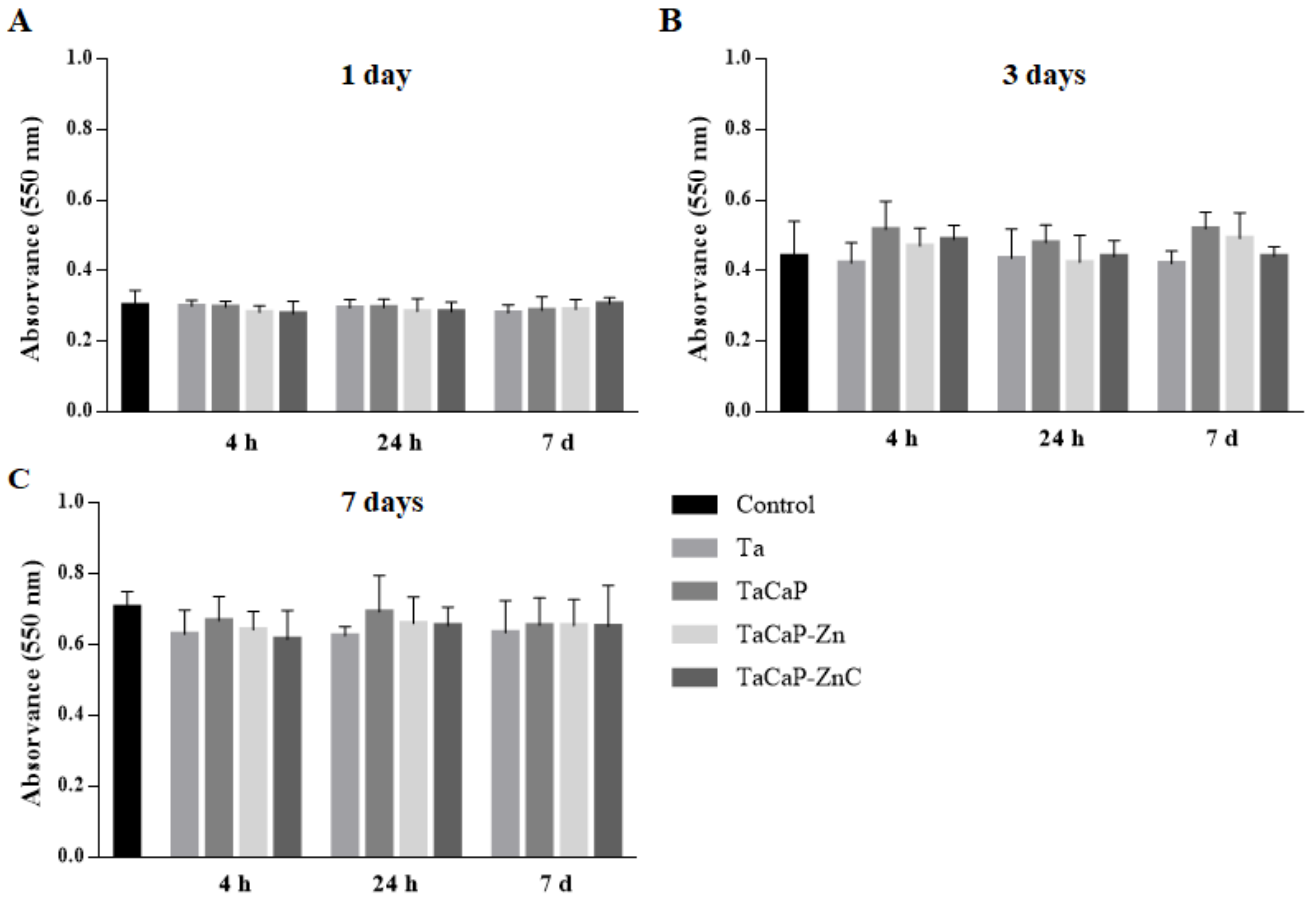

Figure VIII.7. Metabolic activity of MG-63 osteoblastic cells exposed to the materials leachates resulting from the immersion of the samples for of 4 h, 24 h and 7 days; exposure time: A) 1, B) 3 and C) 7 days.

8.2.3 Cytocompatibility overview

Treatment of Ta surface by MAO, by developing a porous oxide layer enriched with Ca and P (TaCaP), clearly improved cell adhesion, viability and proliferation. With the incorporation of Zn/ZnO nanoparticles (TaCaP-Zn), main topography features were kept but the surface appeared coated with a layer of Zn/ZnO nanoparticles. A variety of studies shows that the biological outcome of surfaces with Zn/ZnO nanoparticles is highly dose dependent. Several works reported that Zn-containing oxide layers with a certain dosage can be beneficial to *in vitro* and *in vivo* biological performance, such as osteoblast-like cells adhesion, proliferation, differentiation and bone formation around the implant [2, 5-7]. Interestingly, a comparative study of two Zn-containing coatings, one with entire incorporation of Zn in the coating while the other with a superficial incorporation, disclosed that the second coating, which possessed the smallest total Zn concentration and a more controllable ions release, had the best osteogenic characteristics and bone regeneration capacity, suggesting that the biological responses can be enhanced with the introduction of a safe Zn amount [6]. High surface amounts cause cytotoxicity by several mechanisms, namely by the generation of ROS at the material surface as well as the uncontrolled fast release of Zn^{2+}, both leading to cell homeostasis disruption [8]. However, Zn-associated factors merely have a contribution to the cell response, and, for instance, a variety of studies did not find a correlation between Zn ions release and cell adhesion in the first 24 h of culture [8, 9]. The dynamic interactions of the physical and chemical surface features in the physiological fluids (or, in the culture medium, in *in vitro* conditions) are also a major factor in the cell behavior. This seems clear in the present work, comparing the biological performance of TaCaP-Zn and TaCaP-ZnC by integrating the results of the direct and the indirect assays. Over TaCaP-Zn, cell adhesion (inferred from the DNA content at 24 h) was greatly impaired in the samples leached for a short period (4 h) compared to those leached for longer periods (24 h; 7 days), as shown in Figure VIII.3. Interestingly, coating TaCaP-Zn samples with a thin carbon layer markedly improved cell behavior. The coating created a smoother surface morphology (Figure VII.3-B and Table VII.2) and, also, allowed a different Zn^{2+} kinetic release (Figure VII.5). On TaCaP-ZnC samples, cell adhesion was clearly improved for all the immersion times. Additionally, the better cell adhesion translated into an increased amount of metabolic active cells throughout the culture time (Figure VIII.4 and Figure VIII.5). Accordingly, several studies demonstrated that carbon substrates (nanoparticles, nanotubes, layers etc.) provided an important support for adhesion and spreading of human osteoblast cells (MG-63 cells) [10]. However, another relevant factor should be noted. Considering that in the ZnO rich surfaces, the local generation of ROS is an important source of cytotoxicity, the thin carbon layer on TaCaP-ZnC might prevent/decrease this direct surface-associated ZnO toxicity. These thoughts are corroborated by the results observed in the indirect assay of cytocompatibility (Figure VIII.6 and Figure VIII.7). Thus, the leachates from TaCaP-

Zn and TaCaP-ZnC obtained upon incubation of the material samples in PBS for 4 h, 24 h and 7 days did not affect cell viability/proliferation through an exposure period of 7 days. This observation suggests that the dissolved Zn^{2+} levels in the leachates are too low and not associated to cytotoxic effects, strengthening the relevance of the surface features of the two Zn-containing samples in their biological outcome. In terms of cytocompatibility, the combined morphologic and chemical surface features of TaCaP-ZnC sustains a better initial cell adhesion. This initial cell/biomaterial interaction is of upmost relevance, and the enhancement of the cell adhesion on modified surfaces is determinant on the following cell proliferation associated to the production of the extracellular matrix that subsequently become mineralized, contributing to a faster osseointegration [11]. Thus, considering a translational view, different biological outcomes might be anticipated with the two developed Zn-containing materials. Upon the material implantation, improved cell adhesion would be expected on TaCaP-ZnC. On the other hand, the direct cellular interactions with the Zn/ZnO nanoparticles layer on TaCaP-Zn would be impaired due to the associated initial surface toxicity. However, due to the dynamic *in vivo* conditions, i.e., the continuous extracellular fluid flow, clearing excessive ion release and further conditioning the material surface (with dynamic release/deposition events), the initial surface toxicity is expected to be quickly overcome compared to that observed in the *in vitro* static conditions. Thus, it can be hypothesized that, *in vivo*, the differences between TaCaP-Zn and TaCaP-ZnC would be attenuated compared with that observed *in vitro*. This is supported by a variety of studies, namely Li *et al.* [12] demonstrating that the material samples with high Zn ions release showed *in vitro* cytotoxicity, but improved *in vivo* biological performance, which was explained by the dilution effect of blood flow leading to Zn clearance from the vicinity of the implant.

8.3 Antibacterial activity of porous Ta_2O_5

As after the first 24 h post-implantation a pathogenic biofilm can be formed, the inhibition of bacterial adhesion is a critical step to prevent an implant-associated infection [13]. Thus, the antibacterial activity of the developed surfaces was evaluated by assessing the inhibition of planktonic and sessile *S. aureus* (Figure VIII.8). In the resazurin assay, which evaluates viable bacteria, a statistically significant reduction of approximately 70% and 63% was observed in the presence of TaCaP-Zn and TaCaP-ZnC surfaces respectively, when compared to Ta control (Figure VIII.8-A). OD data, accounting the total mass of bacteria in suspension (dead and live), showed a reduction in the presence of the Zn-containing materials, although without statistical significance compared to the other materials (Figure VIII.8-A). On the other hand, CFU method revealed a significant reduction of viable bacteria in the presence of TaCaP-Zn surface, with no significant differences among the other modified surfaces, comparing to Ta control (Figure VIII.8-B). However, no log reduction in bacteria growth was registered. In light of these results, live planktonic

bacteria were significantly reduced on the presence of the samples with Zn/ZnO nanoparticles showing their antibacterial activity, although not clinically significant. Similarly, a study demonstrated a reduction of planktonic bacteria activity tendency in line with the zinc ions release from the ZnO nanoparticles, attributing to the Zn^{2+} release the responsibility for bacteria functions disruption [14].

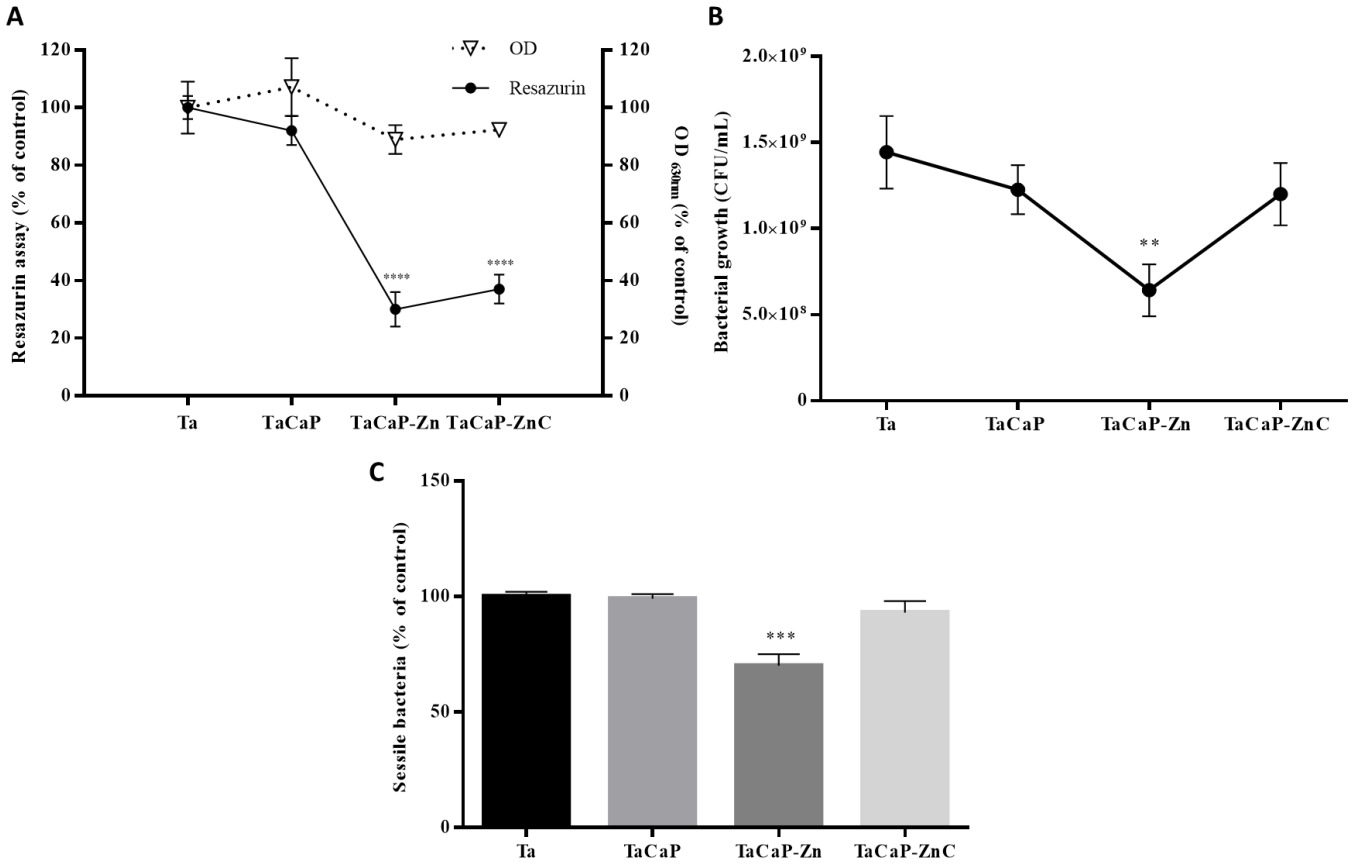

Figure VIII.8. Planktonic population of *S. aureus* after 24 h of incubation in Ta (control), TaCaP, TaCaP-Zn and TaCaP-ZnC surfaces. Quantification of A) OD and resazurin assay method and B) CFU/mL. C) . *S. aureus* sessile population on Ta (control), TaCaP, TaCaP-Zn and TaCaP-ZnC surfaces (as a percentage of sessile population on control), after 24 h of incubation; Quantification by resazurin assay method. Significant values as *p ≤ 0.05, significant reduction compared to control (Ta surface).

Furthermore, regarding sessile bacteria ((Figure VIII.8-C), TaCaP-Zn surface also caused a reduction (~30%) of the metabolic active bacteria on its surface, whereas TaCaP-ZnC surface showed a small inhibition (~7%). The morphology and membrane integrity of the sessile bacteria were examined by SEM (Figure VIII.9), *S. aureus* has a typical spherical morphology [7] as that observed on TaCaP and TaCaP-ZnC surfaces. On these surfaces, bacteria preferentially adhere and grow around and inside pores, where it is already possible to obverse an initial biofilm formation. However, over TaCaP-Zn bacteria presented significant alterations in the membrane integrity, mostly reflected by a disrupted morphology and lysed cells, unable to attach and proliferate. Accordingly, a significant reduction in the amount of adhered bacteria was evident, compared to the other materials. The underlying antibacterial mechanism is believed to be associated to several factors, namely complex interactions of surface topographical

features, Zn content and distribution, Zn^{2+} kinetics release profile [2, 5, 15], resulting in the generating of ROS, such as H_2O_2, and the accumulation of nanoparticles in the bacterial cytoplasm or on the outer membranes [15]. Back to the present work, TaCaP-Zn has the best bacterial activity against *S. aureus in vitro*, having the ability to reduce both planktonic and sessile bacteria.

In fact, a strong antibacterial ability is necessary in the initial stage after the surgery, as the implant in this point is more susceptible to infection [13]. The higher initial Zn^{2+} release from the TaCaP-Zn can efficiently kill adherent bacteria and the surrounding planktonic bacteria in this early stage to prevent perioperative infection. Inhibition of biofilm formation by preventing bacterial colonization on the implant surface is expected to be sufficient to prevent further infection with the help of the host defense response. Following, osseointegration is progressively established by the osteogenic activity at the implant surface.

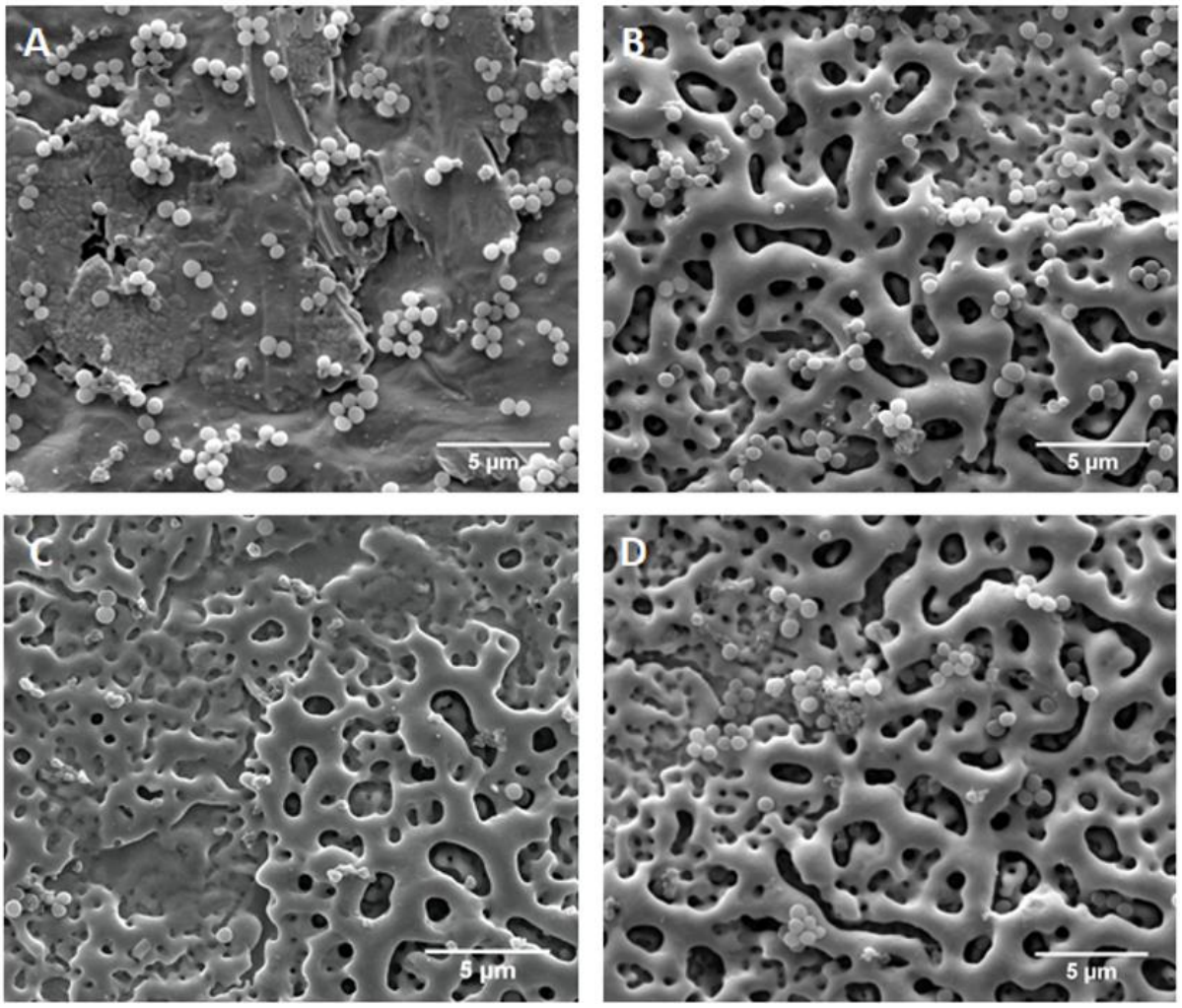

Figure VIII.9. Top-views SEM micrographs of S. aureus sessile population after 24 h incubation on A) Ta, B) TaCaP, C) TaCaP-Zn and D) TaCaP-ZnC sample's surfaces. Scale bar: 5 µm.

In the present study both MAO and DC magnetron sputtering techniques were combined in order to endow Ta-based surfaces with cytocompatibility and antibacterial activity. The present results demonstrated that micro-porous Ta_2O_5 containing CaP significantly improved the initial cell adhesion which

was significantly enhanced by the coating of Zn/ZnO nanoparticles with a carbon layer (TaCaP-ZnC), due to surface induced alterations in the morphology together to an appropriate modulation of the interfacial cell/ZnO interactions. The *in vitro* results suggested a paradigm in which these surface features improve the biological response compromising the antibacterial ability, compared to that observed with TaCaP-Zn samples. Thereby, these data highlight the importance of balance the desired cytocompatibility and antibacterial mechanisms in order to optimize surface coatings for the next generation of hard tissues implants. Thus, modified surface of Ta combining MAO and DC magnetron sputtering techniques is a potential alternative to Ti implants.

8.4 Partial conclusions

The modified samples were cytocompatible to osteoblastic cells. Comparatively, TaCaP-ZnC presented improved cell adhesion and proliferation, as the carbon coating provided a cell friendly based carbon smoother morphology and, eventually, modulate the interfacial cellular interactions with the Zn/ZnO nanoparticles layer by decreasing direct contact-mediated Zn^{2+} toxicity. Although not clinically significant, both TaCaP-Zn and TaCaP-ZnC demonstrated activity against planktonic *S. aureus*, however only TaCaP-Zn inhibit the sessile bacteria colonization. In light of these results, combining both techniques endowed Ta-based implants with superior biocompatibility by promoting the initial cell adhesion and proliferation as well as an antibacterial activity, being promising pointers for osseointegration and for prevention of initial bacterial colonization, respectively. Therefore, due to the excellent *in vitro* performance of the nanostructured Ta surface, this work is clearly a progress on the strategy to develop a new generation of dental implants.

8.5 References

[1] A. A. Khalili and M. R. Ahmad, "A Review of cell adhesion studies for biomedical and biological applications," *International Journal of Molecular Sciences,* vol. 16, pp. 18149-18184, 2015.

[2] H. Hu, W. Zhang, Y. Qiao, X. Jiang, X. Liu, and C. Ding, "Antibacterial activity and increased bone marrow stem cell functions of Zn-incorporated TiO2 coatings on titanium," *Acta Biomaterialia,* vol. 8, pp. 904-915, 2012.

[3] T. D. Zaveri, N. V. Dolgova, B. H. Chu, J. Lee, J. Wong, T. P. Lele*, et al.*, "Contributions of surface topography and cytotoxicity to the macrophage response to zinc oxide nanorods," *Biomaterials,* vol. 31, pp. 2999-3007, 2010.

[4] W. Song, J. Zhang, J. Guo, J. Zhang, F. Ding, L. Li*, et al.*, "Role of the dissolved zinc ion and reactive oxygen species in cytotoxicity of ZnO nanoparticles," *Toxicology Letters,* vol. 199, pp. 389-397, 2010.

[5] K. Huo, X. Zhang, H. Wang, L. Zhao, X. Liu, and P. K. Chu, "Osteogenic activity and antibacterial effects on titanium surfaces modified with Zn-incorporated nanotube arrays," *Biomaterials,* vol. 34, pp. 3467-3478, 2013.

[6] Y. Qiao, W. Zhang, P. Tian, F. Meng, H. Zhu, X. Jiang*, et al.*, "Stimulation of bone growth following zinc incorporation into biomaterials," *Biomaterials,* vol. 35, pp. 6882-6897, 2014.

[7] G. Jin, H. Qin, H. Cao, S. Qian, Y. Zhao, X. Peng*, et al.*, "Synergistic effects of dual Zn/Ag ion implantation in osteogenic activity and antibacterial ability of titanium," *Biomaterials,* vol. 35, pp. 7699-7713, 2014.

[8] L. Sopchenski, K. Popat, and P. Soares, "Bactericidal activity and cytotoxicity of a zinc doped PEO titanium coating," *Thin Solid Films,* vol. 660, pp. 477-483, 2018.

[9] F. Velard, D. Laurent-Maquin, J. Braux, C. Guillaume, S. Bouthors, E. Jallot*, et al.*, "The effect of zinc on hydroxyapatite-mediated activation of human polymorphonuclear neutrophils and bone implant-associated acute inflammation," *Biomaterials,* vol. 31, pp. 2001-2009, 2010.

[10] L. Bacakova, L. Grausova, and M. Vandrovcova, "Carbon nanoparticles as substrates, for cell adhesion and growth," L. Simone Luca, Ed., ed, 2008, pp. 1-71.

[11] L. Bai, Z. Du, J. Du, W. Yao, J. Zhang, Z. Weng*, et al.*, "A multifaceted coating on titanium dictates osteoimmunomodulation and osteo / angio-genesis towards ameliorative osseointegration," *Biomaterials,* vol. 162, pp. 154-169, 2018.

[12] Y. Li, W. Xiong, C. Zhang, B. Gao, H. Guan, H. Cheng*, et al.*, "Enhanced osseointegration and antibacterial action of zinc-loaded titania-nanotube-coated titanium substrates: In vitro and in vivo studies," *Journal of Biomedical Materials Research - Part A,* vol. 102, pp. 3939-3950, 2014.

[13] E. M. Hetrick and M. H. Schoenfisch, "Reducing implant-related infections: Active release strategies," *Chemical Society Reviews,* vol. 35, pp. 780-789, 2006.

[14] J. T. Seil and T. J. Webster, "Reduced Staphylococcus aureus proliferation and biofilm formation on zinc oxide nanoparticle PVC composite surfaces," *Acta Biomaterialia,* vol. 7, pp. 2579-2584, 2011.

[15] K. R. Raghupathi, R. T. Koodali, and A. C. Manna, "Size-dependent bacterial growth inhibition and mechanism of antibacterial activity of zinc oxide nanoparticles," *Langmuir,* vol. 27, pp. 4020-4028, 2011.

CHAPTER IX- Conclusions, Current and Future Developments

9 Conclusions, current and future developments

In this work it was demonstrated that tantalum is more bioactive than the commercial pure Ti, and consequently Ta surface modification was deeply investigated by anodization in order to achieve a bone-like morphology and chemical composition. By anodization, an economic and versatile technique, with the challenge of use HF-free electrolytes, it was possible to create a nanoporous structure followed by a second optimized anodization step to incorporate osteoconductive elements from the precursors present on the electrolyte reaching the Ca/P ratio similar to the theoretical value of the HAp, with a top layer composed by amorphous calcium phosphates and calcium carbonates. This second step was also investigated combining reverse polarization and anodization, whose approach strongly promoted the cations incorporation on the anodic layer affecting the porous structure and the Ca/P ratio. Moreover, both surface roughness and surface hydrophilicity increased with anodization treatment. The achieved surface properties were good pointers for an enhancement of osseointegration. However, HF-free anodization process revealed to be very complicated since it demonstrated adhesion problems during its optimization and ultimately resulted in stacked porous layers instead of one anodic porous layer. Face to this unwanted morphology, a different approach had to be adopted. Micro-arc oxidation (MAO) process was selected as it is a process derived from anodization that in practice only differs on the working applied potential, that, in this case, has to be above the tantalum oxide dielectric breakdown potential. MAO allows to create simultaneously a micro/nano-porous morphology and incorporation of the osteoconductive elements on one single step. According to previous background of Ta treated by MAO, the process was optimized changing the electrolyte composition to reach the desired Ca/P ratio. This modification process induced a significant increase in the surface roughness but did not show a significant impact on water contact angle.

Zn/ZnO core-shell nanoparticles were deposited above the optimized MAO-treated Ta by DC magnetron sputtering. The deposition conditions allowed a deposition of nanoparticles (and not a layer) with different sizes and shapes over the all surface. An additional thin carbon layer was also deposited after the nanoparticles deposition to control the zinc ions release over time in order to have a more controlled antibacterial effect and non-toxicity for osteoblastic cells. TEM analysis showed that this carbon layer had a thickness of 1 nm. The Ta surface modified by both MAO and magnetron sputtering become rougher and hydrophobic. In fact, the ICP-OES assay demonstrated that the presence of the carbon layer delays the zinc ions release to 7 days of immersion instead of the total release in the first 24 h of immersion.

The biological characterization was assessed by the initial cell adhesion (DNA content and cell viability) and cell proliferation by direct (cell viability and SEM images) and indirect assays (MTT and CLSM images) in order to evaluate the cytocompatibility of the Ta surfaces which were leached in PBS for 4 h, 24 h and 7 days. All the Ta modified surfaces exhibited better biological responses comparing with the untreated Ta (control group), but the MAO-treated Ta surface with Zn/ZnO nanoparticles and the carbon layer outstand with statistically higher amount of adherent cell over the 14 days of culture as well as demonstrated thin and long cytoplasmatic extensions, a dense thin network (in the direct assay) and a well-defined F-actin cytoskeleton, well-developed nucleus and perinuclear distribution of the mitochondria (in the indirect assay). The results suggested that the Zn content/kinetic release was associated with no or minimal cytotoxicity to osteoblasts. Regarding the surface properties, firstly a porous structure showed a dense cell layer when compared to the flat untreated-Ta surface, translating the significant improvement on cell adhesion and proliferation. Then, the surface roughness showed a beneficial effect on cell responses as both rougher surfaces (i.e., both Zn-containing samples) had significantly enhanced the initial cell adhesion and cell proliferation. Curiously, these Zn-containing samples were the more hydrophobic surfaces which is not in line to the theory that hydrophilic surface induces better cell behaviour. Thus, according to these results the surface morphology and chemistry had a great impact on cell responses.

Antibacterial activity was evaluated by optical density and cell viability assays on both planktonic and sessile *S. aureus* bacteria. Statistically significant reduction of planktonic *S. aureus* related to total mass of bacteria and its viability, which was significantly more pronounced, were registered on both Zn-containing surfaces, but the sample without the carbon layer outstand in this point. Furthermore, this sample was the only one that showed statistically inhibition of sessile bacteria where the bacteria membrane integrity was compromised. For bacteria adhesion and colonization, neither surface morphology nor surface roughness appear to have any influence, but rather the presence of the Zn/ZnO nanoparticles and/or the zinc ions release. Although the balance between cell cytocompatibility and antibacterial activity has been achieved, the antibacterial performance does not show a clinical significance, thus it is crucial to be improved.

Face to these results, the current development is related to change the deposition conditions by DC magnetron sputtering in order to have more Zn/ZnO nanoparticles on the surface (and not a film), and after that perform viability assays (more specifically CFU method) to have an idea about the potentiality of each deposition condition in antibacterial inhibition. Over the best depositions, a deposition of a thin carbon layer will be performed and a possible matrix of carbon and zinc will be studied. Both

cytocompability and quantitative antibacterial assays have to be performed. Further, it should be also interesting to predict the actuation mechanism of antibacterial activity (zinc ions release, ROS formation, Zn/ZnO nanoparticles internalization) as well as study the osteoblastic differentiation and macrophages activation.

Currently, a prototype of a MAO-treated Ta implant is being developed. For that, a new anodizing cell was design and the anodizing parameters have been optimizing in order to reproduce the surface properties/characteristics achieved on the Ta surface. When a porous Ta dental implant surface with the desired Ca/P ratio is accomplished, the mechanical performance will be evaluated as implant insertion on the jawbone of pig, determining the bone-implant contact, and the tribological performance will be assessed using a chewing simulator.

Moreover, it will be interesting to characterize the cross-sectional MAO-treated Ta_2O_5 to correlate the porous structure and chemical elements distribution over the anodic layer. It is also relevant to determine the degree of porosity as well as the surface area to correlate with the biological and mechanical performances.

As the first mechanical stability is crucial to guarantee an adequate osseointegration, as future developments, it is important to study the oxide layer adhesion and mechanical properties, such as Young's modulus and fracture strength, as well as bio-tribocorrosion (wear and friction evaluation under simulated oral environments and different conditions of micromovements, cycle loads, pH). If all achievements are promising, the *in vivo* performance of Ta dental implant treated by MAO and DC magnetron sputtering will be proposed as a proof-of-concept.

ANNEX

ANNEX I: Bioactive performance of CP-Ti versus Ta

As a preliminary experiment, the starting Ta sheet was tested for its bioactivity, as compared to a CP-Ti surface (commercially pure Titanium grade 2). Samples were immersed in SBF for 28 days and observed by SEM, operating at 10 kV. The figure bellow displays A) the top-views SEM micrographs of the CP-Ti and B) Ta surfaces after immersion in SBF. For the same immersion time, no vestiges of apatite are observed on CP-Ti surface whereas some spherical-like particles are found in Ta surface. In light to this result, it is possible to confirm that Ta sheet is more bioactive (i.e. has higher ability to induce the apatite formation) than CP-Ti [1].

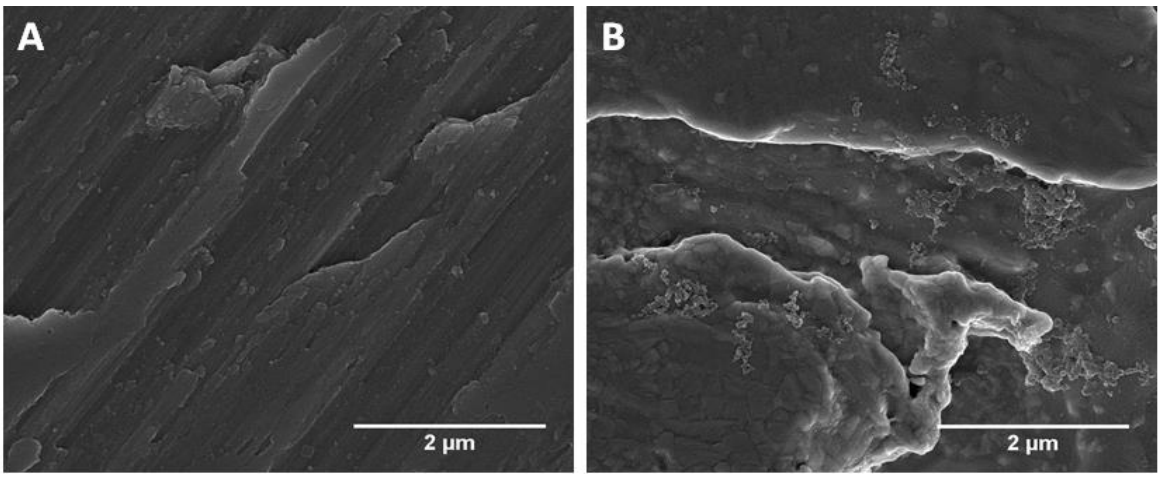

[1] T. Miyazaki, H. M. Kim, T. Kokubo, C. Ohtsuki, H. Kato, and T. Nakamura, "Mechanism of bonelike apatite formation on bioactive tantalum metal in a simulated body fluid," *Biomaterials,* vol. 23, pp. 827-832, 2002.

ANNEX II: Metabolic activity of MG-63 osteoblastic cells cultured for 12 days over CP-Ti and Ta surfaces.

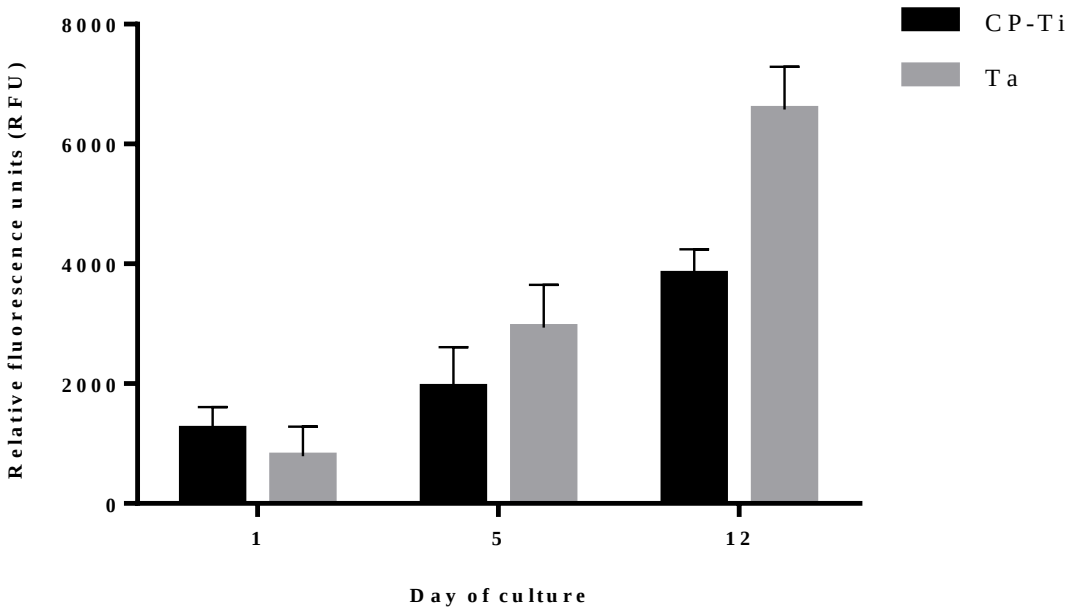

ANNEX III: XRD analysis of TaCaPMg5 sample

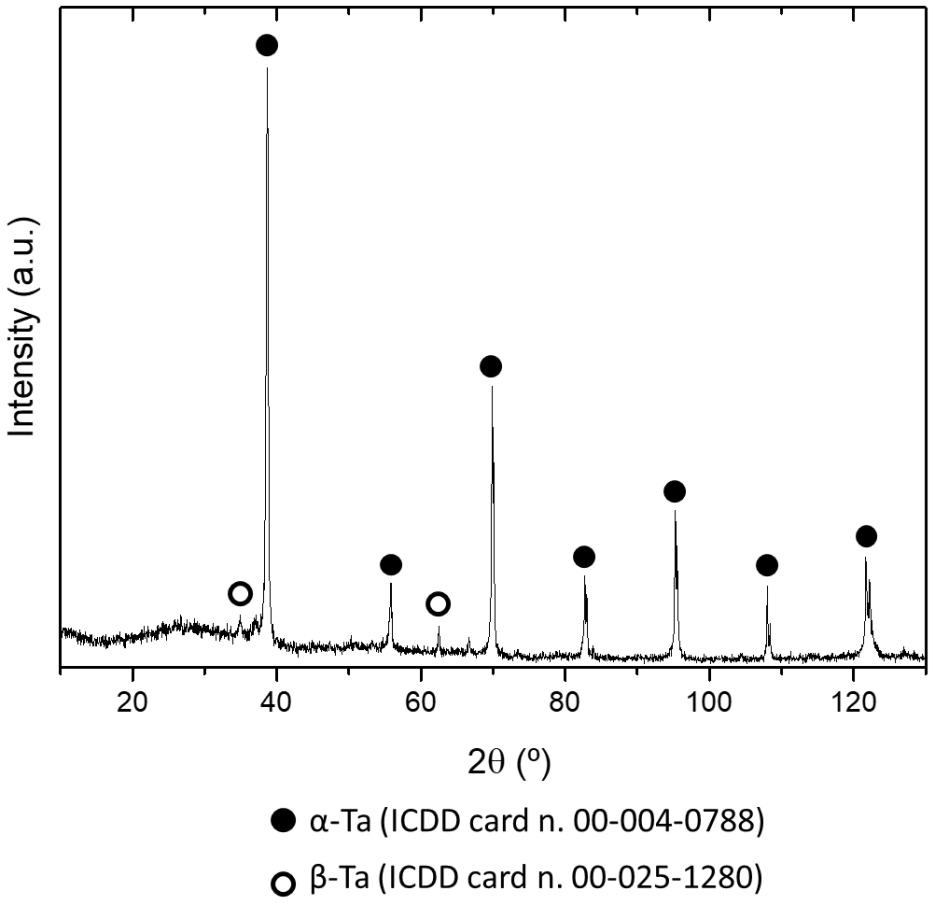

ANNEX IV: Cross-sectional micrograph and elemental distribution mappings of the TaCaP sample.

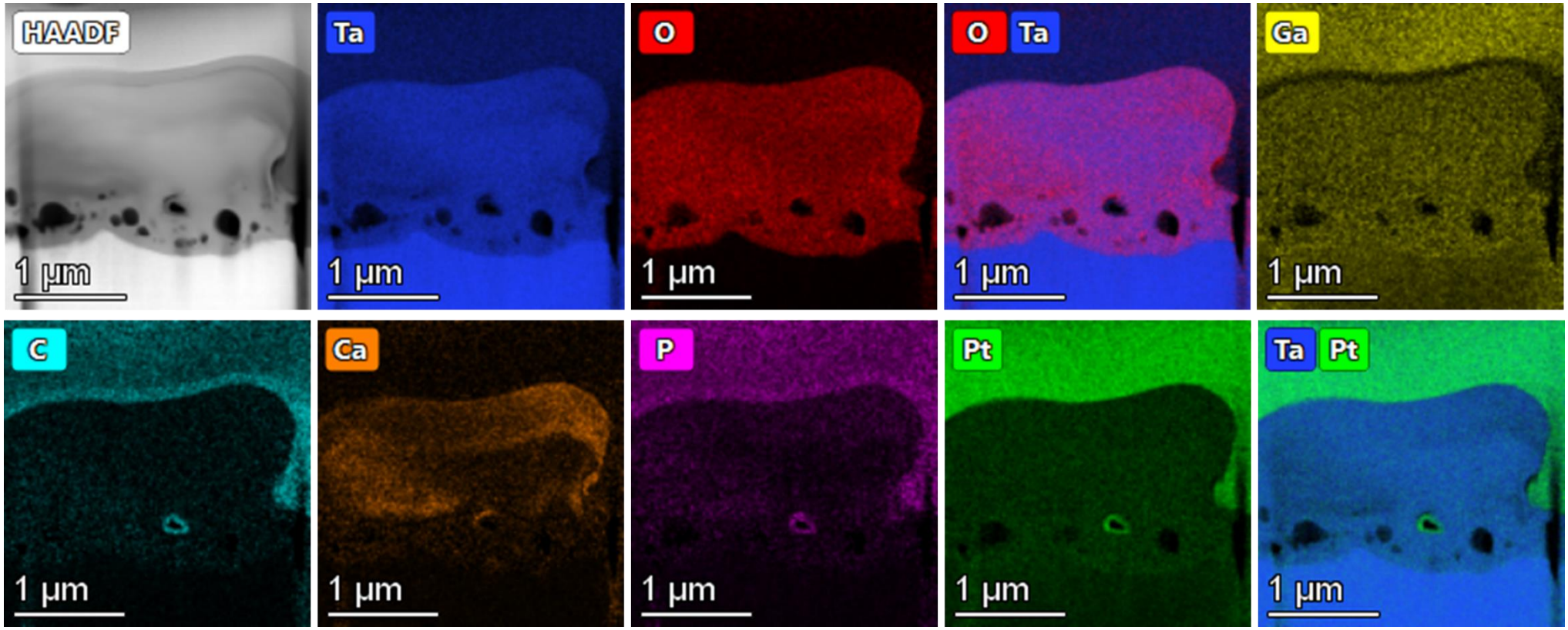

ANNEX V: XPS analysis of TaCaP-ZnC sample